Graduate School ETD Form 9
(Revised 12/07)

PURDUE UNIVERSITY
GRADUATE SCHOOL
Thesis/Dissertation Acceptance

This is to certify that the thesis/dissertation prepared

By Mariya Petrenko

Entitled
The Use of Satellite-Measured Aerosol Optical Depth to Constrain Biomass Burning Emissions Source Strength in a Global Model GOCART

For the degree of Doctor of Philosophy

Is approved by the final examining committee:

Dr. S. Lasher-Trapp
Chair

Dr. R. Kahn

Dr. Harshvardhan

Dr. M. Chin

Dr. W.-w. Tung

Dr. G. Michalski

To the best of my knowledge and as understood by the student in the *Research Integrity and Copyright Disclaimer (Graduate School Form 20)*, this thesis/dissertation adheres to the provisions of Purdue University's "Policy on Integrity in Research" and the use of copyrighted material.

Approved by Major Professor(s): Harshvardhan

Approved by: Jon Harbor — 04/20/2012
Head of the Graduate Program — Date

Graduate School Form 20
(Revised 9/10)

PURDUE UNIVERSITY
GRADUATE SCHOOL

Research Integrity and Copyright Disclaimer

Title of Thesis/Dissertation:

The Use of Satellite-Measured Aerosol Optical Depth to Constrain Biomass Burning Emissions Source Strength in a Global Model GOCART

For the degree of Doctor of Philosophy

I certify that in the preparation of this thesis, I have observed the provisions of *Purdue University Executive Memorandum No. C-22,* September 6, 1991, *Policy on Integrity in Research.**

Further, I certify that this work is free of plagiarism and all materials appearing in this thesis/dissertation have been properly quoted and attributed.

I certify that all copyrighted material incorporated into this thesis/dissertation is in compliance with the United States' copyright law and that I have received written permission from the copyright owners for my use of their work, which is beyond the scope of the law. I agree to indemnify and save harmless Purdue University from any and all claims that may be asserted or that may arise from any copyright violation.

Mariya Petrenko

Printed Name and Signature of Candidate

04/12/2012

Date (month/day/year)

*Located at http://www.purdue.edu/policies/pages/teach_res_outreach/c_22.html

THE USE OF SATELLITE-MEASURED AEROSOL OPTICAL DEPTH TO CONSTRAIN BIOMASS BURNING EMISSIONS SOURCE STRENGTH IN A GLOBAL MODEL GOCART

A Dissertation

Submitted to the Faculty

of

Purdue University

by

Mariya Petrenko

In Partial Fulfillment of the

Requirements for the Degree

of

Doctor of Philosophy

May 2012

Purdue University

West Lafayette, Indiana

ACKNOWLEDGEMENTS

First and foremost, I am grateful to Dr. Ralph Kahn, Dr. Mian Chin and Dr. Harshvardhan for providing their support, advice and guidance during the writing of this dissertation, and doing the research on which it is based. Thank you for keeping track of the big picture for me. I thank Dr. Sonia Lasher-Trapp, Dr. Wen-Wen Tung and Dr. Greg Michalski for providing much needed constructive criticism in the process of defining my research path, providing a motivation to deliver a good quality work, and for being supportive and open-minded. I am grateful to my professors and fellow students at EAS, with whom I had a great pleasure to work as a student, teaching assistant and a colleague during my stay at Purdue. A large part of this work was inspired and significantly influenced by scientists and research assistants at NASA Goddard Space Flight Center (GSFC), who taught me the basics and beyond of aerosol modeling and remote sensing, and continue to provide a thought-stimulating and challenging environment.

The invaluable opportunity to obtain a first-hand research experience at NASA GSFC while a student at Purdue University was made possible by the NASA Graduate Student Summer Program and NASA Earth and Space Science Graduate Fellowship, and I am grateful to all faculty and staff of Purdue University who were patient and willing to work out all the administrative details, as I was doing research away from campus.

I am grateful to my husband, Dr. Maksym Petrenko for his endless support and help in every aspect of my life and work, for keeping me motivated, filling the gaps, looking from a different perspective at the same problems, and sharing a load of daily tasks to make my graduate school a positive experience. And, of course, big thanks to Anna and Daniel for being easy and cheerful children, and providing laughs, rays of sunshine and patience training, so necessary for a young scientist.

TABLE OF CONTENTS

Page

LIST OF TABLES vii

LIST OF FIGURES viii

ABSTRACT xviii

CHAPTER 1 INTRODUCTION 1

1.1 Biomass Burning Aerosols and Their Representation in the Global Aerosol Models 1

1.2 Spaceborne Observations of Fires and Aerosol Properties 8

1.2.1. Moderate Resolution Imaging Spectroradiometer (MODIS) 8

1.2.2. Multiangle Imaging Spectroradiometer (MISR) 9

1.2.3. Cloud-Aerosol Lidar with Orthogonal Polarization (CALIOP) on CALIPSO Satellite 10

CHAPTER 2 METHODOLOGY 12

2.1 Estimating BB Emissions Based on Burned Area 12

2.1.1. Burned Area (*A*) 13

2.1.1. Biomass Density (*B*) and Fuel Consumption (*B**C*) 15

2.1.3. Emission Factors (F_j) 20

2.1.4 Global Fire Emission Dataset (GFED) Emission Estimates 21

2.2 Estimating BB Emissions Based on Fire Radiative Power (FRP) 22

2.3 BB Emission Options 23

Page

2.4 GOCART model 26
2.4.1 Biomass Burning Emissions in GOCART 27
2.4.2 Aerosol Optical Depth (AOD) 27
2.5 Satellite Observations of Aerosol 28
2.5.1 MODIS Aerosol Optical Depth 28
2.5.2 MISR Stereo Height and Aerosol Product 28
2.5.3 CALIPSO Vertical Feature Mask 29
2.6 Biomass Burning Events 29
CHAPTER 3 COMPARISON OF EMISSION OPTIONS 37
3.1 Comparison of Emission Estimates 37
3.2 Burned Area Comparison 45
3.3 Fuel Consumption Comparison 50
3.4 Emission Factors Comparison 51
3.5 Regional Specifics of Biomass Burning and Its Effects 53
CHAPTER 4 EVALUATION OF EMISSION OPTIONS USING GOCART AND MODIS AOD 55
CHAPTER 5 THE USE OF MODIS AOD TO CONSTRAIN BB AEROSOL EMISSIONS QUANTITATIVELY 75
5.1 Effect of Plume Dispersion on AOD 75
5.1.1 Height of Smoke Plumes and Vertical Dispersion 76
5.1.2 Wind Speed and Horizontal Dispersion 78
5.2 Use of MODIS AOD as a Quantitative Constraint on BC+OC Aerosol Emissions84
5.3 Limitations of the Method and Topics for Further Study 86
CHAPTER 6 CONCLUSIONS, FUTURE WORK AND SYNOPSIS OF RESEARCH PATH 89
6.1 Conclusions 89
6.2 Future Work 91

Page

6.3 Synopsis of Research Path....93
REFERENCES 97
APPENDIX.... 109
VITA 234

LIST OF TABLES

Table Page

Table 1 GLC2000 vegetation types defined and their corresponding physical properties and emission factors (Liousse et al., 2003; Michel et al., 2005; Liousse, 2010, personal communication) 17

Table 2 Values of the Haines Index Stability term (A) and the Moisture term (B) associated with various lapse rates and dewpoint depressions for low- middle- and high-level calculations (Werth and Ochoa, 1993) 19

Table 3 Relationship between potential for fire growth and Haines index values (Werth and Ochoa, 1993) 20

Table 4 GFED3 emission factors used for different fire types, in g species per kg DM (Van der Werf et al., 2010) 21

Table 5 Emission estimates used as input to GOCART model 25

Table 6 Study cases by region with the regional specifics of biomass burning 33

Table 7 Ratios of GOCART average case AOD to MODIS average case AOD, and qualitative summary of plume shape for each emission option in each of the world regions 67

Table 8 Regional fit coefficients for Equation 4 by wind speed range 85

LIST OF FIGURES

Figure Page

Figure 1 Fire occurence on the 15th of each month between June 2006 and May 2007 (time period for this study). Red dots show the locations of fires detected by MODIS both on Aqua and Terra satellites on a particular day.............................. 3

Figure 2 Studied fire cases, case boxes color-coded by the world region. Underlying colors represent the GLC vegetation types described in section 2.1.2 32

Figure 3 (a): Total dry mass burned globally in 2006, reported by GOCART emission input options considered in this study; (b): total global emissions of BC; (c): total global emissions of OC; (d): total global emissions of SO_2, each column representing one emission option. Colors in each bar correspond to dry mass burned (a) or aerosol component emissions (b-d) from the GLC vegetation types outlined in Fig.2 38

Figure 4a Global total daily estimates of BC emissions in kg, as estimated by 8 of 13 emission options.. 40

Figure 4b Global total daily estimates of BC emissions in kg, as estimated by GFED emission options and QFED 41

Figure 5a Annual emissions of black carbon in 2006 estimated by each emission option. In units of kg per GOCART grid box. mod1 (fire counts-based) emission options 42

Figure Page

Figure 5b Annual emissions of black carbon in 2006 estimated by each emission option. In units of kg per GOCART grid box. MCD45 (surface change-based) emission options 43

Figure 5c Annual emissions of black carbon in 2006 estimated by each emission option. In units of kg per GOCART grid box. GFED emission options and QFED2 44

Figure 6 Total area burned during years 2006 (top row) and 2007 (bottom row) estimated by mod1 (left column), MCD45 (middle column) and GFED3 (right column). In units of km^2 per 1°lat×1.25°lon GOCART grid box. 48

Figure 7 Global total area burned daily during 2006 and 2007 as estimated by mod1 (blue line), MCD45 (green line), GFED3-daily (red line), and GFED3-monthly (purple line). Labels for the regions dominating global BA total during certain months are colored by the dominant BA product. 49

Figure 8 Fuel consumption estimates in kg/m^2, by Carbon Consumption (CC) inventory for low (a), medium (b) and high (c) fire severity, GLC (d), and GFED3 (e) datasets. Absolute differences between CCm, GLC, and GFED3 fuel consumption are in (f), (g), and (h). 52

Figure 9 Case 11: Russia, 20 July 2006. Top Row: Terra-MODIS visible image of the scene with fire locations marked in red; total column MODIS AOD with original 10-km resolution, as provided by MOD04 data product; MODIS total TOA AOD averaged to GOCART grid; followed by maps of the temporally closest 3-hour output of instantaneous GOCART AOD values for different emission options. . 56

Figure Page

Figure 10 Average GOCART AOD for each fire case and each model run against average emission rate for the corresponding case in the corresponding emission option. Data points are colored by the region, with colors defined in Fig. 2. 57

Figure 11a GOCART AOD vs average BC+OC emission rate. Different symbols distinguish individual fire cases. Colors represent different emission options in GOCART. Output of the GOCART run to which the MODIS AOD is closest is marked in black. The black line from each such data point shows the magnitude of GOCART AOD under- or overestimation compared to the average MODIS AOD.Regions: SAmerica, LAmerica, SEAsia, Russia 60

Figure 11b As in Fig. 11a but for regions: SCAfrica, NCAfrica, NAustralia, SAustralia 61

Figure 11c As in Fig. 11a but for regions: Indonesia, Canada, WUSA, EUSA 62

Figure 11d As in Fig. 11a but for regions: Europe, India, China, Alaska 63

Figure 12a Ratios of GOCART average AOD to MODIS average AOD for each of the 124 cases studied, with different emission options used as input to GOCART. mod1 (fire counts-based) emission options. 64

Figure 12b Ratios of GOCART average AOD to MODIS average AOD for each of the 124 cases studied, with different emission options used as input to GOCART. MCD45 (surface change-based) emission options. 65

Figure 12c Ratios of GOCART average AOD to MODIS average AOD for each of the 124 cases studied, with different emission options used as input to GOCART. GFED emission options. 66

Figure 13 Average MODIS AOD for each of 124 analyzed fire cases. 70

Figure Page

Figure 14 Case 11: Russia, 20 July 2006. Top Row: Terra-MODIS visible image of the scene with fire locations marked in red; schematic tracks of CALIPSO and MISR tracks during the same day in orange, and light green respectively. Satellites are moving in the direction marked with the arrows parallel to the orbits. Maps of MISR AOD and Stereo heights, and the histograms of the pixel heights in two regions A (source region) and B (transported aerosol downwind) are shown in the upper panel. Lower panel shows CALIPSO Vertical feature mask overlaid by the GEOS-4 PBL height for the coordinates of the case box at the time of CALIPSO overpass. CALIPSO-Night observation also shows in dashed line the height of the mixing layer, approximated as the PBL height at 6:30 UTC (13:30 local time). . 77

Figure 15 Distribution of average PBL wind speeds in all cases for all model runs........ 79

Figure 16a As in Fig. 11a but colors represent average PBL wind speed at each case BB sources.. 80

Figure 16b As in Fig. 11b but colors represent average PBL wind speed at each case BB sources.. 81

Figure 16c As in Fig. 11c but colors represent average PBL wind speed at each case BB sources.. 82

Figure 16d As in Fig. 11d but colors represent average PBL wind speed at each case BB sources.. 83

Appendix Figure

Figure A - 1 MODIS and GOCART AOD for case 42.. 110

Figure A - 2 MODIS and GOCART AOD for case 43... 111

Appendix Figure Page

Figure A - 3 MODIS and GOCART AOD for case 46.. 112

Figure A - 4 MODIS and GOCART AOD for case 122.. 113

Figure A - 5 MODIS and GOCART AOD for case 1.. 114

Figure A - 6 MODIS and GOCART AOD for case 2.. 115

Figure A - 7 MODIS and GOCART AOD for case 3.. 116

Figure A - 8 MODIS and GOCART AOD for case 31.. 117

Figure A - 9 MODIS and GOCART AOD for case 70.. 118

Figure A - 10 MODIS and GOCART AOD for case 74.. 119

Figure A - 11 MODIS and GOCART AOD for case 113.. 120

Figure A - 12 MODIS and GOCART AOD for case 114.. 121

Figure A - 13 MODIS and GOCART AOD for case 37.. 122

Figure A - 14 MODIS and GOCART AOD for case 55.. 123

Figure A - 15 MODIS and GOCART AOD for case 59.. 124

Figure A - 16 MODIS and GOCART AOD for case 60.. 125

Figure A - 17 MODIS and GOCART AOD for case 61.. 126

Figure A - 18 MODIS and GOCART AOD for case 94.. 127

Figure A - 19 MODIS and GOCART AOD for case 51.. 128

Figure A - 20 MODIS and GOCART AOD for case 53.. 129

Figure A - 21 MODIS and GOCART AOD for case 54.. 130

Figure A - 22 MODIS and GOCART AOD for case 69.. 131

Figure A - 23 MODIS and GOCART AOD for case 85.. 132

Figure A - 24 MODIS and GOCART AOD for case 86.. 133

Appendix Figure Page

Figure A - 25 MODIS and GOCART AOD for case 87 134

Figure A - 26 MODIS and GOCART AOD for case 132 135

Figure A - 27 MODIS and GOCART AOD for case 133 136

Figure A - 28 MODIS and GOCART AOD for case 17 137

Figure A - 29 MODIS and GOCART AOD for case 41 138

Figure A - 30 MODIS and GOCART AOD for case 123 139

Figure A - 31 MODIS and GOCART AOD for case 124 140

Figure A - 32 MODIS and GOCART AOD for case 125 141

Figure A - 33 MODIS and GOCART AOD for case 126 142

Figure A - 34 MODIS and GOCART AOD for case 127 143

Figure A - 35 MODIS and GOCART AOD for case 128 144

Figure A - 36 MODIS and GOCART AOD for case 129 145

Figure A - 37 MODIS and GOCART AOD for case 13 146

Figure A - 38 MODIS and GOCART AOD for case 14 147

Figure A - 39 MODIS and GOCART AOD for case 15 148

Figure A - 40 MODIS and GOCART AOD for case 16 149

Figure A - 41 MODIS and GOCART AOD for case 135 150

Figure A - 42 MODIS and GOCART AOD for case 136 151

Figure A - 43 MODIS and GOCART AOD for case 32 152

Figure A - 44 MODIS and GOCART AOD for case 33 153

Figure A - 45 MODIS and GOCART AOD for case 35 154

Figure A - 46 MODIS and GOCART AOD for case 36 155

Appendix Figure Page

Figure A - 47 MODIS and GOCART AOD for case 107 156

Figure A - 48 MODIS and GOCART AOD for case 108 157

Figure A - 49 MODIS and GOCART AOD for case 110 158

Figure A - 50 MODIS and GOCART AOD for case 112 159

Figure A - 51 MODIS and GOCART AOD for case 57 160

Figure A - 52 MODIS and GOCART AOD for case 58 161

Figure A - 53 MODIS and GOCART AOD for case 65 162

Figure A - 54 MODIS and GOCART AOD for case 66 163

Figure A - 55 MODIS and GOCART AOD for case 67 164

Figure A - 56 MODIS and GOCART AOD for case 68 165

Figure A - 57 MODIS and GOCART AOD for case 103 166

Figure A - 58 MODIS and GOCART AOD for case 104 167

Figure A - 59 MODIS and GOCART AOD for case 105 168

Figure A - 60 MODIS and GOCART AOD for case 106 169

Figure A - 61 MODIS and GOCART AOD for case 21 170

Figure A - 62 MODIS and GOCART AOD for case 62 171

Figure A - 63 MODIS and GOCART AOD for case 63 172

Figure A - 64 MODIS and GOCART AOD for case 64 173

Figure A - 65 MODIS and GOCART AOD for case 118 174

Figure A - 66 MODIS and GOCART AOD for case 119 175

Figure A - 67 MODIS and GOCART AOD for case 120 176

Figure A - 68 MODIS and GOCART AOD for case 10 177

Appendix Figure Page

Figure A - 69 MODIS and GOCART AOD for case 11 178

Figure A - 70 MODIS and GOCART AOD for case 47 179

Figure A - 71 MODIS and GOCART AOD for case 48 180

Figure A - 72 MODIS and GOCART AOD for case 50 181

Figure A - 73 MODIS and GOCART AOD for case 102 182

Figure A - 74 MODIS and GOCART AOD for case 38 183

Figure A - 75 MODIS and GOCART AOD for case 39 184

Figure A - 76 MODIS and GOCART AOD for case 40 185

Figure A - 77 MODIS and GOCART AOD for case 44 186

Figure A - 78 MODIS and GOCART AOD for case 45 187

Figure A - 79 MODIS and GOCART AOD for case 56 188

Figure A - 80 MODIS and GOCART AOD for case 89 189

Figure A - 81 MODIS and GOCART AOD for case 18 190

Figure A - 82 MODIS and GOCART AOD for case 19 191

Figure A - 83 MODIS and GOCART AOD for case 20 192

Figure A - 84 MODIS and GOCART AOD for case 96 193

Figure A - 85 MODIS and GOCART AOD for case 97 194

Figure A - 86 MODIS and GOCART AOD for case 100 195

Figure A - 87 MODIS and GOCART AOD for case 101 196

Figure A - 88 MODIS and GOCART AOD for case 134 197

Figure A - 89 MODIS and GOCART AOD for case 12 198

Figure A - 90 MODIS and GOCART AOD for case 49 199

Appendix Figure Page

Figure A - 91 MODIS and GOCART AOD for case 115 ... 200

Figure A - 92 MODIS and GOCART AOD for case 116 ... 201

Figure A - 93 MODIS and GOCART AOD for case 117 ... 202

Figure A - 94 MODIS and GOCART AOD for case 121 ... 203

Figure A - 95 MODIS and GOCART AOD for case 25 ... 204

Figure A - 96 MODIS and GOCART AOD for case 27 ... 205

Figure A - 97 MODIS and GOCART AOD for case 28 ... 206

Figure A - 98 MODIS and GOCART AOD for case 90 ... 207

Figure A - 99 MODIS and GOCART AOD for case 91 ... 208

Figure A - 100 MODIS and GOCART AOD for case 92 ... 209

Figure A - 101 MODIS and GOCART AOD for case 93 ... 210

Figure A - 102 MODIS and GOCART AOD for case 95 ... 211

Figure A - 103 MODIS and GOCART AOD for case 23 ... 212

Figure A - 104 MODIS and GOCART AOD for case 24 ... 213

Figure A - 105 MODIS and GOCART AOD for case 75 ... 214

Figure A - 106 MODIS and GOCART AOD for case 76 ... 215

Figure A - 107 MODIS and GOCART AOD for case 109 ... 216

Figure A - 108 MODIS and GOCART AOD for case 111 ... 217

Figure A - 109 MODIS and GOCART AOD for case 4 ... 218

Figure A - 110 MODIS and GOCART AOD for case 5 ... 219

Figure A - 111 MODIS and GOCART AOD for case 7 ... 220

Figure A - 112 MODIS and GOCART AOD for case 8 ... 221

Appendix Figure Page

Figure A - 113 MODIS and GOCART AOD for case 9 222

Figure A - 114 MODIS and GOCART AOD for case 71 223

Figure A - 115 MODIS and GOCART AOD for case 72 224

Figure A - 116 MODIS and GOCART AOD for case 73 225

Figure A - 117 MODIS and GOCART AOD for case 77 226

Figure A - 118 MODIS and GOCART AOD for case 78 227

Figure A - 119 MODIS and GOCART AOD for case 79 228

Figure A - 120 MODIS and GOCART AOD for case 80 229

Figure A - 121 MODIS and GOCART AOD for case 81 230

Figure A - 122 MODIS and GOCART AOD for case 82 231

Figure A - 123 MODIS and GOCART AOD for case 83 232

Figure A - 124 MODIS and GOCART AOD for case 84 233

ABSTRACT

Petrenko, Mariya. Ph.D., Purdue University, May 2012. The Use of Satellite-Measured Aerosol Optical Depth to Constrain Biomass Burning Emissions Source Strength in a Global Model GOCART. Major Professor: Dr. Harshvardhan.

Biomass burning (BB) is one of the major contributors to emissions of carbonaceous atmospheric aerosol. Optically and chemically potent BB particles play important roles in atmospheric processes through their impact on air quality, visibility, human health, and as one of the factors affecting global climate through direct and indirect radiative effects. As chemistry transport models are among the major tools for studying earth and atmospheric processes, it is important to represent BB processes as accurately as possible.

Simulations of BB emissions in aerosol models strongly depend on the inventories that define emission source locations and strength. In this work, we use 13 global biomass burning emission estimates, including widely used Global Fire Emission Database (GFED) monthly and daily versions, Fire Radiative Power (FRP)-based Quick Fire Emission Dataset QFED, and several combinations of fuel consumption estimates, aerosol emission factors and Moderate Resolution Imaging Spectroradiometer (MODIS)-based burned area products as alternative inputs to the global Goddard Chemistry Aerosol Radiation and Transport (GOCART) model. The resultant simulated aerosol optical depth (AOD) and its spatial distributions are compared to AOD snapshots measured by the

MODIS instrument for 124 fire events occurring between 2006 and 2007. BB aerosol emission estimates by all 13 emission options are compared on a global scale and implications of regional differences are discussed. Performance of all emission options, with the exception of FRP-based QFED, when used as a source of BB emissions in the GOCART model, were assessed on a regional basis, showing where and to what degree the different options overestimate, underestimate and provide good agreement with the observation. QFED developers use MODIS AOD as one of the parameters to calibrate their product during its production, so comparison of QFED-based GOCART-simulated AOD with MODIS measurements was not performed. It is also shown that the quantitative relationship between BB aerosol emissions and model-simulated AOD is related to the horizontal plume dispersion, which can be approximated by the wind speed in the planetary boundary layer. Thus, given average wind speed of the smoke plume environment, MODIS-measured AOD can provide a constraint to the strength of BB sources.

CHAPTER 1 INTRODUCTION

1.1 Biomass Burning Aerosols and Their Representation in the Global Aerosol Models

Aerosol particles are important players in many atmospheric processes. They affect the Earth radiation budget directly by scattering and absorbing solar radiation (Yu et al., 2006), and indirectly by serving as cloud condensation nuclei and altering cloud properties (Lohmann and Feichter, 2005). Atmospheric aerosols also impact air quality (NARSTO, 2003; Sapkota et al., 2005; Wiedinmyer et al., 2006), visibility (Mazurek et al., 1997; Bäumer et al., 2008) and human health (Seaton et al., 1995). Major sources of atmospheric particles include fossil fuel combustion, biomass burning, desert dust, biogenic, oceanic, and volcanic emissions (NARSTO, 2003; Textor et al., 2006). This work focuses on aerosols emitted from open biomass burning (BB), such as forest or savanna fires.

Biomass burning is a natural part of the vegetation cycle. In late 1970's Crutzen and colleagues were the first to evaluate the contribution of BB sources to emissions of gases and aerosols (Crutzen et al., 1979; Seiler and Crutzen, 1980; Levine et al., 1993). With the previous research suggesting a link between changing climate and change in the biomass burning activity (Levine et al., 1993; Gillett et al., 2004; IPCC, 2007; Schultz et al., 2007), a steady increase in the amount of biomass burned, by about 50% since 1850

(Houghton, 1991) and a simultaneous increase of the fraction of BB attributed to human activity (Houghton, 1991; Levine et al., 1993; Van der Werf et al., 2010), understanding of BB-related processes and fluxes is important in current efforts to mitigate climate change and to quantitatively represent climate-driving forces in global models.
To appreciate the magnitude of open burning globally, we refer to Fig. 1, where a set of maps is displayed for one day of every month of the year, to illustrate the magnitude and seasonality of biomass burning.

Aerosol emission inventories suggest that biomass burning sources contribute approximately 34 to 38 % of carbonaceous aerosol emissions, which include black carbon (BC) and organic carbon (OC), with the remainder coming from fossil fuel burning (IPCC, 2007). BB is also a source of aerosol precursor gases such as SO_2, NOx, and a suite of volatile organic compounds (Andreae and Merlet, 2001; Akagi et al., 2011). Aerosol precursors and volatile organic compounds condense upon existing particles or participate in a number of chemical reactions to form secondary aerosol (Seinfeld and Pandis, 1998). Biomass burning emissions - containing light-absorbing soot, a wide variety of both hydrophobic and hydrophilic organic compounds with a range of refractive indices, lifetimes and particle sizes - are very chemically and optically potent (Seinfeld and Pandis, 1998), and thus are able to have significant effects on many atmospheric processes both immediately near source and far downwind. Large biomass burning (BB) smoke plumes can reach the free troposphere and travel over long distances to increase aerosol loading in remote locations (Stohl et al., 2003; Colarco et al., 2004; Damoah et al., 2004; Jaffe et al., 2004).

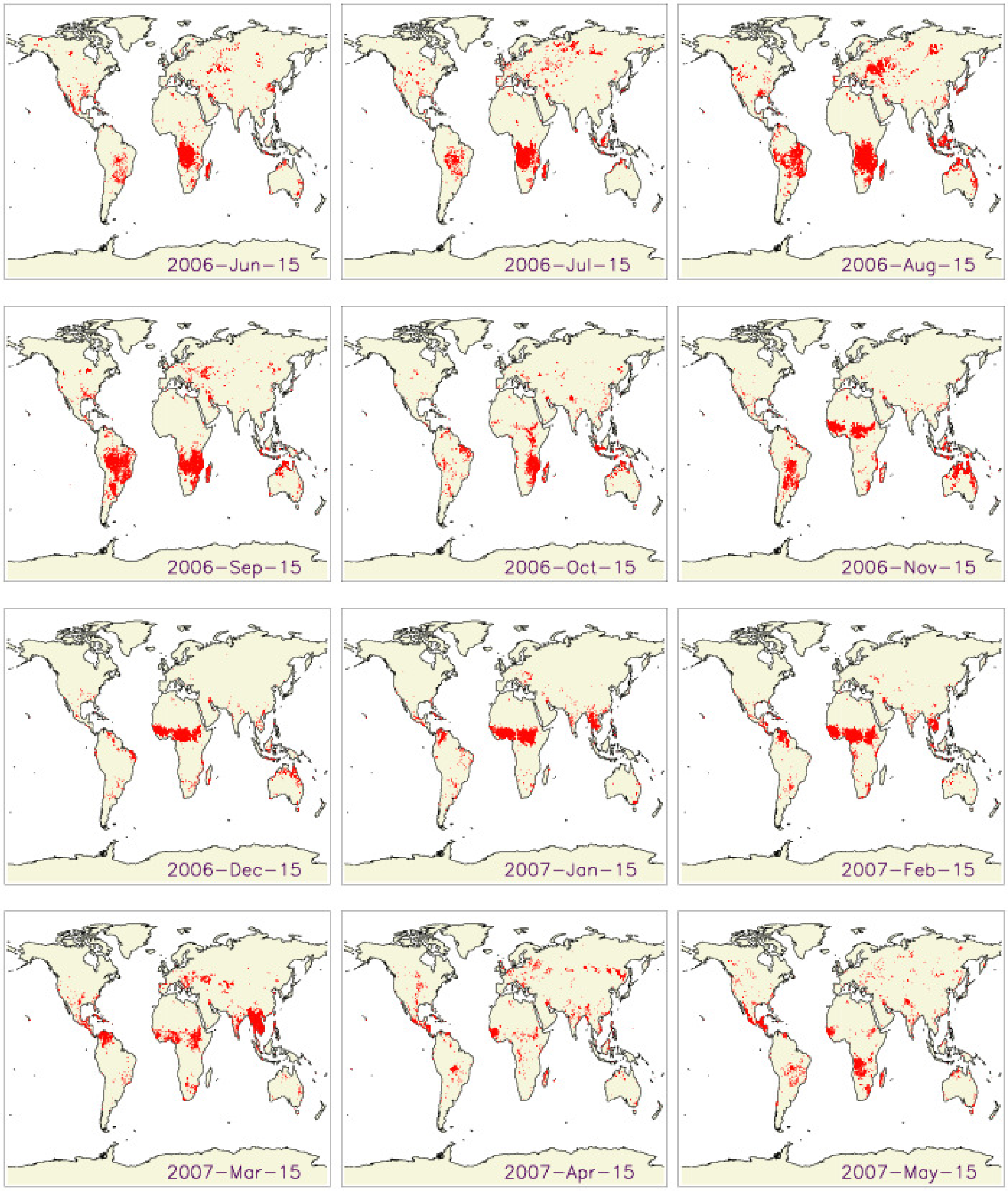

Figure 1 Fire occurrence on the 15th of each month between June 2006 and May 2007 (time period for this study). Red dots show the locations of fires detected by MODIS both on Aqua and Terra satellites on a particular day

Chemistry transport models (CTM) are among the major tools for studying earth and atmospheric processes (CCSP, 2009). Global CTMs are used to estimate climate forcings (Boucher and Anderson, 1995; Dentener et al., 2005; IPCC, 2007), and to study both regional pollution loads (Quinn et al., 2008; Shindell et al., 2008) and long-range transport of emissions (Colarco et al., 2004; Damoah et al., 2004; Jaffe et al., 2004; Warneke et al., 2009). Since BB aerosols can have such profound effects on atmospheric processes, their accurate representation in aerosol models is very important.

To simulate emission and subsequent evolution and transport of aerosol particles from fires, models need two essential pieces of information - strength of the biomass burning sources and height of aerosol injection. Until recently, aerosol vertical distribution has represented one of the largest discrepancies among aerosol models, primarily due to a paucity of observational datasets suitable for model validation (Textor et al., 2006). However, in the last decade, spaceborne observations of aerosol vertical profiles have become available to enhance studies of aerosol vertical transport and, thanks to their regularity and global coverage, facilitate model development. For example, global analysis of aerosol profiles from the spaceborne lidar system CALIPSO (Cloud-Aerosol Lidar and Infrared Pathfinder Satellite Observation) confirmed that most of biomass burning smoke is emitted into and stays in the atmospheric boundary layer (BL) (Labonne et al., 2007). Using the stereo-height product from MISR (Multi-angle Imaging Spectroradiometer), Kahn et al. (2007) concluded that boreal smoke plumes can be injected above the BL, and tend to concentrate in layers of relative atmospheric stability. This relationship between smoke injection and atmospheric stability structure was further explored by Kahn et al. (2008) and then by Val Martin et al. (2010) using an extensive dataset of BB plumes observed by MISR over North America (http://wwwmisr.jpl.nasa.gov/getData/accessData/MisrMinxPlumes). These studies also confirmed the previous finding that about 10-15% of all fire plumes reach heights above the boundary layer. Therefore, the general assumption adopted in most global aerosol models, that BB plumes are vertically distributed within the BL would work well in the majority of the cases. The amount of emitted aerosol, on the other hand, as estimated in different emission inventories, turns out to differ by up to an order of magnitude for some fire events (Al-Saadi et al., 2008), so the aerosol modeling community needs to resolve an issue of estimating BB source strength and discuss ways to constrain these estimates .

Location and strength of the BB sources are usually input into the model from an external emission inventory. A number of global and regional BB emission inventories exist, and are usually constructed bottom-up, considering the properties of the burning ecosystem and the extent and properties of the fires (Ito and Penner, 2004; Michel et al., 2005; Giglio et al., 2006; Turquety et al., 2007; Vermote et al., 2009; Liousse et al., 2010; Van der Werf et al., 2010; Wiedinmyer et al., 2011). Alternatively, a top-down approach, described, for example, by Dubovik et al. (2008), uses inverse modeling to estimate biomass burning source strength from the measured aerosol properties, such as aerosol optical depth (AOD). This approach is labor- and computation-intensive, and is not widely used by the aerosol modeling community.

Natural BB variability (Van der Werf et al., 2006; Schultz et al., 2007), errors and uncertainties associated with the estimates and measurements of emission-related parameters such as burned area (Giglio et al., 2010), biomass type and properties (Fritz and See, 2008), aerosol and gas emission factors (Akagi et al., 2011), properties of the fire and environment in which burning occurs (Soja et al., 2004; Hyer and Reid, 2009; Van der Werf et al., 2010), as well as different approaches to calculating emissions (Al-Saadi et al., 2008) - all lead to discrepancies between emission estimates provided by BB emission inventories. These discrepancies can be quite significant, and propagate in the aerosol models to impact simulated aerosol effects (Chin et al., 2009; Reid et al., 2009).

A way to calibrate the model is to compare its output to observations. Aerosol optical depth, or AOD, discussed in more detail in sections 2.4 and 2.5.1, is one of aerosol properties that can be used for such comparison. AOD observed at the top of the atmosphere is directly proportional to the amount of aerosol in the atmospheric column (Levy et al., 2007; Levy et al., 2010) and is routinely measured by spaceborne instruments. Each such measurement captures the totality of aerosol particles that have been emitted into the atmosphere by the fires, from the beginning of burning until the time of measurement, and were not transported away from the field of view. It is, therefore, possible to use satellite-measured AOD as an instantaneous observational constraint on the strength of biomass burning sources in an aerosol model.

In this work, we use 13 global biomass burning emission estimates, including the widely used Global Fire Emission Database (GFED) monthly and daily versions, Fire Radiative Power (FRP)-based Quick Fire Emission Dataset QFED, and 11 calculated emissions from different combinations of burned area based on the Moderate Resolution Imaging Spectroradiometer (MODIS) products, fuel consumption, and species emission factors as alternative inputs to the global Goddard Chemistry Aerosol Radiation and Transport (GOCART) model. The resultant simulated AOD and its spatial distribution are compared to AOD snapshots measured by the MODIS instrument for 124 fire events occurring between 2006 and 2007, providing information on how satellite AOD data can be used to constrain the BB emission. We describe the approach, emission datasets, GOCART model, satellite observations and a set of studied fire cases in Chapter 2, discuss the differences in the emission estimates provided by different emission options in Chapter 3, and in Chapter 4 show the performance of the GOCART model relative to MODIS observations, when model runs are based on different emission options. We present the method of using MODIS AOD to constrain BB emissions and discuss its limitations in Chapter 5. Conclusions from this study and ideas for future work are given in Chapter 6.

The novelty of this work consists of comparing a range of emission estimates widely available for use in the global models. Even though each emission dataset undergoes validation by comparison to satellite or field measurements, an extensive side-by-side comparison of several such datasets and their critical testing by consistent evaluation of their performance in the global model have not been done before. In addition, assessment of emission options performance on the regional scale presents a valuable result for both emission inventory developers and modelers using these inventories. Lack of this regional assessment resulted in scaling emission by the same factor globally (e.g., Kaiser et al., 2012), which reduced error in some BB regions, but at the same time dramatically increased existing errors in the other regions.

The method for using satellite-measured AOD to quantitatively constrain BB emissions in the model, described in Chapter 5, provides additional valuable approach to fine-tuning the existing BB emission inventories on a case-by-case basis, providing additional insight into BB processes on a finer-than-regional scale.

1.2 Spaceborne Observations of Fires and Aerosol Properties

As has already been mentioned, satellite observations of the Earth present an excellent data source both to provide input to global models and to validate their output. The main features of spaceborne observations so valuable in the modeling community are their global coverage, regularity, and fairly consistent reliability in all regions of the world, which cannot be achieved with the current ground-based fire and aerosol observations. There are several satellite sensors designed to measure aerosol properties and able to detect fires. The satellites and instruments that provided major datasets for this study are introduced below.

1.2.1. Moderate Resolution Imaging Spectroradiometer (MODIS)

MODIS is a key instrument on board NASA's Terra and Aqua satellites. Terra orbits the Earth in sun-synchronous low earth orbit at 705 km, crossing the equator at 10:30 a.m. local time in descending node (moving from North to South on the day side of the Earth) every 99 min. Aqua is part of the "A-train" constellation of satellites, also in a low Earth orbit, which crosses the equator at 1:30 p.m. local time in ascending node. With a wide 2330 km swath, MODIS observes the whole globe in 1 to 2 days with more frequent coverage of higher latitudes. Measurements made in 36 spectral bands between 0.405 and 14.385 μm are a source for a number of land, ocean and atmospheric products with band-dependent nominal spatial resolutions of 250 m, 500 m, or 1 km. The MODIS sensor was designed to include specific characteristics for fire detection, and several infrared channels (1.65, 2.13, 3.95, and 11 μm) are used to produce a range of fire-related data products (Justice et al., 2006).

Data are grouped into three "Levels". Level 1 processing provides corrected (or calibrated) instrument data. Level 2 processing provides retrieval of derived geophysical quantities, such as atmospheric aerosol and cloud measurements and the top of atmosphere albedo. Level 3 processing produces global maps of the level 2 products, such as aerosol properties, surface and vegetation indices.

The data products used directly in this study include visible images, fire location, and aerosol optical depth, and are introduced in the sections describing their use. Several other data products, such as burned area, are also based on MODIS observations and are introduced below as well.

1.2.2. Multiangle Imaging Spectroradiometer (MISR)

MISR, flown on board NASA's Terra satellite, has a unique geometry, where it is looking down on Earth with nine cameras precisely aligned to sequentially view the 380 km swath at nine different angles (0, and 26.1, 45.6, 60.0, and 70.5 degrees forward and aftward of the local vertical) in four spectral bands (blue, green, red, and near-infrared - 446, 558, 672, and 867 nm respectively) to provide global coverage every 9 days (Diner et al., 1998).

MISR can take image data in two spatial resolution modes. In Local Mode, specially selected targets are imaged at the maximum 250 m across track for the nadir camera, and 275 m for all other cameras. The data transmission capabilities prevent all data to be taken with such a fine resolution, so if not observing one of these about 6 per day pre-selected targets, the instrument operates in Global Mode, where data are averaged to 1.1 km in 24 of the 36 channels before being transmitted to the Earth.

Level-based data product nomenclature is similar to that of MODIS, with Level 2 processing using multiple cameras simultaneously taking into account angular radiance signatures, geometric parallax, time lapse between cameras (Mazzoni et al., 2007). The combination of measurements from these cameras is used for addressing a number of scientific questions involving atmospheric and surface scattering at multiple angles.

1.2.3. Cloud-Aerosol Lidar with Orthogonal Polarization (CALIOP) on CALIPSO Satellite

The CALIPSO satellite carrying the CALIOP (Cloud-Aerosol Lidar with Orthogonal Polarization) lidar system is part of the "A-train" constellation of sun-synchronous satellites. CALIOP is a polarization sensitive lidar that makes backscatter measurements at 532 and 1064 nm. Since cloud droplets are large compared to the observed wavelengths their backscatter and extinction coefficients will not vary much across the lidar wavelength spectrum. Aerosol particle sizes, however, are comparable to the lidar wavelengths and their backscattering and extinction coefficients are expected to be smaller at 1064 nm. The ratios of these coefficients at the two lidar wavelengths are the basis for distinguishing aerosol plumes from clouds (Vaughan et al., 2004).

CALIPSO data products are divided into level 1 and 2, where level 1 algorithms control the calibration procedure, determine the range of CALIOP and its geolocation (Winker et al., 2004). Level 2 products utilize level 1 data to produce actual geophysical data, which will be used in this study. Level 2 data products include aerosol layer height and thickness, aerosol optical depth, backscattering and extinction coefficients. CALIOP takes a vertical profile every 333 m along track and has a 70-m field of view. Different resolutions are applicable to different vertical layers due to aerosol variability and their abundance in the lower atmosphere. Thus, aerosol data retrieval algorithms already include averaging techniques to find at-the-ground and elevated aerosol layers. Since aerosol backscattering intensity can be faint compared to, for example, cirrus clouds, a step-by-step process is employed to clear the picture and average several scans to obtain a signal to noise ratio (SNR) sufficiently large to retrieve aerosol height and particle properties (Vaughan et al., 2004). As a result, level 2 aerosol layer height and thickness products are reported on a spatial grid of 5-km horizontally by 60-m vertically, and coarser resolution for backscatter and extinction profiles to account for more averaging required to obtain accurate results due to weaker than clouds aerosol scattering (http://www-calipso.larc.nasa.gov/products/) (Vaughan et al., 2004). Daily CALIOP data are available since June 13, 2006, are archived at the NASA Langley Data Center, and can be previewed and ordered in HDF format on-line at http://eosweb.larc.nasa.gov/PRODOCS/calipso/table_calipso.html.

CHAPTER 2 METHODOLOGY

2.1 Estimating BB Emissions Based on Burned Area

The most common way to estimate BB emissions is the following empirical relationship, which is based on the one originally introduced by Seiler & Crutzen (1980) :

$$M_j=A*B*C*F_j, \quad [1]$$

where M_j is the mass of emitted species j (here BC, OC, and SO_2); A is the burned area; B is the average amount of biomass or organic matter an ecosystem contains per unit area; C is the combustion completeness or burning efficiency, which is the fraction of fuel actually consumed in a fire (Soja et al., 2004; Van der Werf et al., 2006). C is dependent on the fire severity and fuel type, and can range from 98% for standing dry grass to less than 10% for dead logs (Liousse et al., 2003); and F_j is the emission factor of species j, defined as the amount of species j released per unit of fuel consumed (Andreae and Merlet, 2001), expressed in grams of tracer per kilogram of burned dry mass.

The product of A, B and C in Equation 1 represents the amount of fuel consumed within the burned area, or "dry mass burned (DM)", and the product of fuel density B and combustion completeness C the "fuel consumption". Listed below are several data products that provide estimates of each term in Equation 1 individually or as part of a combined quantity, e.g., fuel consumption or dry mass burned. These data products are later combined to provide BB emissions to the aerosol model.

2.1.1. Burned Area (*A*)

Estimates of area burned by fires on a global scale are best made using spaceborne instruments. Two different approaches to estimate burned area products have been developed. One approach is based on detecting and quantifying the change of surface and vegetation properties (such as surface reflectance, surface temperature, vegetation indices etc.) produced by the fire. Spaceborne-instrument-based algorithms utilize these changes to estimate the area burned between consecutive observations.

The other approach involves using active fire detection and previously developed ecosystem-dependent empirical relationships between the number of fires detected from the satellite and the corresponding burned area (estimated previously by other techniques in the training areas) (Giglio et al., 2006). These empirical relationships allow near-real time approximation of the burned areas from the fire counts. However, these techniques are associated with large uncertainties due to large variations of effective burned area per detected fire, even in the same ecosystem, and also with temporal and spatial constraints of satellite observations, leading to omission of fire detections or observing the same fire more than once (Giglio et al., 2006; 2007; 2009; Roy et al., 2008).

Constant progress and refinements of both these approaches currently allow for creation of hybrid algorithms, which supplement the surface and vegetation parameters used for mapping burned area with active fire information. The MODIS-based algorithm presented by Giglio et al. (2009) detects persistent changes in daily time series of burn-sensitive vegetation index. The location of detected active fires is an additional source of information for classifying the pixel as burned or unburned. Also, for the pixels with missing direct 500 m measurements, the burned area was indirectly estimated from active fire counts using previously defined empirical relationships (Giglio et al., 2010).

In this study we use three MODIS-based burned area products:

a) ***The MODIS collection 5 burned area product - MCD45A1*** (Roy et al., 2008) is based on the change of surface reflectance following a fire. The data are available from the Earth Observing System Clearing House (EOSDIS, 2009) in a set of monthly files, each containing one of the ~10°(lat) × 10°(lon) granules defined on the MODIS sinusoidal grid (Giglio, 2010). Each granule contains the locations of burned pixels for each day of the month, at 500 m spatial resolution, which were gridded to the 1°(lat) × 1.25°(lon) GOCART grid. Burned area estimates for the overlapping eight days before and after each month are ignored to avoid duplication. This product is referred to here as ***"MCD45."***

b) Burned area estimated from ***MODIS active fire counts***, where MODIS-Terra (MOD14A1) and MODIS-Aqua (MYD14A1) thermal anomalies are combined, and multiple counting is removed, i.e., pixels classified as fires more than once on the same day are counted only once. These data were also obtained from the EOS Clearing House (EOSDIS, 2009), and the fire counts were gridded to the 1° (lat) × 1.25°(lon) GOCART grid. This product is referred to here as ***"mod1"***.

To estimate the area burned by the detected fires we assume that each pixel classified as burning corresponds to 1 km^2 of burned area. Here, we have to acknowledge the reported large variations of effective burned area per detected fire, even in the same ecosystem (Soja et al., 2004; Giglio et al., 2006; 2007; 2009; Roy et al., 2008). The conversion factors reported previously range from 0.3 km^2 to 6.6 km^2 effective burned area per fire detection, based solely on MODIS-Terra detection analyses in different locations globally (Giglio et al., 2006; 2010). Other estimates include 0.79 km^2/pixel (Soja et al., 2009), and 0.625 km^2/pixel (Reid et al., 2009). According to Soja et al. (2009), counting every pixel and assuming 1 km^2/pixel for every fire detection leads to gross overestimation of burned area (by about a factor of 2 in the western US), highlighting the wide disparity in estimating burned area using fire detection data.

c) ***Global Fire Emission Dataset version 3 (GFED3) burned area***, with 0.5°×0.5° spatial and daily temporal resolution, is another MODIS-based product developed and described by Giglio et al. (2009). This algorithm combines the detection of change in surface properties (vegetation index) with the use of the active fire product. Instructions on downloading GFED data and converting burned area from monthly to daily estimates are available from http://globalfiredata.org/Data/index.html.

2.1.2. Biomass Density (*B*) and Fuel Consumption (*B*C*)

a) ***Global Land Cover dataset (GLC2000)***, referred to here as ***"GLC"***, provides a map of 22 land cover types globally, at the original 1-km and also a 0.5°×0.5° spatial resolution. The global dataset is the result of an international partnership of 30 research groups, coordinated by the Joint Research Center of the European Commission (Bartholome´ and Belward, 2005). The maps of land cover types were developed regionally based on the observations of the VEGETATION sensor on-board the European SPOT-4 satellite, and then aggregated to a global product. GLC methodology and datasets are introduced by Bartholome and Belward (2005) and numerous subsequent publications (e.g., See and Fritz, 2006; Gonsamo and Chen, 2011; Xiao-Peng et al.,

2011) , and available online at

http://bioval.jrc.ec.europa.eu/products/glc2000/glc2000.php. Typical biomass density, combustion completeness, and emission factors are defined for 16 of the 18 vegetated land-cover types (Liousse et al., 2003; 2010; Michel et al., 2005). These properties are summarized in Table 1. The last three columns of Table 1 contain the product of biomass density, burning efficiency and emission factor values given in the previous columns, for BC, OC and SO_2 respectively. The numbers in these last columns represent the amount of potential emissions from each square meter of area burned. The largest amount of emissions is expected from tree covered ecosystems, with values in evergreen and closed forests about 10-20 times larger than those in shrub lands and grassy ecosystems.

All emission calculations involving the GLC dataset were calculated on a sub-grid scale using properties of the original GLC vegetation types, mapped in Figure 2 on the GOCART grid. The vegetation type occupying the largest areal fraction of each grid box is designated as dominant for that box and is the color shown on the map.

Table 1 GLC2000 vegetation types defined and their corresponding physical properties and emission factors (Liousse et al., 2003; Michel et al., 2005; Liousse, 2010, personal communication)

GLC code	**GLC vegetation type description**	**Biomass density, kg/m^2**	**Burning efficiency**	**F_j, g(j)/kg(DM)**			**$B*C*F_j$, $g(j)/m^2$**		
				BC	**OC**	**SO_2**	**BC**	**OC**	**SO_2**
1	Tree Cover broadleaved evergreen	23.35	0.25	0.70	6.40	0.57	4.09	37.36	3.33
2	Tree Cover broadleaved deciduous closed	20.00	0.25	0.60	6.00	1.00	3.00	30.00	5.00
3	Tree Cover broadleaved deciduous open	3.30	0.40	0.62	4.00	0.35	0.82	5.28	0.46
4	Tree Cover needle-leaved evergreen	36.70	0.25	0.60	6.00	1.00	5.51	55.05	9.18
5	Tree Cover needle-leaved deciduous	18.90	0.25	0.60	6.00	1.00	2.84	28.35	4.73
6	Tree Cover mixed leaf type	14.00	0.25	0.60	6.01	0.99	2.10	21.04	3.47
7	Tree Cover regularly flooded fresh water	27.00	0.25	0.70	6.40	0.57	4.73	43.20	3.85
8	Tree Cover regularly flooded saline water	14.00	0.60	0.65	5.15	0.46	5.46	43.26	3.86
9	Mosaic: Tree Cover / Other natural vegetation	10.00	0.35	0.61	5.00	0.68	2.14	17.50	2.38
10	Tree cover, burnt	0	0	0.00	0.00	0.00	0.00	0.00	0.00
11	Shrub Cover closed-open evergreen	1.25	0.90	0.62	4.00	0.35	0.70	4.50	0.39
12	Shrub Cover closed-open deciduous	3.30	0.40	0.62	4.00	0.35	0.82	5.28	0.46
13	Herbaceous Cover closed-open	1.43	0.90	0.62	4.00	0.35	0.80	5.15	0.45
14	Sparse herbaceous or sparse shrub cover	0.90	0.60	0.67	3.11	0.37	0.36	1.68	0.20
15	Regularly flooded shrub and/or herbaceous cover	0	0	0.00	0.00	0.00	0.00	0.00	0.00
16	Cultivated and managed areas	0.44	0.60	0.73	2.10	0.40	0.19	0.55	0.11
17	Mosaic: Cropland / Tree Cover / Other natural v.	1.10	0.80	0.64	3.64	0.36	0.56	3.20	0.32
18	Mosaic: Cropland / Shrub and/or grass cover	1.00	0.75	0.65	3.35	0.37	0.49	2.51	0.28

b) The ***Weather- and Ecosystem-Based Fire Emissions (WEB-FE)***, developed at the National Institute of Aerospace and NASA Langley Research Center, is available upon request from its developers (A. Soja, personal communication, 2011). In this analysis, we use the ***Carbon Consumption (CC)*** database from WEB-FE, which is defined as the potential amount of available carbon consumed by fire.

Spatially-explicit fuel consumption estimates were first developed for Northern Eurasia based on the amount of fuel contained in ecosystems that could be available to burn (Soja et al., 2004), which is ultimately dependent on the weather that initiates fire events. Unique estimates for the potential amount of carbon (or fuel) consumed are calculated for 35 distinct ecoregions across Northern Eurasia, which includes 4 separate peatland estimates. Fuels data were taken from Alexeyev and Birdsey (1998) and include overstory, understory, litter, peat and soil organic matter; carbon is assumed to be 50% of the available fuel. Each ecoregion estimate consists of 3 potential severity classes, resulting in 105 discrete spatially-explicit estimates. For instance, a low-severity surface fire consumes 20% of the accessible understory and litter layer, and a high-severity crown fire consumes 20% of the accessible tree stand vegetation and 100% of the accessible understory and litter. Ecosystem-based estimates range from low-, medium- to high-severity carbon consumption and have been verified. Subsequently, the data were validated with ground-based fuel consumption data for a range of fire severities and ecosystems (r^2=0.86) (Soja et al., 2004).

Global carbon consumption estimates were built from above-ground fuel provided by Olson et al. (1985) and soil carbon by Zinke et al. (1986), and these global estimates are overlaid with detailed data as they become available (currently for Northern Eurasia, Canada and Alaska). The global estimates were developed for near-real-time use and have proven themselves in numerous field campaigns (e.g., Pierce et al., 2007; Choi et al., 2008). The information gleaned from this investigation will lead to improvements in this dataset.

To approximate fire severity, we use the Haines index (HI), also known as the Lower Atmosphere Severity Index (Haines, 1988; Winkler et al., 2007). The Haines index is a number ranging from 2 to 6 that describes the stability and moisture content of the lower atmospheric layer (~1 km high) with topography taken into account. The index is a simple sum of two terms: the Lapse Rate Term (temperature difference between layer bottom and top) describing the stability of the layer, and the Dewpoint depression term (difference between temperature and dew point temperature at the lower level). The values for these terms for HI calculations at low, middle and high surface elevation locations are provided in Table 2. In other words, an unstable, dry atmosphere will have higher HI, indicating a likelihood of more severe fire, the categories of likelihood given in Table 3.

Table 2 Values of the Haines Index Stability term (A) and the Moisture term (B) associated with various lapse rates and dewpoint depressions for low- middle- and high-level calculations (Werth and Ochoa, 1993)

	Lapse Rate (A)			**Dewpoint Depression (B)**		
Value of A or B	**Low (950-850 mb)**	**Middle (850-700 mb)**	**High (700-500 mb)**	**Low (850 mb)**	**Middle (850 mb)**	**High (700 mb)**
1	≤ 3	≤ 5	≤ 17	≤ 5	≤ 5	≤ 14
2	4-7	6-10	18-21	6-9	6-12	15-20
3	≥ 8	≥ 11	≥ 22	≥ 10	≥ 13	≥ 21

Table 3 Relationship between potential for fire growth and Haines index values (Werth and Ochoa, 1993)

Haines Index	**Class of day (potential for large fire growth)**
2 or 3	Very low
4	Low
5	Moderate
6	High

In this study HI was calculated for each GOCART grid box using 3-hourly GEOS4-DAS meteorological fields (Bloom et al., 2005), and the HI value determined the choice of the fuel consumption category from one of the CC datasets - low, medium or high. It should be reminded, that fuel consumption has been defined above as a product of biomass density (*B*) and combustion completeness (*C*). These 3-hourly CC values in each grid box were averaged over the course of 24 hours and the units appropriately converted to provide a fuel consumption estimate for a particular day.

2.1.3. Emission Factors (F_j)

In the ***standard GOCART*** configuration, emission factors of 1, 8, and 1.1 g per kg of burned dry mass are used globally for BC, OC and SO_2, respectively (Chin et al., 2002; 2007 and references therein). Alternatively, for combinations that include GLC vegetation types, we use vegetation-type-dependent emission factors for BC, OC, and SO_2 provided in the ***GLC*** database (Table 1) (Liousse et al., 2003; 2010; Michel et al., 2005).

The ***GFED*** emission inventory, introduced below, works with a set of emission factors based on Andreae and Merlet (2003), which are used in some of the GOCART runs together with the GFED dry mass option. For comparison with other inventories, the

GFED emission factors for the aerosol-related species of interest are given in Table 4, with the full set of species considered in GFED3 listed by Van der Werf et al. (2010).

Table 4 GFED3 emission factors used for different fire types, in g species per kg DM (Van der Werf et al., 2010)

	Deforestation	**Savanna and Grassland**	**Woodland**	**Extratropical forest**	**Agricultural waste burning**	**Peat fires**
OC	4.30	3.21	3.76	9.14	3.71	4.30
BC	0.57	0.46	0.52	0.56	0.48	0.57
SO_2	0.71	0.37	0.54	1.00	0.40	0.71

2.1.4 Global Fire Emission Dataset (GFED) Emission Estimates

In addition to calculating the emissions from different components, as given in Equation 1, we also used emission estimates from the global fire emission dataset (GFED) version 3, which provides emission amounts ready to use in the models, or burned dry mass estimate ($DM=A*B*C$), which can be combined with different emission factor options. The GFED3 daily emission and burned dry mass at the original 0.5°×0.5° spatial resolution (http://www.falw.vu/~gwerf/GFED/GFED3/emissions) were re-gridded to the 1°(lat) × 1.25°(lon) GOCART grid. The GFED3 approach to estimating burned area combines deriving burned area from the change of surface properties with the use of fire detections in places where surface property information is unavailable (Giglio et al., 2010). The Carnegie-Ames-Stanford-Approach (CASA) biogeochemical model used to estimate burned dry mass and emissions is described in detail by Van der Werf et al. (2010), and the method for scaling monthly GFED3 emissions to daily estimates using MODIS active fire counts is described by Mu et al. (2011).

GFED version 2 monthly emission estimates have been widely used in the aerosol modeling community (Dentener et al., 2006), so this dataset is considered here to assess the potential changes with the switch to the newer version of GFED.

2.2 Estimating BB Emissions Based on Fire Radiative Power (FRP)

The relationship between the energy released by the fire and emission of aerosols and gases was suggested by Kaufman et al. (1996), and has subsequently been studied and refined (Ichoku and Kaufman, 2005; Wooster et al., 2005; Vermote et al., 2009; Schroeder et al., 2010). The approach presented by Wooster et al. (2002; 2005) relates the amount of combusted biomass and fire radiative energy (FRE) as follows:

$$DM(kg) = a * FRE(MJ) \quad [2]$$

where a is an empirically derived factor, and DM is burned dry mass. Fire radiative energy FRE is the fire radiative power (FRP) obtained from the 3.9 micron radiative energy flux at the top-of-atmosphere measured by MODIS, and integrated over time for the estimated duration of burning. This relationship has been used by the developers of FRP-based emission inventories, such as Global Fire Assimilation System (GFAS) (Kaiser et al., 2012) and Quick Fire Emission Dataset (QFED) (Darmenov and da Silva, 2012, personal communication). In GFAS, species-specific emission factors are then applied to DM estimates to obtain aerosol emissions. QFED developers work directly with CO emissions, having already pre-multiplied emission factors, to relate their emission rate to the observed FRP. These inventories use monthly GFED estimates of DM (GFAS) and carbon monoxide (CO) (QFED) to find region-specific conversion factors a_{Region}, which are then applied to daily estimates of FRP to obtain daily values of emission rates.

After the initial emissions have been estimated, these estimates are adjusted to improve the agreement between MODIS-measured AOD and model-simulated AOD with these emissions as model input. GFAS applies a global factor of 3.4 to enhance emission estimates (Kaiser et al., 2012), while in QFED, additional regression is performed using MODIS AOD, to find region-specific emission strength factors (Darmenov and da Silva, manuscript in preparation, 2012). GFAS is the BB emission dataset used in the Monitoring Atmospheric Composition and Climate (MACC) atmospheric composition forecasting system (Kaiser et al., 2012), and QFED is the default BB emission inventory in the GEOS-5 modeling system (Rienecker et al., 2008)

We use QFED version 2.2 in this study to compare its emission estimates with those by other inventories. However, due to the use of MODIS AOD to adjust QFED emissions during its development, QFED-based GOCART runs are not used in comparisons with the MODIS AOD, as is described in Chapter 4. QFED-2.2 provides daily estimates of BB emissions at ~0.25°(lat) × 0.3125°(lon) horizontal resolution, and can be obtained from its developers at Global Modeling and Assimilations Office (GMAO, http://gmao.gsfc.nasa.gov/) at NASA Goddard Space Flight Center.

2.3 BB Emission Options

Ready-to-use emission inventories and the combinations of parameters, as described above, resulted in 13 datasets that define BB source location and strength. These products are referred to here as "emission options", and are summarized in Table 5.

The name of the emission option is usually composed of three parts, where the first set of alphanumeric symbols stand for burned area product, next set of symbols signify the fuel consumption product, and the last symbols define the emission factor option. If the emissions came from a ready-to-use inventory (such as GFED3 or QFED), the name of the inventory is kept unchanged.

Table 5 Emission estimates used as input to GOCART model

Emission options (input to GOCART)	**mod1 -CCi -GOCART**	**mod1 -CCm -GOCART**	**mod1 -GLC -GOCART**	**mod1 -GLC -GLC**	**MCD45 -CCi -GOCART**	**MCD45-CCm -GOCART**	**MCD45-GLC -GOCART**	**MCD45-GLC -GLC**	**GFED3d -GOCART**	**GFED3d**	**GFED3m -GOCART**	**GFED2m -GOCART**	**QFED**
Burned area products													
Based on MODIS active fire counts **(mod1)**	X	X	X	X									
MODIS collection 5 burned area product - MCD45A1 **(MCD45)**					X	X	X	X					
Fuel consumption, dry mass, and emission products													
Carbon consumption (CC) dataset, converted to fuel consumption using Haines index **(CCi)**	X				X								
CC dataset, converted to fuel consumption assuming all fires of medium severity **(CCm)**		X				X							
GLC2000 fuel consumption **(GLC)**			X	X			X	X					
GFED version 3 - daily dry mass burned **(GFED3d)**									X	X			
GFED version 3 - monthly dry mass burned **(GFED3m)**											X		
GFED version 2 - monthly dry mass burned **(GFED2m)**												X	
QFED2 - daily BC, OC and SO_2 emissions **(QFED)**													X
Emission factor options													
Standard GOCART F_j **(GOCART)**	X	X	X		X	X	X		X		X	X	
GLC2000 emission factors **(GLC)**				X				X					
GFED version 3 emission factors										X			

2.4 GOCART model

GOCART is a global chemistry and transport model that simulates the major tropospheric aerosol types: sulfate and its precursors, OC, BC, dust, and sea salt. For this work, it uses assimilated meteorological fields from the Goddard Earth Observing System Data Assimilation System version 4 (GEOS-4 DAS) with a spatial resolution of 1.25° longitude by 1° latitude, and 30 vertical layers (Bloom et al., 2005). GEOS-4 DAS includes diagnostic fields - winds, temperature, pressure, specific and relative humidity, cloud fraction, and also extensive prognostic fields, such as cloud mass flux, precipitation, boundary layer depth, surface winds, and surface wetness. Model time step is 20 min for advection, convection, diffusion, and 60 min for emission, chemistry, dry and wet deposition. Instantaneous meteorological fields, which are imported every 3 or 6 hours, are linearly interpolated to the model time (Chin et al., 2000).

The GOCART model is described in detail in several publications (Chin et al., 2000; 2002; 2007; 2009). Briefly, chemical processes in the model include gas and liquid phase reactions that convert sulfate precursors (dimethylsulfide or DMS, and SO_2) to sulfate. Physical processes include aerosol emission, advection, convection, as well as wet and dry deposition. Natural and anthropogenic emissions of sulfate precursors and carbonaceous aerosols are read-in from the available global inventories. Sulfate sources include continuous and sporadic volcanic emissions, SO_2 emissions from Total Ozone Mapping Spectrometer (TOMS) estimates and anthropogenic emissions (cars, ships and air-traffic). Emissions of DMS (sulfate precursor), sea salt and dust are calculated in the model, and are a function of surface type and wind speed (Chin et al., 2000; 2004; 2009). Anthropogenic carbonaceous aerosol emissions (BC and OC) are taken from the global dataset that includes emissions from domestic, transportation, and industrial combustion sources (Chin et al., 2002). Carbonaceous aerosol aging is represented by the conversion of hydrophobic aerosols (original 80% of BC and 50% of OC) to hydrophilic with an e-folding time of 2 days. All aerosol types, except dust, are subject to hygroscopic growth, which depends on relative humidity (Chin et al., 2002).

GOCART output is usually generated every 3, 6 or 24 hours; however, other time steps can be set. The model is run on the supercomputer at NASA Goddard Space Flight Center and the output files can be obtained from the GOCART research group (M. Chin., T. Diehl, personal communication).

2.4.1 Biomass Burning Emissions in GOCART

Biomass burning emissions of SO_2, BC, and OC are provided by external datasets summarized in section 2.2.3. The model was run once with each emission option, each time for the same 13 months (June 2006 - June 2007), preceded by a 3-month spin-up, with all other settings (e.g., anthropogenic and natural emissions) kept the same. Daily BB emissions were prepared off-line and then read into the model. All BB emissions were assumed to be released within the planetary boundary layer.

2.4.2 Aerosol Optical Depth (AOD)

Aerosol optical depth, usually denoted by Greek letter τ, is determined from the dry aerosol mass loads (M_d in g m^{-2}) and mass extinction cross-sections (β, in units of m^2 g^{-1}) for the major aerosol types according to the following relationship:

$$\tau_i = \beta_i M_d, \qquad [3]$$

where *i* is null for total extiction optical depth, *a* for absorption and *s* for extinction optical depth, respectively. Through definitions of dry aerosol mass load and extinction cross-sections, AOD is a function of aerosol size distributions, refractive indices, and humidity-dependent hygroscopic growth. Total AOD is the sum of optical depths of individual aerosol types: dust, black carbon, particulate organic matter, sulfate, and sea salt. The AOD calculation method, as well as the sources and values of the relevant parameters, are reviewed by Chin et al. (2002; 2009).

2.5 Satellite Observations of Aerosol

2.5.1 MODIS Aerosol Optical Depth

We use the 550 nm AOD from the MODIS level II aerosol product (MOD04 or MYD04 from the MODIS instruments on Terra and Aqua satellites, respectively) at 10 km resolution (Remer et al., 2006; Levy et al., 2010). For each BB event, only one MODIS snapshot is used, from MOD04 or MYD04, as appropriate. All 10-km pixels where AOD retrievals are available are averaged to the 1°lat × 1.25°lon GOCART grid for further comparison with the model AOD.

2.5.2 MISR Stereo Height and Aerosol Product

To evaluate the height of smoke layers we use the MISR operational level 2 stereo height product (from http://eosweb.larc.nasa.gov), which reports cloud and near-source aerosol plume heights globally, on a 1.1-km grid, and with vertical accuracy of about 0.5 km (Moroney et al., 2002). Kahn et al. (2007) shows the use of MISR stereo height product and its relationship to aerosol type and amount, to determine BB plume heights. The MISR aerosol product includes AOD and aerosol type constraints, globally (Kahn et al., 2010), and is used here to confirm plume locations when assessing their height.

2.5.3 CALIPSO Vertical Feature Mask

CAIPSO vertical feature mask provides vertical and horizontal distribution of cloud and aerosol layers with 5 km spatial resolution (Vaughan et al., 2004; Winker et al., 2009). Aerosol and cloud layers are classified by associating measured optical or physical parameters (such as attenuated backscatter coefficient, or color ratio) with particular class of known atmospheric scatterer (Cattral et al., 2005). The Vertical Feature Mask is used here to evaluate smoke height for the cases studied, where CALIPSO observations are available. Daily CALIOP data are available at http://eosweb.larc.nasa.gov/PRODOCS/calipso/table_calipso.html.

2.6 Biomass Burning Events

One hundred and twenty four representative fire events, occurring between June 2006 and June 2007 in different regions of the world, were used to evaluate the emission options. These events include a range of fire sizes, seasons, types of vegetation, and burning conditions. Fire cases were selected to include smoke plumes, which are defined as smoke-like features appearing in MODIS visible images, supported by presence of fire pixels reported in MODIS thermal anomalies product (MOD14/MYD14 for Terra and Aqua MODIS respectively), and at the same time showing elevated AOD in the MODIS AOD data. Thus, the sizes of cases vary considerably, and include single fires with associated smoke plumes, such as several events in the US, areas of generally hazy regions containing many fires with or without individual visible plumes, such as the agricultural burning in Africa, Eastern Europe or South America, or cases where large individual smoke plumes merge to produce thick smoke clouds, such as several cases in Russia, Canada, Indonesia, and South Australia. Table 6 provides a list of fire cases studied, which gives their unique identification numbers, specifies their geographic boundaries defined by latitude and longitude corners, reports the date of MODIS observation, and denotes the MODIS-carrying satellite used by letters "A" or "T", which stand for Aqua and Terra, respectively.

To locate the fire events, we used as a starting point events featured on the Earth Observatory web site, which provides a selection of fires in the Natural Hazards/Fires category (http://earthobservatory.nasa.gov/NaturalHazards). We also used a combination of MODIS visible browse images (http://modis-atmos.gsfc.nasa.gov/IMAGES/) and the locations of fire detections from the MOD14A1 and MYD14A1 thermal anomalies products to identify the locations and times of burning events. A subset of these events was chosen for analysis, based on whether smoke or general haziness, un-obscured by condensate cloud, appears in visible images of the region. Figure 2 displays a map showing the locations of the cases studied. They are grouped into geographic regions having roughly similar burning conditions.

In selecting the fire cases, we also considered biomass burning seasons in different regions. These seasons are described elsewhere (Duncan et al., 2003; Giglio et al., 2006; 2010; Dey and Di Girolamo, 2010) and are mentioned in Table 6. Table 6 also provides a description of prevailing vegetation and characteristics of burning in each world region.

In regions with strong dust sources, such as northern India and North Africa, we consider the seasonality of dust emissions as those times when dust significantly contributes to the total AOD. Much of the spring peak of forest and harvest burning in India coincides with the pre-monsoon dust season (Dey and Di Girolamo, 2010), so most burning cases are selected during early spring or during the smaller burning season in November. Similarly, major biomass burning in sub-equatorial Africa during boreal winter coincides with the November-March season of dust transport (Pandithurai et al., 2001), and therefore fire cases were chosen at the onset of the burning season in November to minimize the dust influence.

Years 2006 and 2007 were those of very little biomass burning in Alaska, so a few cases were observed by MODIS, out of which only four were both large enough to be seen from space and sufficiently un-obscured by clouds to be used for this analysis.

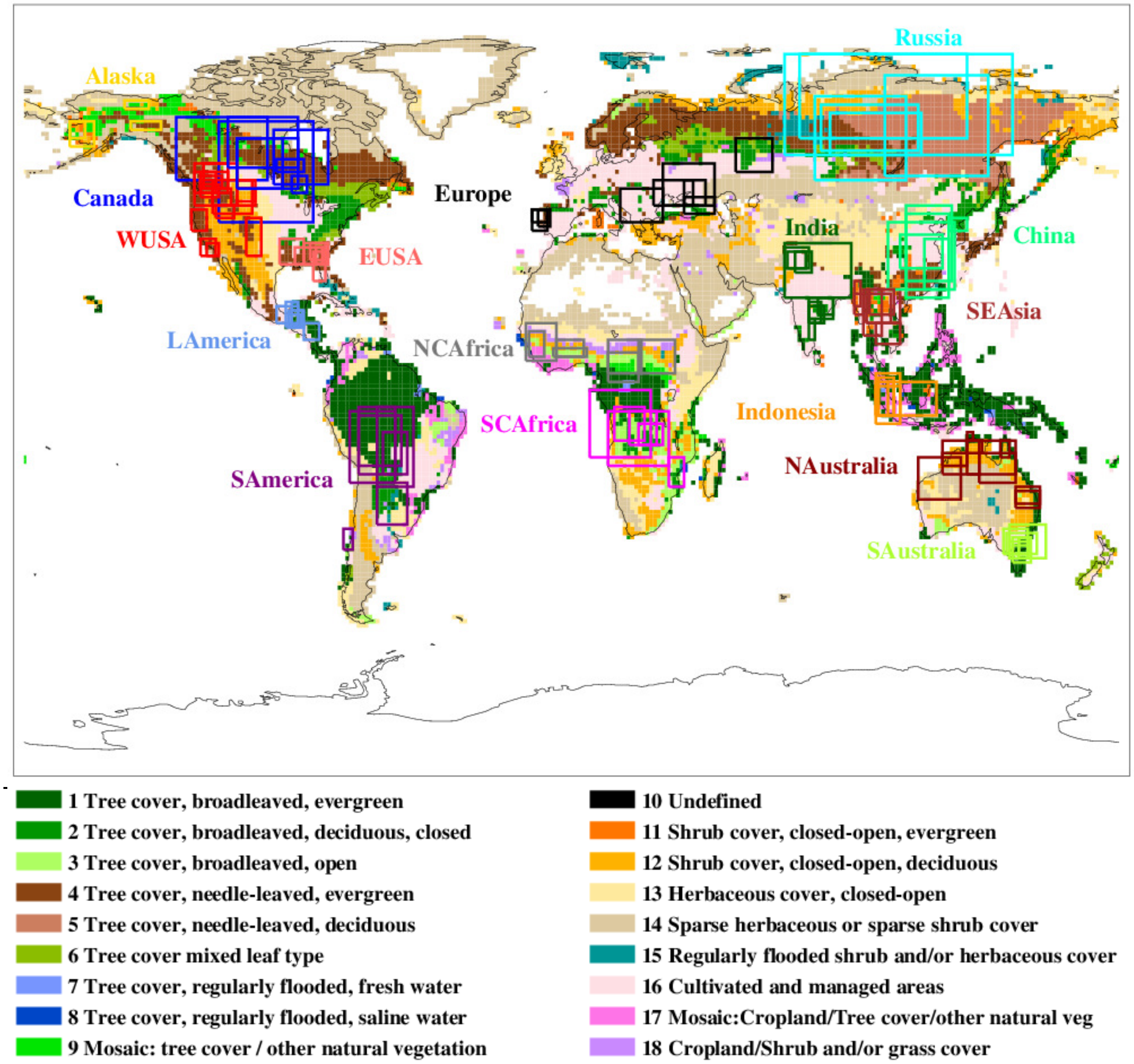

Figure 2 Studied fire cases, case boxes color-coded by the world region. Underlying colors represent the GLC vegetation types described in section 2.1.2

Table 6 Study cases by region with the regional specifics of biomass burning

Region Biomass burning season(s)	**Case number, T/A, Date (yyyy-mm-dd) coordinates [SW corner; NE corner]**	**AOD threshold, symbol in Fig.11**		**Dominant vegetation type(s); Characteristics of burning; some notes on MODIS AOD**
Alaska Jun-Aug	42 T (2006-06-04) [60N 165W; 64N 160W] 43 T (2006-06-05) [58N 165W; 64N 155W] 46 T (2006-07-23) [62N 145W; 64N 135W] 122 T (2006-06-15) [67N 147W; 69N 139W]	0.15 0.15 0.05 0.15	◇ △ □ ○	Tree cover: mosaic with other natural vegetation, evergreen; evergreen shrubs. Individual fires with associated smoke plumes. MODIS AOD is not usually retrieved in plume cores.
Canada Jun-Sep	1 T (2006-07-04) [50N 130W; 65N 100W] 2 T (2006-06-26) [48N 110W; 60N 95W] 3 T (2006-06-27) [40N 116W; 64N 85W] 31 T (2007-05-10) [47N 92W; 51N 87W] 70 A (2006-08-31) [49N 100W; 62N 80W] 74 A (2006-09-06) [52N 97W; 55N 88W] 113 T (2006-07-05) [48N 110W; 60N 90W] 114 T (2006-09-10) [53N 113W; 65N 90W]	0.15 0.15 0.15 0.1 0.15 0.1 0.15 0.15	◇ △ □ ○ ▽ ▹ ◃ ⧖	Tree cover: needleleaved, mixed leaf type, mosaic with other natural vegetation. Individual fires with associated smoke plumes combine into large-scale plumes/smoke regions. MODIS AOD is often not retrieved in plume cores.
China Jan-Apr, Aug-Oct	37 T (2007-05-29) [29N 108E; 37N 122E] 55 T (2006-08-15) [24N 116E; 36N 124E] 59 T (2006-09-22) [24N 104E; 40N 126E] 60 T (2006-10-05) [26N 110E; 44N 125E] 61 T (2006-10-30) [22N 110E; 42N 124E] 94 A (2007-04-29) [38N 124E; 41N 130E]	0.4 0.4 0.4 0.4 0.4 0.15	◇ △ □ ○ ▽ ▹	Mosaic: Cropland, tree cover, other natural vegetation; Tree cover: neddleleaved, broadleaved. Many fires with no distinct smoke plumes create overall hazy/smoky area.
Europe Mar-May, Jun-Oct	51 T (2006-07-28) [40N 16E; 48N 30E] 53 T (2006-08-02) [44N 27E; 50N 40E] 54 T (2006-08-04) [44N 30E; 54N 47E] 69 T (2006-09-01) [52N 54E; 60N 66E] 85 T (2006-08-07) [38N 13W; 43N 8W] 86 T (2006-08-09) [40N 13W; 43N 8W] 87 A (2006-08-13) [39N 11W; 43N 7W] 132 A (2006-08-03) [44N 37E; 50N 44E] 133 T (2006-08-06) [42N 37E; 46N 47E]	0.2 0.2 0.2 0.15 0.15 0.15 0.15 0.15 0.1	◇ △ □ ○ ▽ ▹ ◃ ⧖ ⋈	Cultivated and managed areas; Mosaic: Cropland, tree cover, other natural vegetation. Fires with or without detectable associated smoke plumes create overall hazy/smoky area.
India Mar-May, Oct	17 T (2006-11-05) [22N 70E; 35N 92E] 41 A (2006-10-15) [28N 72E; 33N 80E] 123 A (2007-03-26) [16N 78E; 21N 82E] 124 A (2007-03-01) [12N 78E; 17N 80E] 125 A (2007-03-06) [18N 81E; 22N 86E] 126 A (2007-03-08) [16N 78E; 20N 83E] 127 A (2007-03-17) [17N 78E; 22N 86E] 128 A (2007-05-02) [29N 71E; 33N 77E] 129 A (2007-05-07) [29N 70E; 34N 78E]	0.1 0.1 0.15 0.15 0.15 0.2 0.15 0.2 0.2	◇ △ □ ○ ▽ ▹ ◃ ⧖ ⋈	Cultivated and managed areas. Fires with or without detectable associated smoke plumes create overall hazy/smoky area.

Table 6 Continued

Indonesia Apr, Jul-Nov	13 T (2006-10-12) [6S 104E; 2N 120E] 14 T (2006-10-05) [6S 104E; 2N 120E] 15 T (2006-10-04) [8S 100E; 4N 108E] 16 T (2006-09-27) [6S 100E; 1N 108E] 135 A (2006-10-02) [6S 100E; 2N 106E] 136 A (2006-10-11) [6S 101E; 3N 106E]	0.2 0.1 0.15 0.15 0.15 0.15	◇ △ □ ○▽ ▹	Tree cover: broadleaved; cropland/shrubs and /or grass. Individual fires with associated smoke plumes combine into large-scale plumes/smoke regions. MODIS AOD is often not retrieved in plume cores.
LAmerica Mar-Jun	32 A (2007-05-12) [12N 88W; 16N 83W] 33 A (2007-05-13) [12N 88W; 16N 83W] 35 A (2007-04-11) [15N 93W; 18N 89W] 36 T (2007-04-11) [15N 93W; 19N 88W] 107 T (2007-05-02) [15N 94W; 21N 90W] 108 T (2007-05-11) [15N 92W; 21N 89W] 110 A (2007-04-18) [15N 92W; 19N 88W] 112 A (2007-05-22) [16N 97W; 20N 90W]	0.15 0.15 0.15 0.1 0.1 0.15 0.15 0.15	◇ △ □ ○ ▽ ▹ ◃ ⧖	Tree cover: broadleaved; cropland/shrubs and /or grass. Fires with or without detectable associated smoke plumes create overall hazy/smoky area.
NAustralia Aug-Nov	57 T (2006-09-16) [18S 122E; 15S 130E] 58 T (2006-09-18) [20S 122E; 12S 134E] 65 A (2006-11-22) [28S 146E; 23S 154E] 66 A (2006-11-22) [22S 134E; 15S 146E] 67 A (2006-11-22) [26S 114E; 16S 128E] 68 T (2006-11-24) [20S 130E; 12S 146E] 103 A (2007-06-10) [15S 130E; 12S 135E] 104 A (2006-11-17) [27S 146E; 24S 154E] 105 A (2006-11-20) [16S 141E; 12S 144E] 106 A (2006-10-04) [12S 130E; 10S 132E]	0.1 0.1 0.1 0.1 0.15 0.1 0.15 0.1 0.15 0.1	◇ △ □ ○ ▽ ▹ ◃ ⧖ ⋈ ▯	Shrub cover; herbaceous cover. Individual fires, some with weak associated smoke plumes. MODIS AOD is often not retrieved with intermittent clouds and bright surface.
NCAfrica Oct-Feb	21 A (2007-01-05) [2N 12E; 9N 22E] 62 T (2006-11-16) [4N 22E; 12N 34E] 63 T (2006-11-16) [7N 15W; 16N 5W] 64 T (2006-11-18) [4N 12E; 12N 23E] 118 A (2006-11-26) [8N 6W; 10N 5E] 119 A (2006-11-23) [8N 5W; 12N 4E] 120 A (2006-12-03) [8N 14W; 14N 9W]	0.15 0.15 0.15 0.1 0.15 0.15 0.1	◇ △ □ ○ ▽ ▹ ◃	Tree cover: broadleaved, mixed; shrubs; cropland. Many fires with no distinct smoke plumes create overall hazy/smoky area
Russia Apr-Oct	10 T (2006-07-17) [56N 85E; 66N 115E] 11 T (2006-07-20) [50N 80E; 70N 110E] 47 T (2006-07-25) [60N 75E; 80N 130E] 48 T (2006-07-25) [56N 70E; 80N 145E] 50 T (2006-07-27) [51N 103E; 75N 137E] 102 A (2006-07-24) [57N 82E; 68N 114E]	0.15 0.15 0.15 0.15 0.15 0.15	◇ △ □ ○ ▽ ▹	Tree cover: needleleaved, mixed leaf type, mosaic with other natural vegetation. Individual fires with associated smoke plumes combine into large-scale plumes/smoke regions. MODIS AOD is often not retrieved in plume cores.

Table 6 Continued

SAmerica Jul-Nov	38 A (2006-08-21) [18S 70W; 6S 56W] 39 T (2006-08-21) [20S 70W; 4S 58W] 40 A (2006-08-24) [22S 73W; 5S 58W] 44 A (2006-07-07) [32S 64W; 22S 54W] 45 T (2006-07-12) [20S 62W; 10S 54W] 56 T (2006-08-31) [23S 64W; 4S 52W] 89 A (2007-01-13) [38S 75W; 33S 72W]	0.15 0.15 0.15 0.1 0.1 0.15 0.1	◇ △ □ ○ ▽ ▹ ◃	Tree cover: broadleaved evergreen, deciduous; cropland/shrubs and /or grass. Individual fires with or without associated smoke plumes, generally hazy, but some combine into larger plumes. MODIS AOD is often not retrieved in complex cloudy scenes.
SAustralia Feb-May	18 T (2006-12-04) [39S 142E; 33S 150E] 19 T (2006-12-18) [40S 144E; 32S 156E] 20 T (2006-12-20) [40S 144E; 36S 150E] 96 T (2007-01-10) [39S 145E; 37S 150E] 97 T (2006-12-05) [41S 145E; 35S 151E] 100 A (2006-04-13) [39S 147E; 35S 150E] 101 A (2006-04-20) [40S 147E; 35S 150E] 134 A (2006-12-08) [39S 143E; 34S 153E]	0.1 0.1 0.1 0.15 0.15 0.1 0.1 0.1	◇ △ □ ○ ▽ ▹ ◃ ⧖	Three cover: broadleaved evergreen; cropland. Individual fires with associated smoke plumes combine into large-scale plumes/smoke regions, or Fires with or without detectable associated smoke plumes create overall hazy/smoky area.
SCAfrica Jun-Oct	12 T (2006-06-24) [16S 6E; 0 26E] 49 A (2006-07-26) [18S 12E; 5S 32E] 115 A (2007-06-24) [13S 19E; 5S 28E] 116 A (2007-06-13) [13S 22E; 8S 30E] 117 A (2006-08-04) [23S 32E; 16S 37E] 121 A (2007-05-28) [12S 14E; 4S 24E]	0.15 0.15 0.15 0.1 0.1 0.1	◇ △ □ ○ ▽ ▹	Tree cover: broadleaved. Many fires with no distinct smoke plumes create overall hazy/smoky area
SEAsia Jan-Jun , Sep-Nov	25 A (2007-03-04) [16N 97E; 24N 108E] 27 T (2007-01-26) [11N 100E; 16N 108E] 28 A (2007-01-28) [11N 100E; 16N 108E] 90 A (2007-04-02) [18N 98E; 24N 106E] 91 A (2007-03-13) [16N 97E; 23N 105E] 92 A (2007-03-18) [13N 96E; 24N 102E] 93 A (2007-03-27) [20N 93E; 26N 95E] 95 A (2007-03-02) [18N 93E; 23N 96E]	0.15 0.15 0.15 0.15 0.15 0.15 0.15 0.15	◇ △ □ ○ ▽ ▹ ◃ ⧖	Cropland; tree cover: needleleaved, broadleaved; shrub cover. Fires with or without detectable associated smoke plumes create overall hazy/smoky area.

Table 6 Continued

EUSA Feb-Jun	23 A (2007-03-07) [30N 91W; 34N 82W]	0.1	◇	Cropland; tree cover: needleleaved, broadleaved; shrub cover. Fires with or without detectable associated smoke plumes create overall hazy/smoky area.
	24 T (2007-03-07) [30N 96W; 36N 88W]	0.1	△	
	75 T (2007-03-20) [30N 88W; 35N 80W]	0.15	□	
	76 T (2007-05-20) [30N 84W; 34N 81W]	0.15	○	
	109 A (2007-05-12) [26N 85W; 33N 81W]	0.15	▽	
	111 T (2007-05-22) [1N 86W; 35N 81W]	0.15	▹	
WUSA Jun-Nov	4 T (2006-07-16) [44N 110W; 48N 104W]	0.1	◇	Three cover: needleleaved; shrub cover. Individual fires with associated smoke plumes. Heterogeneous terrain and vegetation leads to many omissions in AOD retrievals and fire detections and characterization. MODIS AOD is often not retrieved in plume cores.
	5 T (2006-07-18) [45N 110W; 50N 104W]	0.1	△	
	7 T (2006-09-12) [42N 118W; 50N 105W]	0.1	□	
	8 T (2006-06-20) [34N 107W; 41N 102W]	0.1	○	
	9 T (2006-12-03) [32N 122W; 36N 117W]	0.1	▽	
	71 A (2006-10-26) [32N 120W; 35N 116W]	0.15	▹	
	72 A (2006-08-16) [41N 117W; 44N 111W]	0.15	◃	
	73 A (2006-09-06) [44N 124W; 54N 110W]	0.15	⧗	
	77 A (2006-07-25) [46N 122W; 49N 116W]	0.1	⋈	
	78 A (2006-08-02) [48N 122W; 50N 117W]	0.15	▯	
	79 A (2006-08-02) [38N 125W; 43N 120W]	0.15	▭	
	80 T (2006-08-07) [48N 121W; 54N 113W]	0.15	⌓	
	81 T (2006-08-20) [47N 122W; 52N 113W]	0.15	◡	
	82 A (2006-08-27) [47N 124W; 52N 117W]	0.15	D	
	83 A (2006-08-28) [48N 122W; 51N 115W]	0.15	◖	
	84 A (2006-08-28) [44N 118W; 48N 112W]	0.15	✶	

CHAPTER 3 COMPARISON OF EMISSION OPTIONS

3.1 Comparison of Emission Estimates

Emission options defined in section 2.3 provide a range of BB emission estimates. Figure 3a shows total dry mass burned globally in 2006, as estimated by each emission option. Since the QFED inventory calculates aerosol emissions directly from MODIS-measured FRP, it does not provide a DM estimate. Figure 3b illustrates the differences in corresponding 2006 global BB emissions of BC. The comparisons for OC and SO_2 produce similar patterns to that of BC. The magnitudes of SO_2 emissions are similar to those of BC, and OC emissions are eight times larger, as expected from the values of species emission factors introduced in section 2.1.3. Comparisons of both DM and emission of individual aerosol species for 2007 (not shown) also show similar patterns.

The differences between individual emission options can be quite large. Thus, the largest estimate of BC emissions by the mod1-CCm-GOCART option is about eight times larger than that in GFED3. These differences can be explained by the choices of parameters that were combined according to Equation 1. Some of these differences are briefly discussed below.

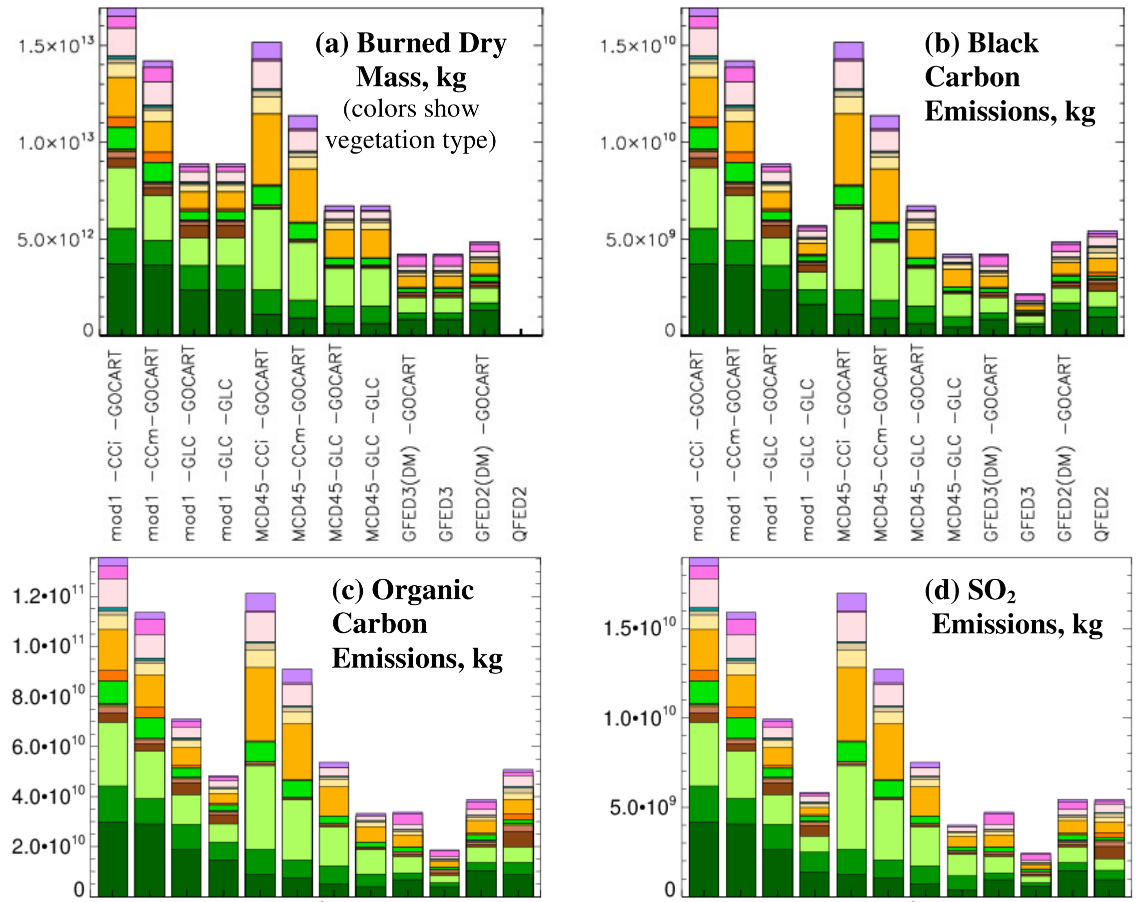

Figure 3 (a): Total dry mass burned globally in 2006, reported by GOCART emission input options considered in this study; (b): total global emissions of BC; (c): total global emissions of OC; (d): total global emissions of SO_2, each column representing one emission option. Colors in each bar correspond to dry mass burned (a) or aerosol component emissions (b-d) from the GLC vegetation types outlined in Fig.2

Regional differences between emission options vary from those on a global scale. To aid this comparison, total estimates of DM and aerosol emissions shown in Figure 3 are broken down by GLC vegetation type defined in Table 1 and Figure 2. In addition, total global daily emissions of Black Carbon are plotted in Figures 4a and 4b as a function of time to emphasize the temporal differences of emission estimates. Daily BC emissions in Figure 4 (a-b) are plotted as 5-day running averages to smooth daily variations. Comparison of individual lines representing different emission options emphasizes the contribution of individual components (burned area, fuel consumption, emission factors) to the emission estimate differences. In addition, total emissions of black carbon during 2006 from biomass burning sources are mapped for each emission option in Figure 5 to show the differences spatially. The most dramatic differences in emission estimates are apparent in the forested regions, where fire-counts-based BA inventory 'mod1', combined with the fuel-rich ecosystem types, produce much larger estimates of emissions than the other inventories. The larger GLC fuel consumption in needle-leaved evergreen forests (mostly boreal) results in more estimated BC emissions, but this difference is barely noticeable with the MCD45 burned area estimates due to the very low estimates of burned areas in this region by the MCD45 dataset. Heavier CCm fuel consumption in crops, non-boreal forest and sparsely vegetated regions leads to noticeably larger emission from these respective vegetation types with both the mod1 and MCD45 BA estimates. The choice of the GOCART emission factor over the GLC or GFED options leads to more emissions. The QFED option has a relative distribution of emissions over vegetation types different from the other products, which were produced based on the method described by Equation 1.

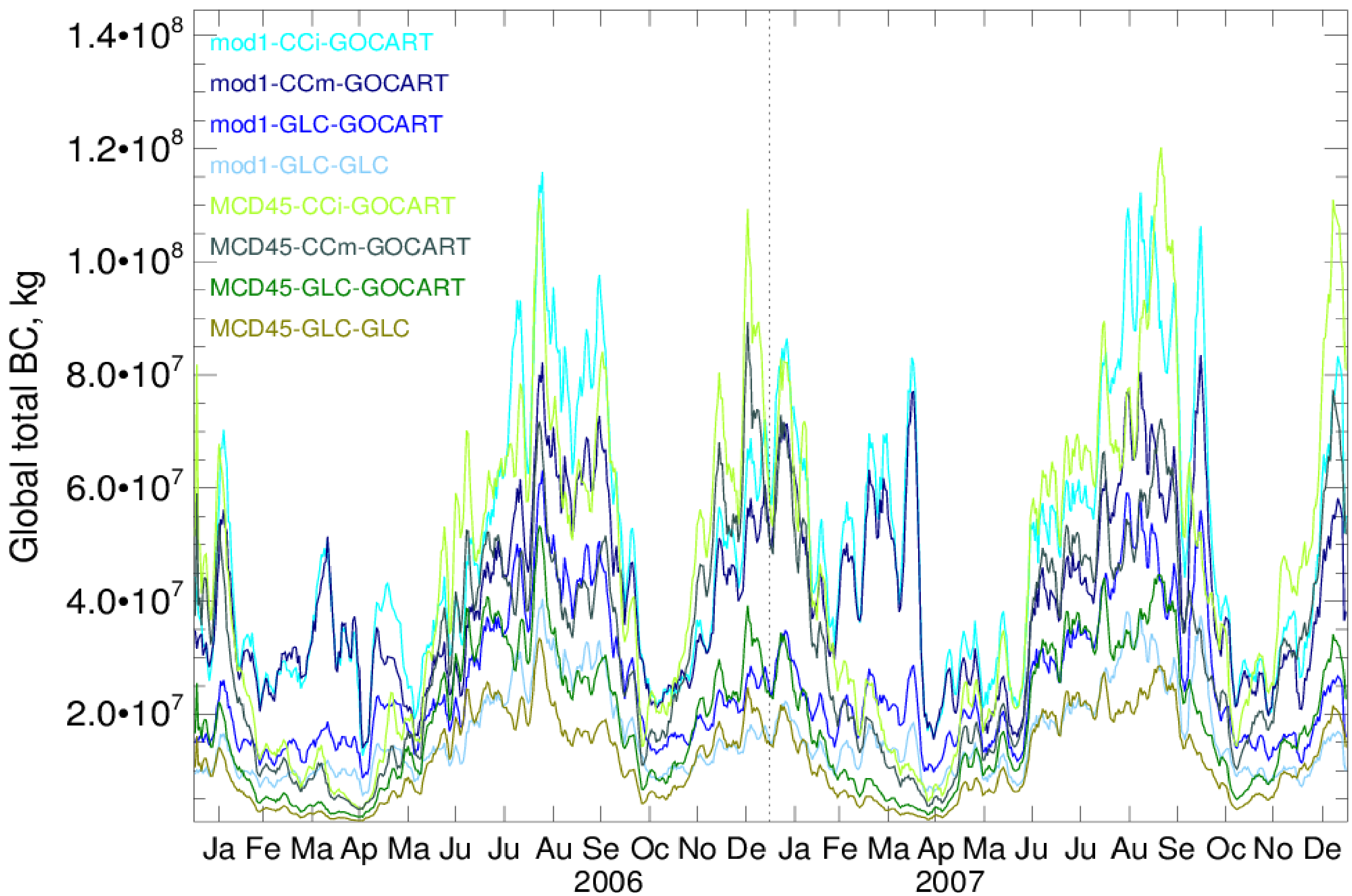

Figure 4a Global total daily estimates of BC emissions in kg, as estimated by 8 of 13 emission options

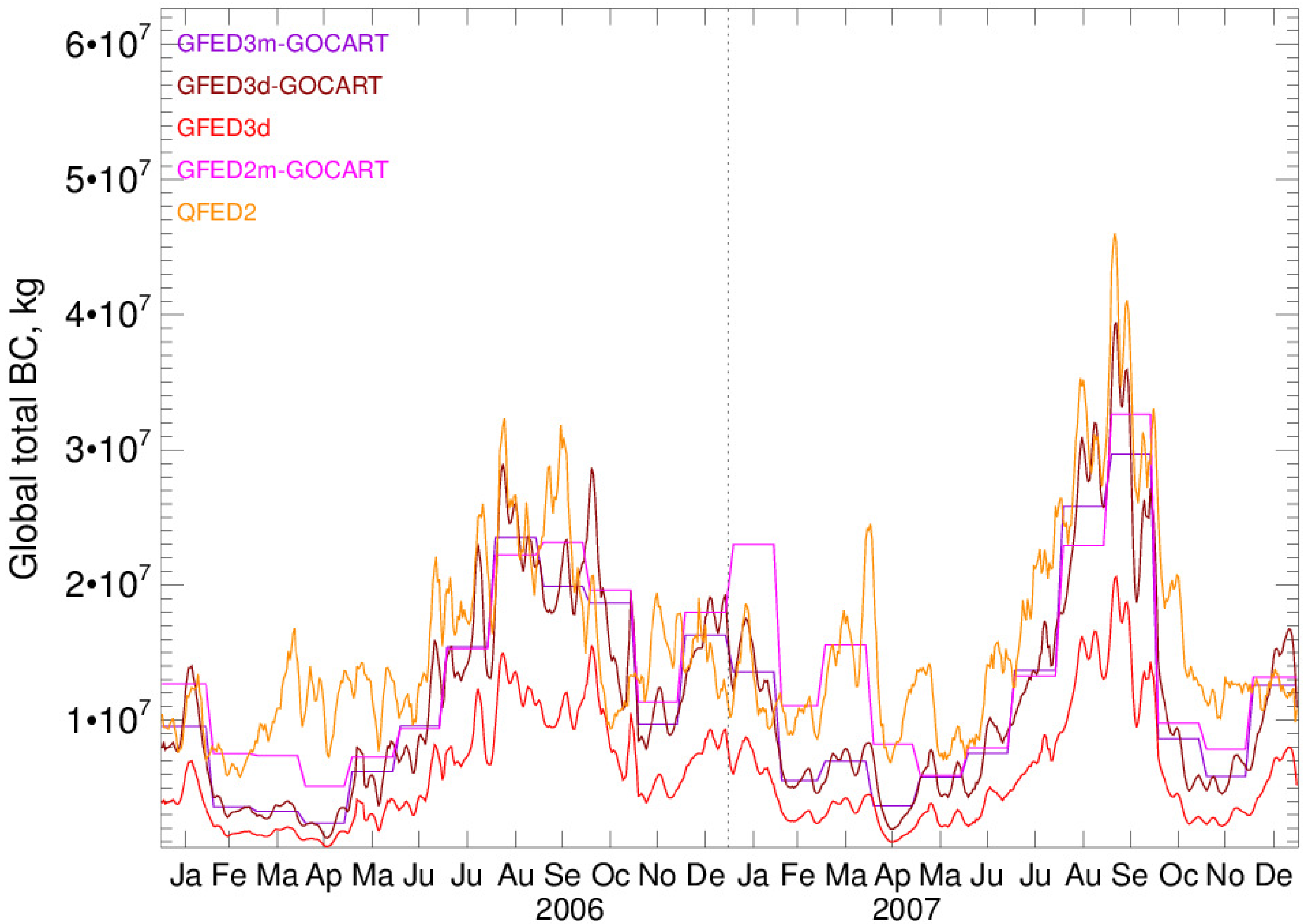

Figure 4b Global total daily estimates of BC emissions in kg, as estimated by GFED emission options and QFED

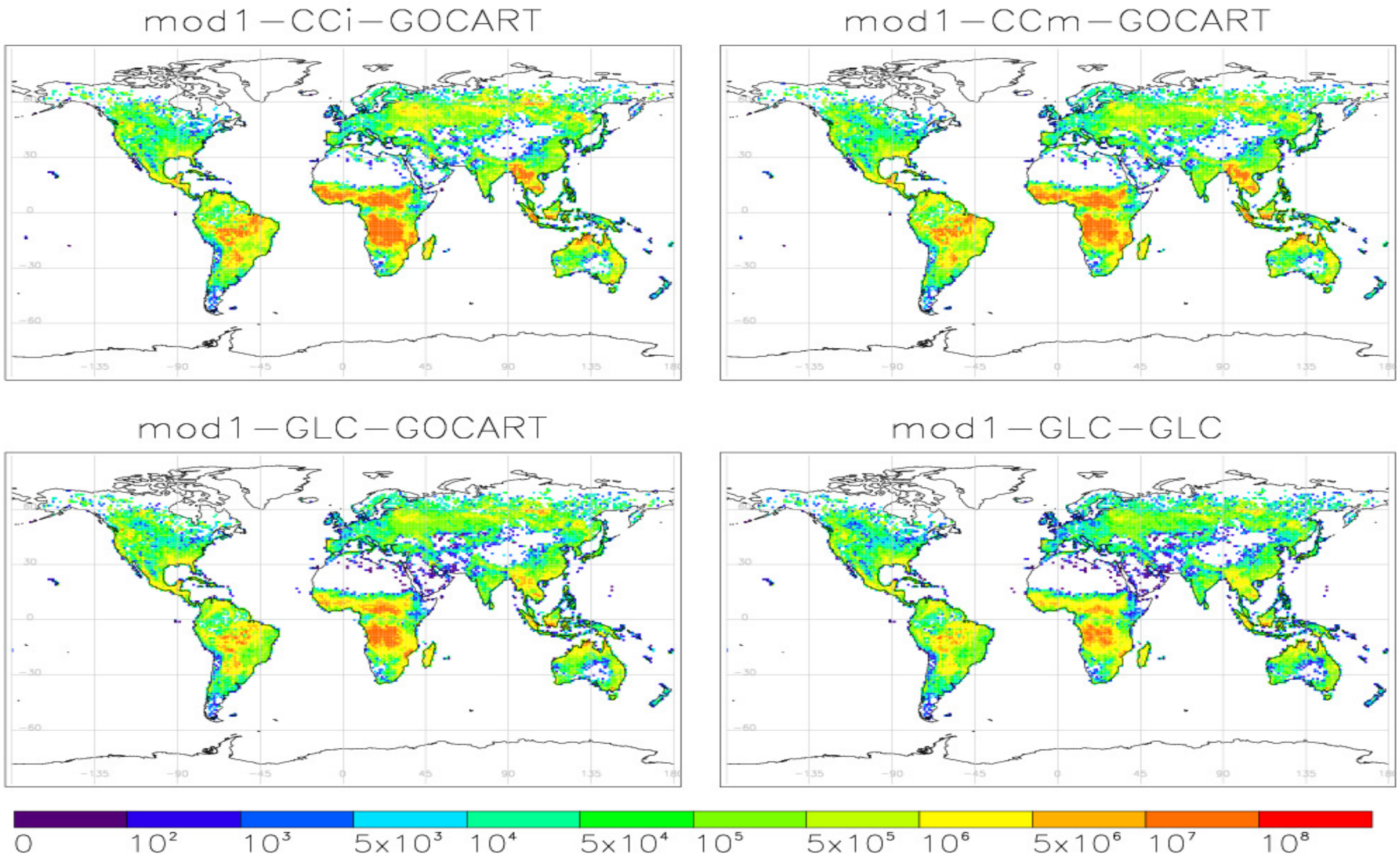

Figure 5a Annual emissions of black carbon in 2006 estimated by each emission option. In units of kg per GOCART grid box. mod1 (fire counts-based) emission options

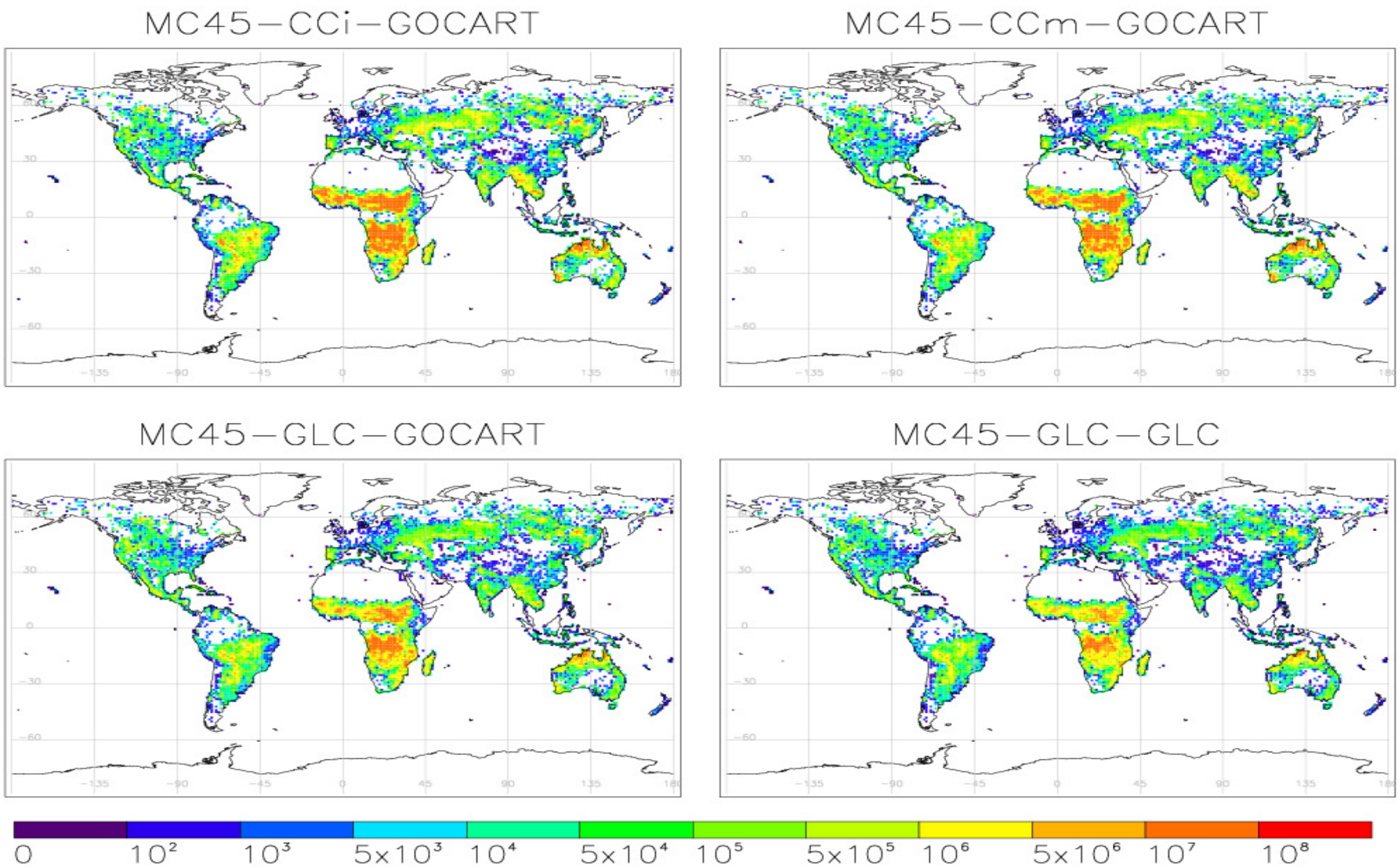

Figure 5b Annual emissions of black carbon in 2006 estimated by each emission option. In units of kg per GOCART grid box. MCD45 (surface change-based) emission options

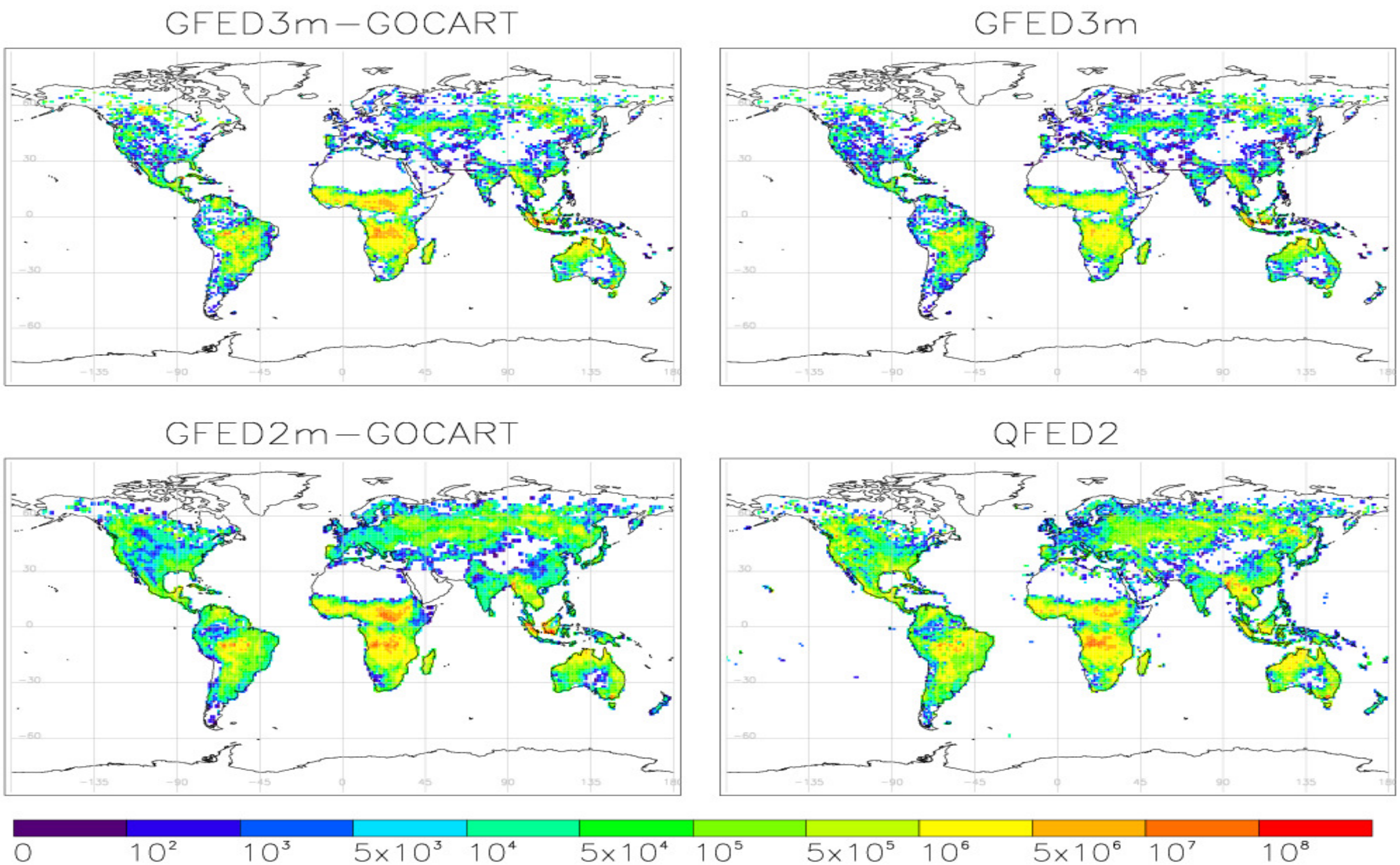

Figure 5c Annual emissions of black carbon in 2006 estimated by each emission option. In units of kg per GOCART grid box. GFED emission options and QFED2

Use of the Haines Index as a proxy for fire intensity, and the subsequent estimation of the amount of burned dry mass, have different effects on BB emission estimates in different regions. In comparison with BB emission estimates when all fires are assumed of medium severity, HI usually leads to aerosol emissions that are larger by about 30-50% in Russia, and about 25% or less larger in Canada and the forested areas of South America. The use of Haines Index in Latin America, however, brings emission estimates down by about 30%. In the other regions, emission estimates using CC biomass density with or without applying the Haines Index are similar, with slight daily variations. Because the Haines Index was developed based on a number of fires in North America, and the highest values of HI are associated with wildfires (Winkler et al., 2007), it is appropriate to use it for wildfires in higher latitudes. However, the application of HI has not been evaluated for other parts of the world, and a prior study of local behavior of the index is needed if one wants to use it to estimate source strength in other regions.

3.2 Burned Area Comparison

Estimates of burned area by MCD45, GFED3, and a version of mod1, mostly for years other than 2006 and 2007, were compared in detail in previous studies by Roy et al. (2008) and Giglio et al. (2010) and their findings are confirmed and illustrated here using the data for the study period. Although the total burned areas reported by all three products globally in 2006 are very similar: 3.94×10^6 km^2 in mod1, 3.96×10^6 km^2 in MCD45, 3.41×10^6 km^2 in GFED3, their performance in different ecosystems is noticeably distinct. Roy, Boschetti et al. (2008) demonstrated that in ecosystems having low Leaf Area Index (LAI) and low percent tree cover - shrublands, grasslands, and savannas, the active fire product (mod1) estimates less burned area than MCD45. On the other hand, when the percent tree cover is high, especially evergreen forests - both needleleaf (mostly in boreal regions) and broadleaf (mostly in equatorial regions), mod1 reports more burned area compared to MCD45. MCD45-type estimates, based on detection of change in surface properties, can be more complete in low LAI regions because the surface is more easily visible from space, whereas active fire detections from once-daily satellite observations can miss events, especially in fast-burning grassland and shrub. In high-LAI forested areas, the surface can be obscured, making direct burned area observation difficult, whereas active fire detections, which are based on identifying hot spots, might be less affected.

GFED3 burned area estimates are similar to those from MCD45 in many regions (Giglio et al., 2010). Croplands are an exception to this pattern, and although having low LAI at the time of burning, more area burned is reported globally by mod1 than the MCD45 algorithm for this category (Roy et al., 2008), with GFED3 burned area being even lower than MCD45 in croplands (Giglio et al., 2010).

Since most of the area burned is a result of fires in Africa, followed by South America and Australia, BB emissions from vegetation types dominant in these regions (GLC codes 1, 3, and 12) show the largest absolute differences, consistent with the described BA detection patterns. The differences in estimated burned area and subsequent emissions can be quite large regionally, such as in boreal regions covered by evergreen needle-leaf forests (GLC code 4), or in tropical crops and shrubs (GLC code 17), but their contribution to total global emissions is relatively small.

Figure 6 shows the global total area burned, as estimated by the three burned area products for 2006 and 2007, in units of km^2 per 1°lat × 1.25°lon GOCART grid box. Most of the area burned is a result of fires in Africa, followed by South America and Australia. Consistent with the patterns observed by Roy et al. (2008), mod1 estimates more burned area than MCD45 in the forested regions - especially noticeable in boreal regions and evergreen broadleaf forests of Central Africa and Amazon. mod1 also estimates more burned area than MCD45 and GFED3 in Southeast Asia, Indonesia, and North America, which are composed of a mixture of vegetation classes. Consistent with the abovementioned trends, mod1 detects less burned area in African and Australian savannas, grasslands, and sparsely vegetated regions than either MCD45 or GFED3.

The distinct seasonality of biomass burning, described in more detail by Giglio et al. (2006; 2010), combined with regional differences of burned area estimates by different inventories, lead to temporal variation of global total estimated area burned. This is demonstrated in Figure 7, where each line represents a three-day running average of global total area burned estimated by each of the three products. The periods showing the largest discrepancies among burned area estimates have been traced to the dominant burning regions during certain periods, and labeled on the graph.

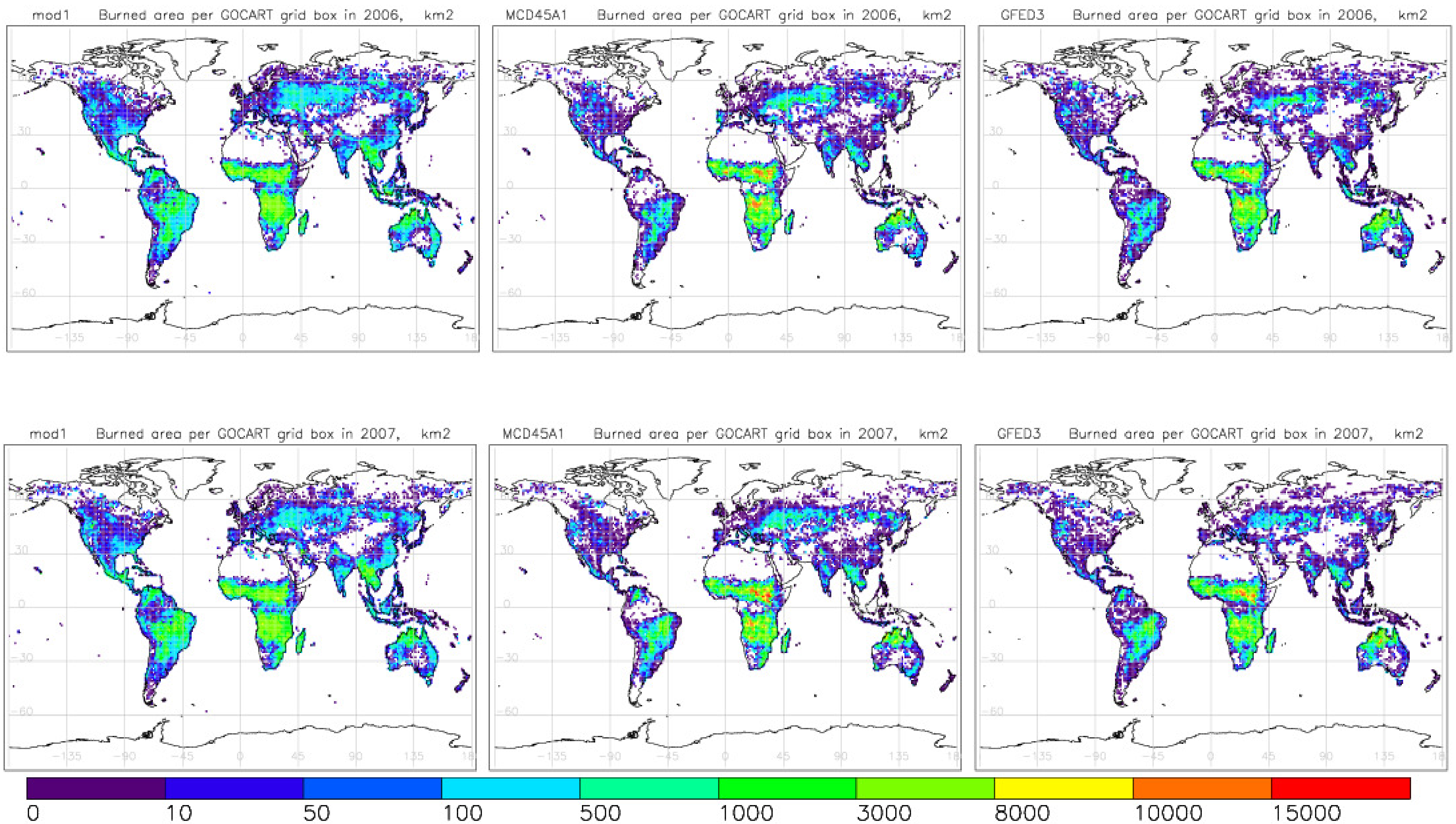

Figure 6 Total area burned during years 2006 (top row) and 2007 (bottom row) estimated by mod1 (left column), MCD45 (middle column) and GFED3 (right column). In units of km^2 per 1°lat×1.25°lon GOCART grid box

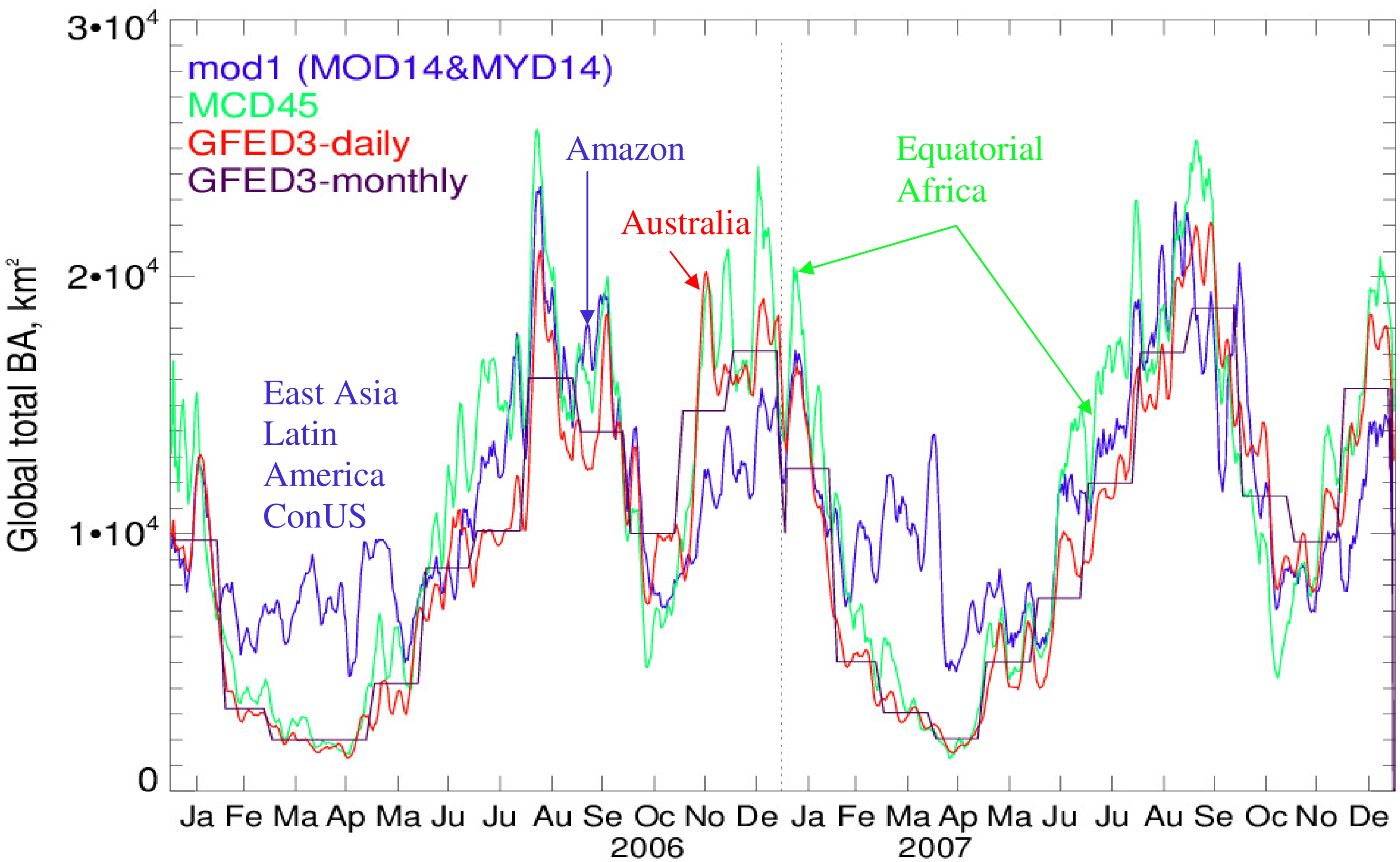

Figure 7 Global total area burned daily during 2006 and 2007 as estimated by mod1 (blue line), MCD45 (green line), GFED3-daily (red line), and GFED3-monthly (purple line). Labels for the regions dominating global BA total during certain months are colored by the dominant BA product

3.3 Fuel Consumption Comparison

The chosen fuel consumption (*B*C* in Eq. 1) products have not been explicitly compared elsewhere. Since no static fuel consumption is provided in the GFED3 dataset, we obtained the equivalent fuel consumption by dividing the GFED3 monthly values of burned dry mass by the corresponding value of burned area in every GOCART grid box. Average fuel consumption from all the available data for the period of 1997-2009 is shown in Fig. 8e. The maps of absolute fuel consumption differences (Fig. 8f, 8g, and 8h) emphasize the discrepancies between the datasets, where the largest differences are in the forested boreal and tropical regions. As can be seen in Fig. 8 (panels a-e) CC estimates of fuel consumption by fires of high severity (CCh) have the largest values, and CCl - the lowest. Assuming all fires of medium fire severity for a reference, we compare the absolute values of fuel consumption in the datasets. The general trend, which shows the CCm dataset including all fires of medium severity (CCm) as giving largest fuel consumption estimates, followed by the GLC and GFED3, is reversed in the boreal needleleaf forest where the GFED3 fuel consumption is the largest, followed by GLC and CCm, and is partially reversed in the parts of tropical forest where GFED3 is the largest, followed by CCm and GLC.

The differences in absolute values of fuel consumptions apparent in Fig. 8 are most prominent in forested regions, both boreal needleleaf and tropical broadleaf, mostly because the absolute values of fuel consumption in these regions are larger than in shrublands and grassy areas, allowing for more variability in estimates. In addition, forested regions allow for a wider range of burning regimes, with fires consuming different fraction of available ecosystem biomass (Soja et al., 2004). Consequently, different assumptions about burning process, such as ratio of flaming to smoldering or assumptions about fractions of fuel consumed at tree tops and understory lead to larger discrepancies in the estimated fuel amount.

3.4 Emission Factors Comparison

GLC and GFED ***emission factors*** are similar and are all generally lower than the GOCART standard F_j's. This difference is smallest in the extra-tropical forest, and is largest in the grasslands and shrublands, where the standard GOCART option can be up to a factor 2 to 3 larger than either the GLC or GFED F_j's.

GLC and GFED emission factors are based mainly on the work of Andreae and Merlet (2001) who presented a thorough compilation of BB species emission factors reported in the literature. Another review work, containing the latest update on the emission factor estimates has recently been published by Akagi et al. (2011), but the values of emission factors for the BB aerosol emissions are similar to those reported by Andreae and Merlet (2001) . GOCART emission factors are based on the earlier works by Patterson et al. (1986) and Andreae et al. (1988), which summarize several laboratory and field measurements of F_j's. The expansion of the body of literature on the subject, recent review publications reporting ecosystem-specific emission factors (Akagi et al., 2011) as well as insights from this work will lead to the re-assessment of the emission factor values to be used in the GOCART model.

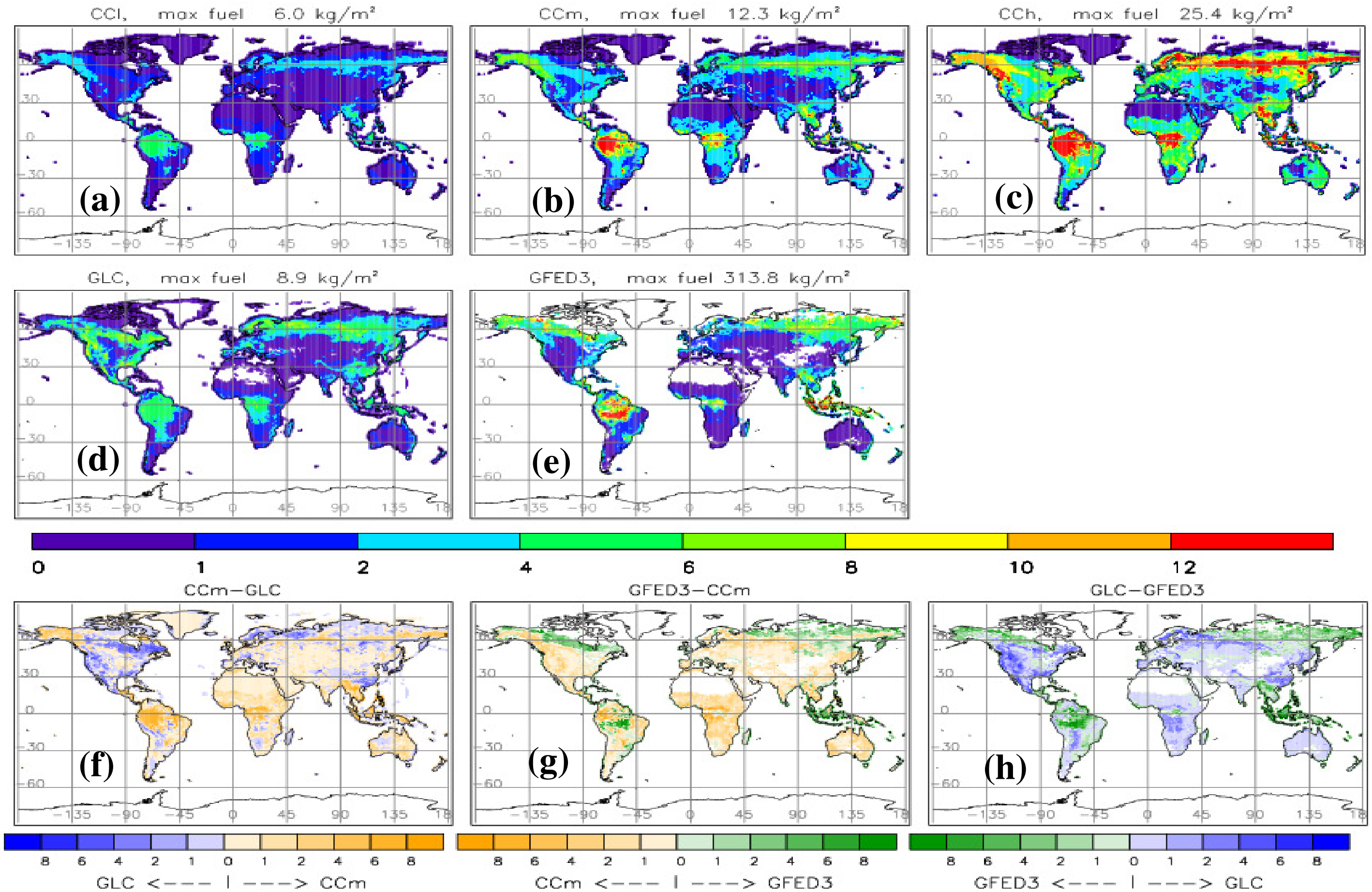

Figure 8 Fuel consumption estimates in kg/m^2, by Carbon Consumption (CC) inventory for low (a), medium (b) and high (c) fire severity, GLC (d), and GFED3 (e) datasets. Absolute differences between CCm, GLC, and GFED3 fuel consumption are in (f), (g), and (h)

3.5 Regional Specifics of Biomass Burning and Its Effects

Although BB occurs globally, there are particular features associated with different types of vegetation and climate regimes. Specifics of biomass burning is briefly listed in the last column of Table 6. Biomass burning can happen in the form of individual isolated plumes, for example in the US, where the vegetation is patchy and the population density is high, which prompts efficient fire-fighting (Houghton, 1991). In the tropical regions, where vast areas of savanna and grasslands are burning annually, complemented by agricultural fires, small and frequent fires create large hazy areas, often without distinguishable individual plumes. In forested regions, such as boreal North America, Russia, Latin America, Indonesia, wildfires often produce large smoke plumes from either one isolated fire or several large and small fires burning in the same general region. Weather conditions, such as dry and hot seasons may lead to extreme fire events where entire regions burn uncontrollably causing damage to infrastructure, crops and human health. Among examples of damaging severe fire seasons are recent outbreaks in Indonesia in 2006 (Bettwy, 2007) and Russia in 2010 (Witte et al., 2011).

It has been mentioned above that the majority of BB emissions comes from annual burning in Africa, Australia and South America, and as can be seen in Fig. 3, relative contribution of BB emissions from forested regions is small, e.g., brown color in Fig. 3, which represents needle-leaved evergreen forest, mostly present in boreal ecosystems. However, boreal regions, or forested regions of mid-latitudes, Asia and Indonesia coincide with highly populated areas, so the effects of these fires on human health, visibility and regional infrastructure is expected to be large (Houghton, 1991;

Witte et al., 2011). Besides, fires in boreal regions due to their proximity to the Arctic and specifics of regional meteorology may affect climate regimes of high latitudes.

Biomass burning emissions from boreal forests of North America and Russia produce a significant perturbation to atmospheric composition and optical properties in the Northern Hemisphere during the summer burning season. Estimates of contributions of biomass burning in the boreal region of North America and Eurasia to the global carbon emissions vary and may differ by an order of magnitude between years of low and high fire activity. Thus, according to some estimates, boreal forests accounted for 9% (Kasischke and Bruhwiler, 2003) to about 20% (Conard et al., 2002) of annual global carbon (C) emissions from forest fires in 1998, which was a year of high burning activity. Transport of smoke within the Arctic Circle is known to affect the arctic atmosphere by contributing to Arctic haze and deposition of black carbon (BC) (Generoso et al., 2007; Warneke et al., 2009). Therefore, regional analysis of BB emissions and regional comparisons of emission inventories are necessary, despite the fact that a contribution to global toal BB aerosol emissions may appear relatively small.

Another regional aspect of biomass burning, which is most observed in Amazon region, is deforestation, which significantly changes the BB regime, and violates the assumptions made by emission inventories developers (van der Werf et al., 2010). This can be illustrated by an example of several acres of forest cut down, the vegetation transported several miles away to what is an agricultural land in the regional database and burned in a pile as a very hot fire, leaving virtually no burned area, but producing emissions equal to several acres of burned rainforest.

CHAPTER 4 EVALUATION OF EMISSION OPTIONS USING GOCART AND MODIS AOD

We compared GOCART AOD, sampled at the closest time to the satellite overpass from each of 13 model runs, with MODIS AOD averaged to the model grid. The maps of MODIS and GOCART AOD within each case box were visually inspected to evaluate the spatial features of the simulated plume. As an example, Figure 9 shows the MODIS visible image, retrieved MODIS AOD with original 10-km resolution, re-gridded MODIS AOD to model grid, and snapshots of GOCART AOD from all runs with different emission options for case 11 in Russia on July 20, 2006. As noted earlier, the QFED dataset uses MODIS AOD as one of the input datasets for estimating emissions, so AOD from QFED-based GOCART runs cannot be fairly compared to MODIS AOD.

To limit analysis of aerosol properties to smoke within the plumes, a threshold AOD value (provided in Table 6) was chosen by visual inspection of MODIS and GOCART AOD maps for each case, with an attempt to separate smoke plumes from the background. The values of all pixels where AOD exceeded the threshold were considered in calculating average AOD values for MODIS observations and model simulations in each case.

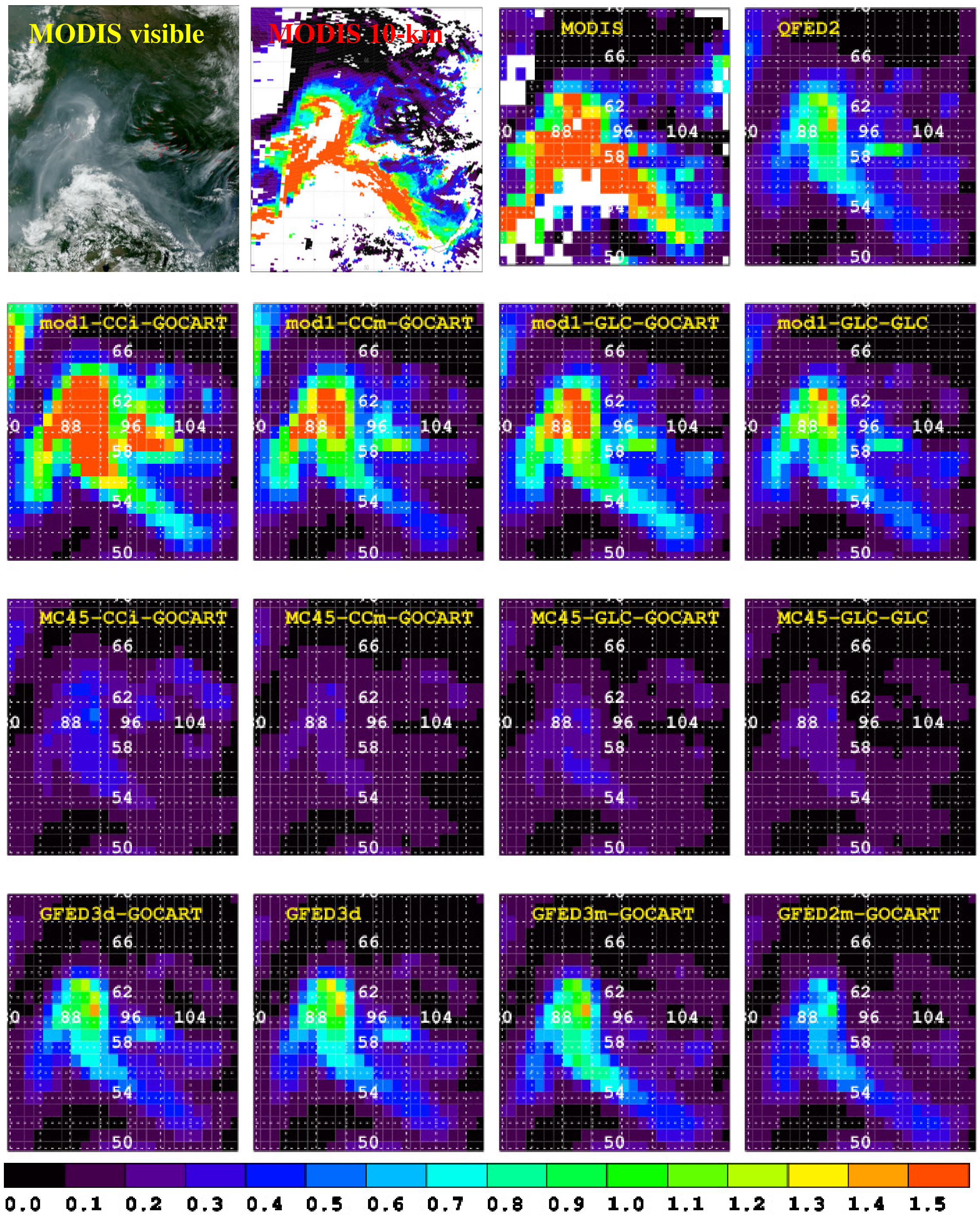

Figure 9 Case 11: Russia, 20 July 2006. Top Row: Terra-MODIS visible image of the scene with fire locations marked in red; total column MODIS AOD with original 10-km resolution, as provided by MOD04 data product; MODIS total TOA AOD averaged to GOCART grid; followed by maps of the temporally closest 3-hour output of instantaneous GOCART AOD values for different emission options

Since the bulk of BB aerosol emissions consists of BC and OC (Seinfeld and Pandis, 1998; Andreae and Merlet, 2001), BB emissions are represented by the sum of BC and OC emissions in subsequent analysis. The GOCART model works with aerosol emissions in terms of emission rates, expressed in units of mass of aerosol species per unit area per unit time. Therefore, to use satellite AOD as a constraint for BB emissions in the model, we first explore the relationship between emissions input into the model and simulated AOD output. This relationship is plotted in Figure 10. To keep the analysis independent of the fire case box size, we use units of emission rate (kgC km^{-2} day^{-1}) to characterize emission amount. The values from all model runs and all fire cases are colored according to the region where the fire is located. The region colors are defined in Figure 2.

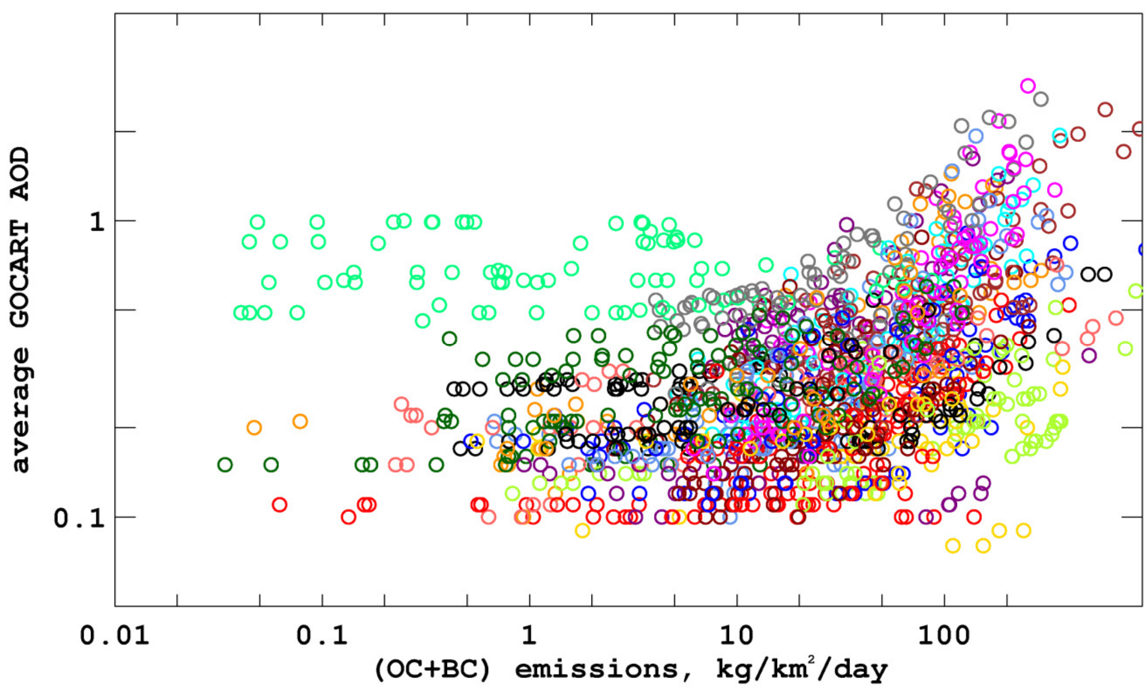

Figure 10 Average GOCART AOD for each fire case and each model run against average emission rate for the corresponding case in the corresponding emission option. Data points are colored by the region, with colors defined in Fig. 2

The same dataset, plotted for each region separately, follows in Figure 11. Colors are used here to represent different emission options, and symbols distinguish fire cases occurring in a given region. Symbols corresponding to each fire case are given in Table 6. The symbol associated with the emission option that produces the average GOCART AOD closest to the average MODIS AOD for each case is highlighted in black. Connected to each such symbol is a black line showing the difference between this model average AOD and the MODIS average AOD for this case (i.e., MODIS measurement would plot at the end of this black line).

The regional performance of the model with different emission inventories is presented in Figure 12 in a series of maps, where each map shows the performance of GOCART with BB aerosol estimated by one of the emission options. The color of each case box in Figure 12 shows the ratio of average GOCART AOD to average MODIS AOD. The darker the red color, the more GOCART overestimates MODIS AOD, and the darker the blue color, the lower the GOCART AOD compared to MODIS. Green color marks the cases where GOCART and MODIS average AOD are within about 20% of each other. Figure 12 is further summarized in Table 7. The table is arranged according to the average MODIS AOD for all cases in the regions, which are shown in Fig. 13, with Alaska having the lowest average AOD, and Russia the highest. The color codes were assigned based on the most common values of ratio of average model AOD to average MODIS AOD. The range of these ratios is given in each table cell. In some cells the range is preceded by "0" or "N×0", where N is the number of model runs in which no grid boxes had AOD above the designated threshold value for that particular model run. Thus, the deeper blue colors mean that GOCART AOD is consistently much lower than

MODIS AOD, and red shows regions where model AOD is higher than MODIS AOD. Lighter red and blue colors and light-green represent regions where model tends to over- or underestimate AOD, but the ratios are within about 30% of unity. The qualitative description of the shapes of model-simulated plumes is also included in each table cell, indicating if the simulated plume is limited, extensive or similar to the one observed by MODIS in the Alaska cases, the model-simulated AOD distribution resembles the visible location of smoke plumes better than the MODIS observed, due to missing AOD retrievals in the complex cloudy scene and mistaking of the smoke plume core for a cloud.

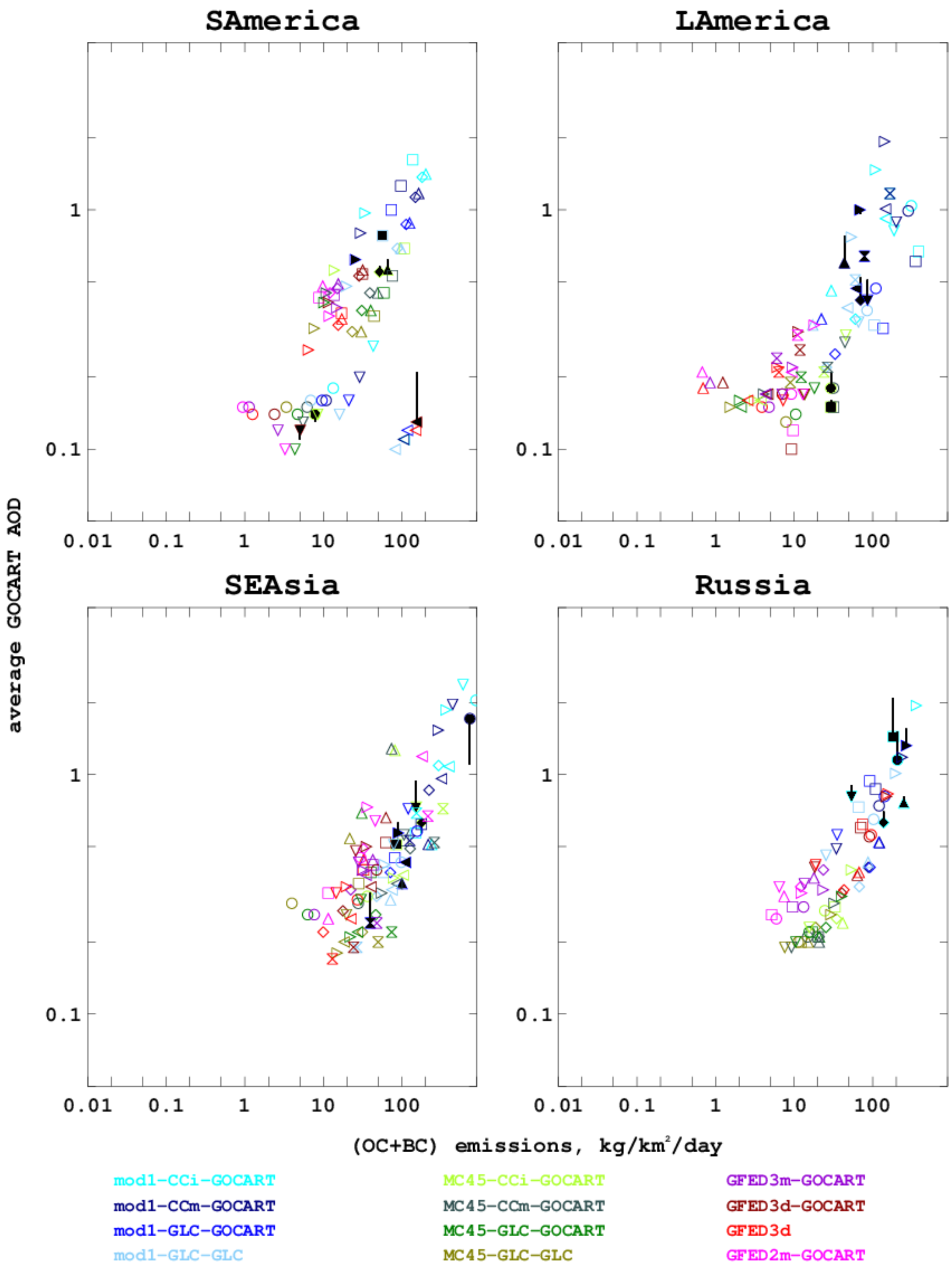

Figure 11a GOCART AOD vs average BC+OC emission rate. Different symbols distinguish individual fire cases. Colors represent different emission options in GOCART. Output of the GOCART run to which the MODIS AOD is closest is marked in black. The black line from each such data point shows the magnitude of GOCART AOD under- or overestimation compared to the average MODIS AOD. Regions: SAmerica, LAmerica, SEAsia, Russia

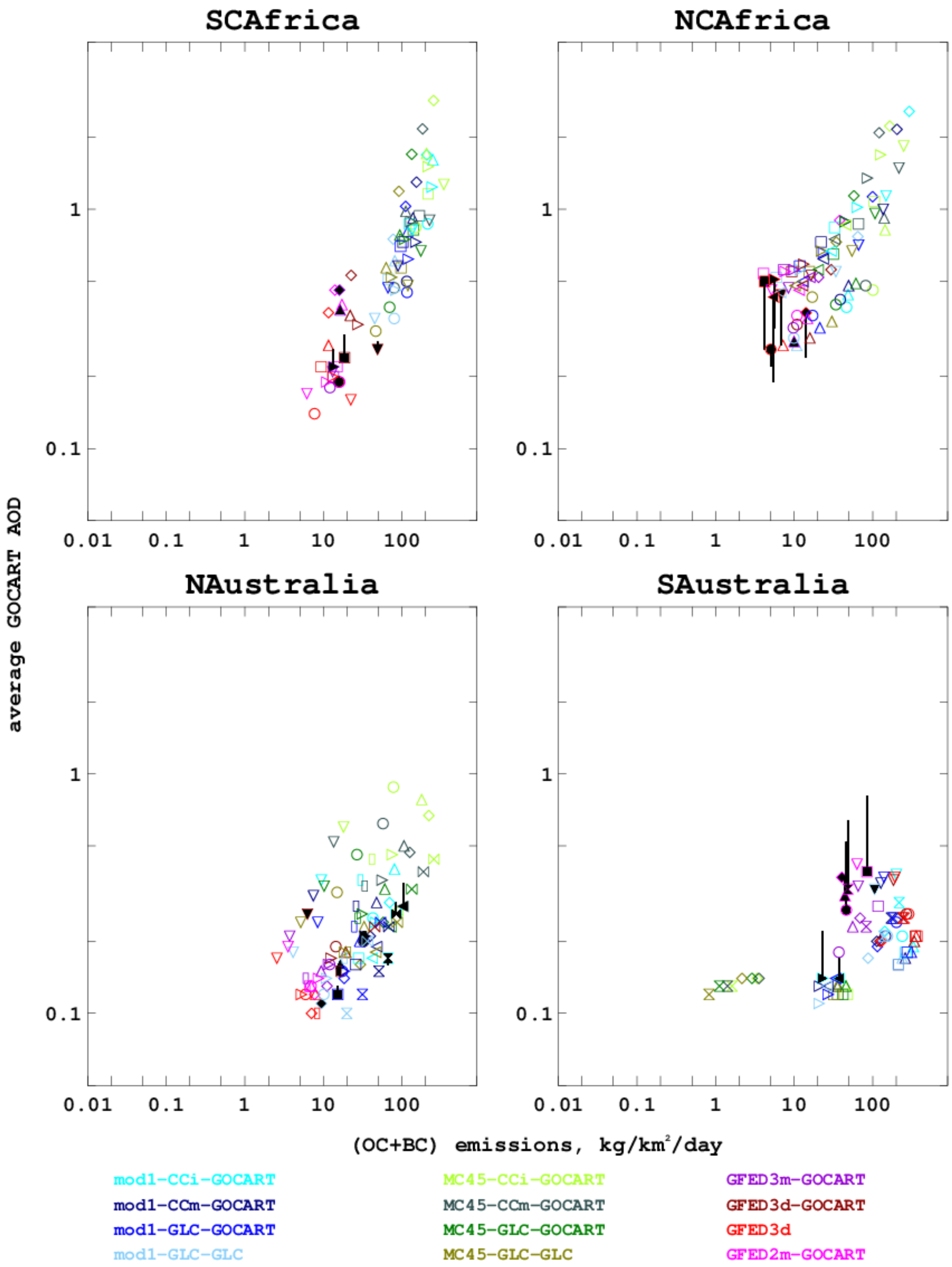

Figure 11b As in Fig. 11a but for regions: SCAfrica, NCAfrica, NAustralia, SAustralia

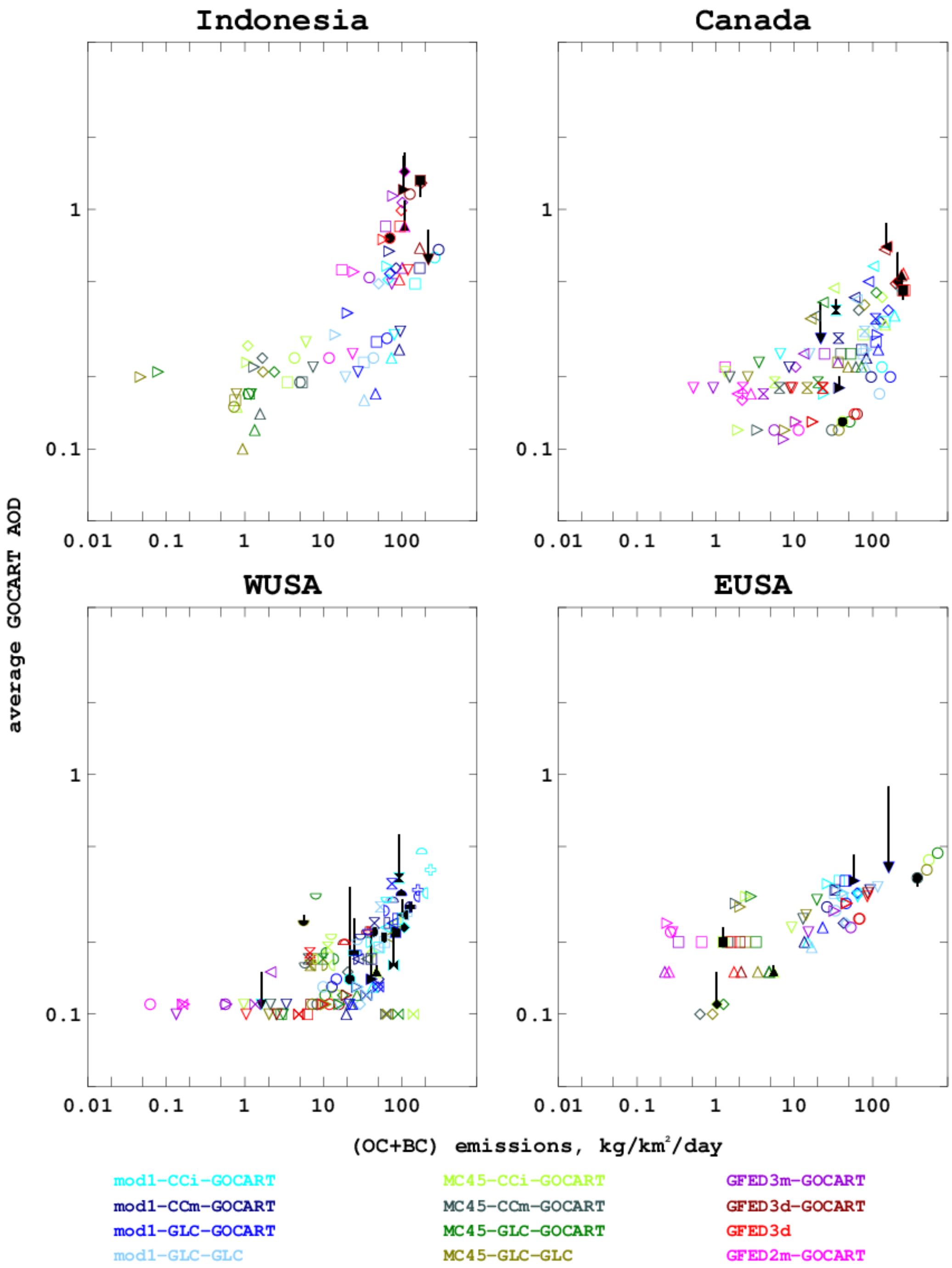

Figure 11c As in Fig. 11a but for regions: Indonesia, Canada, WUSA, EUSA

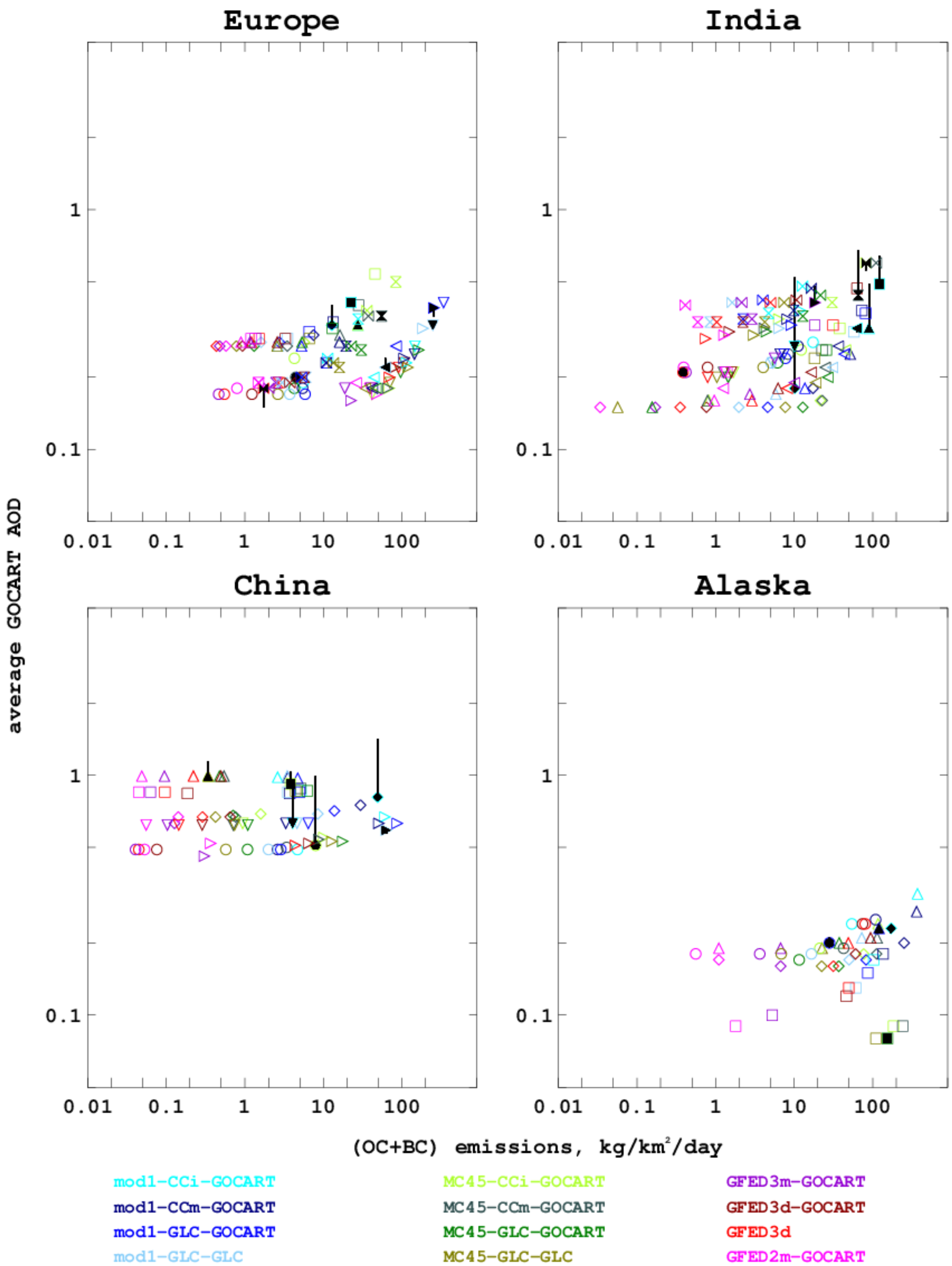

Figure 11d As in Fig. 11a but for regions: Europe, India, China, Alaska

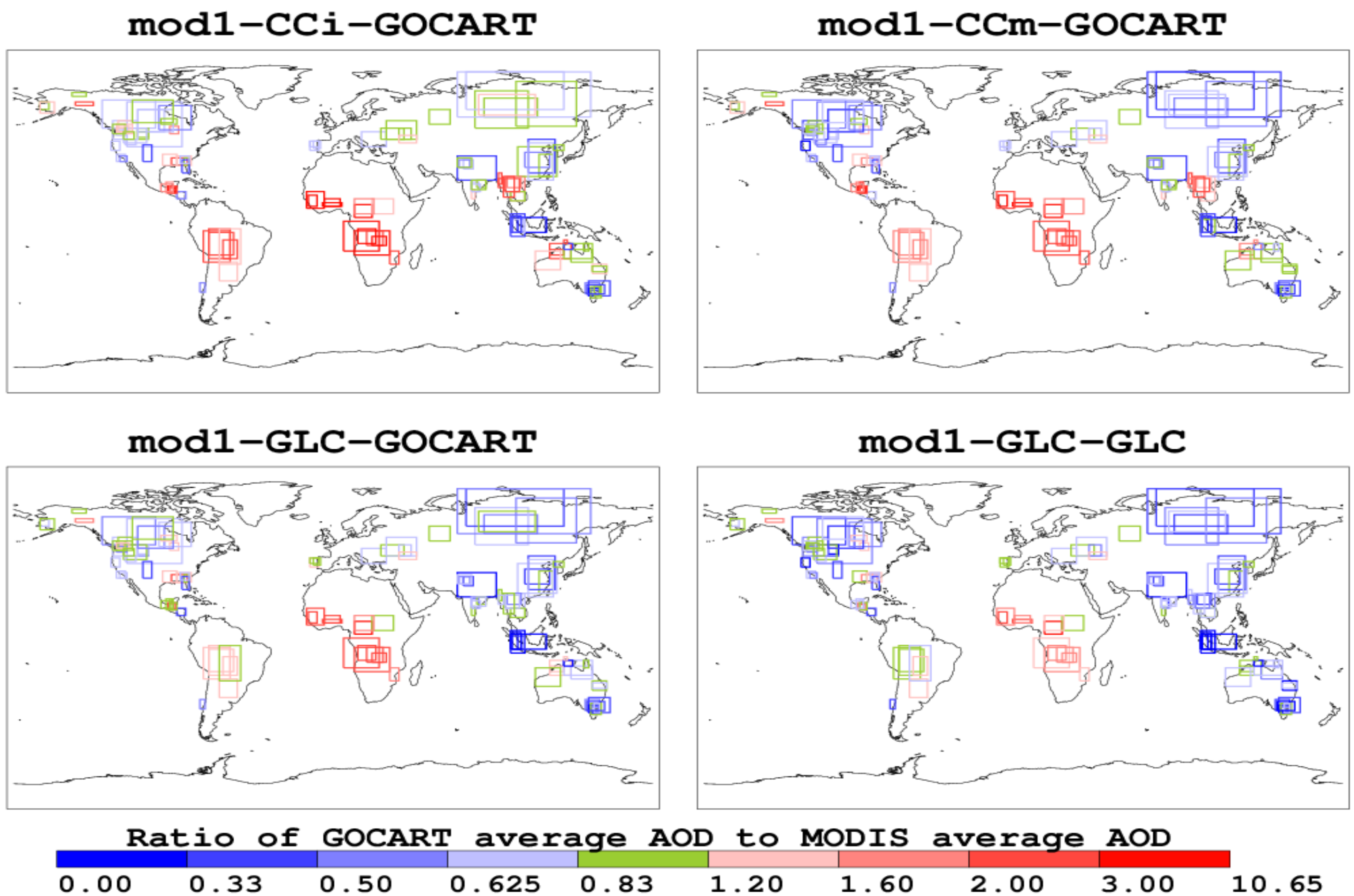

Figure 12a Ratios of GOCART average AOD to MODIS average AOD for each of the 124 cases studied, with different emission options used as input to GOCART. mod1 (fire counts-based) emission options

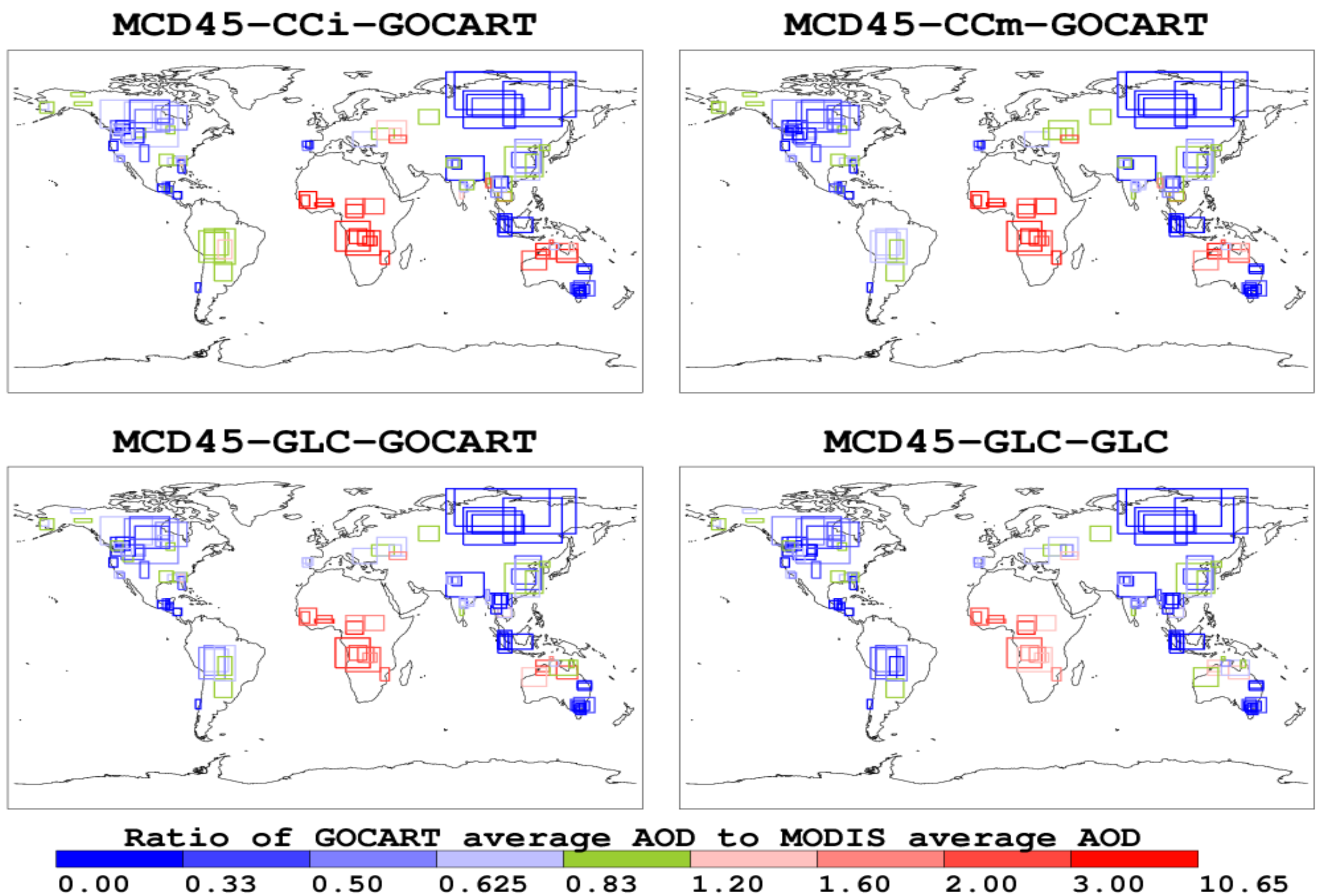

Figure 12b Ratios of GOCART average AOD to MODIS average AOD for each of the 124 cases studied, with different emission options used as input to GOCART. MCD45 (surface change-based) emission options

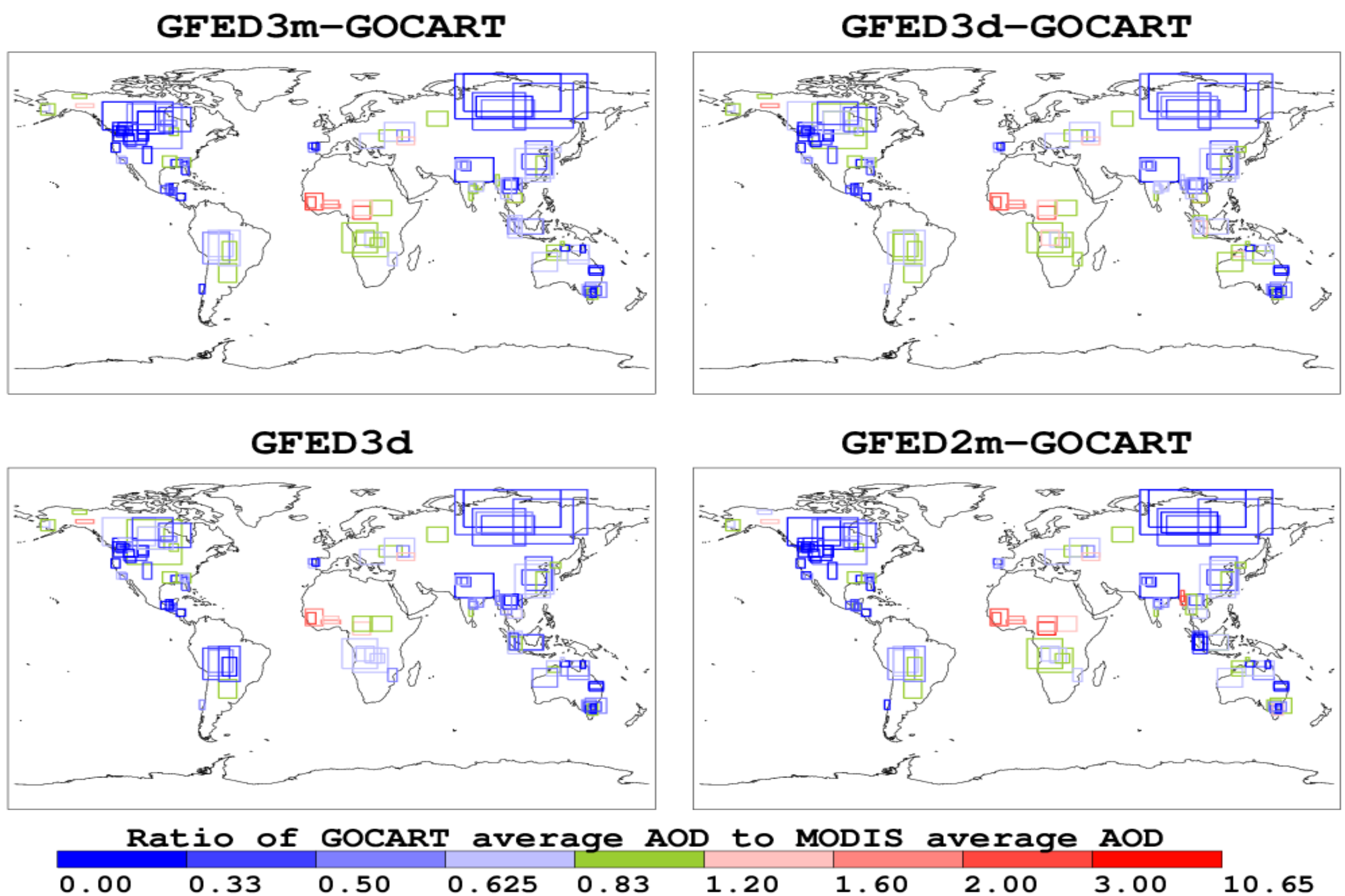

Figure 12c Ratios of GOCART average AOD to MODIS average AOD for each of the 124 cases studied, with different emission options used as input to GOCART. GFED emission options

Table 7 Ratios of GOCART average case AOD to MODIS average case AOD, and qualitative summary of plume shape for each emission option in each of the world regions

	mod1-CCi-GOCART	**mod1-CCm-GOCART**	**mod1-GLC-GOCART**	**mod1-GLC-GLC**	**MC45-CCi-GOCART**	**MC45-CCm-GOCART**
Alaska (4) * 0.08-0.22	1.1-(1.4)-2.2 as visible	0.9-(1.4)-2.3 as visible	0.8-(1.2)-1.9 as visible	0.8-(1.1)-1.7 as visible	0.8-(1.0)-1.1 as visible	0.8-(1.0)-1.1 as visible
LAmer (8) * 0.16-0.96	0.6-(2.2)-5.0 similar	0.8-(2.2)-4.8 similar	0.5-(1.1)-2.3 similar	0.4-(1.0)-2.0 similar	0/ 0.2-(0.5)-0.9 similar/ltd	0/ 0.2-(0.5)-0.9 similar/ltd
NAustralia(10)* 0.11-0.35	0.5-(1.5)-2.6 similar	0.5-(1.2)-1.9 similar	0/ 0.7-(1.0)-1.5 similar	0/ 0.6-(0.8)-1.1 limited	0/ 0.8-(3.0)-5.9 similar/ext	0/ 0.8-(2.3)-4.1 similar/ext
WUSA (16) (*some) 0.15-0.56	0.4-(0.9)-1.5 similar	0/ 0.4-(0.7)-1.2 similar/ext	0.4-(0.8)-1.2 similar/ext	2x0/ 0.4-(0.7)-1.0 similar/ext	5x0/ 0.3-(0.6)-0.9 similar/ltd	7x0/ 0.3-(0.5)-0.7 similar/ltd
EUSA (6) 0.15-0.89	0.4-(1.2)-2.1 similar	0.4-(1.0)-1.6 similar	0.5-(1.2)-2.1 similar	0.4-(1.0)-1.6 similar	0.3-(0.8)-1.3 similar	0.3-(0.7)-1.1 similar
Europe (9) + 0.2-0.42	0.8-(0.9)-1.0 similar	0.8-(0.9)-0.9 similar	0.7-(0.9)-1.2 similar	0.7-(0.9)-1.0 similar	0/ 0.5-(1.1)-1.3 similar	0/ 0.5-(1.0)-1.0 similar
SCAfrica (6) 0.2-0.47	2.9-(3.8)-4.7 similar	2.1-(2.5)-2.8 similar	1.7-(2.2)-2.4 similar/ext	1.3-(1.6)-1.8 similar	3.9-(4.8)-6.0 similar	2.3-(3.2)-4.6 similar
NCAfrica (7) 0.22-0.54	1.6-(4.0)-10.7 similar	1.7-(3.6)-9.0 similar/ext	1.1-(2.4)-4.7 similar	1.0-(2.0)-3.2 similar	2.1-(5.0)-9.3 similar	2.2-(4.5)-8.7 similar
SAmerica (7) *(some) 0.11-0.75	0.5-(1.8)-2.4 similar	0.6-(1.5)-1.9 similar	0.6-(1.2)-1.5 similar	0.5-(1.0)-1.2 similar	0/ 0.9-(1.0)-1.3 similar/ltd	0/ 0.7-(0.9)-1.1 similar/ltd
SEAsia (8) + 0.32-1.1	1.1-(2.8)-3.0 similar/m-a	1.2-(1.8)-2.4 similar/m-a	0.5-(0.8)-1.0 similar	0.4-(0.6)-0.8 similar	0.3-(1.3)-3.6 similar/m-a	0.3-(1.2)-3.6 similar/m-a
Canada (8) 0.13-0.88	0.6-(0.9)-1.7 similar	0.5-(0.7)-1.5 similar	0.6-(0.9)-1.5 similar	0.5-(0.7)-1.3 similar	0.5-(0.6)-1.0 similar	0.4-(0.6)-0.9 similar
India(9)^+ ' 0.21-0.68	0.3-(0.8)-1.3 similar	0.3-(0.7)-1.3 similar	0.3-(0.7)-1.1 similar	0.3-(0.6)-1.1 similar	0.3-(0.7)-1.2 similar	0.3-(0.7)-1.1 similar
SAustralia (8) 0.17-0.81	0.2-(0.6)-1.2 limited	0.2-(0.5)-1.1 limited	0.2-(0.6)-1.1 limited	0.2-(0.5)-1.0 limited	3x0/ 0.2-(0.3)-0.4 limited	3x0/ 0.2-(0.3)-0.4 limited
China (6) +^' 0.57-1.42	0.5-(0.8)-1.2 similar/ltd	0.5-(0.8)-1.1 similar/ltd	0.5-(0.7)-1.1 similar/ltd	0.5-(0.7)-1.0 similar/ltd	0.5-(0.7)-1.0 similar/ltd	0.5-(0.7)-0.9 similar/ltd
Indonesia (6) 0.78-1.73	0.2-(0.4)-0.8 similar	0.2-(0.5)-0.9 similar	0.2-(0.3)-0.4 similar	0.2-(0.2)-0.3 similar	0.1-(0.2)-0.3 limited	0.1-(0.2)-0.3 limited
Russia(6)* 0.7-2.09	0.7-(0.9)-1.3 similar	0.4-(0.6)-0.8 similar	0.5-(0.6)-0.9 similar	0.4-(0.5)-0.7 similar	0.1-(0.2)-0.4 similar/ltd	0.1-(0.2)-0.3 similar/ltd

Table 7 Ratios of GOCART average case AOD to MODIS average case AOD, and qualitative summary of plume shape for each emission option in each of the world regions (Continued)

	MC45-GLC-GOCART	MC45-GLC-GLC	GFED3d-GOCART	GFED3d	GFED3m-GOCART	GFED2m-GOCART
Alaska (4) * 0.08-0.22	0.7-(0.9)-1.1 as visible	0.7-(0.9)-1.1 as visible	0.8-(1.1)-1.6 as visible	0.7-(1.1)-1.6 as visible	0.8-(0.9)-1.3 as visible	0.8-(0.9)-1.2 as visible
LAmer (8) * 0.16-0.96	0/ 0.2-(0.4)-0.7 similar/ltd	0/ 0.2-(0.4)-0.6 similar/ltd	0/ 0.2-(0.5)-0.8 similar/ltd	0/ 0.2-(0.4)-0.7 similar/ltd	0/ 0.2-(0.4)-0.7 similar/ltd	0/ 0.3-(0.5)-0.8 similar/ltd
NAustralia(10)* 0.11-0.35	0/ 1.1-(1.5)-2.2 similar/ext	0/ 0.8-(1.1)-1.4 similar	0/ 0.8-(1.0)-1.3 similar	0/ 0.5-(0.7)-0.9 limited	0/ 0.7-(0.9)-1.2 similar	0/ 0.6-(0.8)-1.0 similar
WUSA (16) (*some) 0.15-0.56	4x0/ 0.3-(0.6)-1.2 similar/ltd	7x0/ 0.3-(0.6)-0.9 similar/ltd	8x0/ 0.3-(0.5)-0.7 limited	8x0/ 0.3-(0.5)-0.8 limited	11x0/ 0.3-(0.5)-0.7 limited	13x0/ 0.3-(0.4)-0.5 limited
EUSA (6) 0.15-0.89	0.3-(0.8)-1.4 similar	0.3-(0.8)-1.2 similar	0/ 0.4-(0.7)-0.9 similar	0/ 0.4-(0.7)-1.0 similar	0/ 0.3-(0.7)-0.9 similar	0/ 0.3-(0.6)-0.9 similar
Europe (9) + 0.2-0.42	0.6-(0.9)-0.9 similar	0.6-(0.8)-0.9 similar	0/ 0.6-(0.8)-0.9 similar	0/ 0.6-(0.7)-0.9 similar	0/ 0.5-(0.7)-0.9 similar	0.5-(0.7)-0.9 similar
SCAfrica (6) 0.2-0.47	1.9-(2.6)-3.6 similar	1.5-(1.9)-2.5 similar	0.8-(1.0)-1.3 similar	0.6-(0.7)-0.8 Similar	0.7-(0.9)-1.0 similar	0.6-(0.9)-1.1 similar
NCAfrica (7) 0.22-0.54	1.8-(2.9)-4.7 similar	1.2-(2.2)-3 .0 similar	1.0-(1.9)-2.6 similar	1.0-(1.6)-2.3 Similar	1.0-(1.9)-2.7 similar	1.3-(2.1)-3.7 similar
SAmerica (7) *(some) 0.11-0.75	2x0/ 0.6-(0.8)-1.1 limited	2x0/ 0.5-(0.6)-1.1 limited	0.6-(0.8)-1.1 Similar	0/ 0.4-(0.6)-1.1 Similar	0/ 0.6-(0.8)-1.1 similar	0/ 0.6-(0.8)-1.1 similar
SEAsia (8) + 0.32-1.1	0.2-(0.7)-2.0 similar/m-a	0.3-(0.6)-1.5 similar/m-a	0.4-(0.8)-1.9 similar/m-a	0.3-(0.6)-1.2 similar/m-a	0.2-(0.7)-1.2 similar/ltd	0.4-(1.2)-2.8 similar
Canada (8) 0.13-0.88	0.5-(0.6)-1.0 similar	0.4-(0.6)-0.9 similar	0.4-(0.8)-1.1 similar#	0.4-(0.8)-1.2 similar#	0.3-(0.5)-0.9 similar	0.2-(0.5)-0.9 similar
India(9)^+ ' 0.21-0.68	0.3-(0.6)-1.1 similar	0.3-(0.6)-1.0 similar	0.3-(0.6)-1.0 similar	0.3-(0.6)-1.0 similar	0.3-(0.6)-1.0 similar	0.3-(0.6)-1.0 similar
SAustralia (8) 0.17-0.81	3x0/ 0.2-(0.3)-0.4 limited	3x0/ 0.2-(0.3)-0.4 limited	2x0/ 0.3-(0.6)-1.1 limited	2x0/ 0.3-(0.6)-1.1 Limited	2x0/ 0.3-(0.6)-1.0 similar	2x0/ 0.5-(0.8)-1.3 similar
China (6) +^' 0.57-1.42	0.5-(0.7)-0.9 similar/ltd	0.5-(0.7)-0.9 similar/ltd	0.5-(0.7)-0.9 similar/ltd	0.5-(0.7)-0.9 similar/ltd	0.5-(0.7)-0.9 similar/ltd	0.5-(0.7)-0.9 similar/ltd
Indonesia (6) 0.78-1.73	0.1-(0.2)-0.2 limited	0.1-(0.1)-0.2 limited	0.6-(1.0)-1.5 similar	0.5-(0.7)-1.0 similar	0.5-(0.6)-0.8 similar	0.3-(0.5)-0.8 similar
Russia(6)* 0.7-2.09	0.1-(0.2)-0.3 similar/ltd	0.1-(0.2)-0.3 similar/ltd	0.3-(0.4)-0.5 similar/ltd	0.3-(0.4)-0.5 similar/ltd	0.1-(0.3)-0.6 similar/ltd	0.1-(0.3)-0.5 similar/ltd

Table 7 Ratios of GOCART average case AOD to MODIS average case AOD, and qualitative summary of plume shape for each emission option in each of the world regions. (Continued)

The following symbols are used in Table 7:

*	MODIS AOD omits many pixels - plume cores and cloud contamination or bright surface (in Alaska cases GOCART simulation resembles visible image more than AOD averaged to model grid)
#	AOD distribution is skewed. Model has higher AOD values at the source and loses much of it in what looks like transported part of the plume. MODIS - more transported AOD.
+	Sulphate AOD is unproportionally high or has a different spatial pattern in the model runs, compared to BC/OC suggesting anthropogenic pollution
^	Significant dust AOD signal in the model runs
'	All model runs are very similar regardless of the choice of BB emission inventory, suggesting that BB is not the major source of aerosol in these cases
m-a	Misaligned
ltd	Limited
ext	Extensive

The table is color-coded according to the average model-simulated AOD with the respective emission product, relative to the average MODIS AOD.

GOCART AOD is much lower than MODIS AOD	GOCART AOD is lower than MODIS AOD	GOCART AOD tends to be lower than MODIS AOD	GOCART AOD is approximately the same as MODIS AOD	GOCART AOD tends to be higher than MODIS AOD	GOCART AOD is higher than MODIS AOD	GOCART AOD is much higher than MODIS AOD

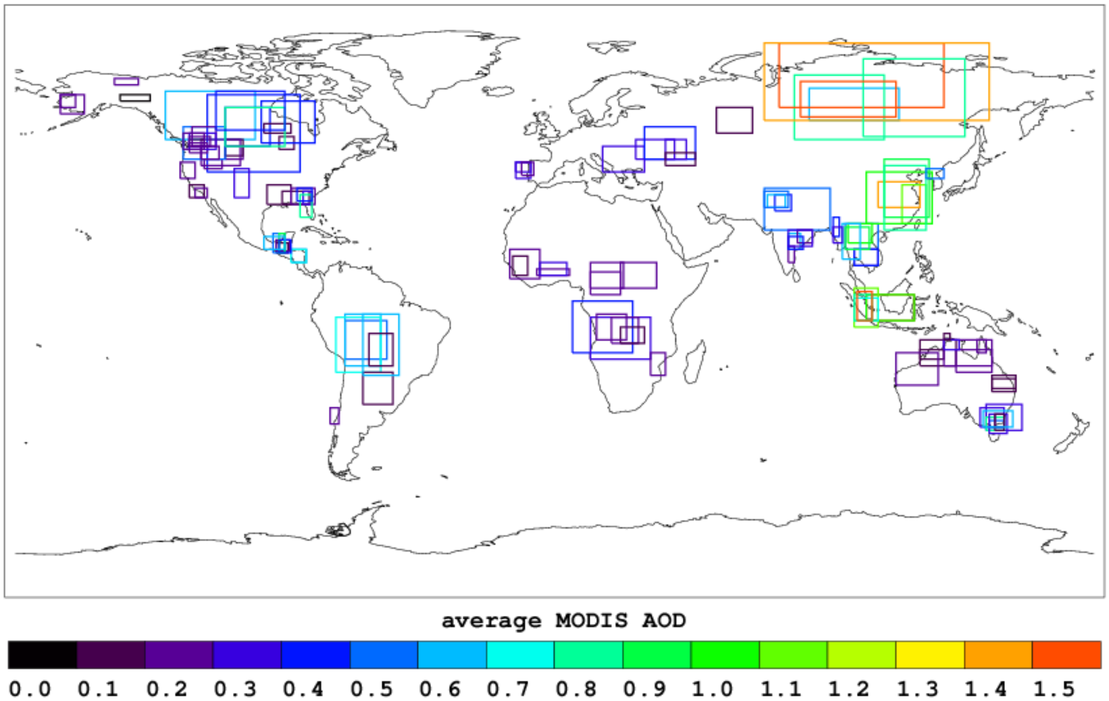

Figure 13 Average MODIS AOD for each of 124 analyzed fire cases

The major trends highlighted in Figures 10-13 follow.

- Data points in Figures 10 and 11 form a pattern of two distinct regimes:
    - In one regime the points are clustered parallel to the horizontal axis. These are regions dominated by background aerosol, where the BB contribution does not significantly affect the total AOD. This happens, for example, when the BB AOD is very low and is not much higher than AOD of the environment, such as in some cases in the USA. Alternatively, the background aerosol loading can be so high that even substantial BB emissions do not contribute a dominant fraction to the total AOD. Such are the cases in China and India. Qualitatively, in the areas where AOD is dominated by non-BB aerosols, different BB

inventories make little differences in GOCART AOD. In contrast, even though the non-BB background AOD is also rather high in South-East Asia, North-Central Africa, and Central and Eastern Europe, the contribution of BB aerosol is significant enough that the choice of emission inventory measurably affects the total AOD. The contribution to total AOD in the model from different aerosol types was evaluated both spatially and in magnitude to come to this conclusion. Wind dispersal, which also tends to flatten the curves in Figure 11 regardless of background aerosol level, is discussed in Section 5.2 below.

  - In the other regime, AOD depends on the amount of smoke emissions. This "BB-dominated" regime appears after a certain amount of emissions has been reached, i.e., after the contribution of BB aerosol to total AOD starts to noticeably overweigh the background aerosol components.

- The spread of the data points along the X-axis in each case in Figure 11 (cases are distinguished by different symbols here) shows the range of estimates provided by different emission options. The spread of values is generally larger, i.e. the discrepancies between emission rates estimated by different inventories are large, in background-dominated areas where the area is polluted (India, China, Eastern Europe), the observed plume is not well-defined or small (some US cases, Alaska), or the event is long-lasting so overlying thick smoke prevents good observations of burned area and fire properties (some cases in Canada, Indonesia). In BB emission-dominated regions (Russia, North Australia, South America), emission estimates from different emission options are fairly similar, but given a steep slope of the AOD vs. (BC+OC) emissions relationship, even a small change in emission amount has a significant effect on the simulated AOD.

- Qualitative comparison of the GOCART and MODIS AOD maps shows that the model performs better spatially and more consistently in magnitude in the cases having large, distinct biomass burning plumes, such as the case in Russia, shown in Figure 9. Thus, intense fires in the forested areas of Russia, Indonesia and Canada are best modeled by GOCART spatially, and the relative performance of the model is consistent from case to case when different emission inventories are used. These are the regions where the majority of emissions are only from BB sources and the plumes are significantly thick and distinct from the background. These are also regions of dark, densely vegetated surface, the best conditions for MODIS over-land AOD retrieval (Levy et al., 2010).

- Figure 13 shows average MODIS AOD for each case. Examination of this figure together with maps of Figure 12 suggests that in regions having average MODIS AOD 0.5 or larger, the simulated AOD is lower than observed, regardless of the emission option used (except "mod1-CCi-GOCART" option in Russia). These regions include Russia, South Australia, part of Latin America (Honduras), and Indonesia. In the regions with average MODIS AOD values of 0.5 or lower, the GOCART vs. MODIS AOD comparison is less consistent.

- Persistent low bias of GOCART BB AOD in Indonesia, South Australia and Russia merits further investigation, but is immediately related to omissions in biomass burning emission estimates.

- Model underestimation of total AOD in heavily pollution dominated regions of India and China have been shown previously (Chin et al., 2009), a problem that is mostly associated with the modeling of anthropogenic and dust emissions and transport.
- Regarding the regional performance of individual emission options:
  - The choice of MCD45-based emission options can lead to extreme AOD overestimation in the tropical regions - Africa, Latin America, North Australia, South-East Asia and very low AOD values in the forest regions for Russia, Canada, Indonesia, and South Australia.
  - As mentioned above, assuming 1 km^2 per fire count produces a higher-end estimate of burned area, and the "mod1"-based emission options tend to overestimate emissions, often by large factors in some regions (Latin and South America, Africa), but these high emission estimates bring simulated AOD close to MODIS-observed values in the boreal regions.
  - The use of GFED emission inventories generally leads to the best AOD comparison in Africa, where other inventories overestimate MODIS AOD, but in most other regions GFED-based model runs have AOD lower than MODIS, more so with monthly (GFEDv2, and GFED3) than daily inventories, as expected Also as expected, monthly GFED inventories appear to perform well for the long-burning events in the sparsely vegetated regions of Africa, North Australia, South-East Asia, and tend to underestimate emissions more for intense

individual fires in Russia, Canada, and the USA. . This is due to the fact that BB aerosol input into the model from an emission inventory with monthly temporal resolution equates to the total monthly estimate divided by the number of days in the month. If the fire was burning during the entire month, this assumption would roughly represent the reality. However, if all the BB emissions in a given grid box occurred in a course of a few days, their total amount divided by the number of days in the entire month may significantly lower the aerosol concentration on the day of the event or smear out the event and reduce the amount of aerosol to background levels.

- Using the GFED3-daily emission inventory does not lead to a consistent improvement in all regions over monthly GFED3 estimates, but, as expected, it improves performance for shorter-lived fires. However, the larger values of GOCART standard emission factors bring the emission estimates up, and closer to observations.

CHAPTER 5 THE USE OF MODIS AOD TO CONSTRAIN BB AEROSOL EMISSIONS QUANTITATIVELY

5.1 Effect of Plume Dispersion on AOD

Spatial distribution of AOD depends not only on the source strength, but also on the rate at which the plume is dissipated. Therefore, to quantitatively evaluate AOD-emissions relationships we have to account for smoke dissipation. Smoke plume dispersion is governed by wind shear and turbulence in the surrounding environment. Thus, strong vertical and horizontal atmospheric motions within the environment promote clear air entrainment, mixing, and plume dispersion. Plumes in stable air tend to stay more confined vertically. Since smoke plume optical depth is proportional to smoke density, it is reasonable to assume that compact and well-contained plumes will be optically thicker than more dispersed plumes containing the same amount of aerosol particles. Therefore, in the BB-dominated regime, we expect similar changes in emission amount to have different effects on the resultant AOD. Further, we investigate the relationship between plume environment, aerosol dispersion and their effects on simulated AOD values.

5.1.1 Height of Smoke Plumes and Vertical Dispersion

The vertical structure of the smoke events studied was investigated by visually examining the MISR stereo height of the plumes or CALIPSO profiles whenever these observations were available. Since vertical dispersion of aerosol in the atmospheric column in itself has little effect on total column AOD, we mostly checked whether the smoke was confined to the relatively well-mixed planetary boundary layer (PBL, as defined by GEOS4-DAS). Figure 14 provides an example of how MISR and CALIPSO observations are used to evaluate the plume height. Both instruments passed over the plume in case 11 on the same day as MODIS. It is worth remembering that CALIPSO-Day measurement was made approximately 2.5 hours after MISR, and CALIPSO-Night observation, spatially coincident with MISR, occurred about 16 hours after MISR and MODIS snapshots. CALIPSO profiles are overlaid with the GEOS-4 PBL height, which is between about 2 and 3 km above the terrain. Both CALIPSO aerosol profiles and histograms of MISR pixel heights indicate aerosol signature within the boundary layer, especially at the source, while detecting some higher clouds around 10 km. MISR heights away from the BB emission sources and CALIPSO-Day measurements have signature of aerosol possibly transported above the PBL. As the PBL height is considerably lower at night, the height of the mixed layer, approximated by PBL height at 6:30 AM UTC (13:30 local time), is also shown as dashed line in Figure 14 on the CALIPSO-Night plot.

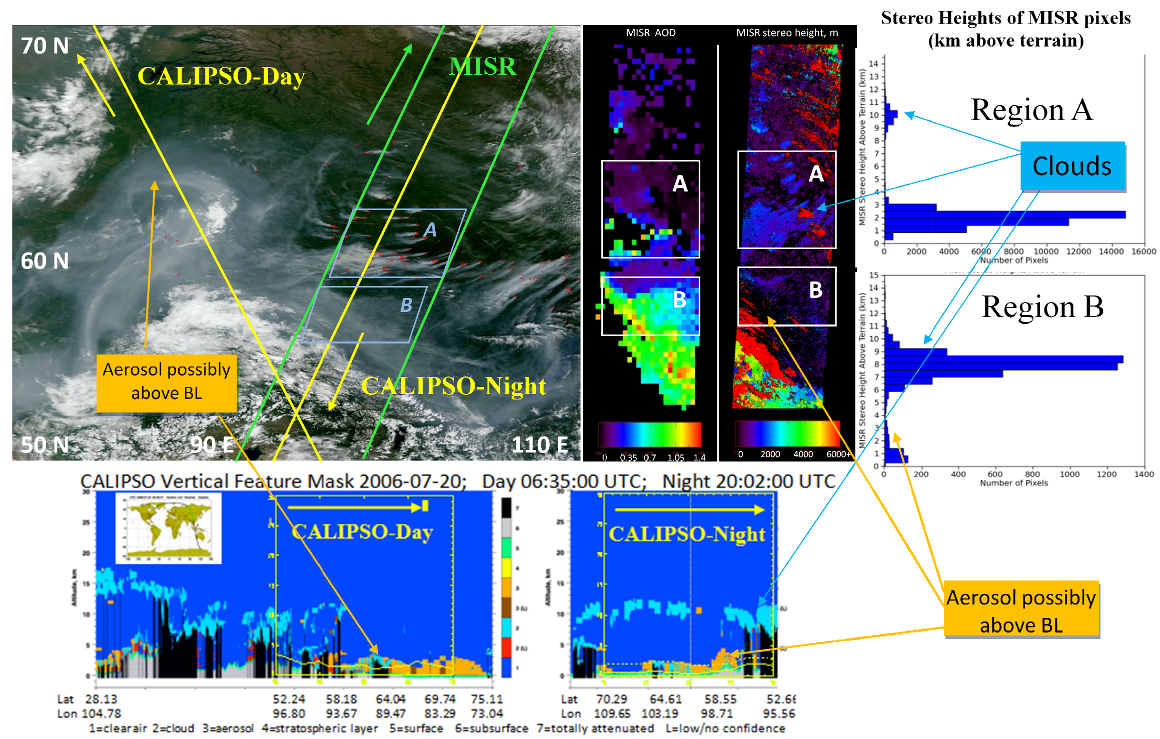

Figure 14 Case 11: Russia, 20 July 2006. Top Row: Terra-MODIS visible image of the scene with fire locations marked in red; schematic tracks of CALIPSO and MISR tracks during the same day in orange, and light green respectively. Satellites are moving in the direction marked with the arrows parallel to the orbits. Maps of MISR AOD and Stereo heights, and the histograms of the pixel heights in two regions A (source region) and B (transported aerosol downwind) are shown in the upper panel. Lower panel shows CALIPSO Vertical feature mask overlaid by the GEOS-4 PBL height for the coordinates of the case box at the time of CALIPSO overpass. CALIPSO-Night observation also shows in dashed line the height of the mixing layer, approximated as the PBL height at 6:30 UTC (13:30 local time)

If the smoke is injected directly into the free troposphere, the horizontal winds can transport it away fast enough to prevent accumulation of smoke and affect our conclusions about total AOD as a proxy for cumulative strength of BB sources. Although smoke injection above the PBL does occur in some cases (Kahn et al., 2008; ValMartin et al., 2010), except for the 10 large burning events in Russia, Canada, Indonesia and South Australia studied here (cases 47, 48, 50, 2, 3, 14, 15, 16, 18, 20) where smoke was found in the free troposphere, analysis similar to that shown in Figure 14 suggests it was lifted there after initial injection into the boundary layer.

5.1.2 Wind Speed and Horizontal Dispersion

To calculate average PBL wind speed for each case we average absolute mid-PBL wind speeds in all model grid boxes where the BB sources are defined. The same data points as in Figure 11 are plotted in Figure 16, now colored by the average PBL wind speed for every case. To calculate average PBL wind speed in the case box we first find the GOCART grid boxes where BB emissions are positive, and then average wind speed values found at the level of PBL height in all of these boxes to get average PBL wind speed for the case. A number of factors affect the apparent relationship between the AOD, which reflects the local concentration of aerosol particles, and the plume emission strength. We expect the AOD to be directly related to the emission strength, and inversely related to the local wind speed, which dissipates the aerosol. So other factors being equal, the slope of the AOD vs. emission strength line would be steeper in cases having lower wind speeds, and shallower when the wind speed is higher. However, the atmospheric stability structure also affects the result, as the aerosol will tend to dissipate more readily in a less stable atmosphere, and if background aerosol dominates the emission source, the ambient AOD might not be significantly affected by changes in the strength of a local source, as discussed in Chapter 4 above.

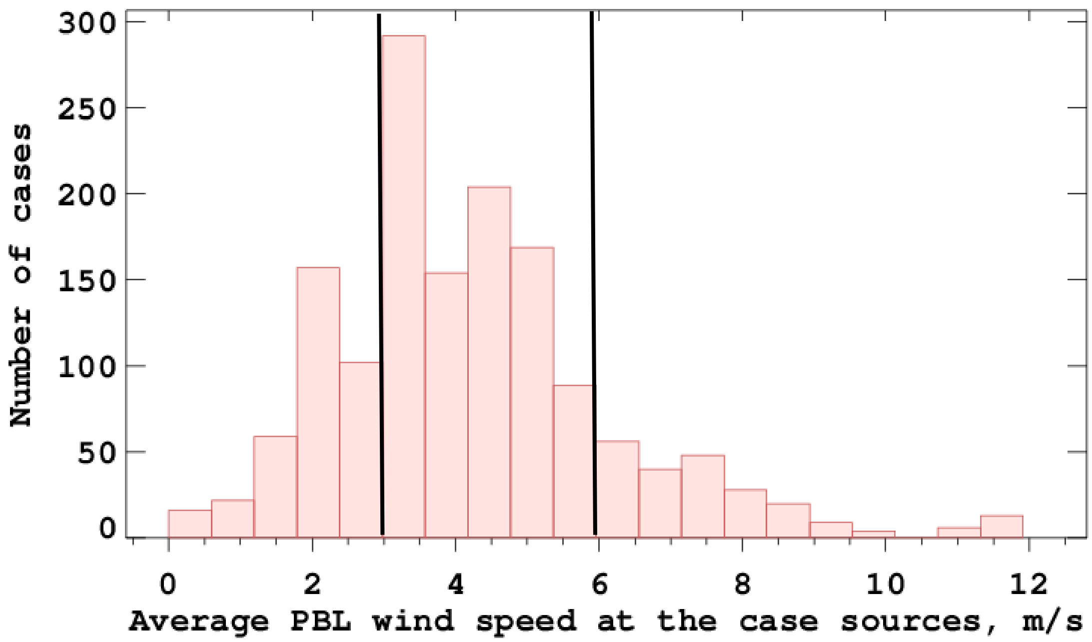

Figure 15 Distribution of average PBL wind speeds in all cases for all model runs

The frequency distribution of average PBL wind speeds for all cases in all model runs is shown in Fig. 15. The overall wind speed range can be divided into three categories to roughly represent wind conditions: 0-3 m/s, 3-6 m/s, which is also the most frequent, and above 6 m/s, which occurs relatively infrequently in the data set.

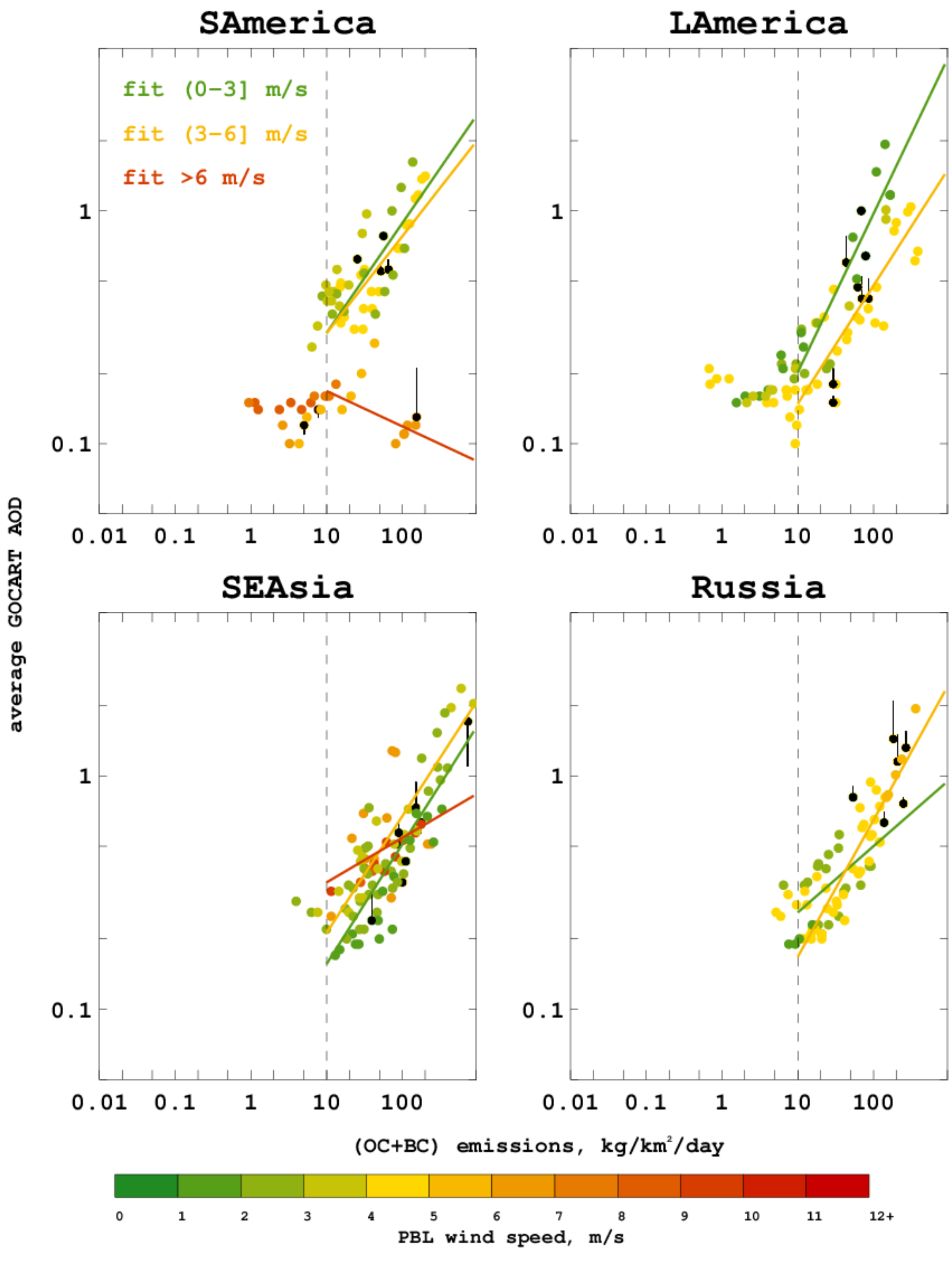

Figure 16a As in Fig. 11a but colors represent average PBL wind speed at each case BB sources

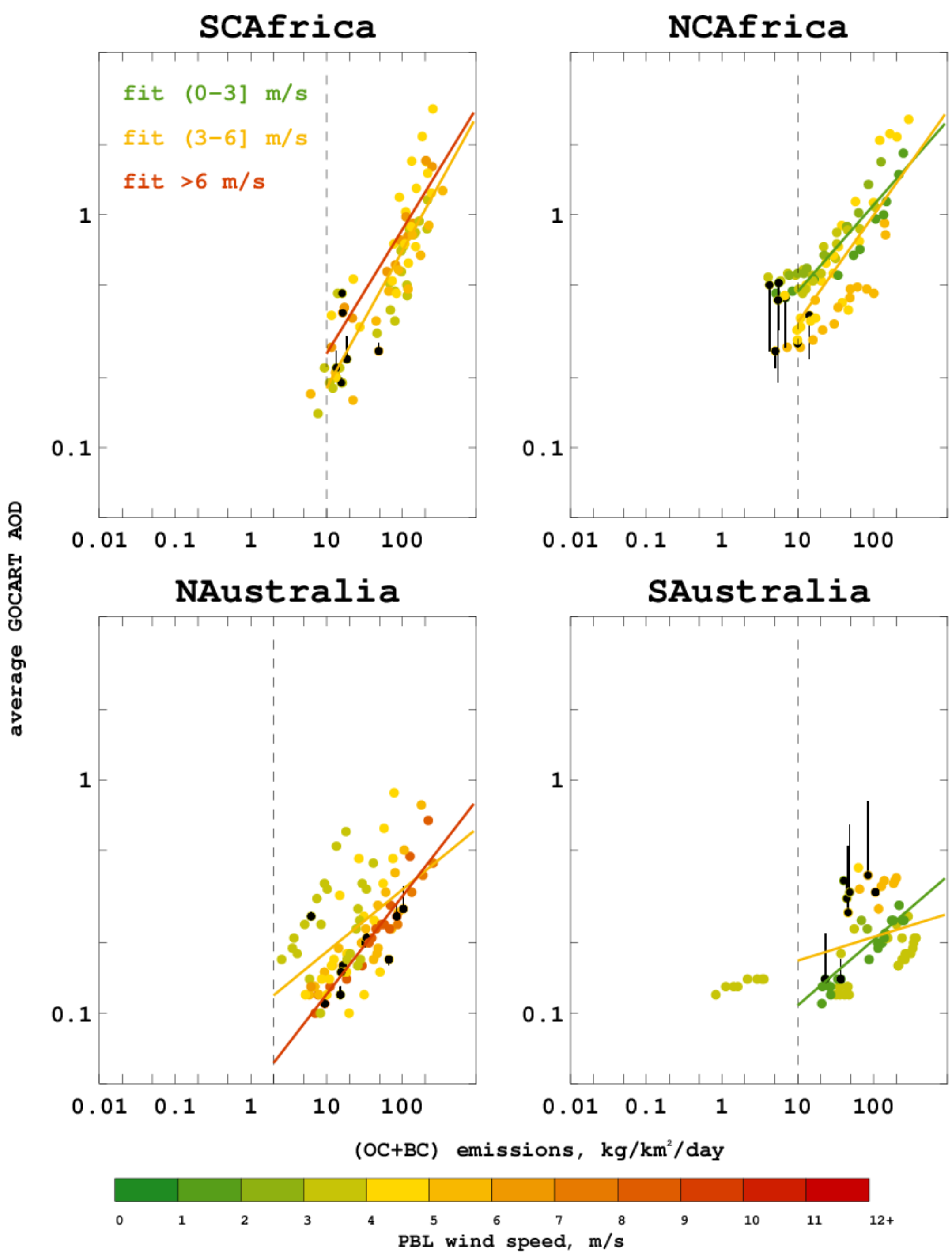

Figure 16b As in Fig. 11b but colors represent average PBL wind speed at each case BB sources

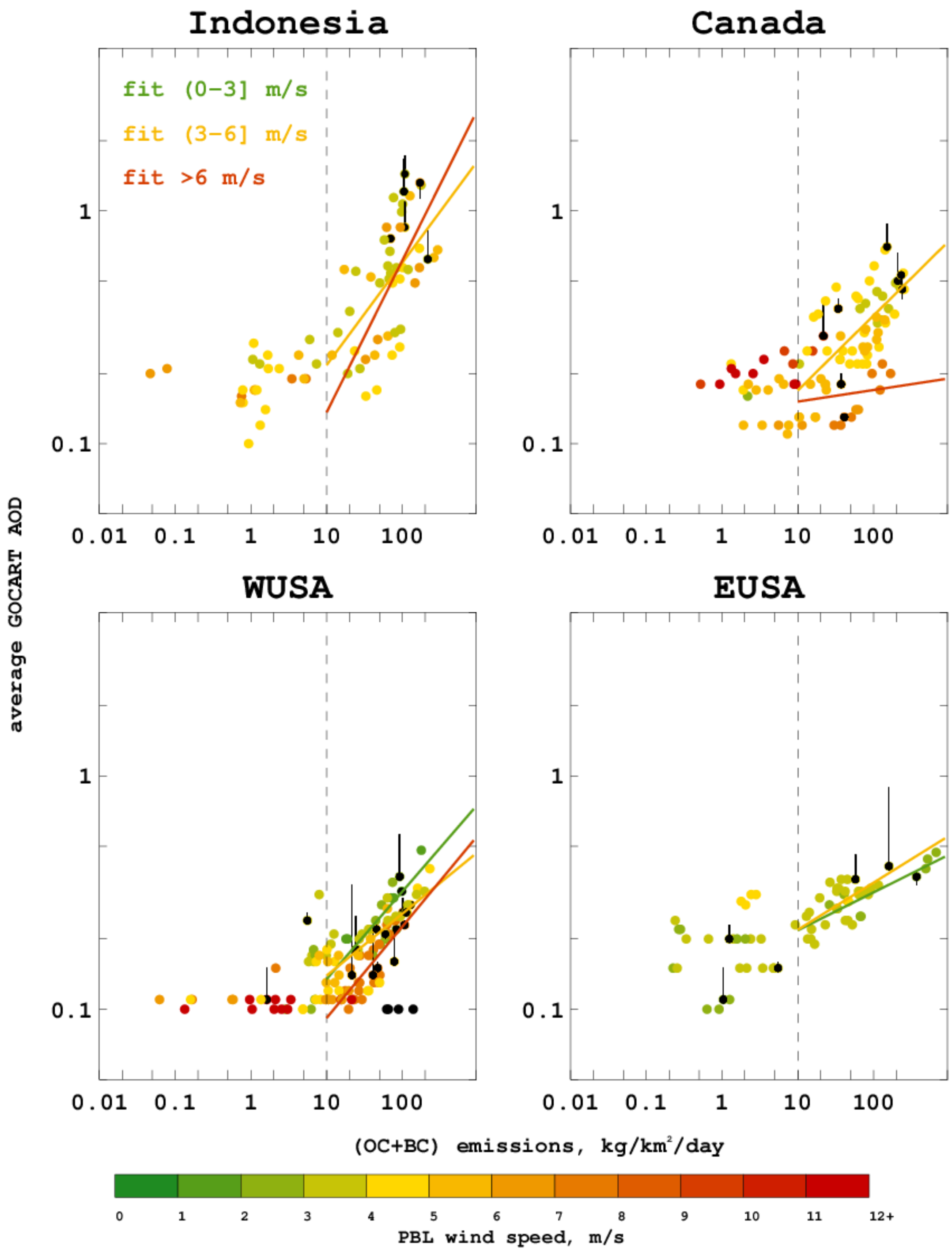

Figure 16c As in Fig. 11c but colors represent average PBL wind speed at each case BB sources

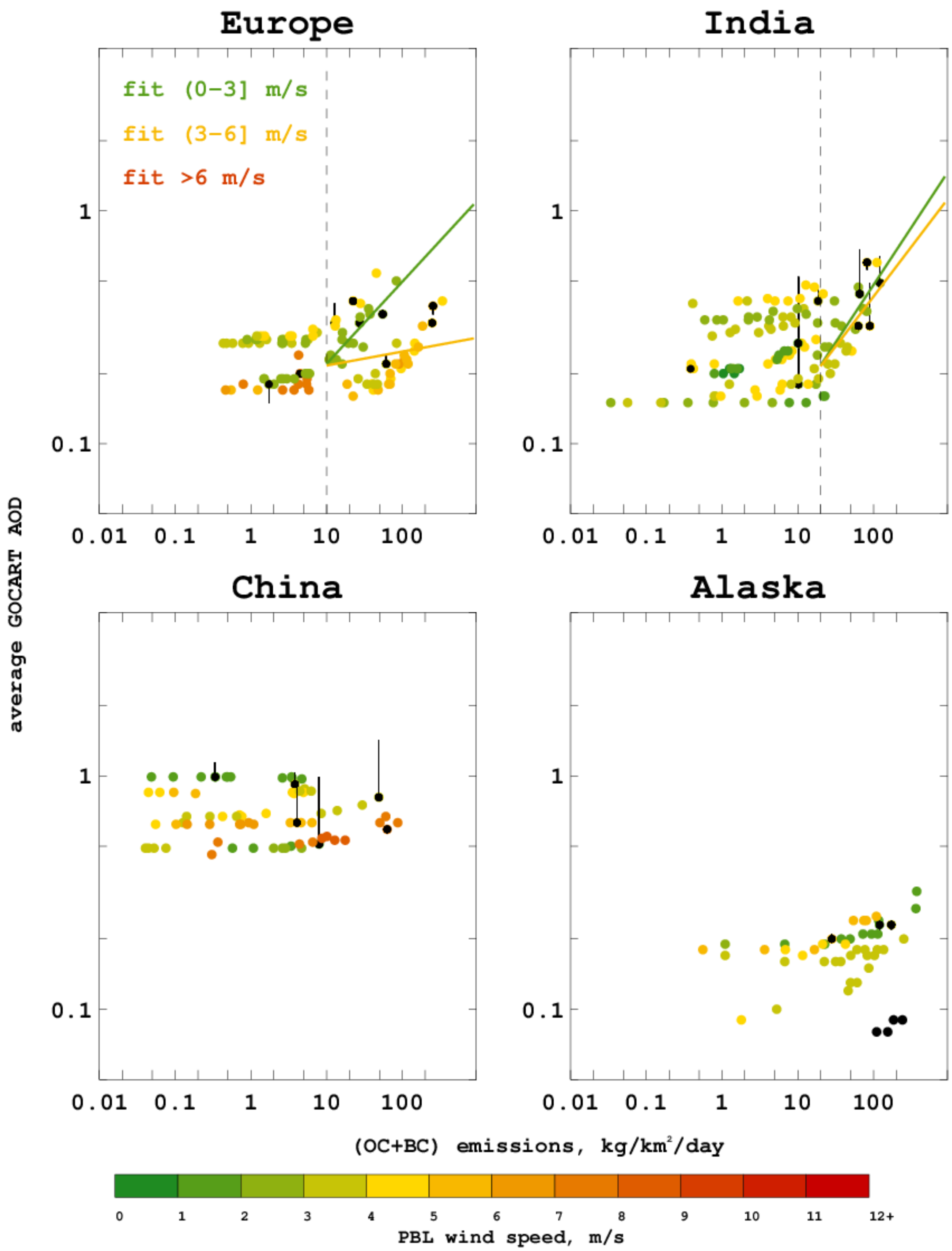

Figure 16d As in Fig. 11d but colors represent average PBL wind speed at each case BB sources

5.2 Use of MODIS AOD as a Quantitative Constraint on BC+OC Aerosol Emissions

To use satellite observation of AOD as a constraint to model emissions, a quantitative relationship must exist between the actual BB emission rate and MODIS-observed AOD, and one needs to assume that the GOCART model can reproduce this relationship. We have already established that wind speed is an important factor that governs the AOD-emissions relationship in BB-dominated regions. Therefore, we find a fit to the data points in the AOD vs. emissions plots for every region as is described below, and this relationship is the one needed to find the emission rate required to produce the observed AOD in the given environmental conditions. The GOCART average AOD closest to the MODIS average AOD for each case has been marked with black symbols, as in Figure 11, with a line from each such data point showing the magnitude of AOD under- or overestimation compared to the average MODIS AOD.

In each region, several lines, each corresponding to one of the three wind speed categories (0-3, 3-6, and > 6 m/s) were fitted to the data points in the BB-dominated regime in Figure 16. An empirical emission density cutoff between background-dominated and BB-dominated regimes was chosen in each region where a BB-dominated regime is observed, and these cutoff values are listed in table 8. The emission rate cutoff value is found to be around 10 kg/km^2/day, where stronger emissions are likely to measurably affect the total column AOD, but varying depending on the background AOD. The data suggest that a larger cutoff value is required for India, probably due to a more polluted background, and a lower value in North Australia, for which there are no data clusters parallel to the X-axis to form a background-dominated regime. No emission density cutoff could be selected for Alaska and China due to very faint plumes in the former (in the cases studied here) and a total domination of background aerosol in the latter.

Table 8 Regional fit coefficients for Equation 4 by wind speed range

Region	**Emission rate cutoff, kg/m^2/day**	**Fit coefficients (a; b) for average wind speed ranges**		
		0-3 m/s	**3-6 m/s**	**6+ m/s**
SAmerica	10	-2.29; 0.47	-2.17; 0.41	-1.43;0.15
LAmerica	10	-3.17; 0.68	-3.08; 0.50	
SEAsia	10	-3.04; 0.51	-2.70; 0.50	-1.49; 0.19
Russia	10	-2.00; 0.28	-3.14; 0.59	
SCAfrica	10		-3.07; 0.59	
NCAfrica	10	-1.61; 0.37	-2.12; 0.46	
NAustralia	2		-2.31; 0.27	-3.08; 0.42
SAustralia	10	-2.87; 0.28	-2.02; 0.10	
Indonesia	10		-2.54; 0.44	-3.49; 0.65
Canada	10		-2.52; 0.32	-2.00; 0.05
WUSA	10	-2.80; 0.38	-2.58; 0.27	-3.29; 0.39
EUSA	10	-1.89; 0.16	-1.98; 0.20	
Europe	10	-2.32; 0.35	-1.66; 0.60	
India	20	-3.01; 0.49	-2.82; 0.42	
China				
Alaska				

The data points falling into three wind speed categories (0-3, 3-6, and > 6 m/s) can be fit to equations of the form (linear fit on a log-log plot):

$$\boldsymbol{Y = X^{b} exp(a)} \qquad [4]$$

where X is the OC+BC daily-integrated fire emission in kg per km^2, Y is the average GOCART AOD within the plume, and the resulting wind-regime-dependent regional fit coefficients *a* and *b* are listed in Table 8. The quantitative relationship between AOD and aerosol emission rate allows the use of MODIS AOD to constrain the BC+OC emission rate in the model, assuming the plume is emitted into the PBL and the average PBL wind speed is known. Such estimates should be more certain under lower wind speed conditions (due to small changes in emissions leading to significant changes in AOD), and less certain under higher wind speed conditions, where a larger range of emission rates is allowed within available constraints.

5.3 Limitations of the Method and Topics for Further Study

Our method of using MODIS AOD to constrain BB emissions in the global model has some limitations:

- The method is based on the assumption that the discrepancies between MODIS and GOCART AOD are predominantly caused by the under- or over-estimation of emissions, such that the errors in aerosol removal or mass extinction efficiency (converting aerosol mass to AOD) are much smaller than that in emissions. This assumption could be wrong in some cases. Mass extinction efficiency is calculated in the model based on the aerosol properties such as size distribution, refractive index of aerosol particles, and RH, and its average value can differ by a factor of about 3 for BC and OC and up to 7 for SO_2 between different models, GOCART values being close to the median values (CCSP, 2009; Chin, et al., 2002; Kinne,2006). Removal rates for BB-related species may vary by a factor of 2-3 between aerosol models (CCSP, 2009; Textor, 2006), while the emission rates can differ by an order of magnitude in some regions (e.g., Canada, West and East USA) in Fig. 11.
- It has been shown that total column AOD provides a poor constraint on BB emissions in background-dominated regions.

- The effect of wind speed on the AOD-emissions relationship has to be explored further in the light of interaction of smoke plume with more or less polluted environments.
- Even though physically sound, the relationship between AOD and BB aerosol emission rate has been quantitatively described for one version of the GOCART model only, and its application to models having different spatial resolution and physical aerosol processes needs to be investigated.
- The use of the MODIS AOD product brings a set of its own limitations, such as missing AOD retrievals in the cores of very optically thick plumes, over bright surfaces, or in regions with complex cloud cover, and AOD over- or underestimation in some situations (Levy et al., 2010). Notes are provided in Table 6 for the regions where AOD retrievals were missing. In the cases where MODIS AOD cannot be retrieved, AOD from other satellite instruments could be used when available.
- Since the global model is too coarse to simulate individual smoke plumes of sub-grid size, the method is rendered insensitive to small AOD variations when averaging MODIS AOD, and is similarly insensitive to small aerosol concentration changes, when the model requires an aerosol emission source the size of an entire grid box.
- The results in this study are based on one year of fire observations. Inter-annual variability of fire locations and intensity merits further investigation, to test the applicability of the method quantitatively in regions where fire seasons, and thus, fire and smoke properties and amount, can vary significantly.
- Selection of the cases, assignment of case boundaries and AOD threshold values to distinguish smoke plumes from the background, and qualitative comparison of GOCART-simulated and MODIS-observed plume shapes are based on the subjective

judgement of the author. Even though maximally objective and equal treatment of the data was practiced, involvement of a human operator is prone to introduction of human error or subjective bias. We have to note, however, that personal involvement of the human operator is necessary to perform thorough case studies of the fire events, due to the random nature of fires and ease of mistaking smoke for cloud or dust storm in automated satellite aerosol retrieval.

CHAPTER 6 CONCLUSIONS, FUTURE WORK AND SYNOPSIS OF RESEARCH PATH

6.1 Conclusions

We used ready-to-use global biomass burning aerosol emission inventories GFEDv2, GFED3, and QFED, as well as several combinations of burned area, fuel consumption and aerosol emission factor estimates for this study, which resulted in a total of thirteen global BB emission options. We compared the amounts of BB aerosol emitted during the year 2006, as estimated by all thirteen emission options, and found that annual global total BC or OC emission estimates can differ by a factor of eight, with GFED3 providing the lowest estimate, and emission options based on MODIS fire counts, Langley Carbon Consumption estimates and GOCART emission factors producing the largest. Although emission factor and fuel consumption choices can each lead to about a factor of two-to-three difference in a given region, burned area estimates can vary dramatically between the inventories, producing the largest differences between emission options. The performance of these emission options in the GOCART model was evaluated by comparing model simulated AOD to the MODIS-measured AOD. AOD from QFED-based model runs could not be fairly used in such comparison, due to the use of MODIS AOD as one of the parameters in calibrating QFED emissions.

Twelve GOCART runs, each with a different emission option, comprise an ensemble of runs, providing a range of input emissions and output AOD estimates that were evaluated for 124 representative fire events chosen globally. In general, the model performs best spatially and most consistently in magnitude when simulating large biomass burning events of Russia and Canada, and less consistently in the regions where other sources of aerosol, such as anthropogenic pollution or dust, make significant contributions to the background - Asia, Africa, Central-Eastern Europe. In regions of complex terrain and patchy vegetation, such as the US, the inventories do not agree well, and the comparison between GOCART and MODIS is not consistent.

The use of GFED inventories leads to the best AOD agreement in Africa, where other inventories overestimate MODIS AOD, but in most other regions GFED-based runs produce lower-than-MODIS AOD. The use of daily GFED emissions generally improves AOD comparison compared to the use of monthly emission estimates in the cases of short-lived individual fires. Emission estimates based on MCD45 burned area lead to significant AOD underestimation in higher latitudes, and overestimation in Africa. 'mod1'(thermal anomalies)-based model runs result in the best AOD comparisons in the boreal regions, while mostly overestimating AOD in the tropical regions.

The relationship between BB aerosol, expressed as a sum of BC and OC emissions, and the resultant AOD, forms two distinct regimes. First is the "BB-dominated" regime where BB is the main aerosol source, and changes in BB emission rate clearly affects the total AOD in the region. Second is the "background-dominated" regime, in which a contribution of BB smoke to the total AOD is small enough that changes in smoke emission rate do not produce significant total-AOD changes. The rate of BC+OC emission from BB (in units of $kg/km^2/day$) needs to be larger than a certain threshold for the emissions-AOD relationship to be in the BB-dominated regime. This threshold is around 10 kg/km^2/day in most regions studied, when the source is of the size of the GOCART model grid box, but varies depending on the background AOD level.

The rate of change of AOD in response to a change in amount of BB emissions is affected by the dispersion potential of the plume environment, which is usually dominated by the wind speed and atmospheric stability. In clean environments, higher wind speeds lead to shallower slopes of the AOD vs. emissions relationships, meaning larger changes in emissions are needed to noticeably affect the total column AOD. Thus, given a quantitative relationship between AOD and BB emissions in each geographic region, satellite-measured AOD can be used to constrain the BB source strength, given the average wind speed in the region. However, MODIS total column AOD cannot be used to constrain BB emissions in the background-dominated regime, and the regional quality of the MODIS AOD product also has to be considered when using it as a quantitative constraint.

6.2 Future Work

Section 5.3 above lists some of the topics for future study, which should be addressed to improve the method of using satellite-observed AOD as a constraint for model BB emissions. The more immediate tasks resulting from this study are:

- to investigate the effect of different meteorological datasets and model settings on the simulated AOD and AOD-emissions relationship. The GOCART model has been recently upgraded to work with the new GEOS-5 meteorological fields, and the effects of different meteorology, spatial resolution and transport, and removal settings on the simulated aerosol fields can be readily explored;

- to conduct a smaller similar investigation for a different year to address the lack of fire cases in regions like Alaska. For example, 2004 was a year of high BB activity in Alaska (Morris et al., 2006; Warneke et al., 2006);
- to investigate environmental parameters other than horizontal wind speed in the boundary layer that affect the AOD-emission relationship to obtain a more robust quantitative relationship for use in the present method to constrain BB emissions;
- in light of the results from this study, re-visit current settings and assumptions in the GOCART BB emission simulations model, to suggest and test possible improvements to the model itself and possibly participate in the construction of the "best" BB emission inventory in collaboration with inventory developers.

In the more general sense, the improved understanding of the differences between the BB emission inventories and their strengths and weaknesses on a regional scale, will enhance our ability to model BB emission amount by making an informed decision in designating different sources for BB emissions for each world region, and provide grounds for further collaboration with inventory developers. In addition, lower uncertainty in BB emissions will benefit the calculations of climate forcings, and be a step to improved understanding of complex aerosol environments, where aerosol particles from many sources interact. And finally, because the model is based on two key inputs for BB - 1) location and strength of BB sources and 2) height of emission injection, improvement of source strength simulation allows for closer study of aerosol transport details.

6.3 Synopsis of Research Path

This section briefly summarizes some turning points and decisions that were made in the course of this research. It introduces some methods and approaches that were attempted, but were dismissed in favor of the more efficient or relevant ways of data analysis and presentation. When presenting the results and methods that came out of the study, one rarely documents the other approaches that were attempted, and the reasons for their dismissal are later forgotten.

Defining the project. The project was originally conceived and proposed as a study aimed at investigating the relationship between the BB emission injection height, environmental conditions, such as atmospheric stability and moisture, and fire intensity. I planned to use a suite of satellite observations to quantify smoke plume heights and use the model to relate the plume heights to the meteorological parameters and fire characteristics. This goal determined the study period and the approach to selecting fire cases to study. I also proposed to use the Haines Index, described in section 2.1.2 above, as a proxy for emission injection height, assuming that a dryer and less stable atmosphere would support taller smoke plumes. Several factors affected the change of the research course and are outlined below. First, Val Martin et al. (ValMartin et al., 2010) analyzed in depth EIH-environment relationships and plume height parameterization for the global aerosol model similar to GOCART, and concluded that atmospheric stability is arguably the most important factor affecting the BB emission injection height, with fire radiative power playing a role in some circumstances. Since a model needs both emission amount and injection height to simulate aerosol effects and transport correctly, and with the necessary steps already made towards improvement of EIH parameterization, the emission amount still remained a subject of great uncertainty. Therefore, with help of Dr. Kahn and Dr. Chin, I have changed the focus of my research to aerosol amount.

After some data analysis and discussions with colleagues (M. Val Martin, 2010, personal communication, M. Davis, 2010, personal communication) it was discovered that Haines Index (HI) does not correlate with the plume emission injection height. Since HI was developed and tested for North America, and does not show correlation with plume height here, we dismissed this approach, still keeping HI as a proxy for fire severity in one of the emission options, using HI for its original purpose.

Selection of fire cases. The original plan was to study each fire case in detail, including merging MODIS and MISR AOD and evaluating observed and simulated model heights. Therefore, the fire cases that were originally selected for the study had to be measured by all three instruments (MISR, MODIS and CALIPSO) in the same day. Because of the difference in satellite orbits and overpass time, finding such cases presented to be a non-trivial task, and in the beginning I found around 20 cases which satisfied this criterion during the study period (June 2006-June 2007). There are more of such cases, however, and the refinement of the fire event identification algorithm in the course of this research made this process a lot less time-consuming.

I co-located and compared MISR and MODIS AOD for several case studies, and found that they agreed fairly well, and in many fire cases MISR does not provide much additional AOD information. Additionally, MISR having a narrower swath does not detect all the smoke plumes seen by MODIS, so it was decided to use MODIS AOD alone, and use the MISR and CALIPSO products to evaluate plume height. The decision to use only MODIS AOD for all cases allowed us to add a number of other cases to improve global coverage and regional representation of burning events.

The *number of model runs* depended on the number of emission datasets available at the early stages of the project. In the course of the study I realized that there are other global datasets that could be used in this comparison, but to keep the number of model runs manageable, I could not use all the datasets developed. Using several combinations of the same parameters is valuable to explore the impact of each of these parameters on the overall value, so such combinations were created. Besides, having the GFED inventory, which is the most known and widely used BB emission inventory, makes it possible for the developers to relate to our results by knowing how their inventory performs compared to GFED.

In the *choice of the GLC fuel consumption product*, another widely-known University of Maryland (UMD) MODIS-based land cover dataset was considered. Both of these datasets have their strengths, and although the UMD dataset is more dynamic and provides a monthly map of vegetation cover (Hansen et al., 2000), the GLC dataset was developed by a collaborative effort of several research teams, which are composed of regional vegetation experts, thus possibly resolving ambiguities in small-scale vegetation type classification. A number of comparisons between these datasets were performed (See and Fritz, 2006; Fritz and See, 2008), and they appeared to be of equal quality for this project, so we selected GLC, since it came with a complimentary dataset of biomass properties and aerosol emission factors ready to be used on a global scale (C. Liousse, 2010, personal communication).

My original *idea was to group fire cases by vegetation type* and thus perform emission comparisons, based on the assumption that fires behave similarly in similar ecosystems, and we can expect to find some general features specific for burning of a certain type of vegetation. Upon some preliminary analysis this approach was found impractical, mainly because some vegetation types, such as tree cover needle-leaved evergreen (GLC code 4), sparse herbaceous or sparse shrub cover (GLC code 14), or cultivated and managed areas (GLC code 16) span such vast areas globally that they need to be separated into smaller regional subtypes to account for specifics of climate and burning characteristics, for example, to distinguish boreal grass and shrubs from African or Australian grasslands, which appear to have different burning regimes, and biomass and burning properties. The other vegetation types cover only small areas, and are often mixed with other vegetation types (e.g., GLC codes 7, 8, 9) so that they have to be aggregated into more general vegetation categories, which leads to a regional characteristics. Thus, grouping fire cases by regions of different size rendered the generalization necessary to capture specifics of the location, while being big enough to still keep the analysis dataset manageable.

REFERENCES

REFERENCES

Akagi, S. K., R. J. Yokelson, C. Wiedinmyer, M. J. Alvarado, J. S. Reid, T. Karl, J. D. Crounse and P. O. Wennberg (2011). "Emission factors for open and domestic biomass burning for use in atmospheric models." Atmospheric Chemistry and Physics **11**: 4039-4072.

Al-Saadi, J., A. Soja, R. B. Pierce, J. Szykman, C. Wiedinmyer, L. Emmons, S. Kondragunta, X. Zhang, C. Kittaka, T. Schaack and K. Bowman (2008). "Intercomparison of near-real-time biomass burning emissions estimates constrained by satellite fire data." Journal of Applied Remote Sensing **2**(021504).

Alexeyev, V. A. and R. A. Birdsey (1998). Carbon storage in forests and peatlands of Russia. Radnor, PA, USDA, Forest Service, Northeast Research Station.

Andreae, M. O., E. V. Browell, M. Garstang, G. L. Gregory, R. C. Harriss, G. F. Hill, D. J. Jacob, M. C. Pereira, G. W. Sachse, A. W. Setzer, P. L. S. Dias, R. W. Talbot, A. L. Torres and S. C. Wofsy (1988). "Biomass-burning emissions and associated haze layers over Amazonia." Journal of Geophysical Research **93**(D2): 1509-1527.

Andreae, M. O. and P. Merlet (2001). "Emission of trace gases and aerosols from biomass burning." Global Biogeochemical Cycles **15**(4): 955-966.

Bartholome´, E. and A. S. Belward (2005). "GLC2000: a new approach to global land cover mapping from Earth observation data." International Journal of Remote Sensing **26**(9): 1959–1977.

Bäumer, D., B. Vogelb, S. Versickb, R. Rinkeb, O. Möhlerb and M. Schnaiter (2008). "Relationship of visibility, aerosol optical thickness and aerosol size distribution in an ageing air mass over South-West Germany " Atmospheric Environment **42**(5): 989-998.

Bettwy, M. (2007). "NASA data links Indonesian wildfire flare-up to recent El Nino." Goddard News Top Story Retrieved 20 April, 2012, from http://www.nasa.gov/centers/goddard/news/topstory/2007/elnino_wildfire.html.

Bloom, S., A. d. Silva, D. Dee, M. Bosilovich, J.-D. Chern, S. Pawson, S. Schubert, M. Sienkiewicz, I. Stajner, W.-W. Tan and M.-L. Wu (2005). Documentation and validation of the Goddard Earth Observing System (GEOS) data assimilation system - version 4. Technical Report Series on Global Modeling and Data Assimilation. M. J. Suarez. Greenbelt, MD, NASA Goddard Space Flight Center.

Boucher, O. and T. L. Anderson (1995). "General circulation model assessment of the sensitivity of direct climate forcing by anthropogenic sulfate aerosols to aerosol size and chemistry." Journal of Geophysical Research **100**(D12): 26,117-126,134.

Cattrall, C., J. Reagan, K. Thome and O. Dubovik (2005). "Variability of aerosol and spectral lidar and backscatter and extinction ratios of key aerosol types derived from selected Aerosol Robotic Network locations." Journal of Geophysical Research **110**(D10S11): doi:10.1029/2004JD005124.

CCSP (2009). Atmospheric aerosol properties and climate impacts, a report by the U.S. Climate Change Science Program and the subcommittee on global change research. Synthesis and Assessment Product 2.3. U. S. C. C. S. Program. D.C., USA, National Aeronautics and Space Administration.

Chin, M., R. B. Rood, S.-J. Lin, J.-F. Muller and A. M. Thompson (2000). "Atmospheric sulfur cycle simulated in the global model GOCART: Model description and global properties." Journal of Geophysical Research **105**(D20): 24,671-624,687.

Chin, M., P. Ginoux, S. Kinne, O. Torres, B. N. Holben, B. N. Duncan, R. V. Martin, J. A. Logan, A. Higurashi and T. Nakajima (2002). "Tropospheric aerosol optical thickness from the GOCART model and comparisons with satellite and sun photometer measurements." Journal of the Atmospheric Sciences **59**: 461-483.

Chin, M., T. Diehl, P. Ginoux and W. Malm (2007). "Intercontinental transport of pollution and dust aerosols: implications for regional air quality." Atmospheric Chemistry and Physics **7**: 5501-5517.

Chin, M., T. Diehl, O. Dubovik, T. F. Eck, B. N. Holben, A. Sinyuk and D. G. Streets (2009). "Light absorption by pollution, dust, and biomass burning aerosols: a global model study and evaluation with AERONET measurements." Annales Geophysicae **27**: 3439–3464.

Choi, Y., S. A. Vay, K. P. Vadrevu, A. J. Soja, J.-H. Woo, S. R. Nolf, G. W. Sachse, G. S. Diskin, D. R. Blake, N. J. Blake, H. B. Singh, M. A. Avery, A. Fried, L. Pfister and H. E. Fuelberg (2008). "Characteristics of the atmospheric CO2 signal as observed over the conterminous United States during INTEX-NA." Journal of Geophysical Research **113**(D07301): doi:10.1029/2007JD008899.

Colarco, P. R., M. R. Schoeberl, B. G. Doddridge, L. T. Marufu, O. Torres and E. J. Welton (2004). "Transport of smoke from Canadian forest fires to the surface near Washington, D.C.: Injection height, entrainment, and optical properties." Journal of Geophysical Research **109**(D06203): doi:10.1029/2003JD004248.

Conard, S. G., A. I. Sukhinin, B. J. Stocks, D. R. Cahoon, D. P. Davidenko and G. A. Ivanova (2002). "Determining effects of area burned and fire severity on carbon cycling and emissions in Siberia." Climatic Change **55**(1-2): 197-211.

Crutzen, P. J., L. E. Heidt, J. P. Krasnec, W. H. Pollock and W. Seller. (1979). "Biomass burning as a source of atmospheric gases CO, H_2, N_20, NO, CH_3Cl, and COS." Nature **282**: 253-256.

Damoah, R., N. Spichtinger, C. Forster, P. James, I. Mattis, U.Wandinger, S. Beirle, T.Wagner and A. Stohl (2004). "Around the world in 17 days – hemispheric-scale transport of forest fire smoke from Russia in May 2003." Atmospheric Chemistry and Physics **4**: 1311–1321.

Dentener, F., D. Stevenson, J. Cofala, R. Mechler, M. Amann, P. Bergamaschi, F. Raes and R. Derwent (2005). "The impact of air pollutant and methane emission controls on tropospheric ozone and radiative forcing: CTM calculations for the period 1990–2030." Atmospheric Chemistry and Physics **5**: 1731–1755.

Dentener, F., S. Kinne, T. Bond, O. Boucher, J. Cofala, S. Generoso, P. Ginoux, S. Gong, J. J. Hoelzemann, A. Ito, L. Marelli, J. E. Penner, J.-P. Putaud, C. Textor, M. Schulz, G. R. v. d. Werf and J.Wilson (2006). "Emissions of primary aerosol and precursor gases in the years 2000 and 1750 prescribed data-sets for AeroCom." Atmospheric Chemistry and Physics **6**: 4321–4344.

Dey, S. and L. Di Girolamo (2010). "A climatology of aerosol optical and microphysical properties over the Indian subcontinent from 9 years (2000–2008) of Multiangle Imaging Spectroradiometer (MISR) data." Journal of Geophysical Research **115**(D15204): doi:10.1029/2009JD013395.

Diner, D. J., J. C. Beckert, T. H. Reilly, C. J. Bruegge, J. E. Conel, R. A. Kahn, J. V. Martonchik, T. P. Ackerman, R. Davies, S. A. W. Gerstl, H. R. Gordon, J.-P. Muller, R. B. Myneni, P. J. Sellers, B. Pinty and M. M. Verstraete (1998). "Multi-angle Imaging SpectroRadiometer (MISR) instrument description and experiment overview." IEEE Transactions on Geoscience and Remote Sensing **36**(4): 1072-1087.

Dubovik, O., T. Lapyonok, Y. J. Kaufman, M. Chin, P. Ginoux, R. A. Kahn and A. Sinyuk (2008). "Retrieving global aerosol sources from satellites using inverse modeling." Atmospheric Chemistry and Physics **8**: 209-250.

Duncan, B. N., R. V. Martin, A. C. Staudt, R. Yevich and J. Logan (2003). "Interannual and seasonal variability of biomass burning emissions constrained by satellite observations." Journal of Geophysical Research **108**(D2): doi:10.1029/2002JD002378.

EOSDIS. (2009). "Earth Observing System Data and Information System (EOSDIS), Earth Observing System ClearingHOuse (ECHO) / Warehouse Inventory Search Tool (WIST) version 10.X [online application]." Retrieved 07/22, 2011, from https://wist.echo.nasa.gov/api/

Fritz, S. and L. See (2008). "Identifying and quantifying uncertainty and spatial disagreement in the comparison of global land cover for different applications." Global Change Biology **14**: 1057–1075, doi: 1010.1111/j.1365-2486.2007.01519.x.

Generoso, S. I. B., J.-L. Attie and F.-M. Breon (2007). "A satellite- and model-based assessment of the 2003 Russian fires: Impact on the Arctic region." Journal of Geophysical Research **112**(D15302): doi:10.1029/2006JD008344.

Giglio, L., I. Csiszar and C. O. Justice (2006). "Global distribution and seasonality of active fires as observed with the Terra and Aqua Moderate Resolution Imaging Spectroradiometer (MODIS) sensors." Journal of Geophysical Research **111**(G02016): doi:10.1029/2005JG000142.

Giglio, L., G. R. van der Werf, J. T. Randerson, G. J. Collatz and P. Kasibhatla (2006). "Global estimation of burned area using MODIS active fire observations." Atmospheric Chemistry and Physics **6**: 957-974.

Giglio, L. (2007). MODIS collection 4 active fire product user's guide version 4.3. Greenbelt, MD, NASA Goddard Space Flight Center.

Giglio, L., T. Loboda, D. P. Roy, B. Quayle and C. O. Justice (2009). "An active-fire based burned area mapping algorithm for the MODIS sensor." Remote Sensing Environment **113**: 408-420.

Giglio, L. (2010). MODIS collection 5 active fire product user's guide version 2.4. Greenbelt, MD, NASA Goddard Space Flight Center.

Giglio, L., J. T. Randerson, G. R. v. derWerf, P. S. Kasibhatla, G. J. Collatz, D. C. Morton and R. S. DeFries (2010). "Assessing variability and long-term trends in burned area by merging multiple satellite fire products." Biogeosciences **7**: 1171-1186.

Gillett, N. P., A. J. Weaver, F. W. Zwiers and M. D. Flannigan (2004). "Detecting the effect of climate change on Canadian forest fires." Geophysical Research Letters **31**(L18211): doi:10.1029/2004GL020876.

Gonsamo, A. and J. M. Chen (2011). "Evaluation of the GLC2000 and NALC2005 land cover products for LAI retrieval over Canada." Canadian Journal of Remote Sensing **37**(3): 302-313.

Haines, D. A. (1988). "A lower atmosphere severity index for wildland fires." National Weather Digest **13**: 23-27.

Houghton, R. A. (1991). Biomass burning from the perspective of the global carbon cycle. Global Biomass Burning: Atmospheric, Climatic, and Biospheric Implications. J. S. Levine. Cambridge, Massachusetts, MIT Press**:** 321-325.

Hyer, E. J. and J. S. Reid (2009). "Baseline uncertainties in biomass burning emission models resulting from spatial error in satellite active fire location data." Geophysical Research Letters **36**(L05802): doi:10.1029/2008GL036767.

Ichoku, C. and Y. Kaufman (2005). "A method to derive smoke emission rates from MODIS fire radiative energy measurements." IEEE Transactions on Geoscience and Remote Sensing **43**(11): 2636-2649.

IPCC (2007). Climate change 2007: the physical science basis. Contribution of working group I to the fourth assessment report of the intergovernmental panel on climate change S. Solomon, D. Qin, M. Manning, Z. Chen, M. Marquis, K. B. Averyt, M. Tignor and H. L. Miller. Cambridge, United Kingdom and New York, NY, USA**:** 996 pp.

Ito, A. and J. E. Penner (2004). "Global estimates of biomass burning emissions based on satellite imagery for the year 2000." Journal of Geophysical Research **109**(D14S05): doi:10.1029/2003JD004423.

Jaffe, D., I. Bertschi, L. Jaeglé, P. Novelli, J. S. Reid, H. Tanimoto, R. Vingarzan and D. L. Westphal (2004). "Long-range transport of Siberian biomass burning emissions and impact on surface ozone in western North America." Geophysical Research Letters **31**(L16106): doi:10.1029/2004GL020093.

Justice, C., L. Giglio, L. Boschetti, D. Roy, I. Csiszar, J. Morisette and Y. Kaufman (2006). MODIS fire products. Version 2.3. Algorithm Technical Background Document.

Kahn, R. A., W.-H. Li, C. Moroney, D. J. Diner, J. V. Martonchik and E. Fishbein (2007). "Aerosol source plume physical characteristics from space-based multiangle imaging." Journal of Geophysical Research **112**(D11205): doi:10.1029/2006JD007647.

Kahn, R. A., Y. Chen, D. L. Nelson, F.-Y. Leung, Q. Li, D. J. Diner and J. A. Logan (2008). "Wildfire smoke injection heights: Two perspectives from space." Geophysical Research Letters **35**(L04809): doi:10.1029/2007GL032165.

Kahn, R. A., B. J. Gaitley, M. J. Garay, D. J. Diner, T. F. Eck, A. Smirnov and B. N. Holben (2010). "Multiangle Imaging SpectroRadiometer global aerosol product assessment by comparison with the Aerosol Robotic Network." Journal of Geophysical Research **115**(D23209): doi:10.1029/2010JD014601.

Kaiser, J. W., A. Heil, M. O. Andreae, A. Benedetti, N. Chubarova, L. Jones, J.-J. Morcrette, M. Razinger, M. G. Schultz, M. Suttie and G. R. v. d. Werf (2012). "Biomass burning emissions estimated with a global fire assimilation system based on observed fire radiative power." Biogeosciences **9**: 527–554.

Kasischke, E. S. and L. P. Bruhwiler (2003). "Emissions of carbon dioxide, carbon monoxide, and methane from boreal forest fires in 1998." Journal of Geophysical Research **107**: doi:10.1029/2001JD000461.

Kaufman, Y., L. Remer, R. Ottmar, D. Ward, L. Rong-R, R. Kleidman, R. Fraser, L. Flynn, D. McDougal and G. Shelton (1996). Relationship between remotely sensed fire intensity and rate of emission of smoke: SCAR-C experiment. Global Biomass Burning. J. Levine. Mass., MIT Press**:** 685– 696.

Labonne, M., F.-M. Breon and F. Chevallier (2007). "Injection height of biomass burning aerosols as seen from a spaceborne lidar." Geophysical Reserch Letters **34**(L11806): doi:10.1029/2007GL029311.

Levine, J. S., W. R. Cofer and J. P. Pinto (1993). Biomass Burning. Atmospheric methane: Sources, sinks, and role in global change. M. A. K. Khalil. Berlin Heidelberg, Springer-Verlag 299-313.

Levy, R. C., L. A. Remer and O. Dubovik (2007). "Global aerosol optical properties and application to Moderate Resolution Imaging Spectroradiometer aerosol retrieval over land." Journal of Geophysical Research **112**(D13210): doi:10.1029/2006JD007815.

Levy, R. C., L. A. Remer, R. G. Kleidman, S. Mattoo, C. Ichoku, R. Kahn and T. F. Eck (2010). "Global evaluation of the Collection 5 MODIS dark-target aerosol products over land." Atmospheric Chemistry and Physics **10**: 10399–10420.

Liousse, C., M. O. Andreae, P. Artaxo, P. Barbosa, H. Cachier, J. M. Gregoire, P. Hobbs, D. Lavoue, F. Mouillot, J. Penner, M. Scholes and M. G. Schultz (2003). Deriving global quantitative estimates for spatial and temporal distributions of biomass burining emissions. IGAC book on emissions. C. Granier, P. Artaxo and C. Reeves, Kluwer.

Liousse, C., B. Guillaume, J. M. Gr´egoire, M. Mallet, C. Galy, V. Pont, A. Akpo, M. Bedou, P. Cast´era, L. Dungall, E. Gardrat, C. Granier, A. Konar´e, F. Malavelle, A. Mariscal, A. Mieville, R. Rosset, D. Serc¸a, F. Solmon, F. Tummon, E. Assamoi, V. Yobou´e and P. V. Velthoven (2010). "Updated African biomass burning emission inventories in the framework of the AMMA-IDAF program, with an evaluation of combustion aerosols." Atmospheric Chemistry and Physics **10**: 9631–9646.

Lohmann, U. and J. Feichter (2005). "Global indirect aerosol effects: a review." Atmospheric Chemistry and Physics **5**: 715-737.

Mazurek, M., M. C. Masonjones, H. D. Masonjones, L. G. Salmon, G. R. Cass, K. A. Hallock and M. Leach (1997). "Visibility-reducing organic aerosols in the vicinity of Grand Canyon National Park: Propertiesobserved by high resolution gas chromatography." Journal of Geophysical Research **102**(D3): 3779-3793.

Mazzoni, D., J. A. Logan, D. Diner, R. Kahn, L. Tong and Q. Lia (2007). "A data-mining approach to associating MISR smoke plume heights with MODIS fire measurements " Remote Sensing of Environment **107**: 138–148.

Michel, C., C. Liousse, J.-M. Grégoire, K. Tansey, G. R. Carmichael and J.-H. Woo. (2005). "Biomass burning emission inventory from burnt area data given by the SPOT-VEGETATION system in the frame of TRACE-P and ACE-Asia campaigns." Journal of Geophysical Research **110**(D09304): doi:10.1029/2004JD005461.

Moroney, C., R. Davies and J.-P. Muller (2002). "Operational retrieval of cloud-top heights using MISR data." IEEE Transactions on Geoscience and Remote Sensing **40**(7): 1532-1540.

Morris, G. A., S. Hersey, A. M. Thompson, S. Pawson, J. E. Nielsen, P. R. Colarco, W. W. McMillian, N. I. f. A. R. Department of Regional and Global Pollution Issues, S. Turquety, J. Warner, B. J. Johnson, T. L. Kucsera, D. E. Larko, S. Oltmans and J. Witte (2006). "Alaskan and Canadian forest fires exacerbate ozone pollution over Houston, Texas, on 19 and 20 July 2004." Geophysical Research Letters **111**.

Mu, M., J. T. Randerson, G. R. v. d. Werf, L. Giglio, P. Kasibhatla, D. Morton, G. J. Collatz, R. S. DeFries, E. J. Hyer, E. M. Prins, D. W. T. Griffith, D. Wunch, G. C. Toon, V. Sherlock and P. O. Wennberg (2011). "Daily and hourly variability in global fire emissions and consequences for atmospheric model predictions of carbon monoxide." Journal of Geophysical Research-Atmospheres **116**(D24303): doi:10.1029/2011JD016245.

NARSTO (2003). Particulate matter science for policy makers - a NARSTO assessment. P. H. McMurry, M. F. Shepherd and J. S. Vickery. Pasco, WA, NARSTO management office (Envair)**:** 510.

Olson, J. S., R. M. Garrels, R. A. Berner, T. V. Armentano, M. I. Dyer and D. H. Taalon (1985). The natural carbon cycle. Atmospheric Carbon Dioxide and the Global Carbon Cycle. J. R. Trabalka. Washington, DC, US Department of Energy**:** 175-213.

Pandithurai, G., R. T. Pinker, O. Dubovik, B. N. Holben and T. O. Aro (2001). "Remote sensing of aerosol optical characteristics in sub-Sahel, West Africa." Journal of Geophysical Research **106**(D22): 28,347-328,356.

Patterson, E. M., C. K. McMahon and D. Ward (1986). "Absorption properties and graphitic carbon emission factors of forest fire aerosols." Geophysical Research Letters **13**(1): 129-132.

Pierce, R. B., T. Schaack, J. A. Al-Saadi, T. D. Fairlie, C. Kittaka, G. Lingenfelser, M. Natarajan, J. Olson, A. Soja, T. Zapotocny, A. Lenzen, J. Stobie, D. Johnson, M. A. Avery, G. W. Sachse, A. Thompson, R. Cohen, J. E. Dibb, J. Crawford, D. Rault, R. Martin, J. Szykman and J. Fishman (2007). "Chemical data assimilation estimates of continental U.S. ozone and nitrogen budgets during the Intercontinental Chemical Transport Experiment–North America." Journal of Geophysical Research **112**(D12S21): doi:10.1029/2006JD007722.

Quinn, P. K., T. S. Bates, E. Baum, N. Doubleday, A. M. Fiore, M. Flanner, A. Fridlind, T. J. Garrett, D. Koch, S. Menon, D. Shindell, A. Stohl and S. G. Warren (2008). "Short-lived pollutants in the Arctic: their climate impact and possible mitigation strategies." Atmospheric Chemistry and Physics **8**: 1723–1735.

Reid, J. S., E. J. Hyer, E. M. Prins, D. L. Westphal, J. Zhang, J. Wang, S. A. Christopher, C. A. Curtis, C. C. Schmidt, D. P. Eleuterio, K. A. Richardson and J. P. Hoffman (2009). "Global monitoring and rorecasting of biomass-burning smoke: Description of and lessons from the Fire Locating and Modeling of Burning Emissions (FLAMBE) program." IEEE Journal of Selected Topics in Applied Earth Observations and Remote Sensing **2**(3): 144-162.

Remer, L. A., D. Tanré, Y. J. Kaufman, R. Levy and S. Mattoo (2006). Algorithm for remote sensing of tropospheric aerosol from MODIS: Collection 5. Product ID: MOD04/MYD04. Greenbelt, MD, NASA Goddard Space Flight Center.

Rienecker, M. M., M. J. Suarez, R. Todling, J. Bacmeister, L. Takacs, H.-C. Liu, W. Gu, M. Sienkiewicz, R. D. Koster, R. Gelaro, I. Stajner and J. E. Nielsen (2008). The GEOS-5 Data Assimilation System—Documentation of versions 5.0.1, 5.1.0, and 5.2.0. Technical Report Series on Global Modeling and Data Assimilation. M. J. Suarez. Greenbelt, Maryland, NASA Goddard Space Flight Center.

Roy, D. P., L. Boschetti, C. O. Justice and J. Ju (2008). "The collection 5 MODIS burned area product — global evaluation by comparison with the MODIS active fire product." Remote Sensing Environment **112**: 3690-3707.

Sapkota, A., J. M. Symons, J. Kleissl, L. Wang, M. B. Parlange, J. Ondov, P. N. Breysse, G. B. Diette, P. A. Eggleston and T. J. Buckley (2005). "Impact of the 2002 Canadian forest fires on particulate matter air quality in Baltimore city." Environmental Science and Technology **39**: 24-32.

Schroeder, W., I. Csiszar, L. Giglio and C. C. Schmidt (2010). "On the use of fire radiative power, area, and temperature estimates to characterize biomass burning via moderate to coarse spatial resolution remote sensing data in the Brazilian Amazon." Journal of Geophysical Research **115**(D21121): doi:10.1029/2009JD013769.

Schultz, M. G., A. Heil, J. J. Hoelzemann, A. Spessa, K. Thonicke, J. Goldammer, A. C. Held, and J. M. Pereira (2008), "Global emissions from wildland fires from 1960 to 2000:, Global Biogeochemical Cycles, **22**(GB2002), doi:10.1029/2007GB003031.

Seaton, A., D. Godden, W. MacNee and K. Donaldson (1995). "Particulate air pollution and acute health effects." The Lancet **345**(8943): 176-178.

See, L. M. and S. Fritz (2006). "A method to compare and improve land cover datasets: Application to the GLC-2000 and MODIS land cover products." IEEE Transactions on Geoscience and Remote Sensing **44**(7): 1740-1746.

Seiler, W. and P. J. Crutzen (1980). "Estimates of gross and net fluxes of carbon between the biosphere and the atmosphere from biomass burning." Climatic Change **2**: 207-247.

Seinfeld, J. H. and S. N. Pandis (1998). Atmospheric chemistry and physics, John Wiley and Sons, Inc.

Shindell, D., J.-F. Lamarque, N. Unger, D. Koch, G. Faluveg, S. Bauer and H. Teich (2008). "Climate forcing and air quality change due to regional emissions reductions by economic sector." Atmospheric Chemistry and Physics **8**: 7101–7113.

Soja, A. J., W. R. Cofer, H. H. Shugart, A. I. Sukhinin, P. W. Stackhouse Jr., D. J. McRae and S. G. Conard (2004). "Estimating fire emissions and disparities in boreal Siberia (1998-2002)." Journal of Geophysical Research **109**(D14S06): doi:10.1029/2004JD004570.

Soja, A. J., J. Al-Saadi, L. Giglio, D. Randall, C. Kittaka, G. Pouliot, J. J. Kordzi, S. Raffuse, T. G. Pace, T. E. Pierce, T. Moore, B. Roy, R. B. Pierce and J. J. Szykman (2009). "Assessing satellite-based fire data for use in the National Emissions Inventory." Journal of Applied Remote Sensing **3**(031504).

Stohl, A., C. Forster, S. Eckhardt, N. Spichtinger, H. Huntrieser, J. Heland, H. Schlager, S. W. F. Arnold and O. Cooper (2003). "A backward modeling study of intercontinental pollution transport using aircraft measurements." Journal of Geophysical Research **108(D12)**(4370): doi:10.1029/2002JD002862.

Textor, C., M. Schulz, S. Guibert, S. Kinne, Y. Balkanski, S. Bauer, T. Berntsen, T. Berglen, O. Boucher, M. Chin, F. Dentener, T. Diehl, R. Easter, H. Feichter, D. Fillmore, S. Ghan, P. Ginoux, S. Gong, A. Grini, J. Hendricks, L. Horowitz, P. Huang, I. Isaksen, T. Iversen, S. Kloster, D. Koch, A. Kirkevag, J. E. Kristjansson, M. Krol, A. Lauer, J. F. Lamarque, X. Liu, V. Montanaro, G. Myhre, J. Penner, G. Pitari, S. Reddy, Ø. Seland, P. Stier, T. Takemura and X. Tie (2006). "Analysis and quantification of the diversities of aerosol life cycles within AeroCom." Atmospheric Chemistry and Physics **6**: 1777-1813.

Turquety, S., J. A. Logan, D. J. Jacob, R. C. Hudman, F. Y. Leung, C. L. Heald, R. M. Yantosca, S. Wu, L. K. Emmons, D. P. Edwards and G. W. Sachse (2007). "Inventory of boreal fire emissions for North America in 2004: Importance of peat burning and pyroconvective injection." Journal of Geophysical Research **112**(D12S03): doi:10.1029/2006JD007281.

ValMartin, M., J. A. Logan, R. A. Kahn, F.-Y. Leung, D. L. Nelson and D. J. Diner (2010). "Smoke injection heights from fires in North America: analysis of 5 years of satellite observations." Atmospheric Chemistry and Physics **10**: 1491–1510.

Van der Werf, G. R., J. T. Randerson, L. Giglio, G. J. Collatz and P. S. Kasibhatla (2006). "Interannual variability in global biomass burning emission from 1997 to 2004." Atmospheric Chemistry and Physics **6**: 3423-3441.

Van der Werf, G. R., J. T. Randerson, L. Giglio, G. J. Collatz, M. Mu, P. S. Kasibhatla, D. C. Morton, R. S. DeFries, Y. Jin and T. T. v. Leeuwen (2010). "Global fire emissions and the contribution of deforestation, savanna, forest, agricultural, and peat fires (1997-2009)." Atmospheric Chemistry and Physics **10**: 11707–11735.

Vaughan, M., S. Young, D. Winker, K. Powell, A. Omar, Z. Liu, Y. Hu and C. Hostetler (2004). "Fully automated analysis of space-based lidar data: an overview of the CALIPSO retrieval algorithms and data products". SPIE, Bellingham, WA, SPIE.

Vermote, E., E. Ellicott, O. Dubovik, T. Lapyonok, M. Chin, L. Giglio and G. J. Roberts (2009). "An approach to estimate global biomass burning emissions of organic and black carbon from MODIS fire radiative power." Journal of Geophysical Research **114**(D18205): doi:10.1029/2008JD011188.

Warneke, C., J. A. d. Gouw, A. Stohl, O. R. Cooper, P. D. Goldan, W. C. Kuster, J. S. Holloway, E. J. Williams, B. M. Lerner, S. A. McKeen, M. Trainer, F. C. Fehsenfeld, E. L. Atlas, S. G. Donnelly, V. Stroud, A. Lueb and S. Kato (2006). "Biomass burning and anthropogenic sources of CO over New England in the summer 2004." Journal of Geophysical Research **111**(D23S15): doi:10.1029/2005JD006878.

Warneke, C., R. Bahreini, J. Brioude, C. A. Brock, J. A. de Gouw, D. W. Fahey, K. D. Froyd, J. S. Holloway, A. Middlebrook, L. Miller, S. Montzka, D. M. Murphy, J. Peischl, T. B. Ryerson, J. P. Schwarz, J. R. Spackman and P. Veres (2009). "Biomass burning in Siberia and Kazakhstan as an important source for haze over the Alaskan Arctic in April 2008." Geophysical Research Letters **36**(L02813): doi:10.1029/2008GL036194.

Werth, P. and R. Ochoa (1993). "The evaluation of Idaho wildfire growth using the Haines index." Weather and Forecasting **8**: 223-234.

Wiedinmyer, C., B. Quayle, C. Geron, A. Belote, D. McKenzie, X. Zhang, S. O'Neill and K. K. Wynne (2006). "Estimating emissions from fires in North America for air quality modeling." Atmospheric Environment **40**: 3419–3432.

Wiedinmyer, C., S. K. Akagi, R. J. Yokelson, L. K. Emmons, J. A. Al-Saadi, J. J. Orlando and A. J. Soja (2011). "The Fire INventory from NCAR (FINN): a high resolution global model to estimate the emissions from open burning." Geoscientific Model Development **4**: 625–641.

Winker, D. M., W. H. Hunt and C. A. Hostetler (2004). Status and performance of the CALIOP lidar. SPIE**:** 8-15.

Winker, D. M., M. A. Vaughan, A. Omar, Y. Hu, K. A. Powell, Z. Liu, W. H. Hunt and S. A. Young (2009). "Overview of the CALIPSO mission and CALIOP data processing algorithms." Journal of Atmospheric and Oceanic Technology **26**: 2310–2323,doi: 2310.1175/2009JTECHA1281.2311.

Winkler, J. A., B. E. Potter, D. F. Wilhelm, R. P. Shadbolt, K. Piromsopa and X. Bian (2007). "Climatological and statistical characteristics of the Haines Index for North America." International Journal of Wildland Fire **16**: 139-152.

Witte, J. C., A. R. Douglass, A. d. Silva, O. Torres, R. C. Levy and B. N. Duncan (2011). "NASA A-Train and Terra observations of the 2010 Russian wildfires." Atmospheric Chemistry and Physics **11**: 19113-19142, doi:19110.15194/acpd-19111-19113-12011.

Wooster, M. J. (2002). "Small-scale experimental testing of fire radiative energy for quantifying mass combusted in natural vegetation fires." Geophysical Research Letters **29**(21,2027): doi:10.1029/2002GL015487.

Wooster, M. J., G. Roberts, G. L. W. Perry and Y. J. Kaufman (2005). "Retrieval of biomass combustion rates and totals from fire radiative power observations: FRP derivation and calibration relationships between biomass consumption and fire radiative energy release." Journal of Geophysical Research **110**(D24311): doi:10.1029/2005JD006318.

Xiao-Peng, S., H. Chengquan, J. O. Sexton, F. Min, R. Narasimhan, S. Channan and J. R. Townshend (2011). An assessment of global forest cover maps using regional higher-resolution reference data sets. Geoscience and Remote Sensing Symposium (IGARSS), 2011 IEEE International.

Yu, H., Y. J. Kaufman, M. Chin, G. Feingold, L. A. Remer, T. L. Anderson, Y. Balkanski, N. Bellouin, O. Boucher, S. Christopher, P. DeCola, R. Kahn, D. Koch, N. Loeb, M. S. Reddy, M. Schulz, T. Takemura and M. Zhou (2006). "A review of measurement-based assessments of the aerosol direct radiative effect and forcing." Atmospheric Chemistry and Physics **6**: 613-666.

Zinke, P. J., A. G. Stangenberger, W. M. Post, W. R. Emanuel and J. S. Olson (1986). Worldwide organic soil carbon and nitrogen data. Oak Ridge, Tennessee, Oak Ridge National Laboratory.

APPENDIX

APPENDIX

Maps of MODIS-measured and GOCART-simulated AOD for all the cases considered in this study are presented in the order in which they appear in Table 6.

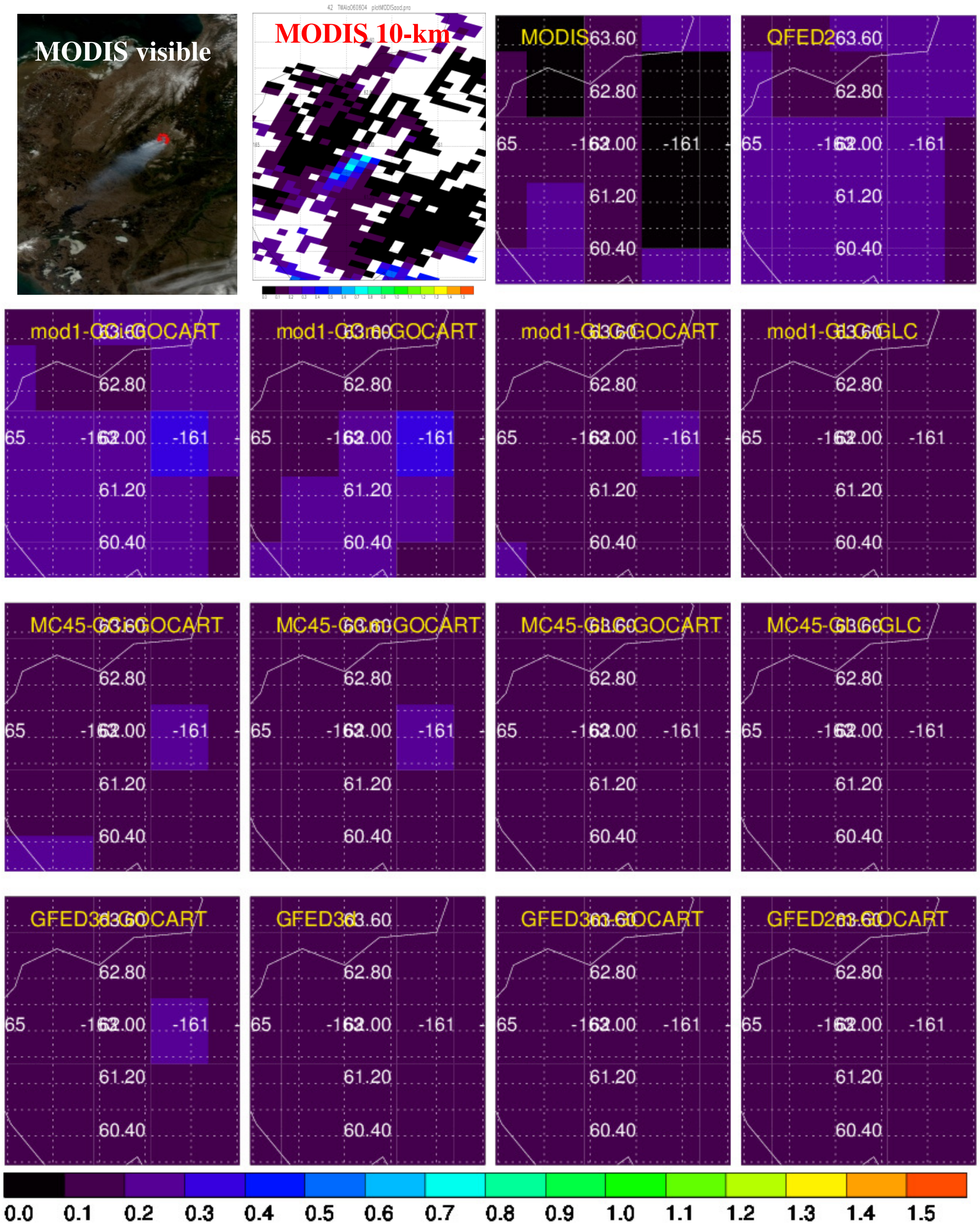

Figure A - 1 MODIS and GOCART AOD for case 42

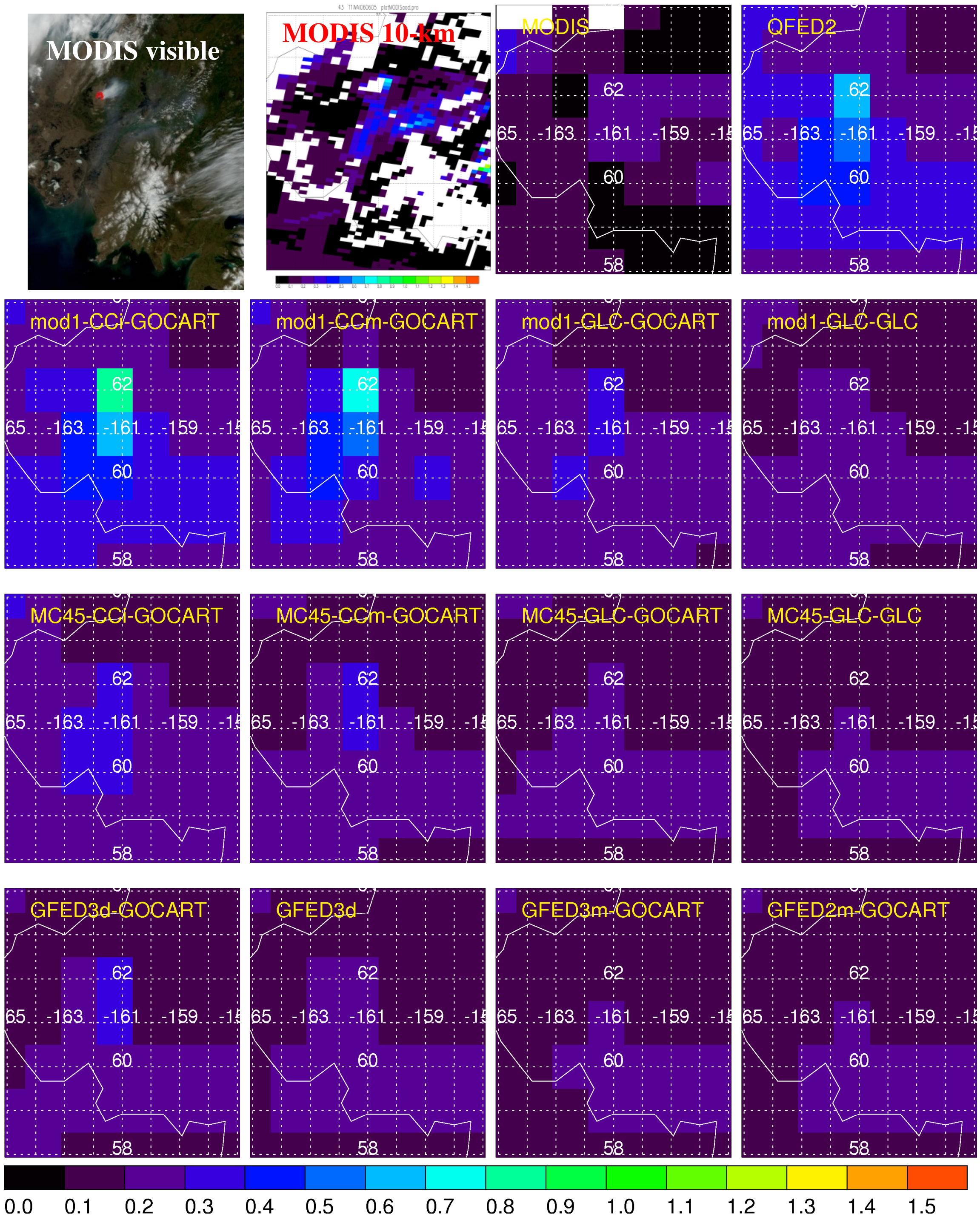

Figure A - 2 MODIS and GOCART AOD for case 43

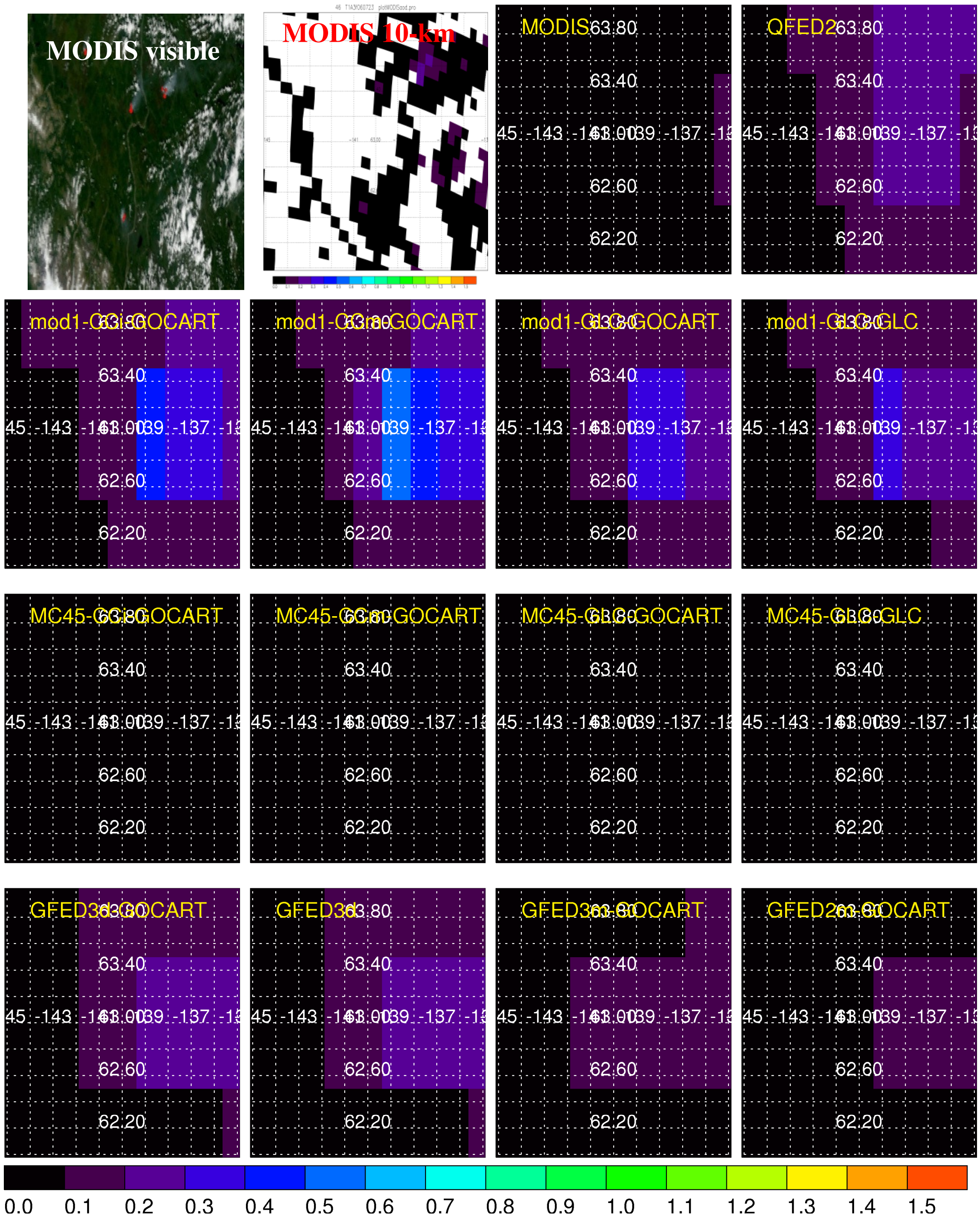

Figure A - 3 MODIS and GOCART AOD for case 46

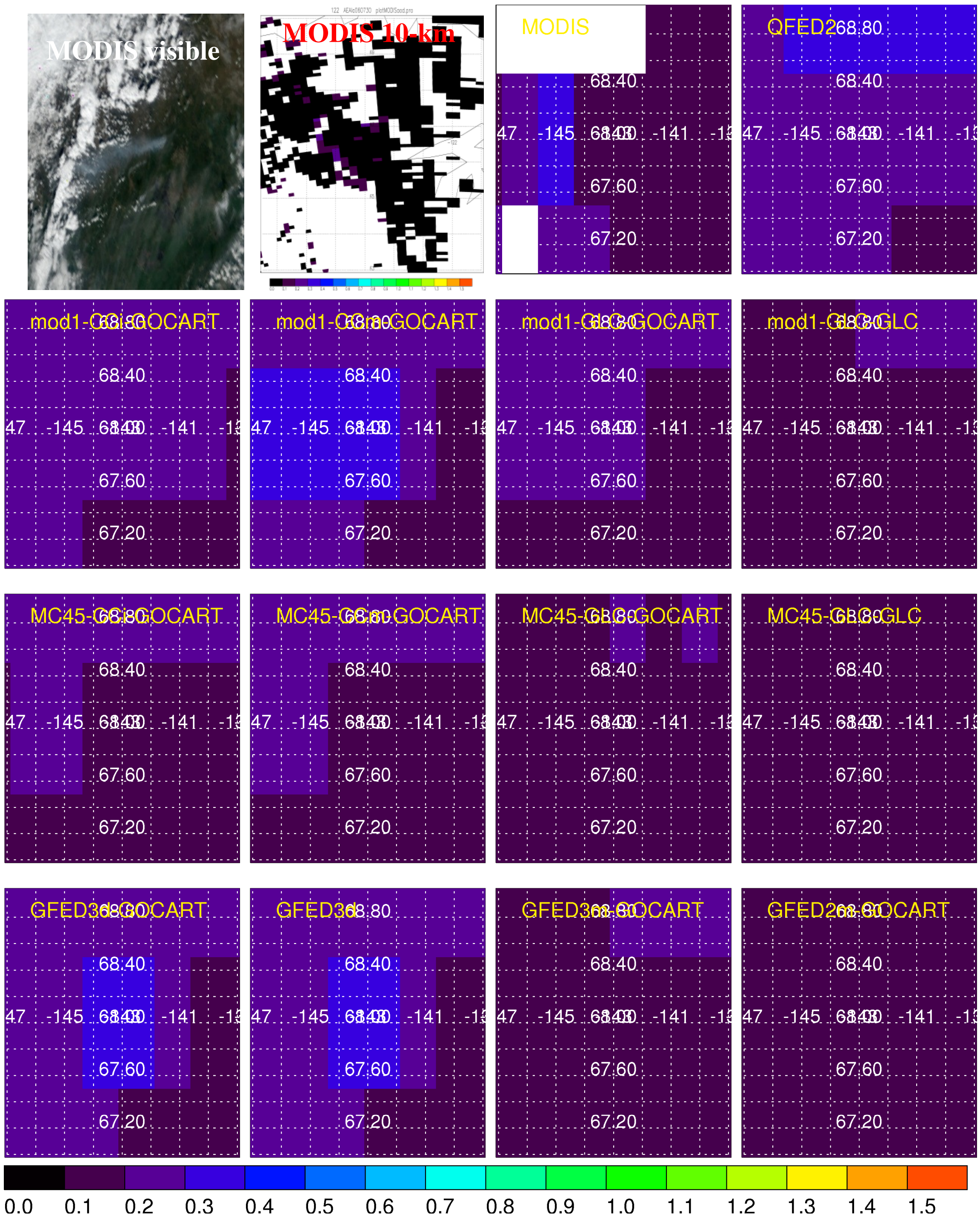

Figure A - 4 MODIS and GOCART AOD for case 122

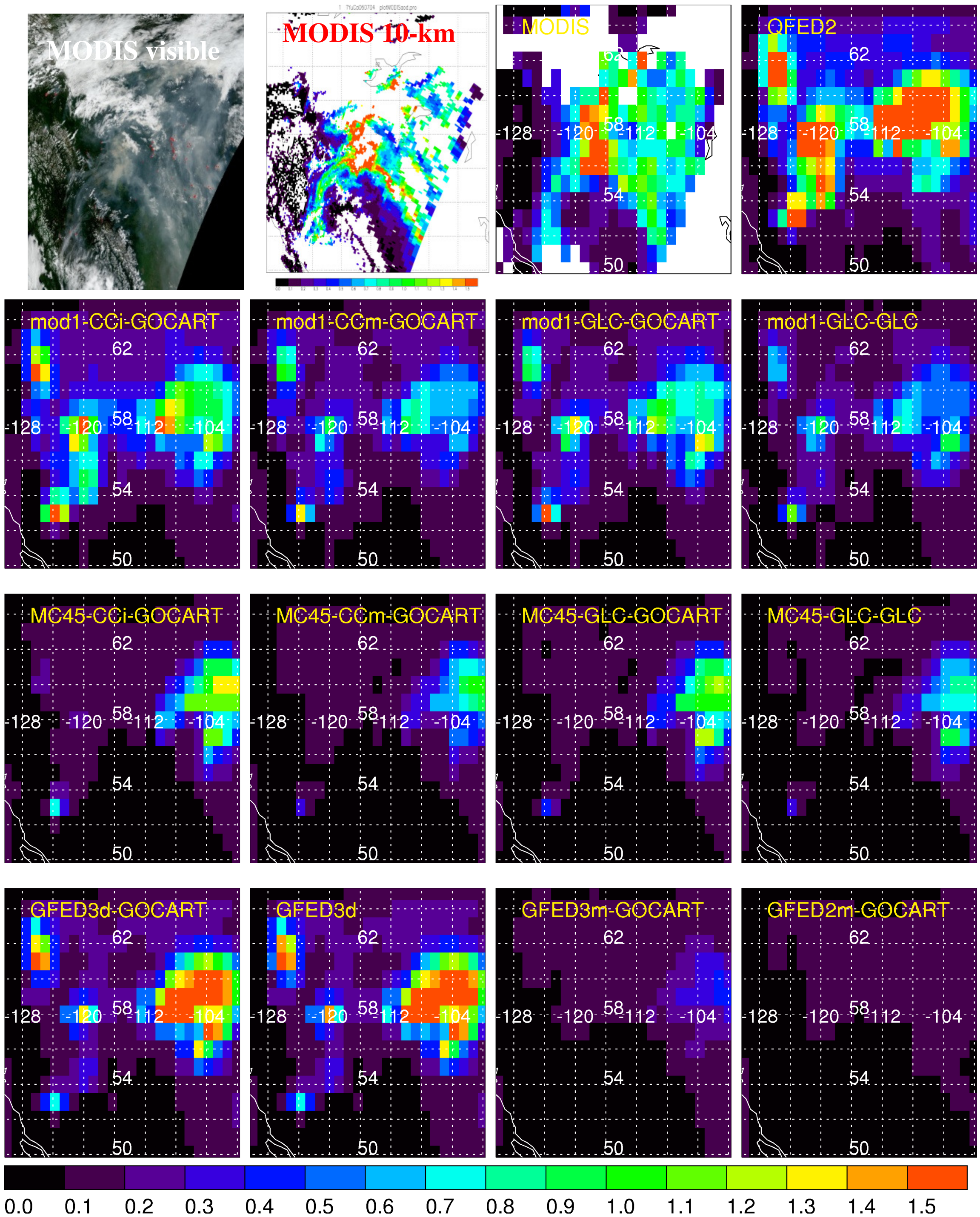

Figure A - 5 MODIS and GOCART AOD for case 1

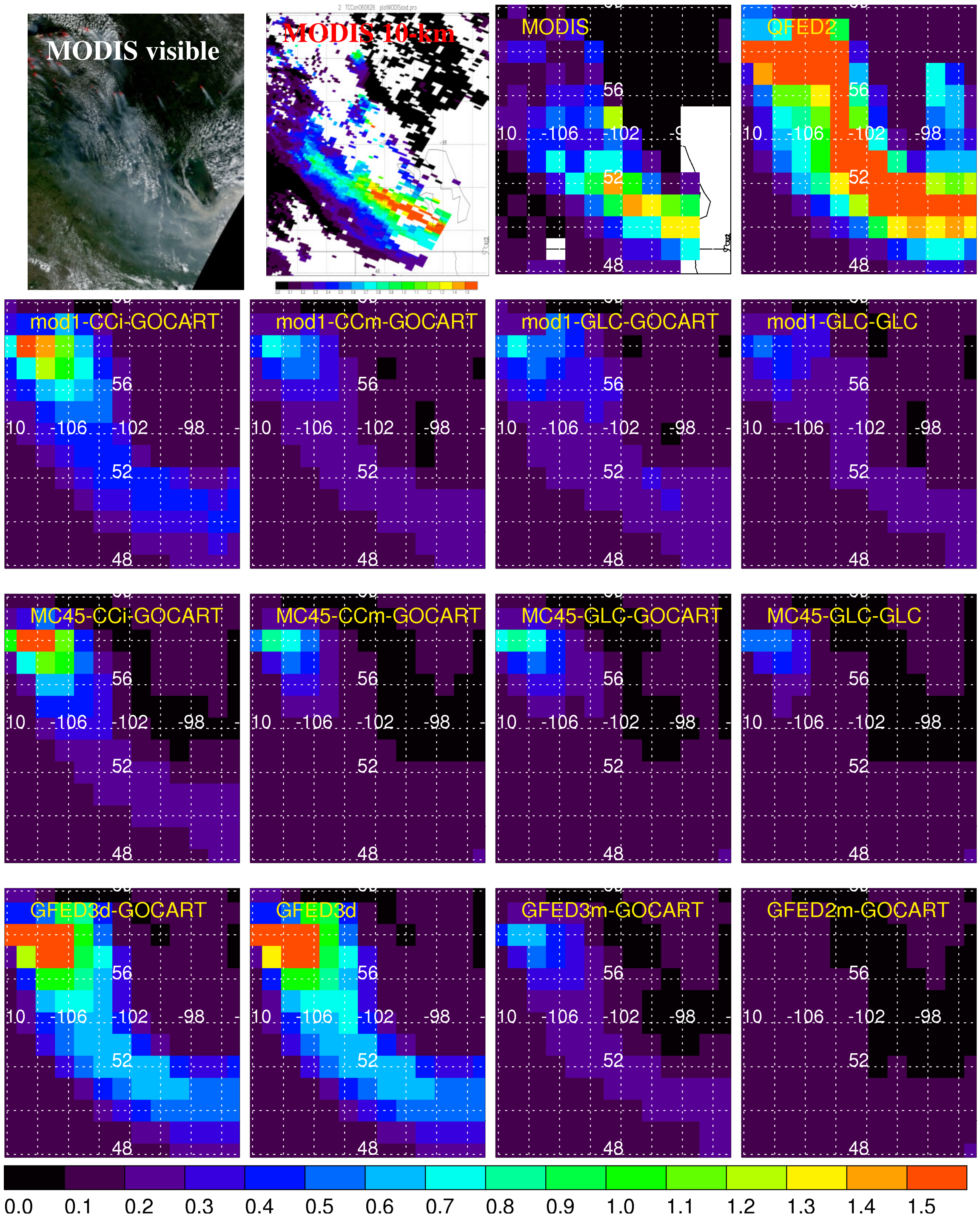

Figure A - 6 MODIS and GOCART AOD for case 2

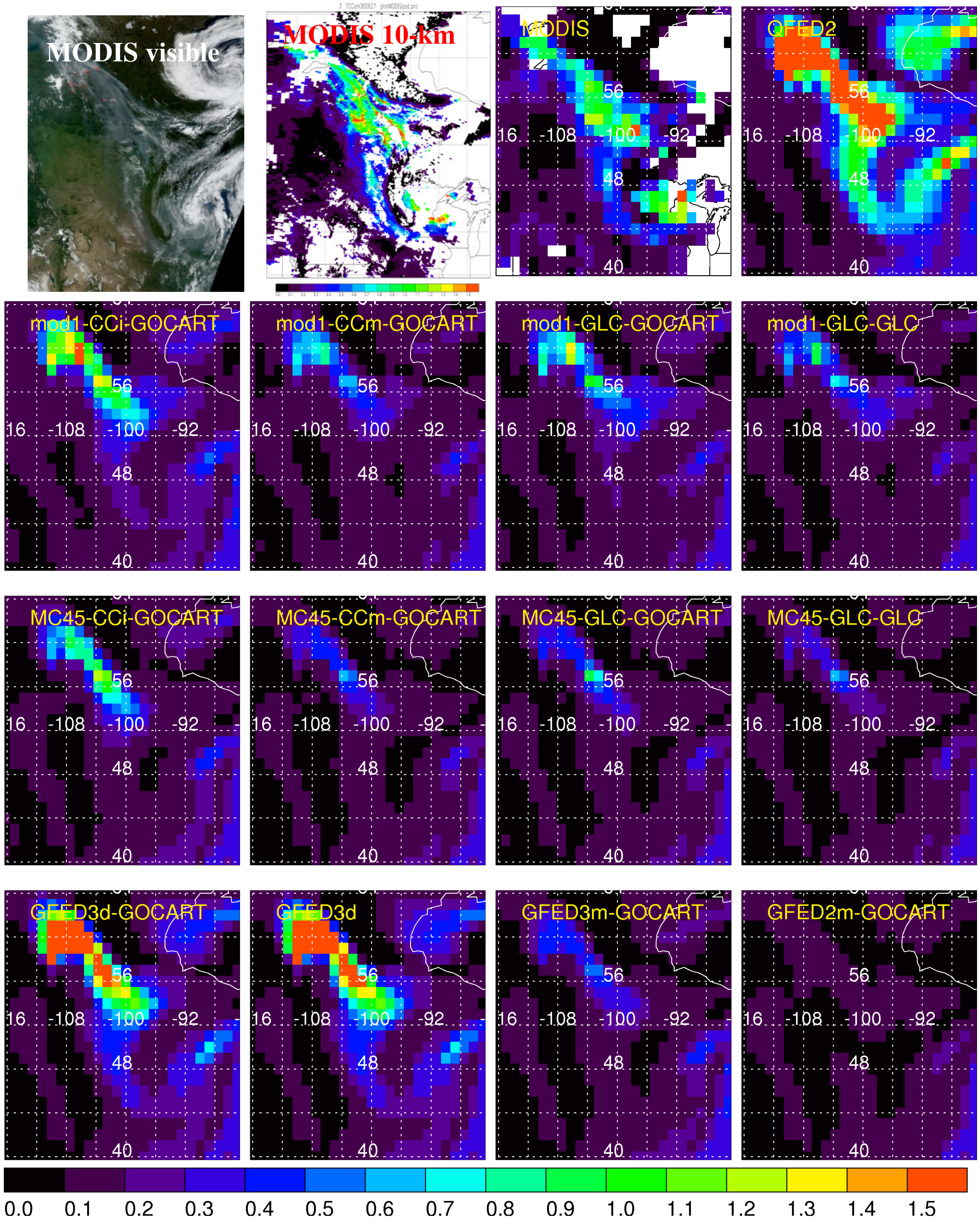

Figure A - 7 MODIS and GOCART AOD for case 3

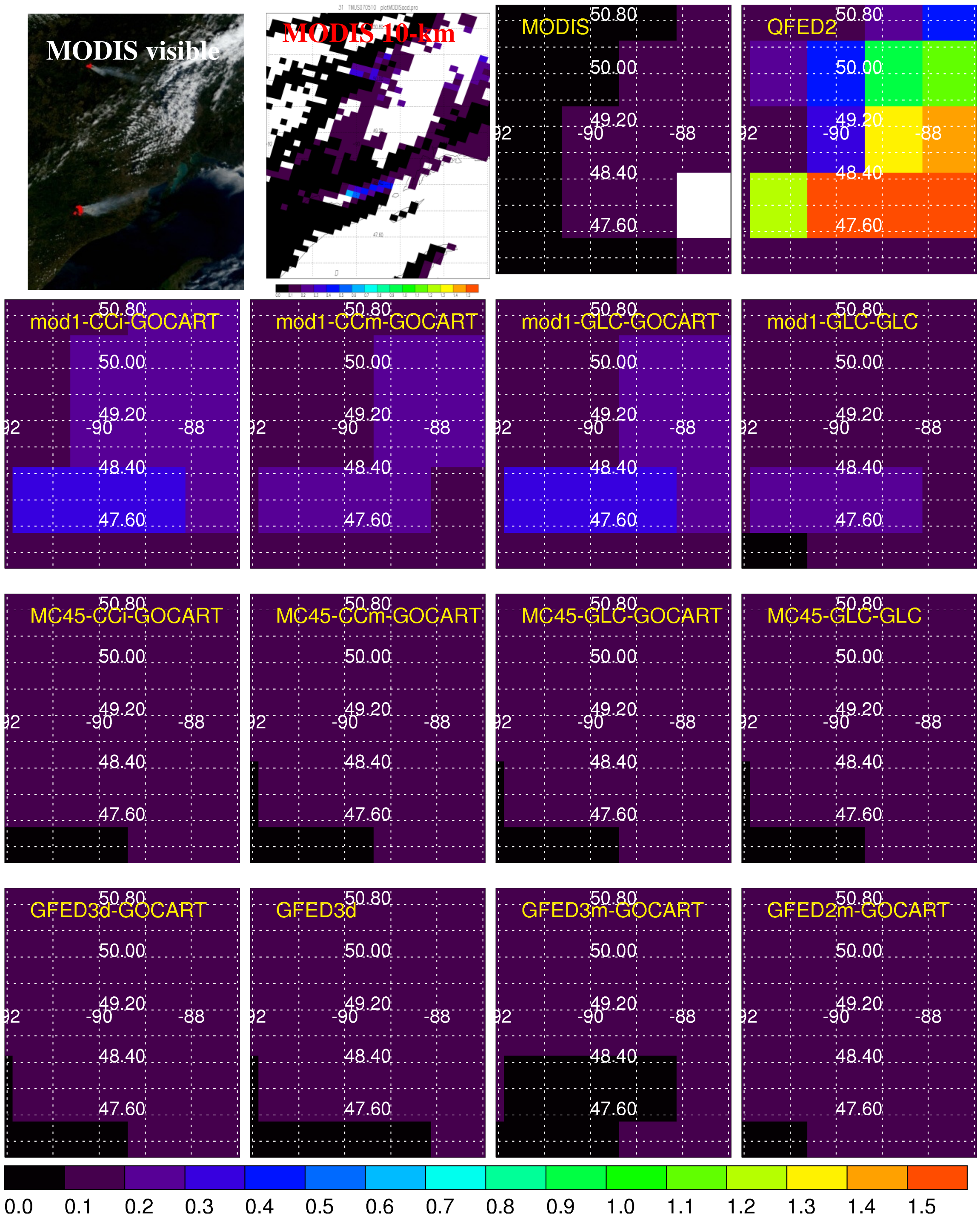

Figure A - 8 MODIS and GOCART AOD for case 31

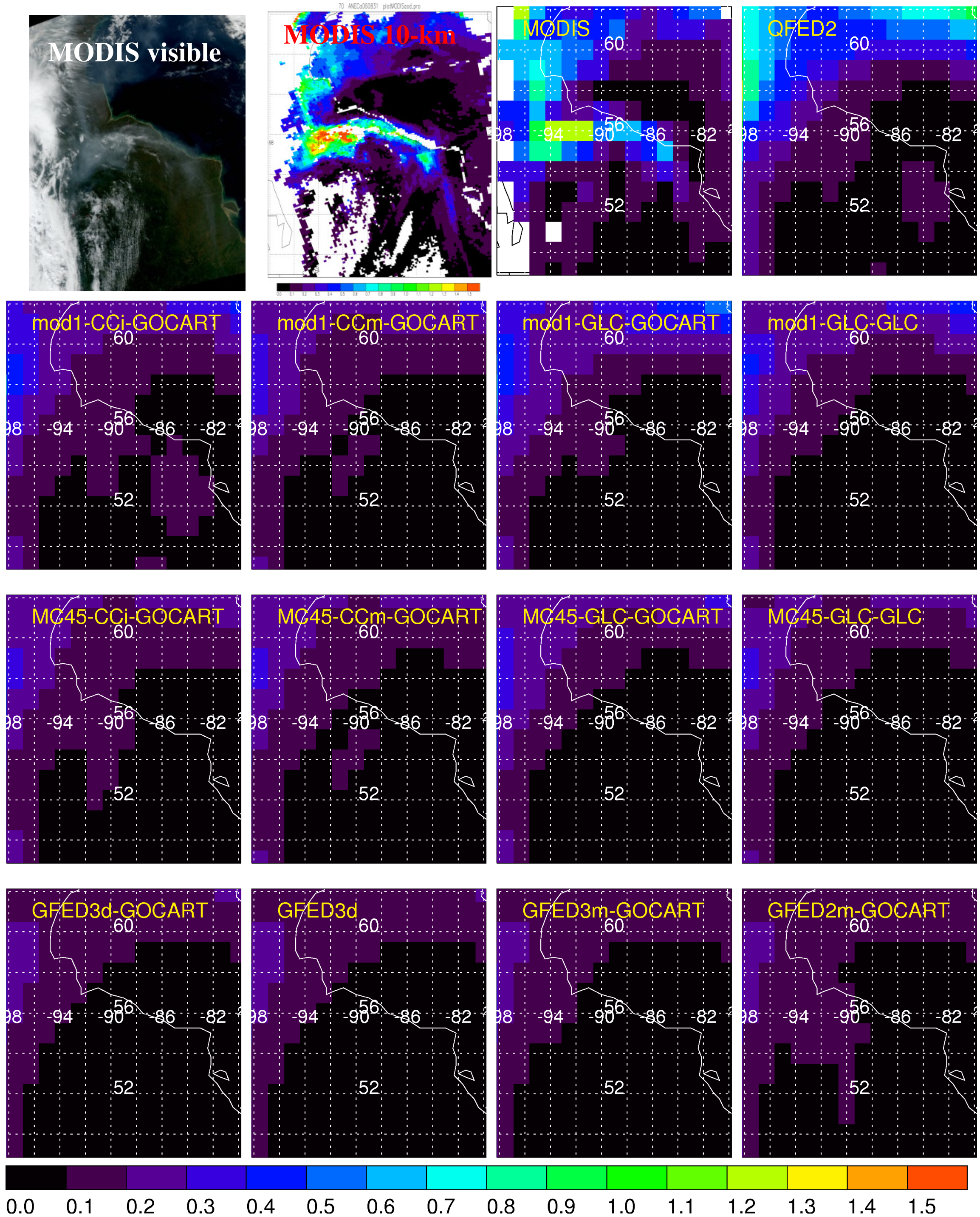

Figure A - 9 MODIS and GOCART AOD for case 70

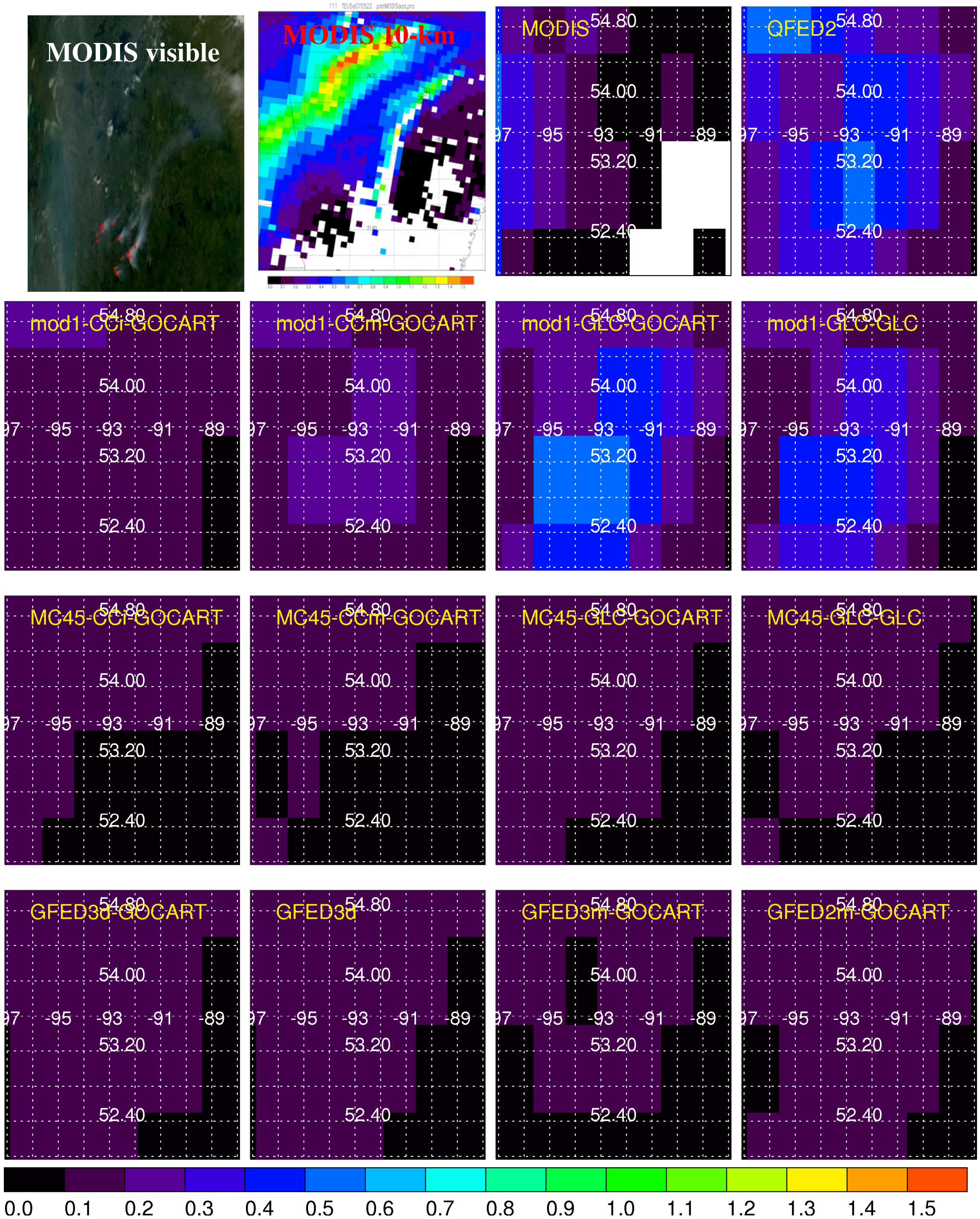

Figure A - 10 MODIS and GOCART AOD for case 74

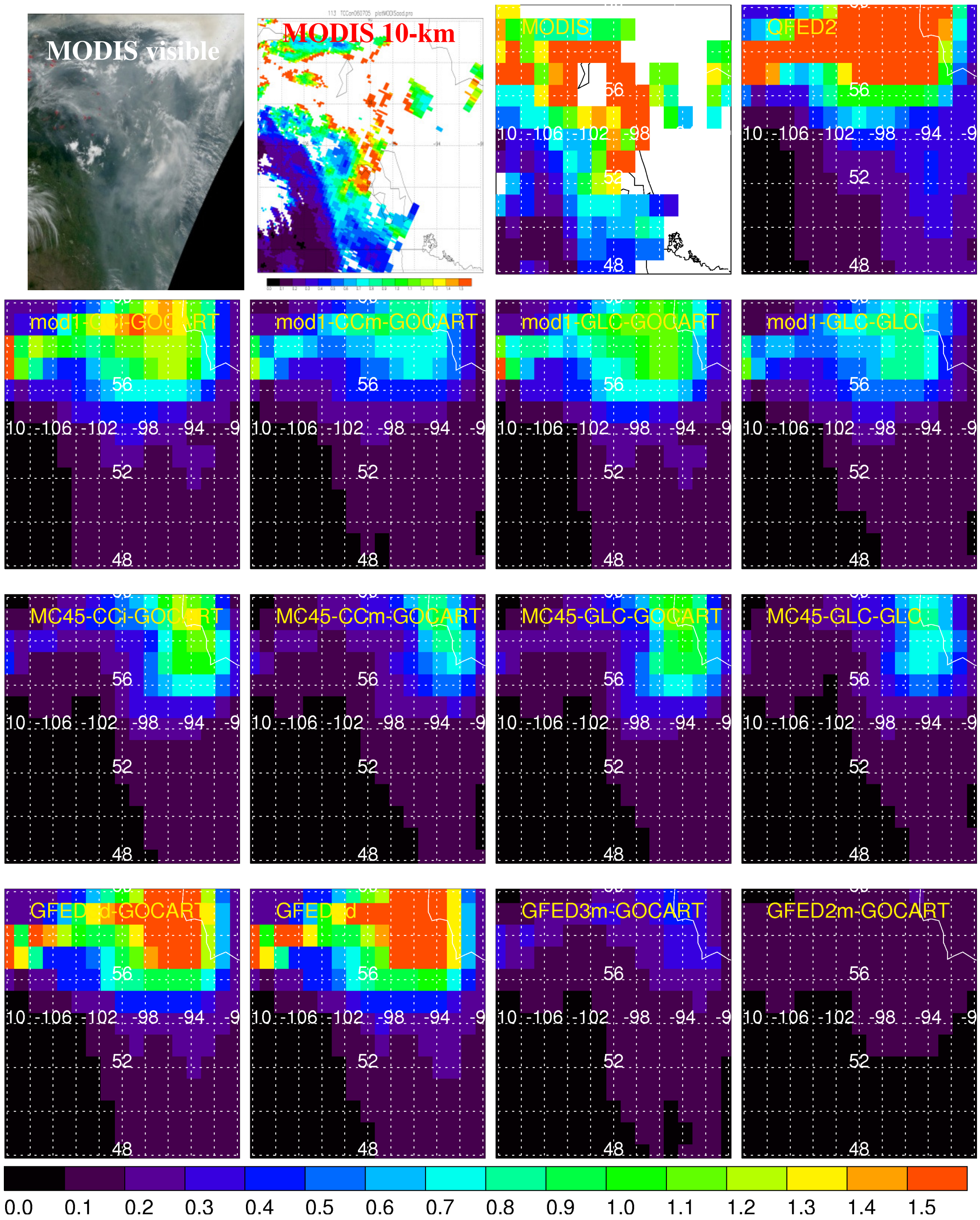

Figure A - 11 MODIS and GOCART AOD for case 113

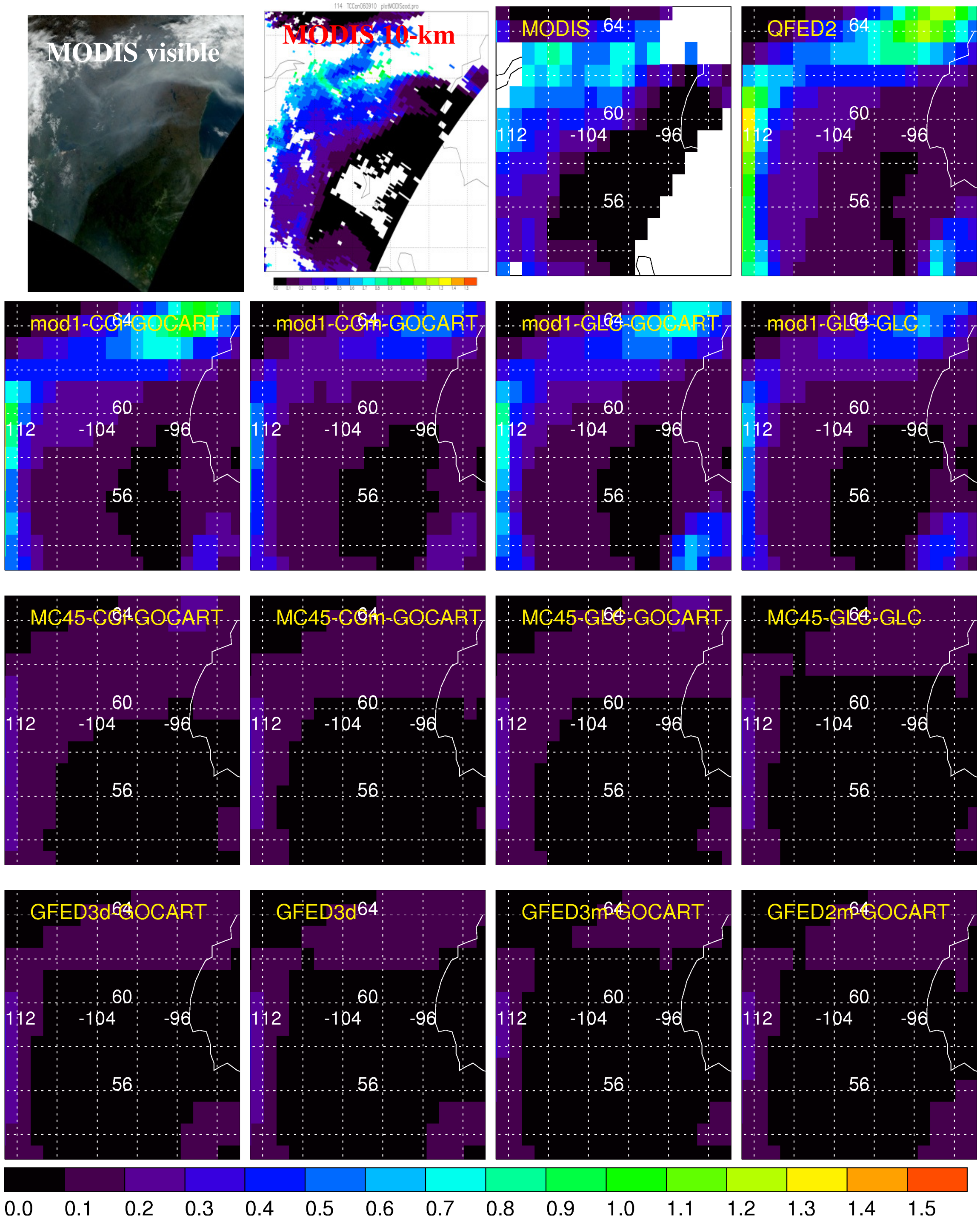

Figure A - 12 MODIS and GOCART AOD for case 114

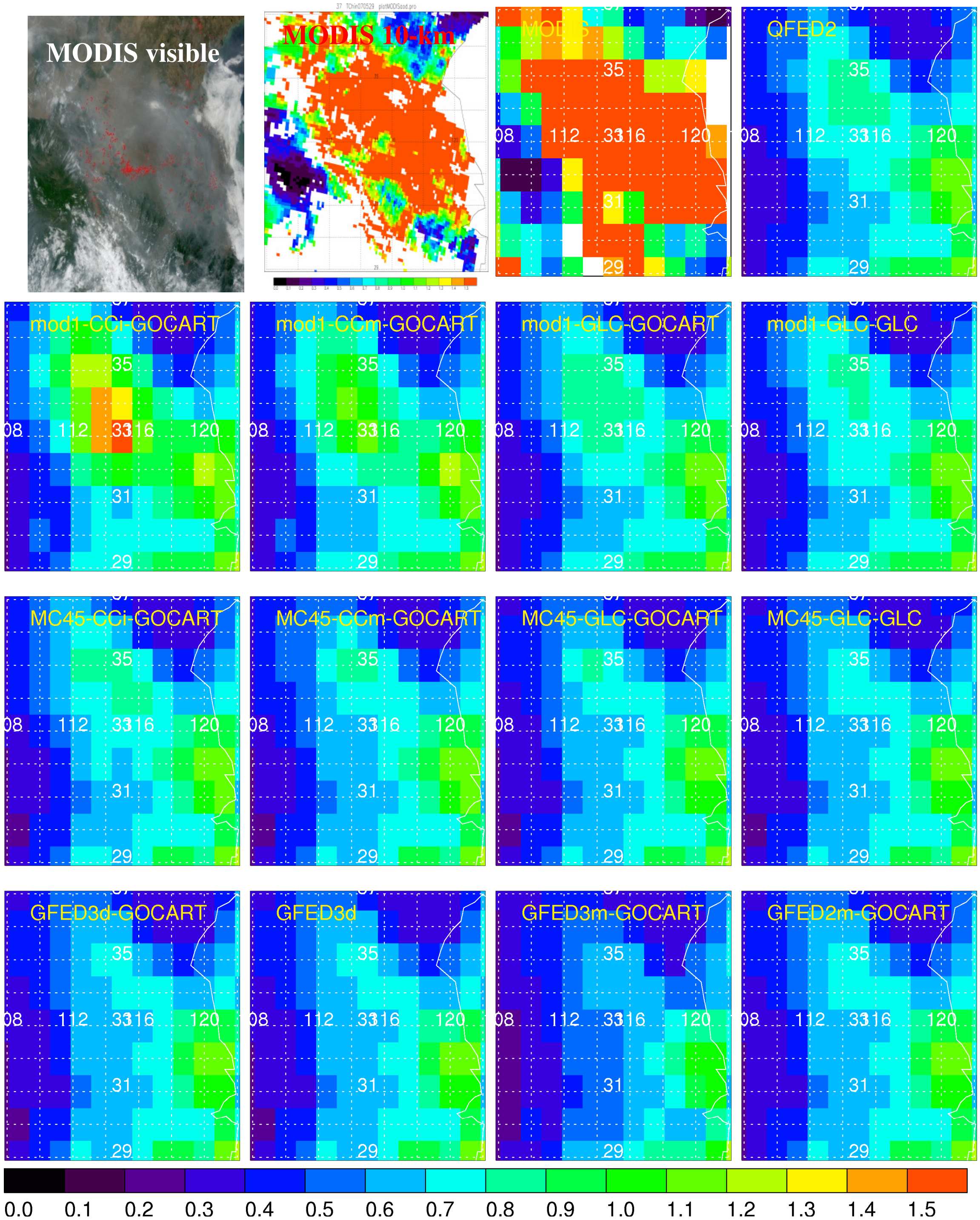

Figure A - 13 MODIS and GOCART AOD for case 37

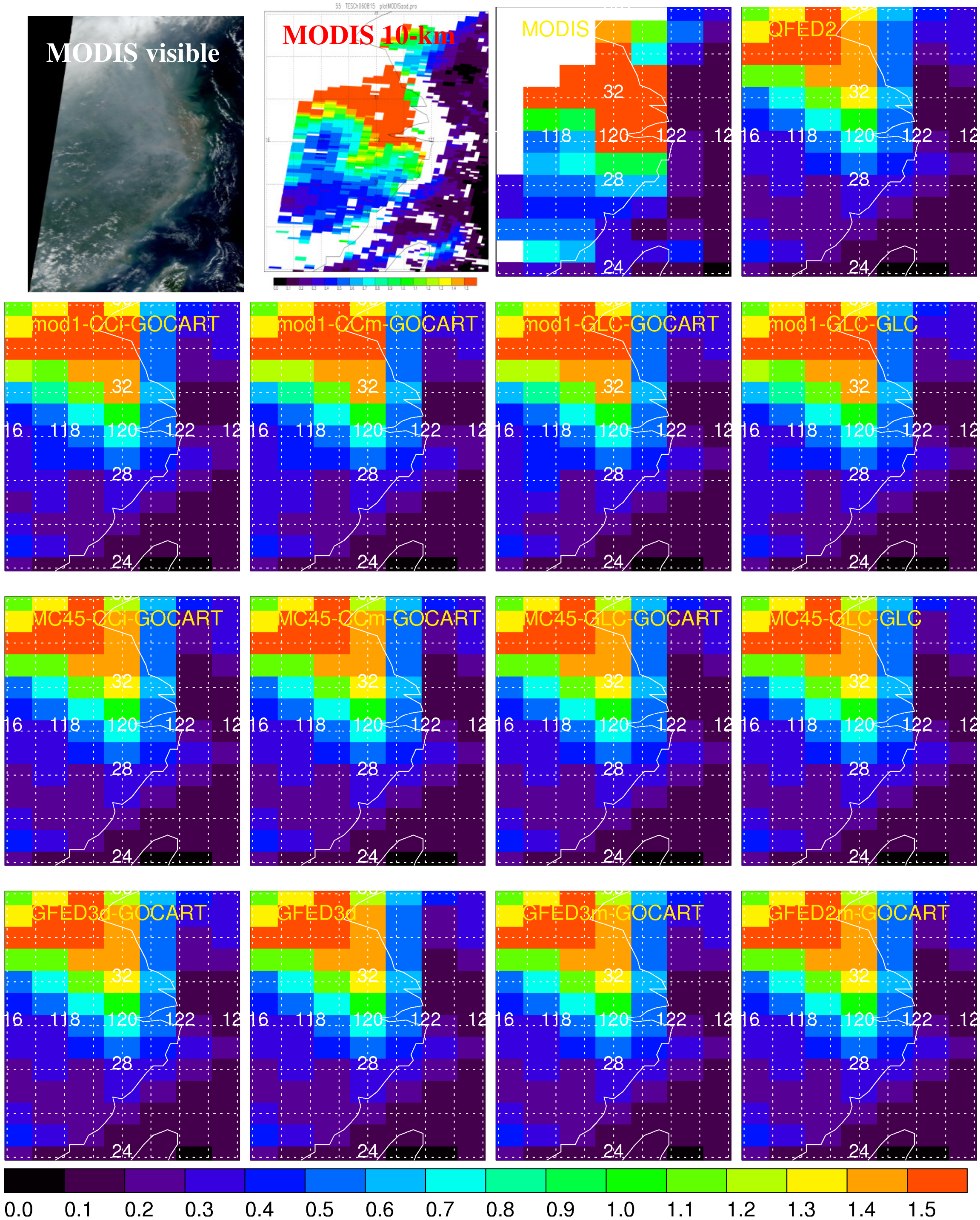

Figure A - 14 MODIS and GOCART AOD for case 55

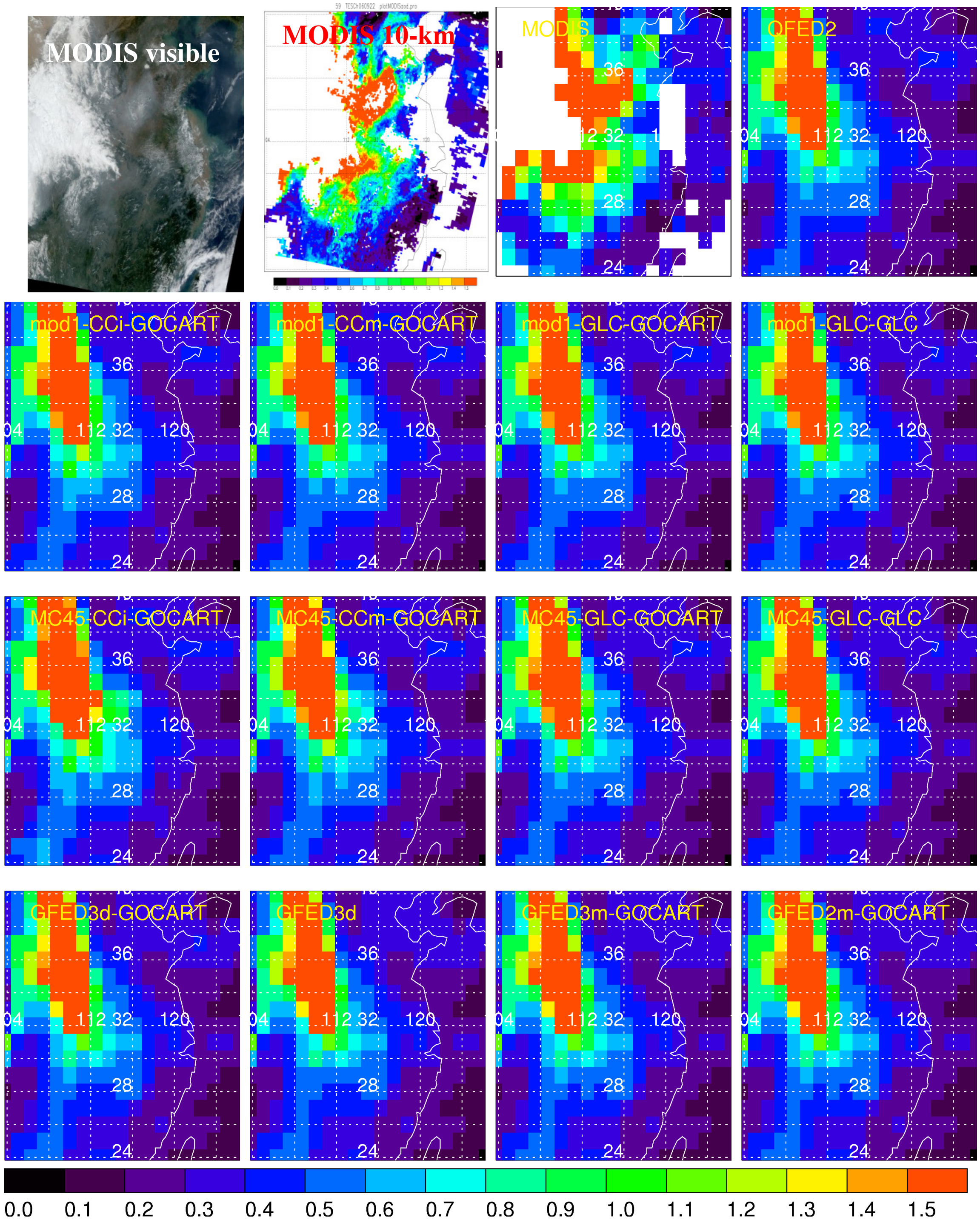

Figure A - 15 MODIS and GOCART AOD for case 59

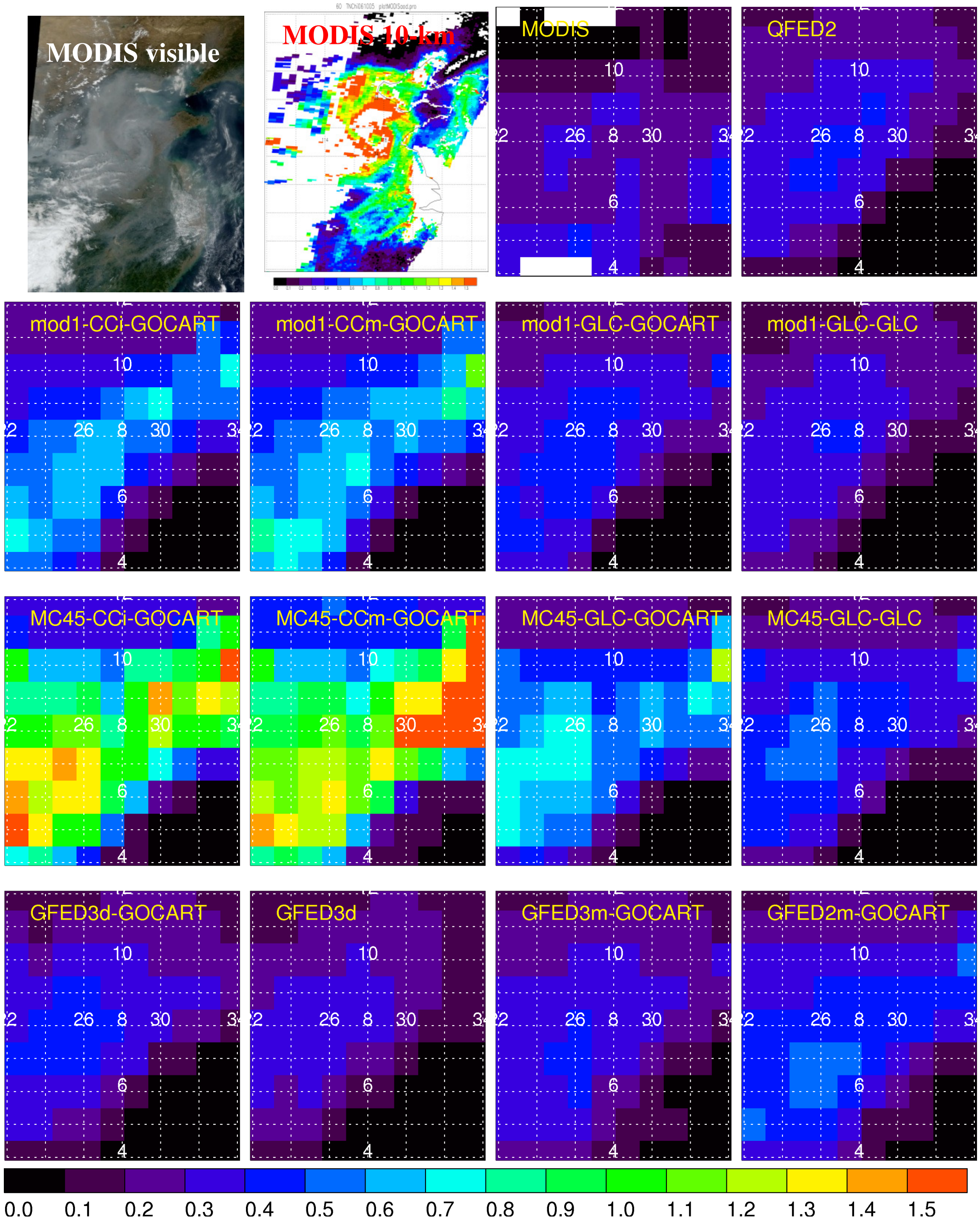

Figure A - 16 MODIS and GOCART AOD for case 60

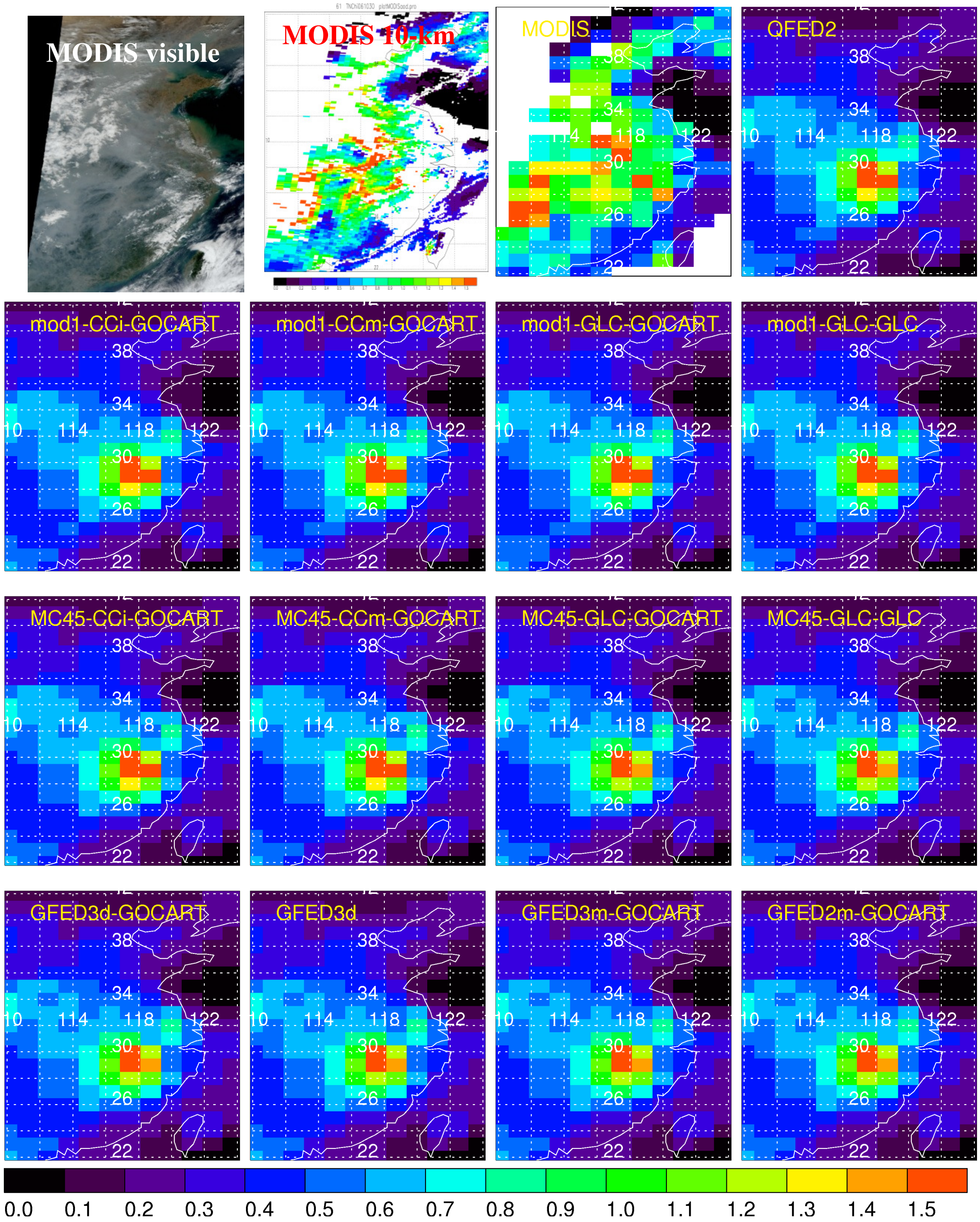

Figure A - 17 MODIS and GOCART AOD for case 61

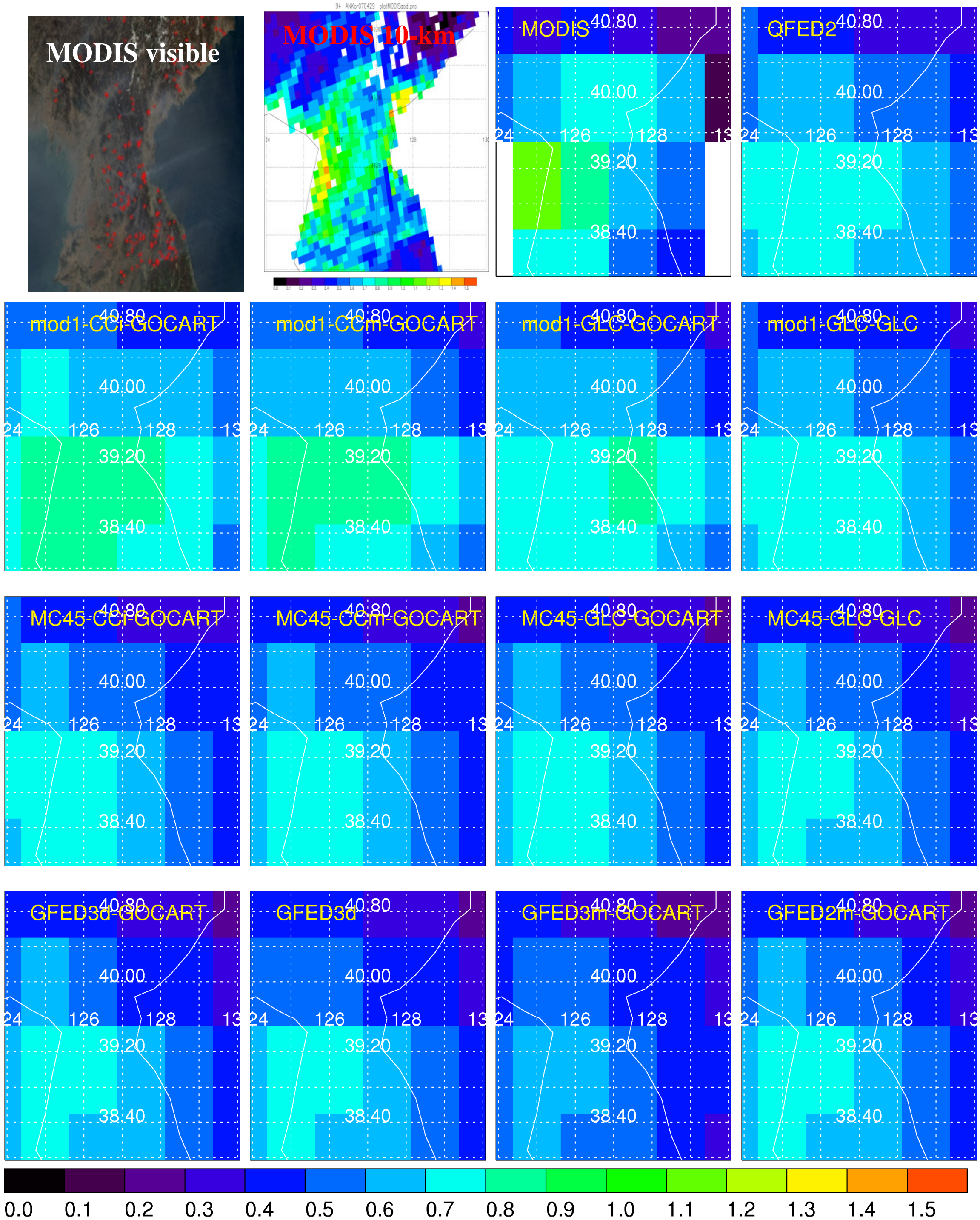

Figure A - 18 MODIS and GOCART AOD for case 94

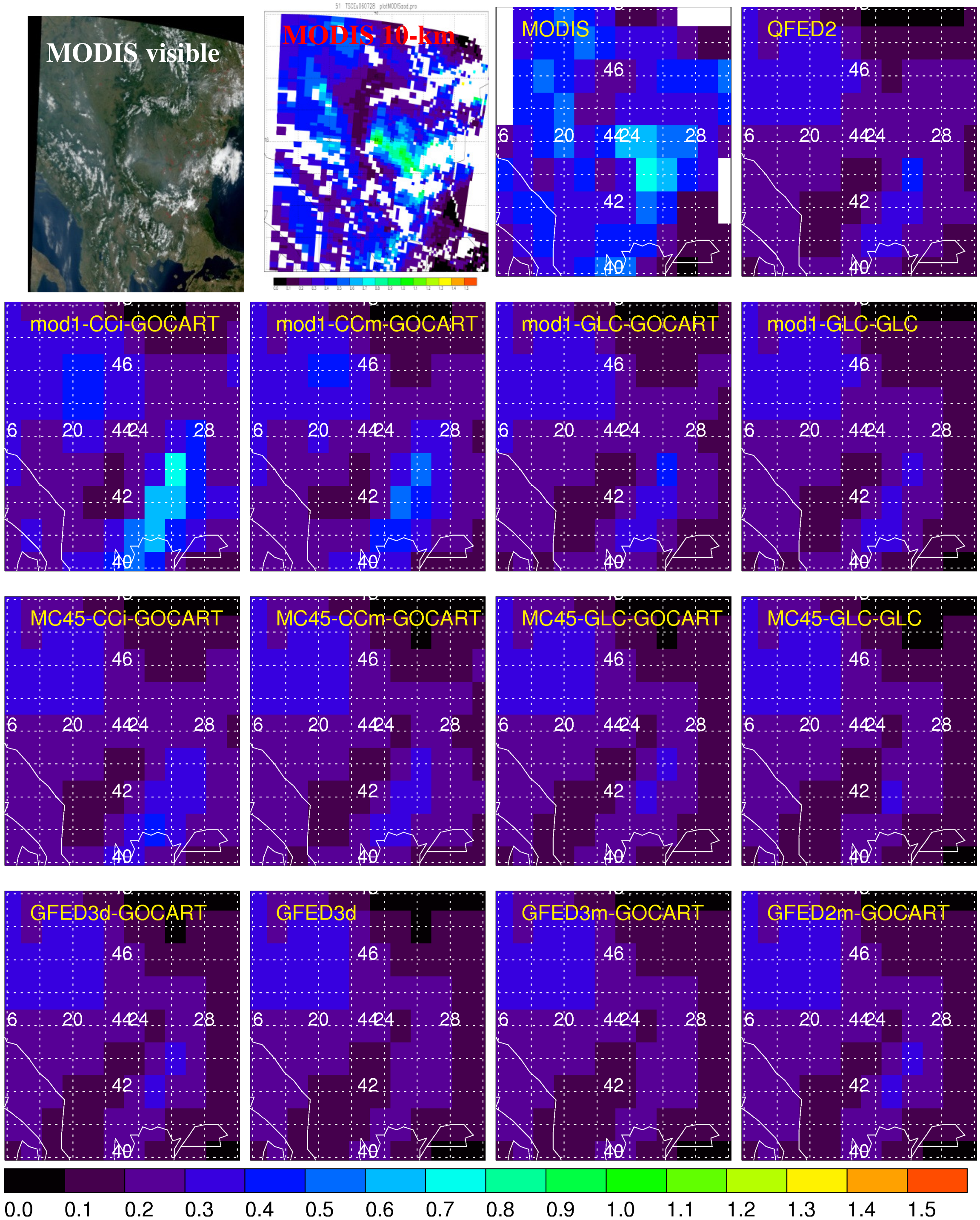

Figure A - 19 MODIS and GOCART AOD for case 51

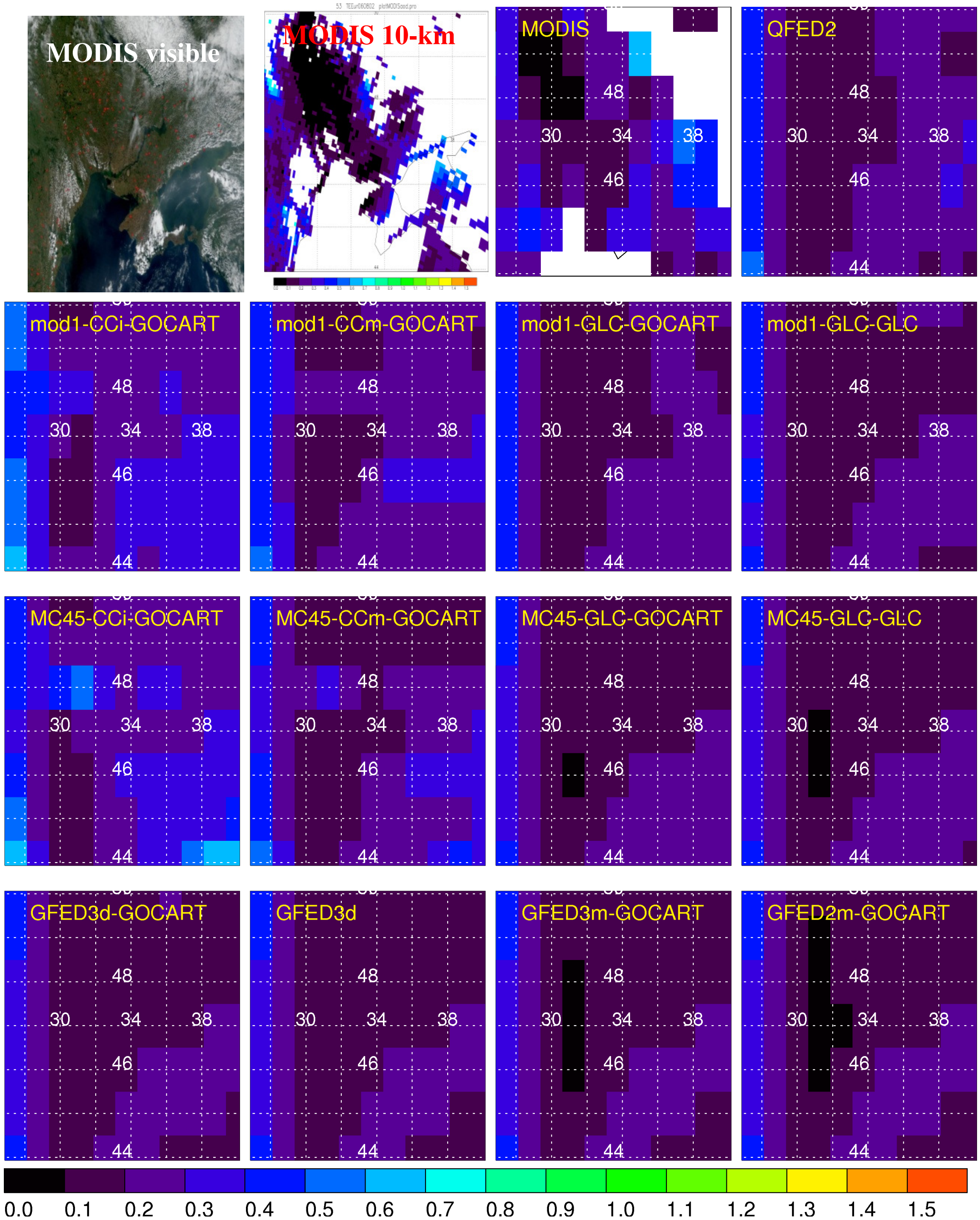

Figure A - 20 MODIS and GOCART AOD for case 53

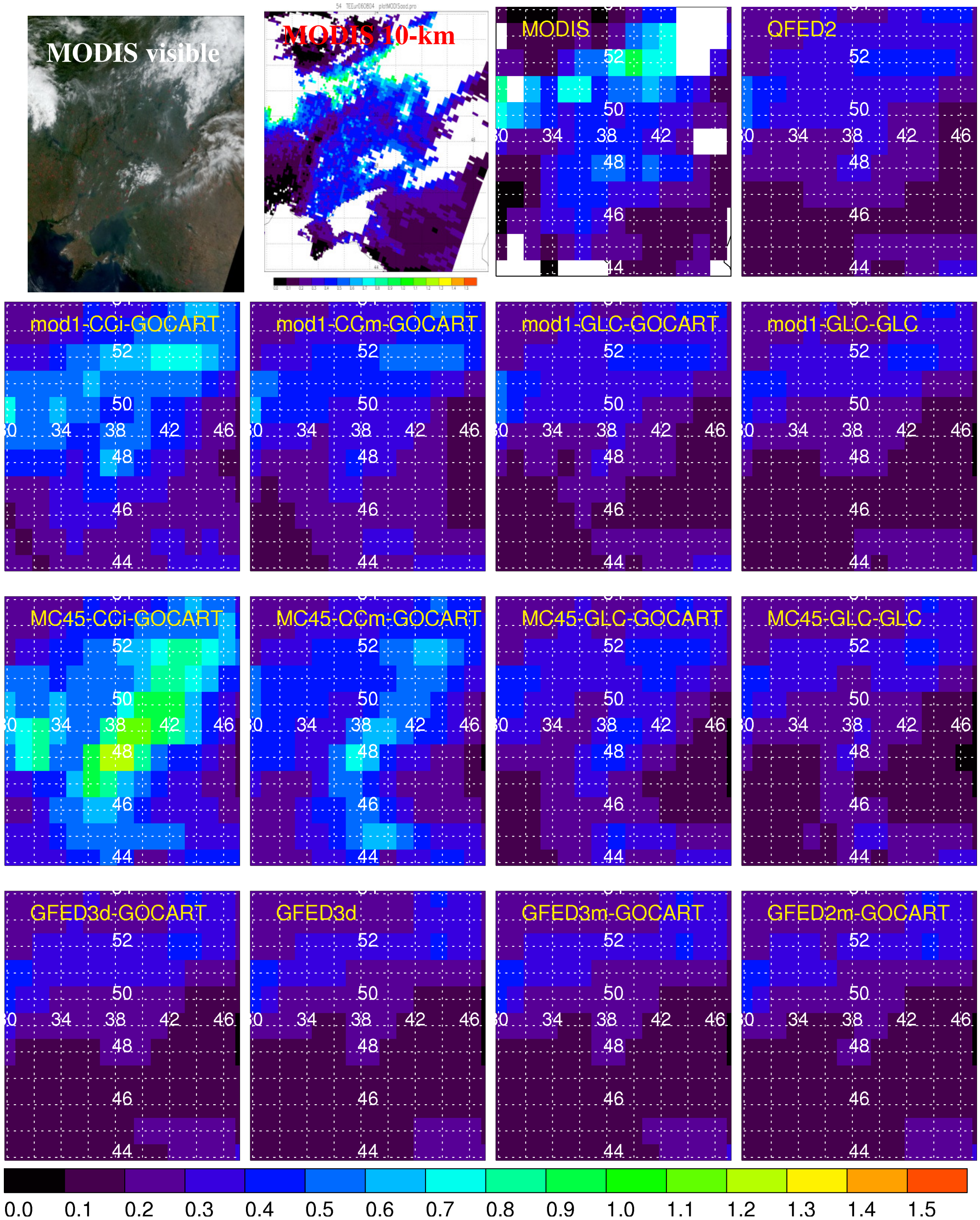

Figure A - 21 MODIS and GOCART AOD for case 54

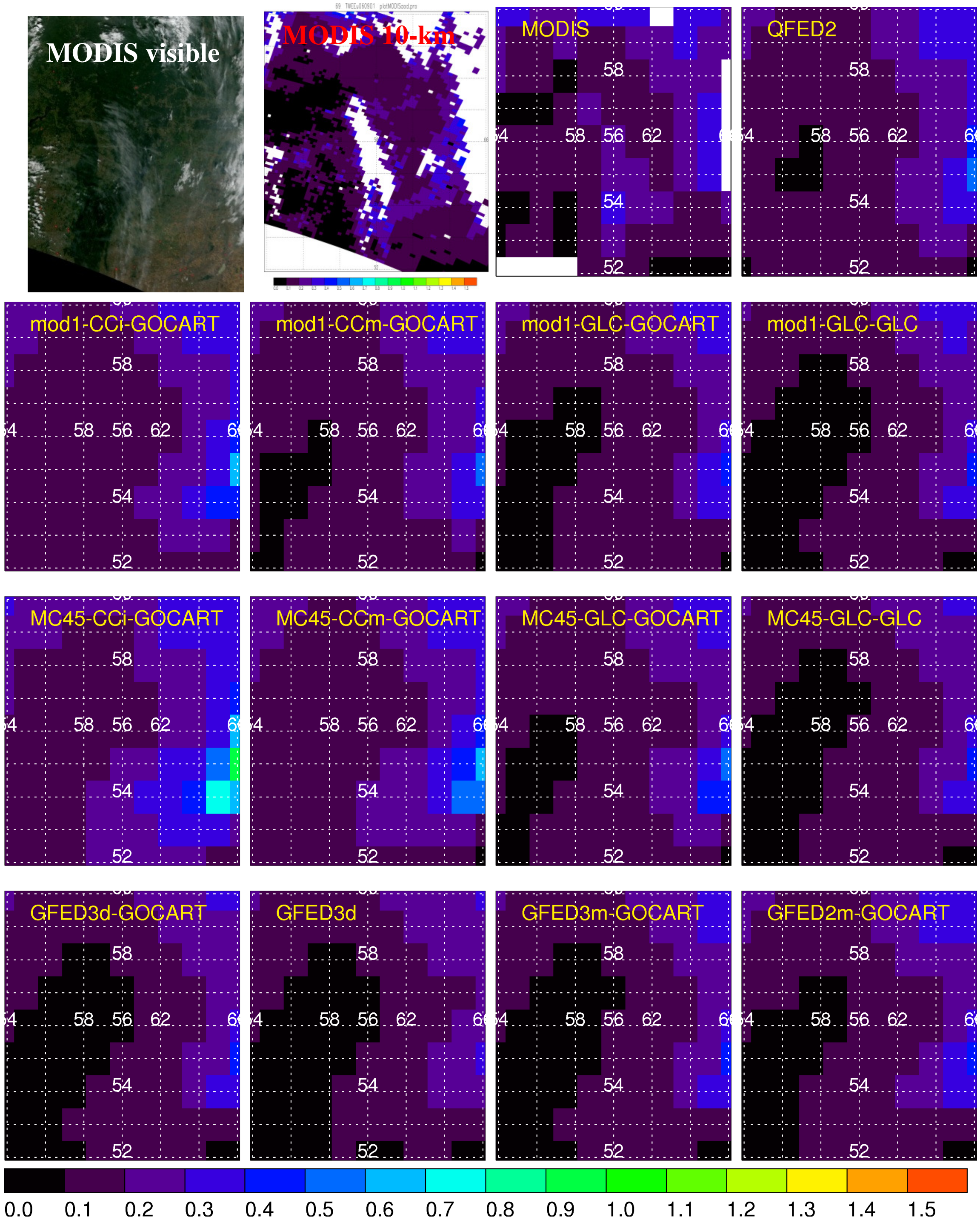

Figure A - 22 MODIS and GOCART AOD for case 69

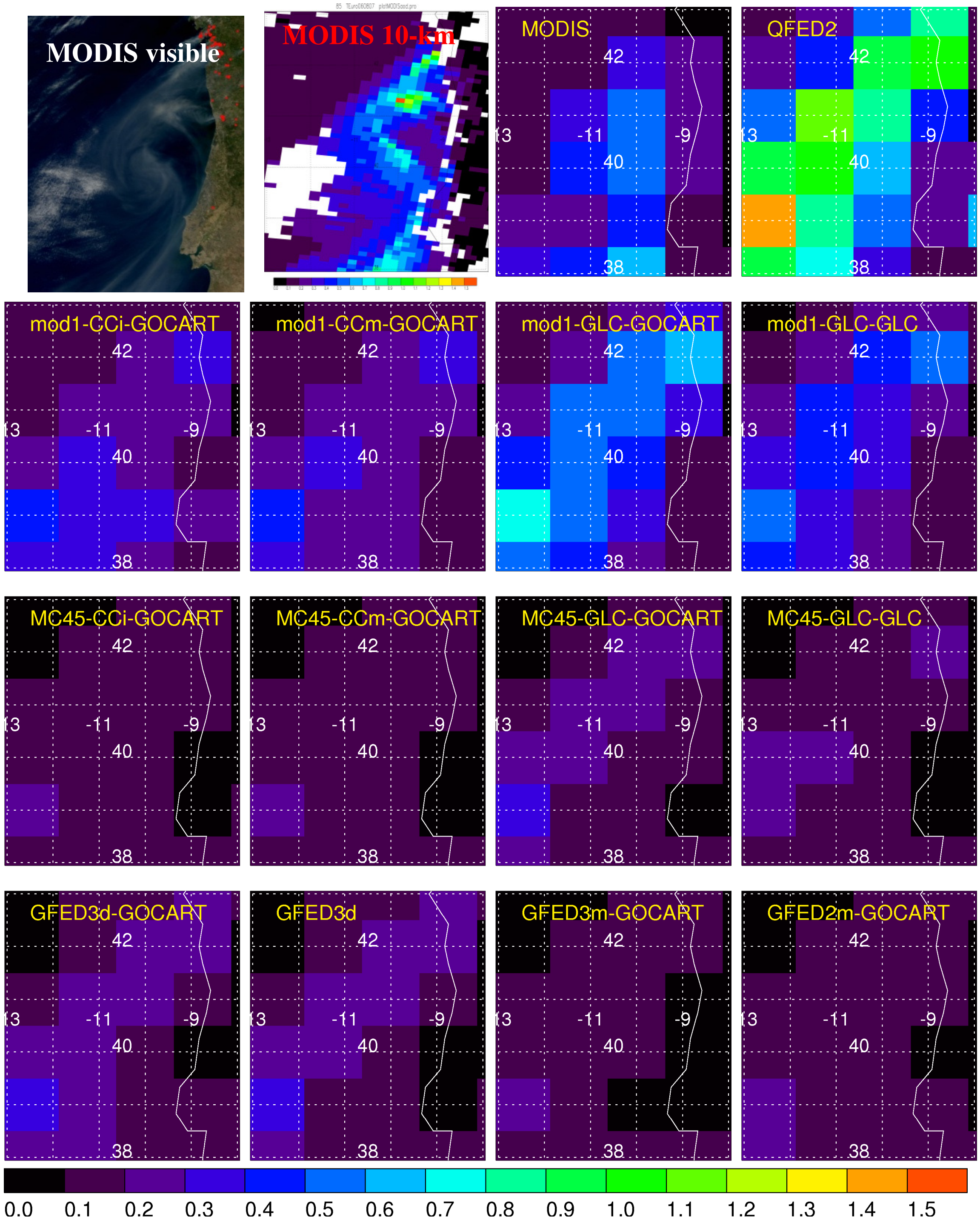

Figure A - 23 MODIS and GOCART AOD for case 85

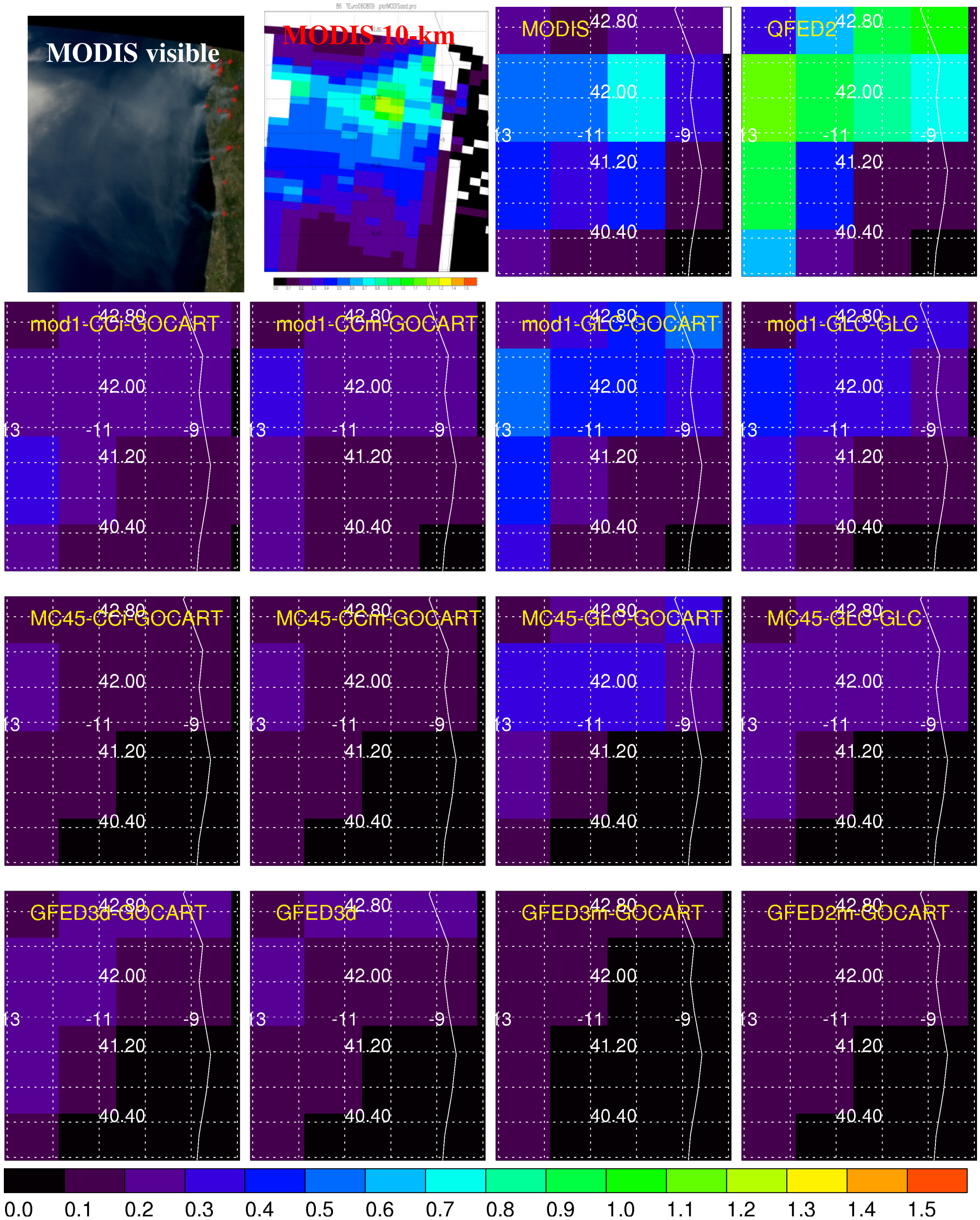

Figure A - 24 MODIS and GOCART AOD for case 86

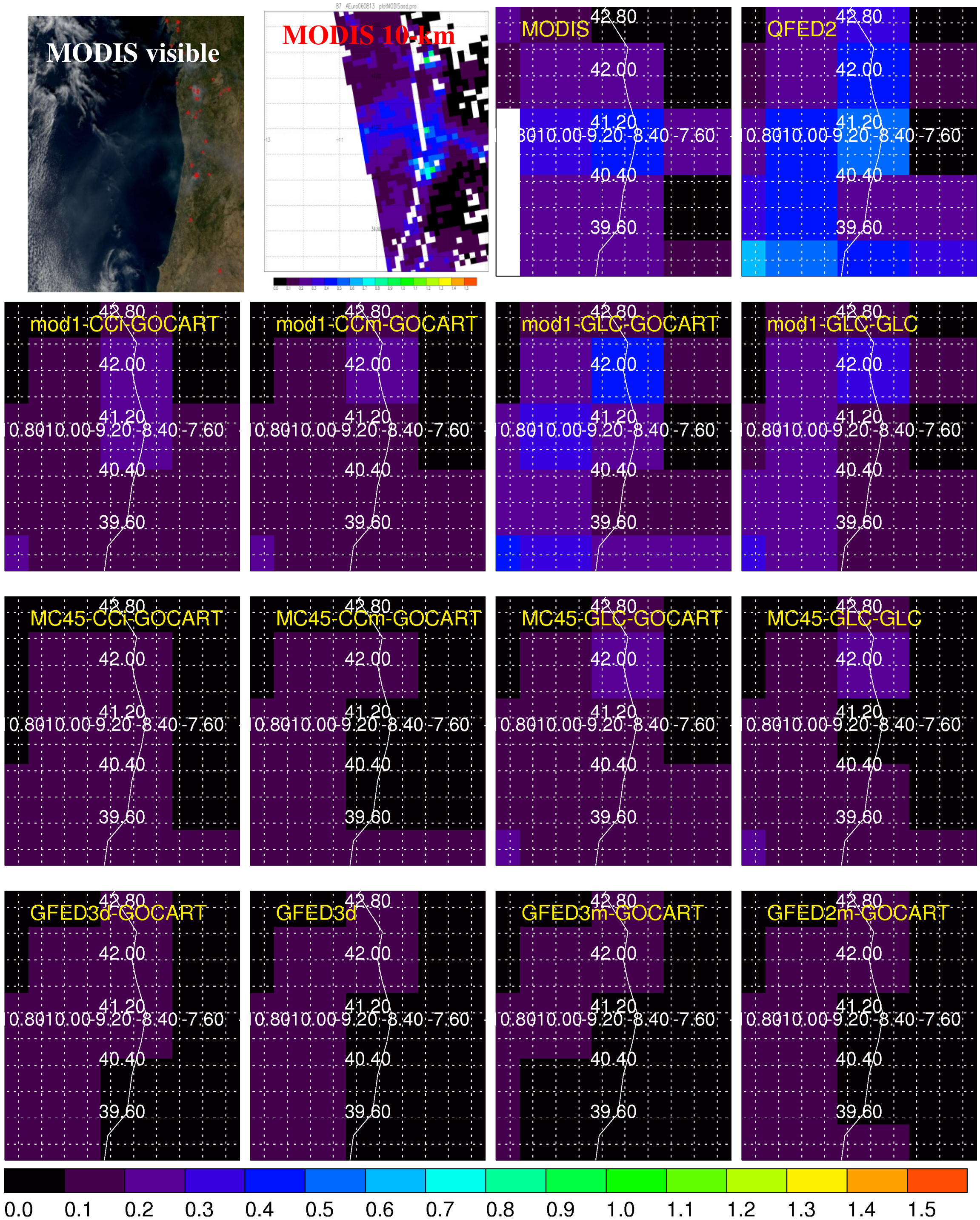

Figure A - 25 MODIS and GOCART AOD for case 87

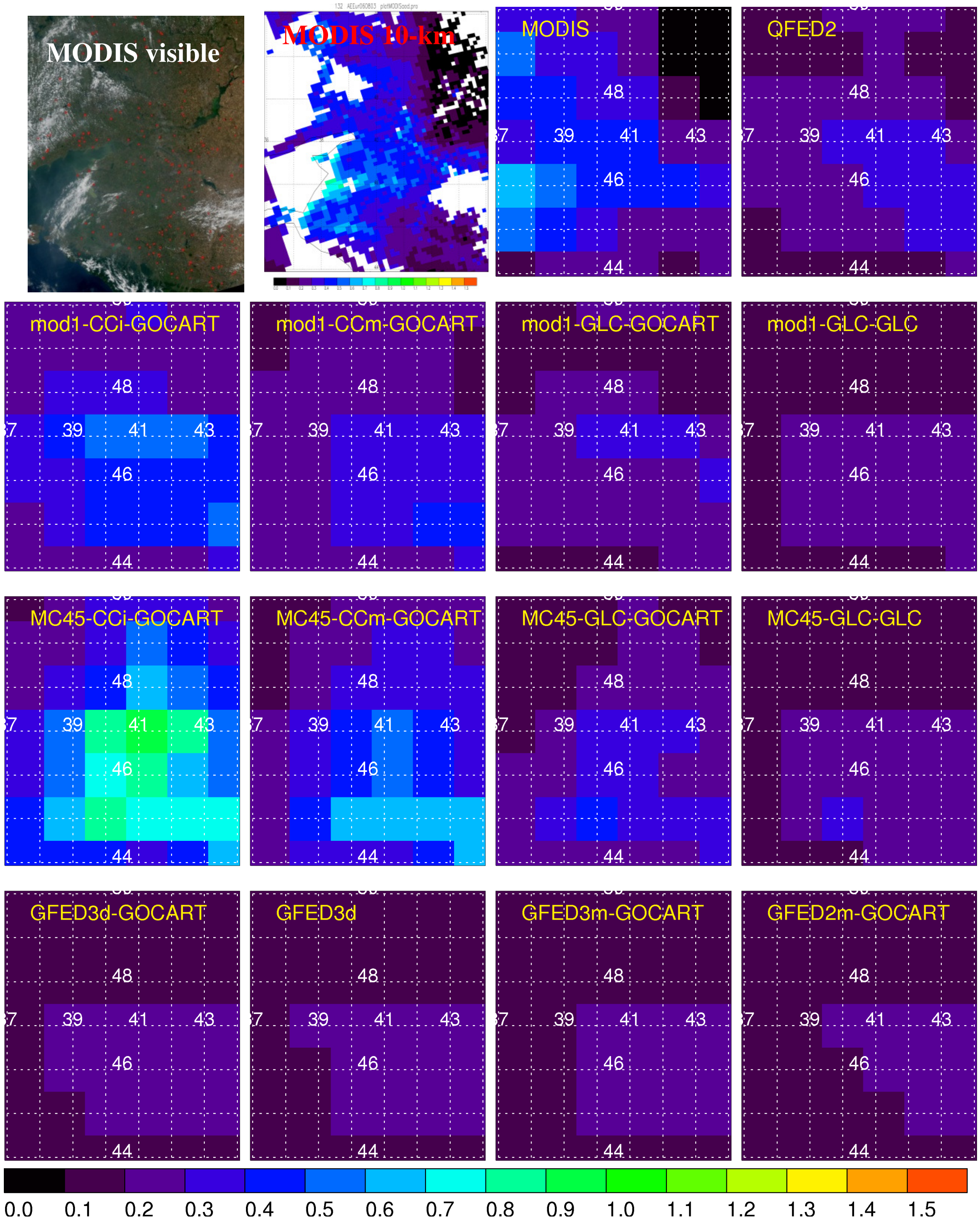

Figure A - 26 MODIS and GOCART AOD for case 132

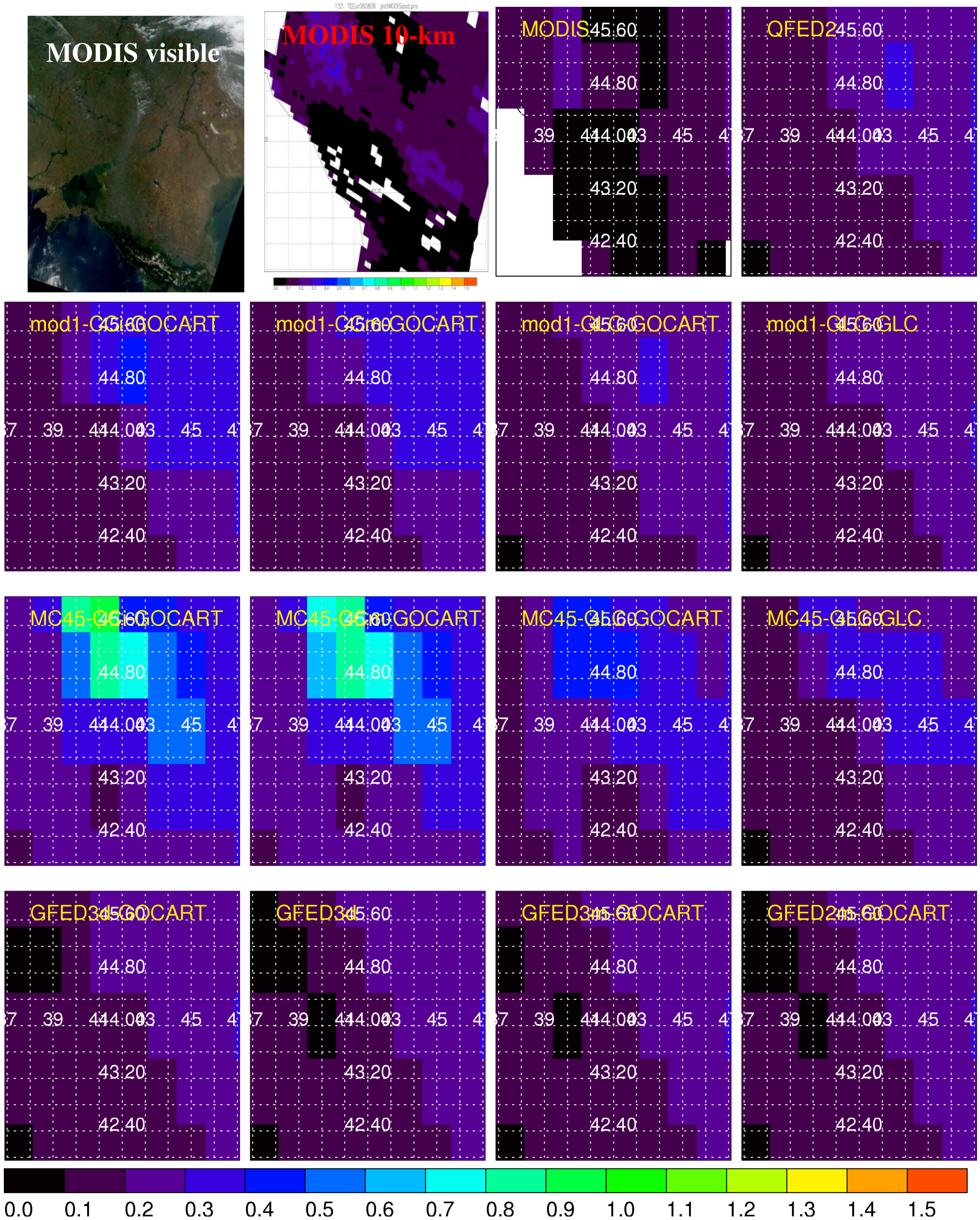

Figure A - 27 MODIS and GOCART AOD for case 133

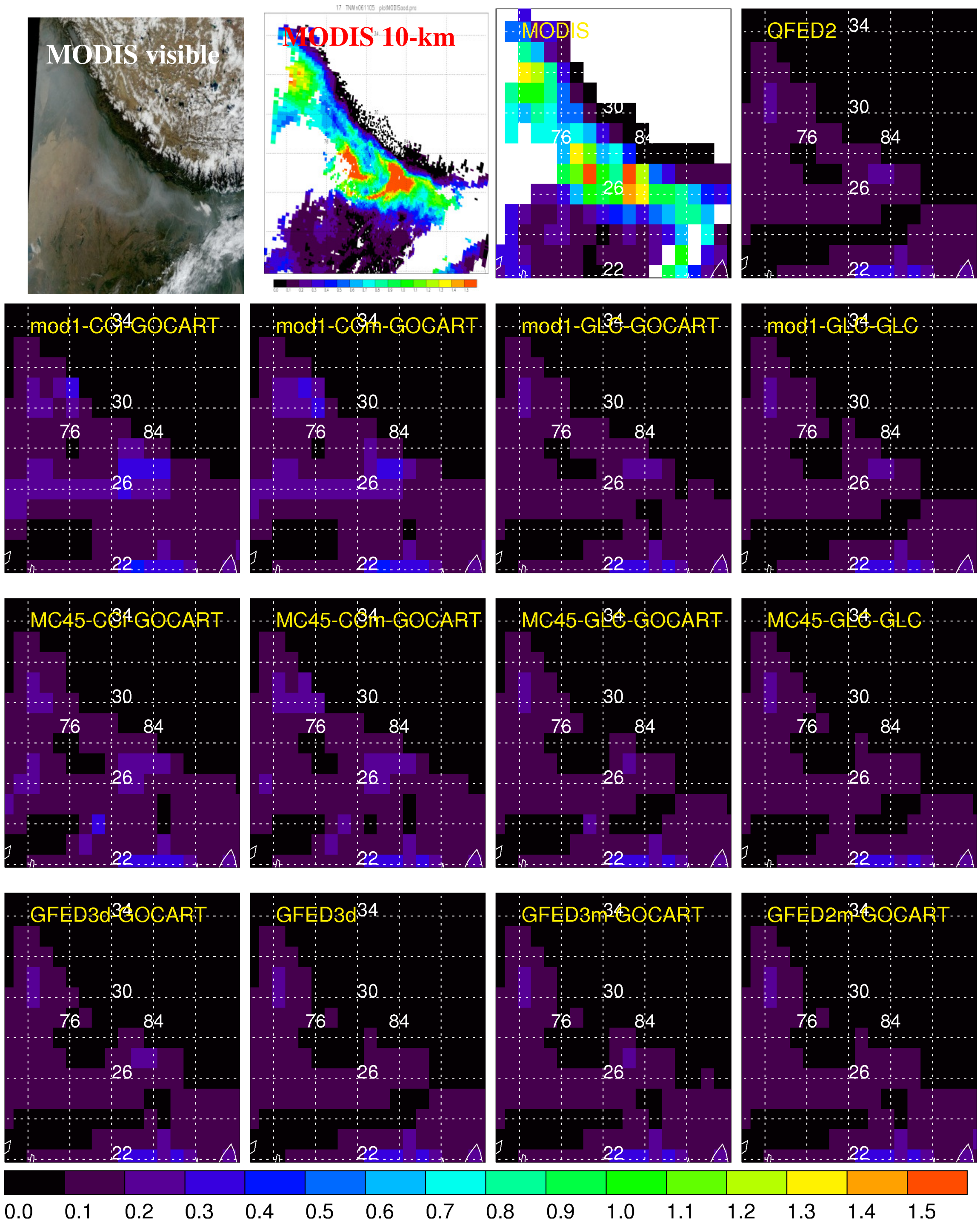

Figure A - 28 MODIS and GOCART AOD for case 17

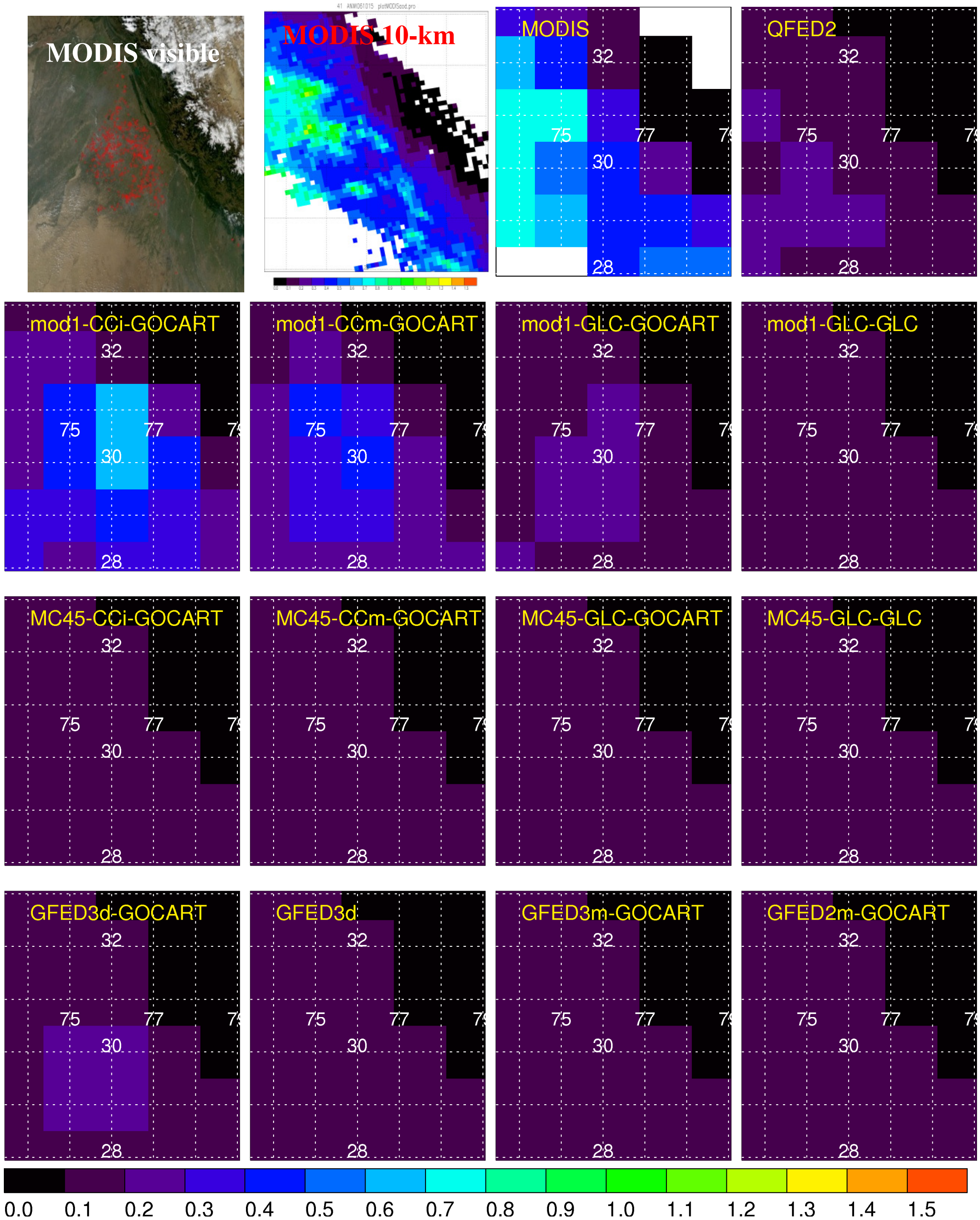

Figure A - 29 MODIS and GOCART AOD for case 41

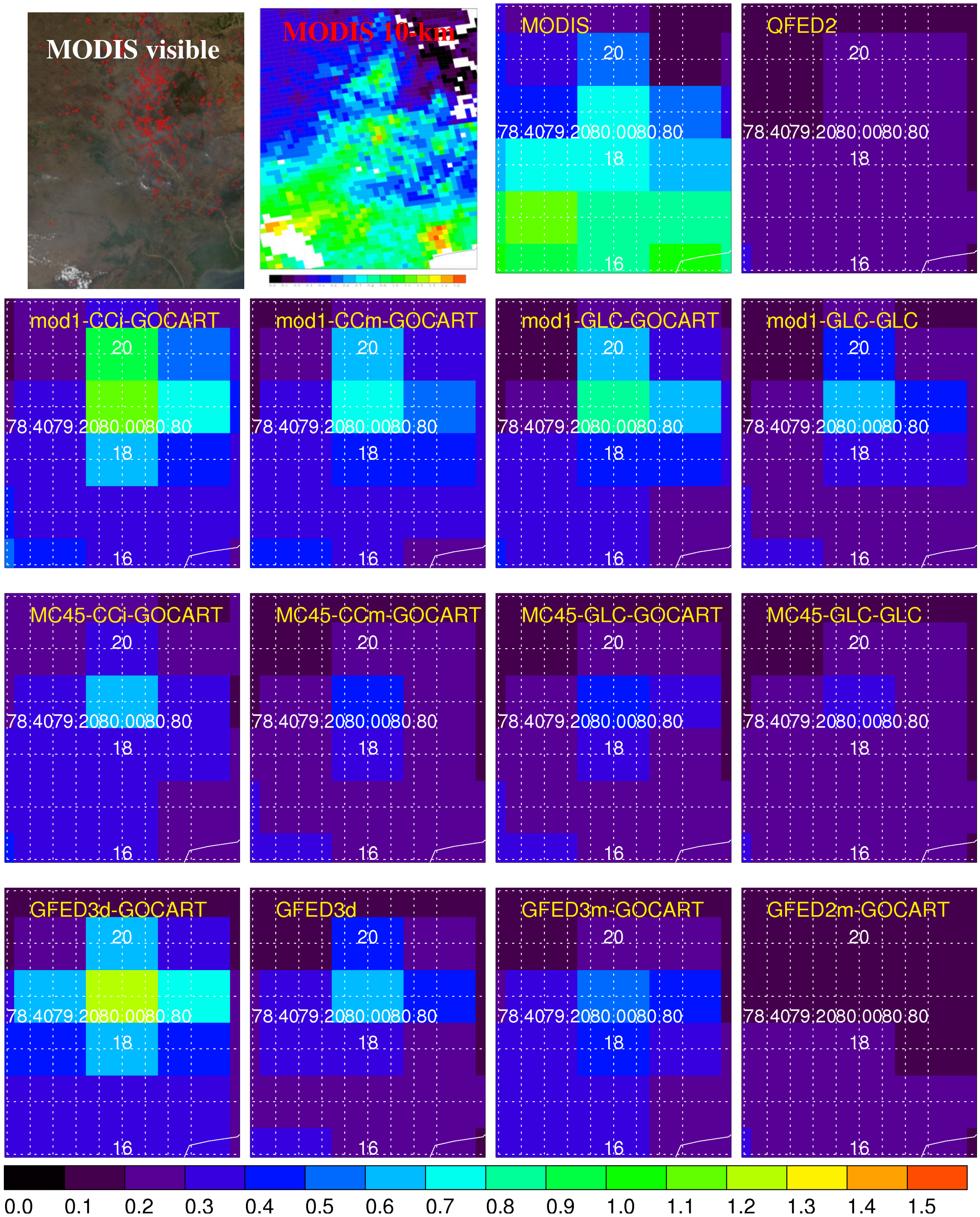

Figure A - 30 MODIS and GOCART AOD for case 123

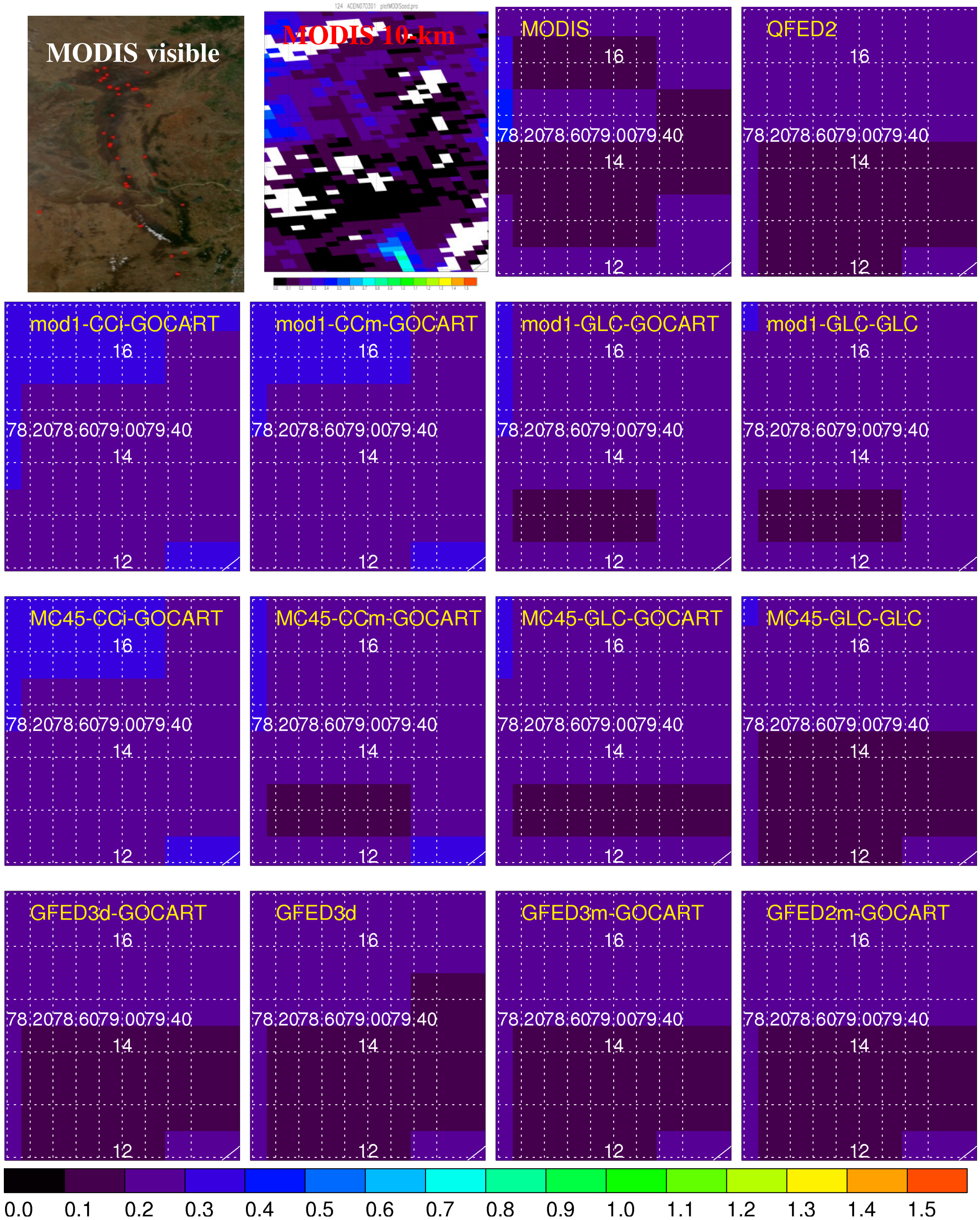

Figure A - 31 MODIS and GOCART AOD for case 124

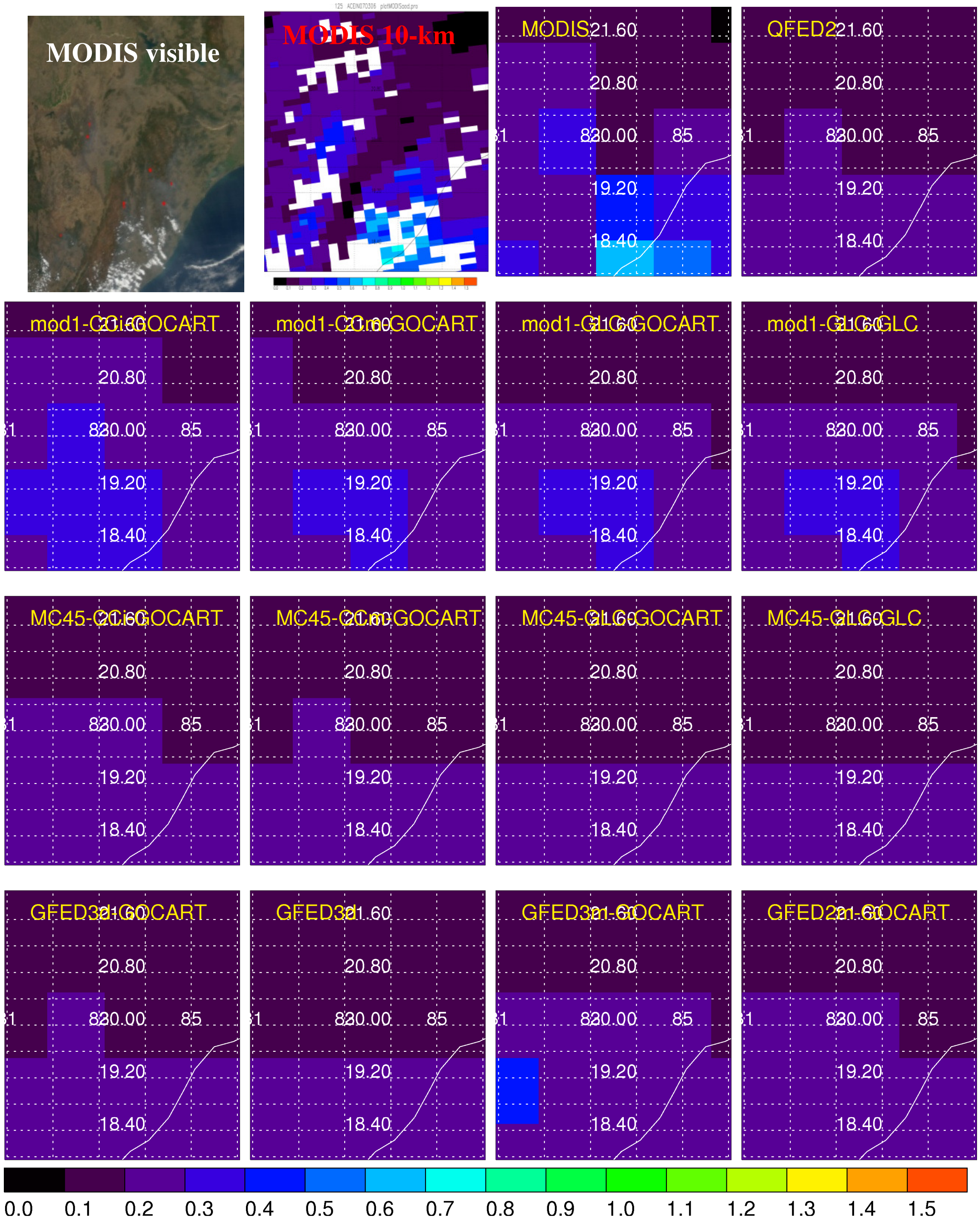

Figure A - 32 MODIS and GOCART AOD for case 125

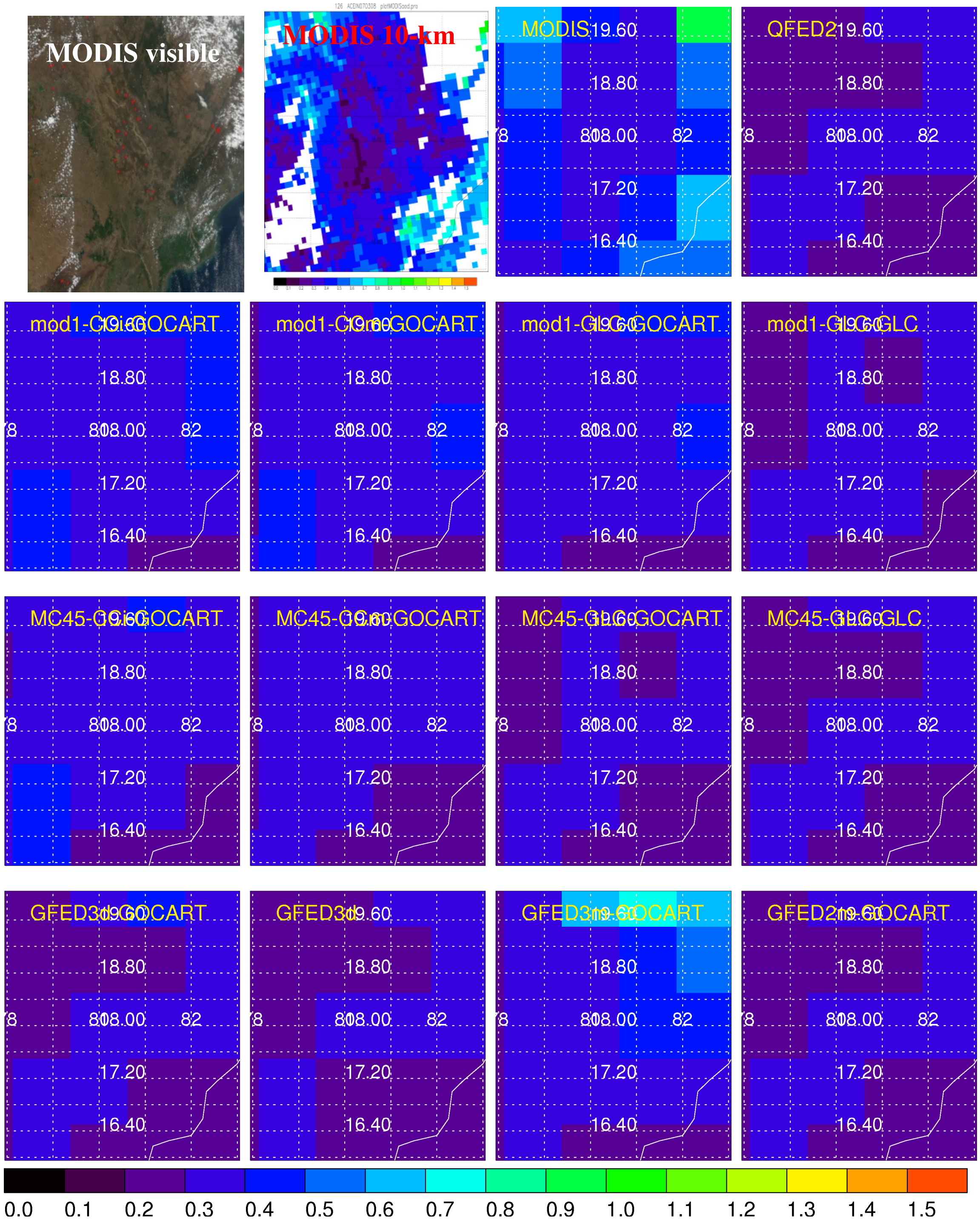

Figure A - 33 MODIS and GOCART AOD for case 126

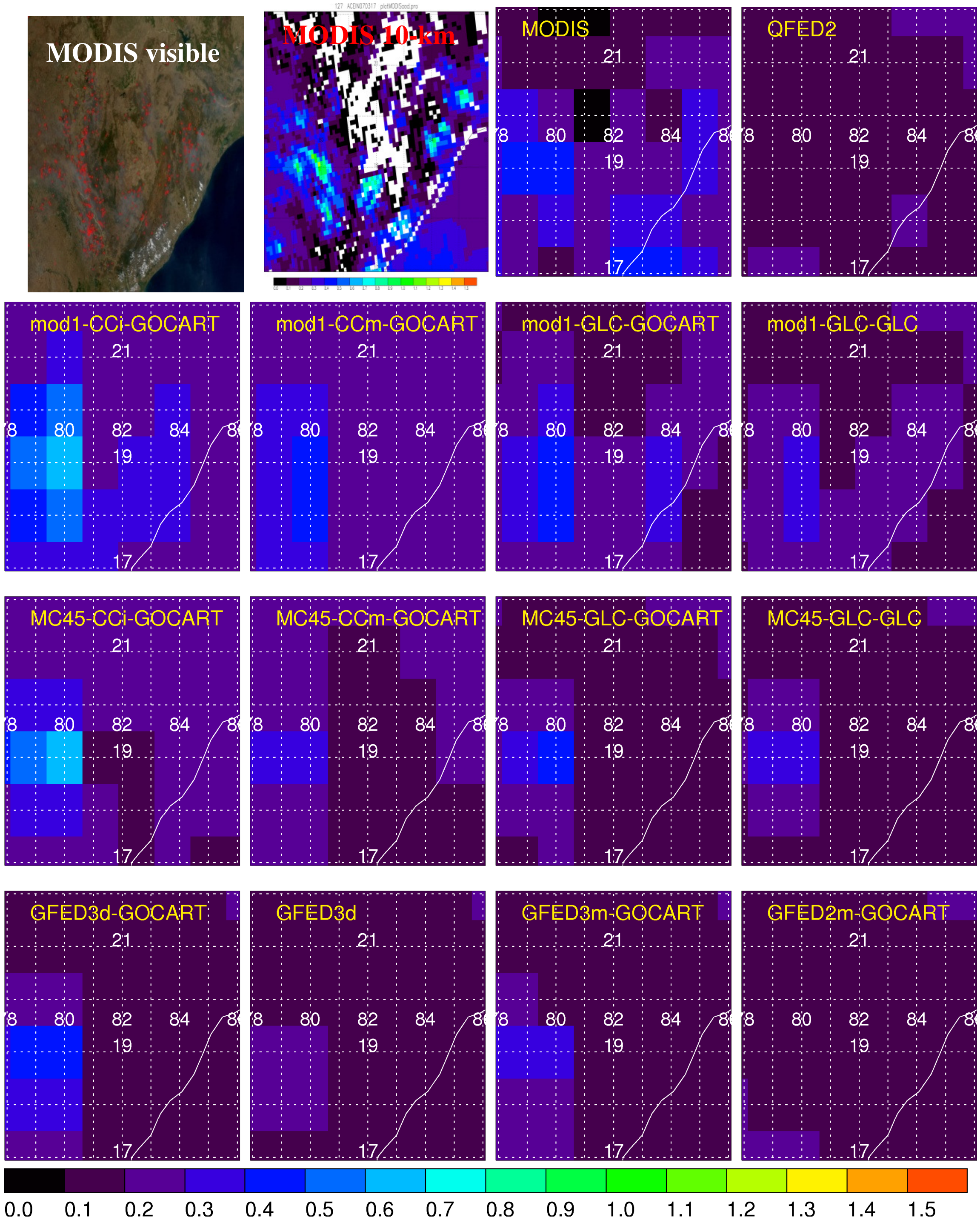

Figure A - 34 MODIS and GOCART AOD for case 127

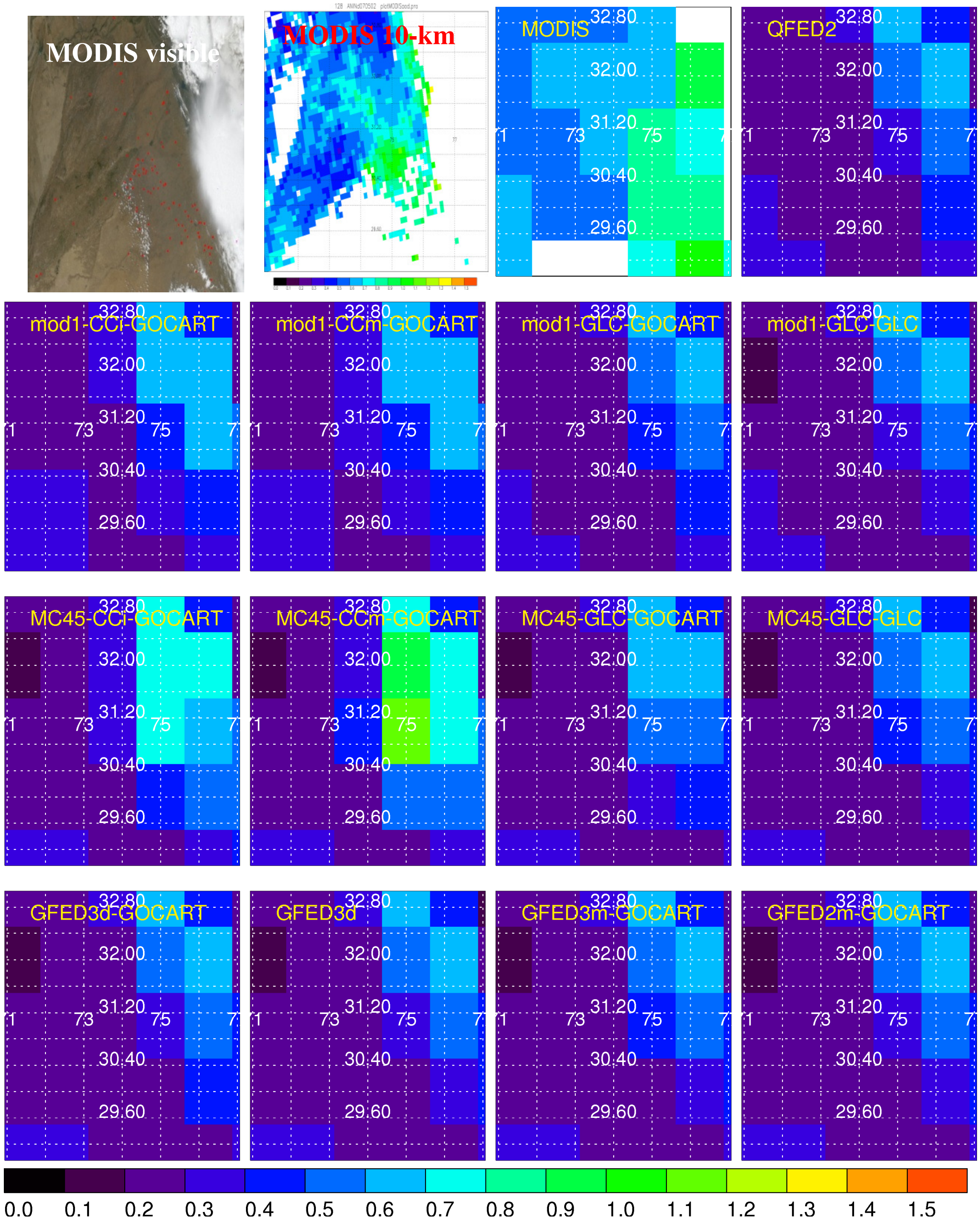

Figure A - 35 MODIS and GOCART AOD for case 128

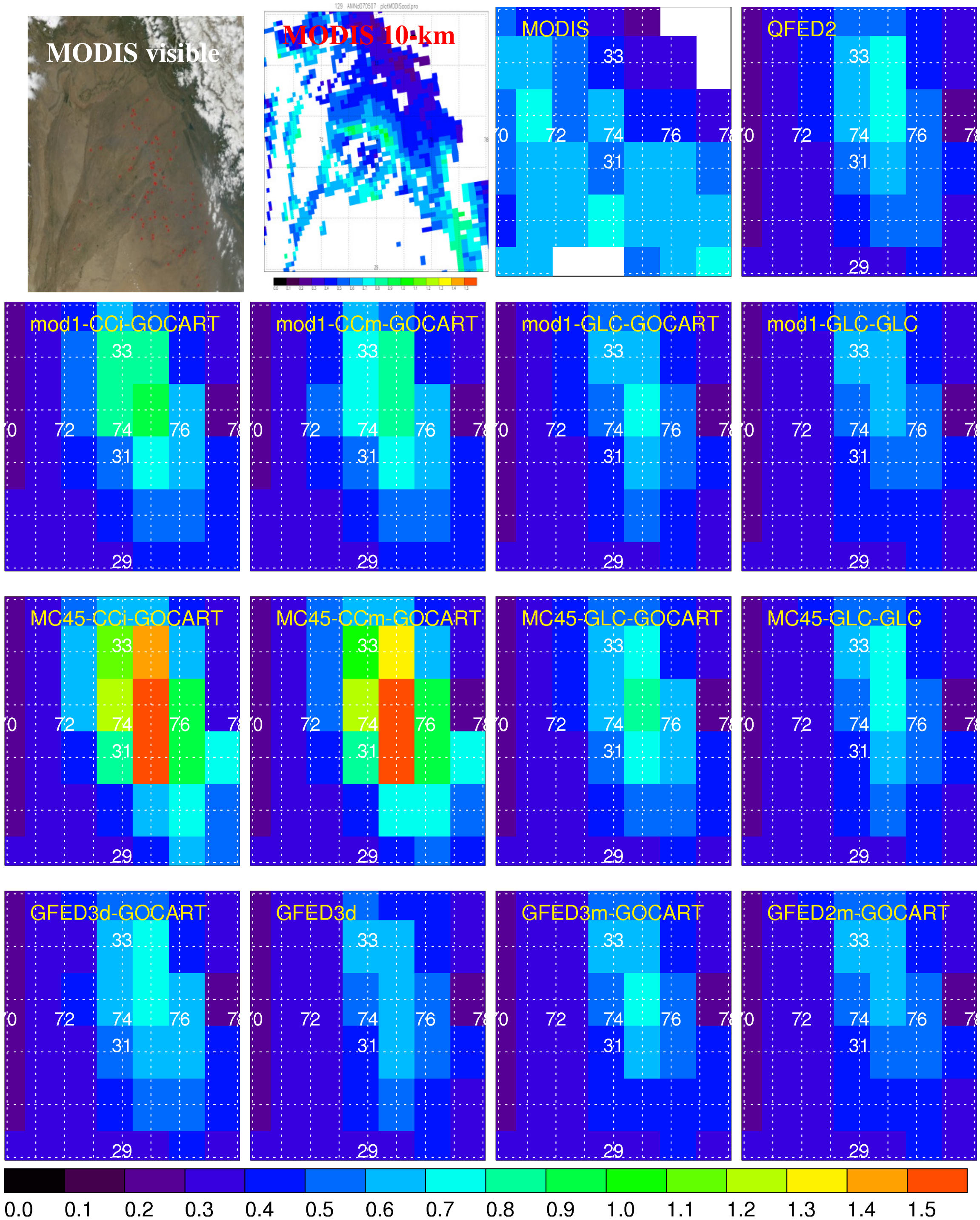

Figure A - 36 MODIS and GOCART AOD for case 129

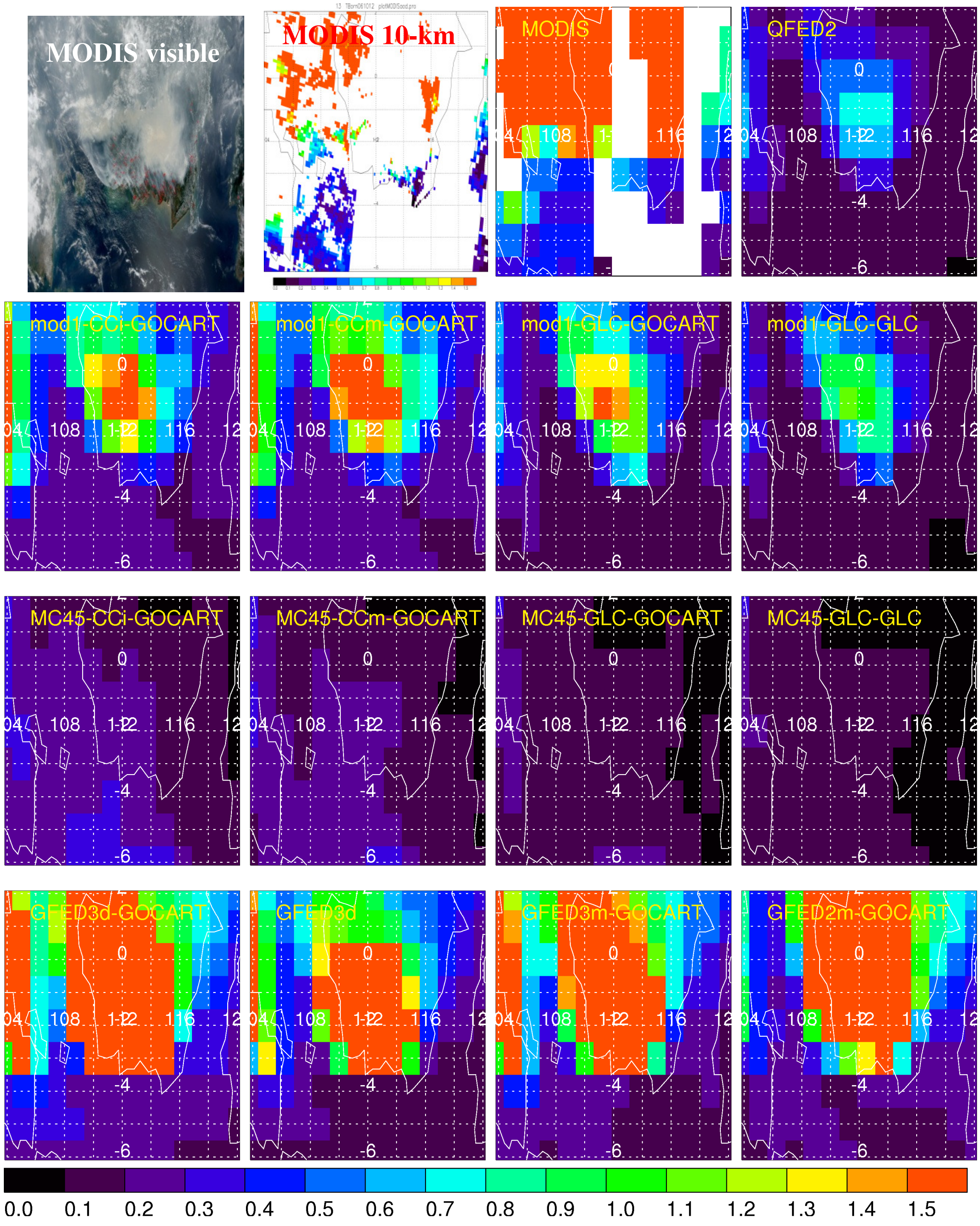

Figure A - 37 MODIS and GOCART AOD for case 13

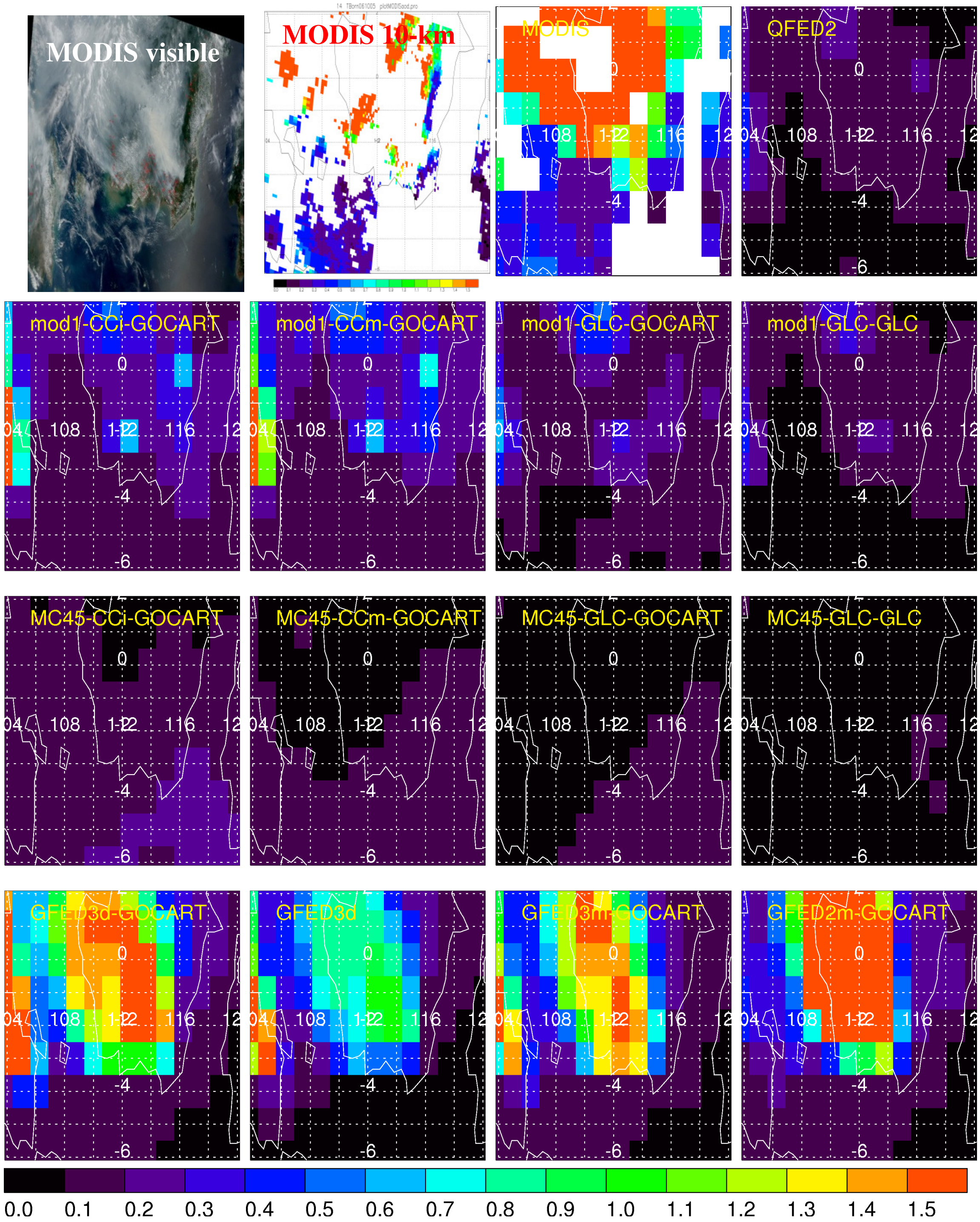

Figure A - 38 MODIS and GOCART AOD for case 14

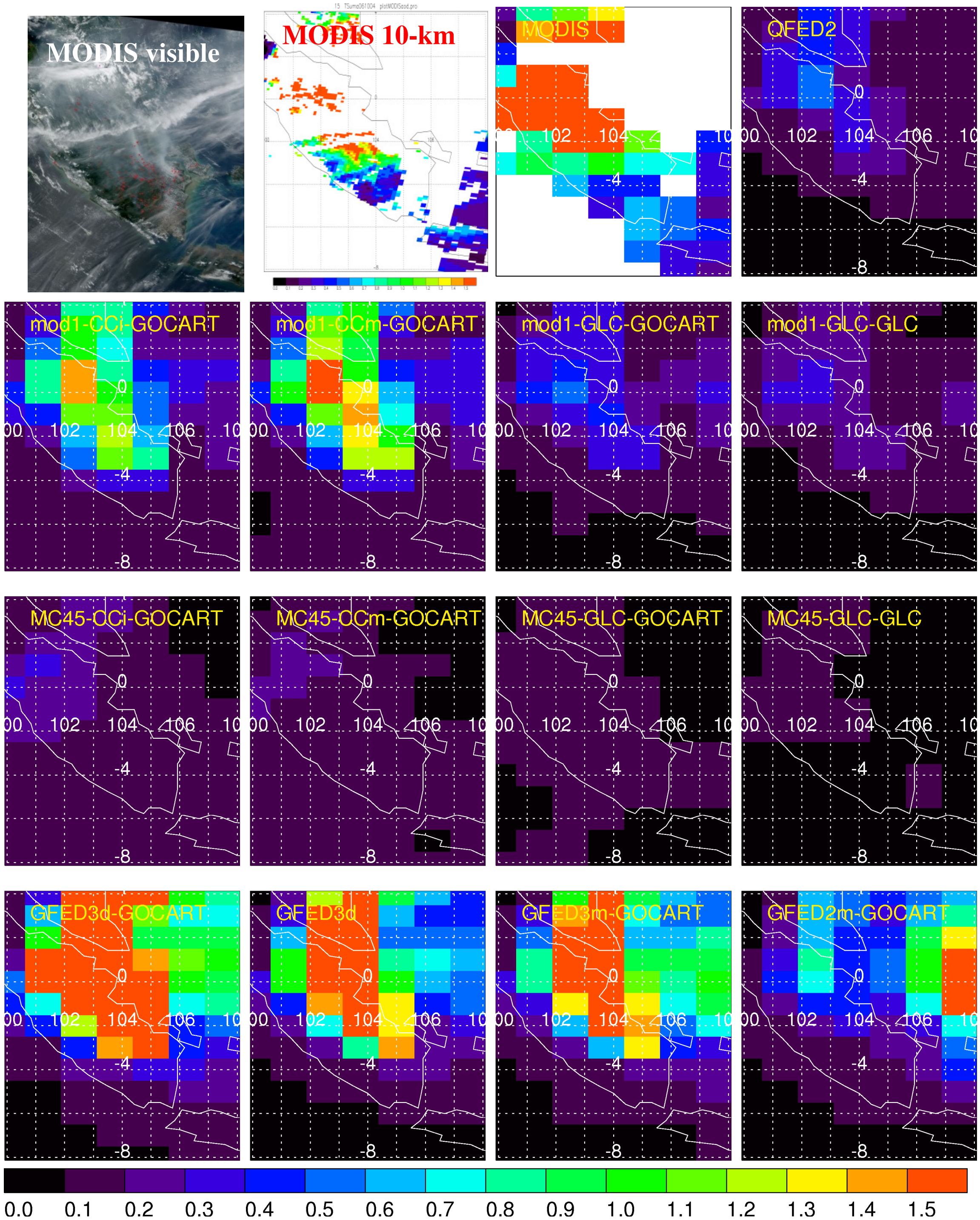

Figure A - 39 MODIS and GOCART AOD for case 15

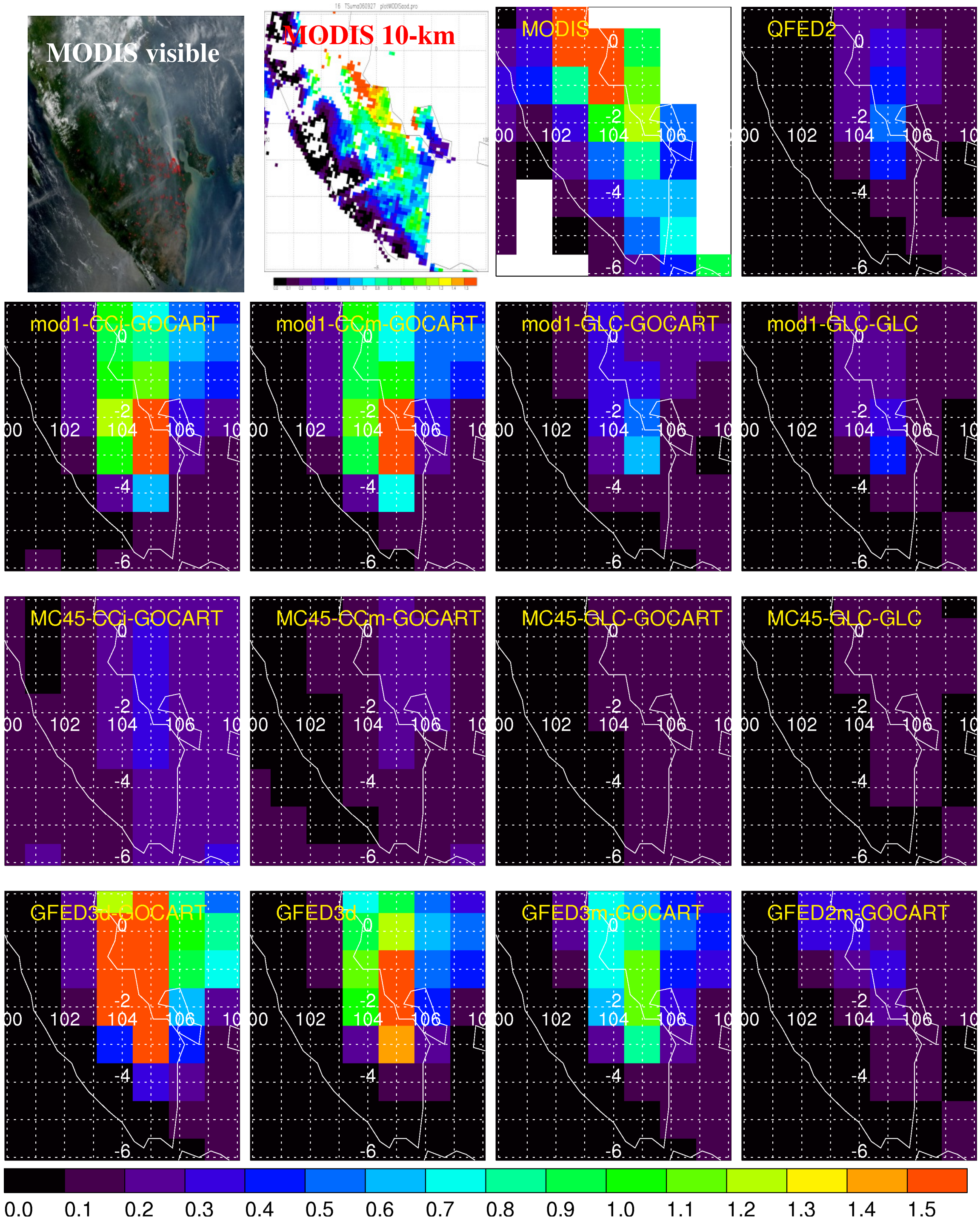

Figure A - 40 MODIS and GOCART AOD for case 16

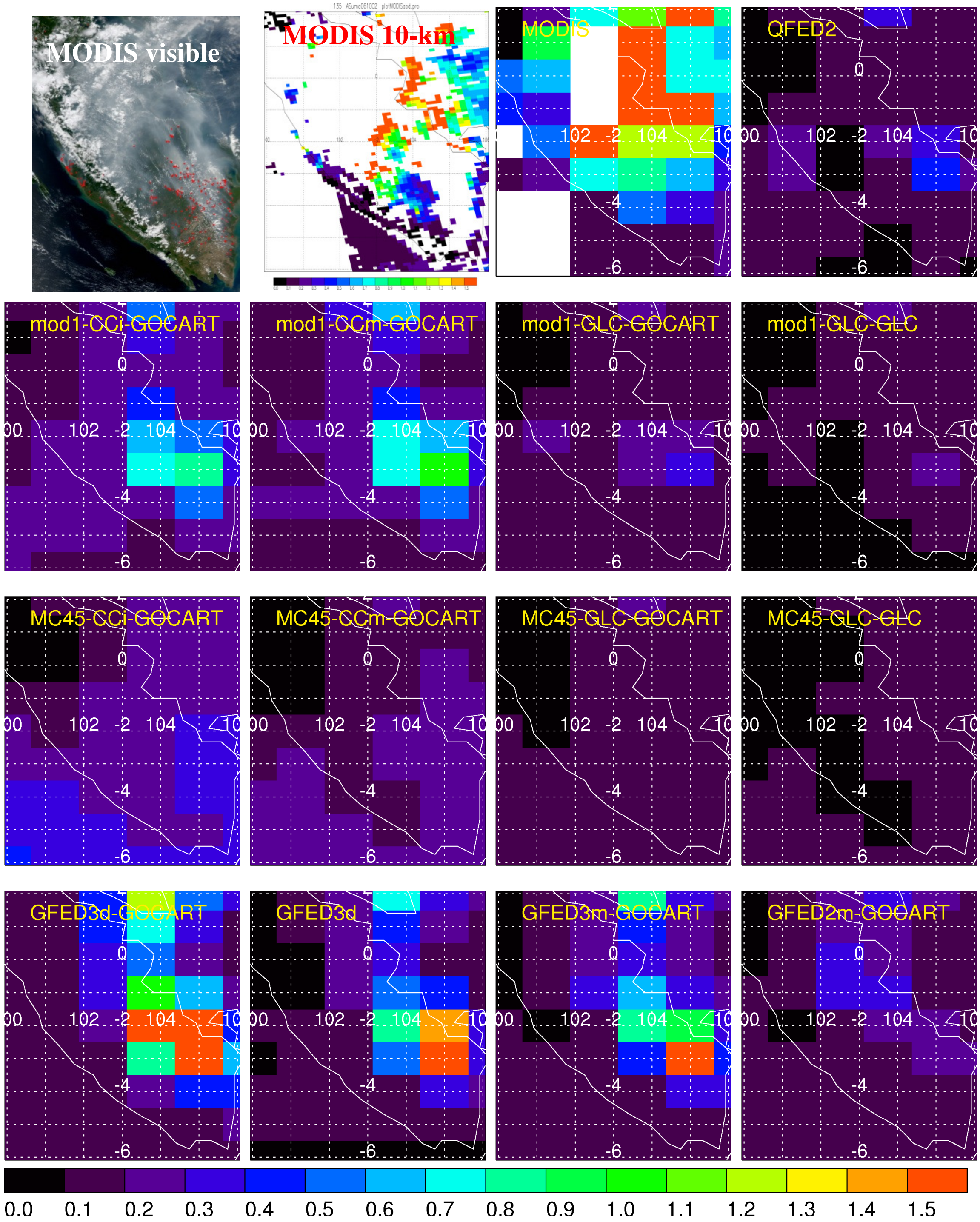

Figure A - 41 MODIS and GOCART AOD for case 135

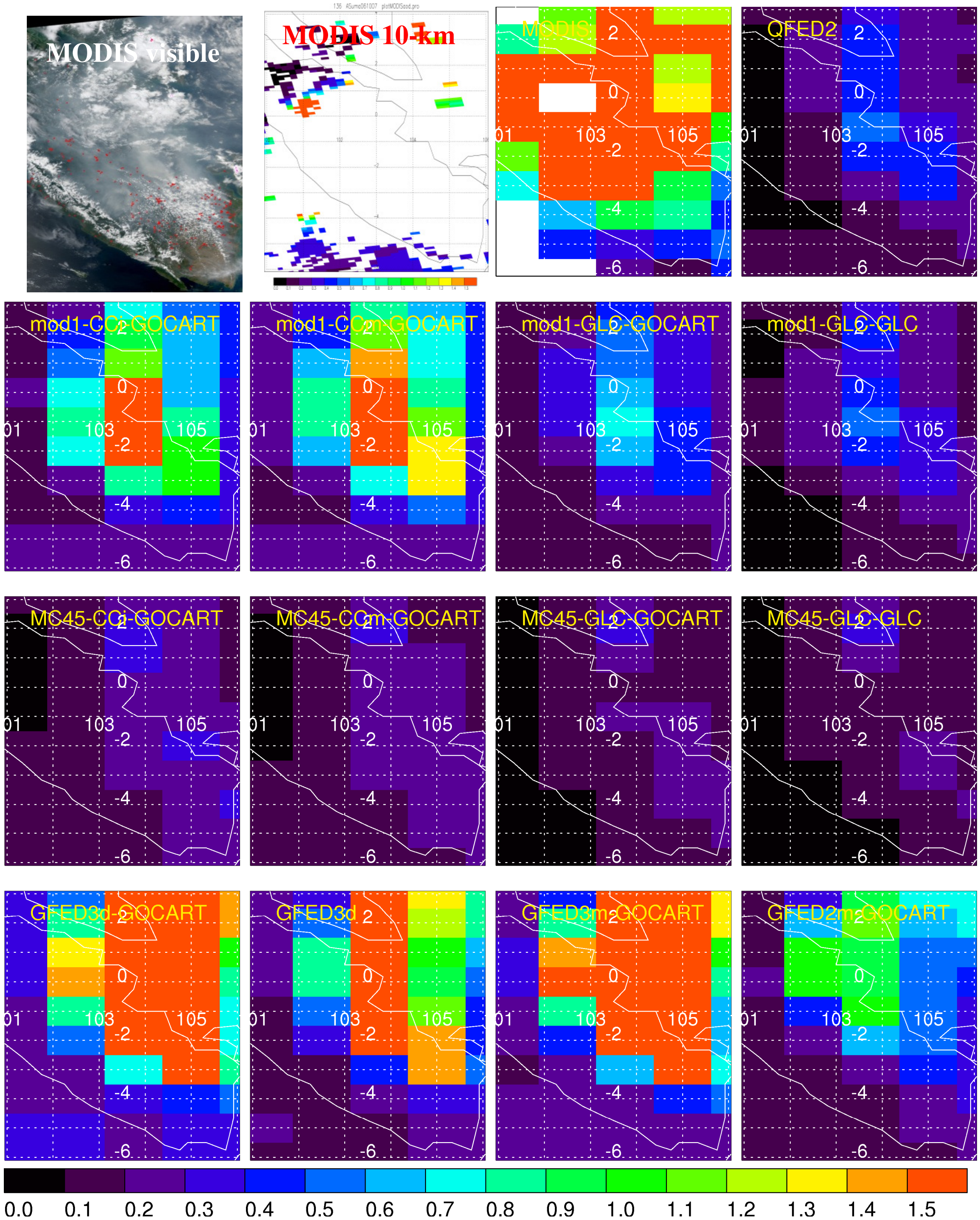

Figure A - 42 MODIS and GOCART AOD for case 136

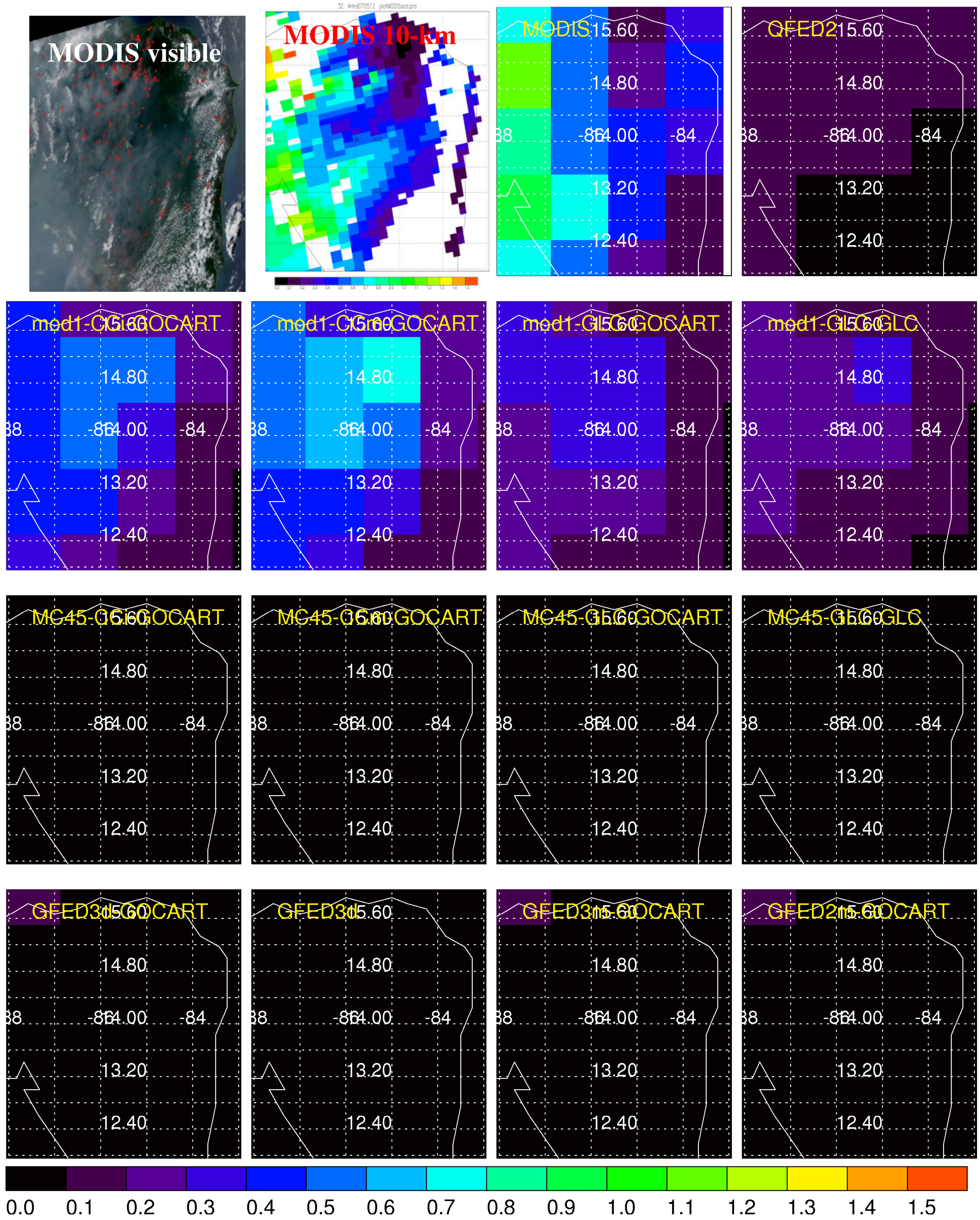

Figure A - 43 MODIS and GOCART AOD for case 32

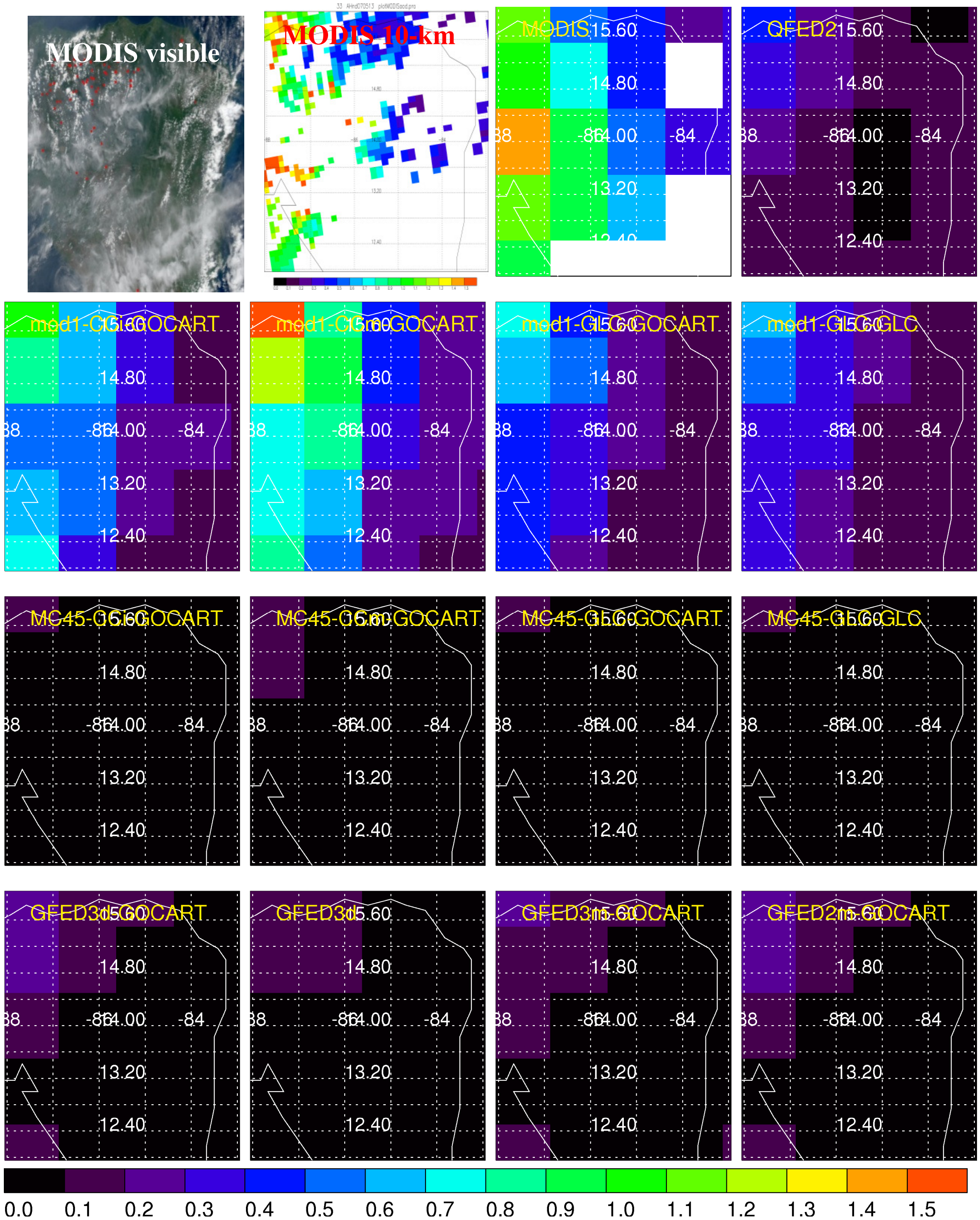

Figure A - 44 MODIS and GOCART AOD for case 33

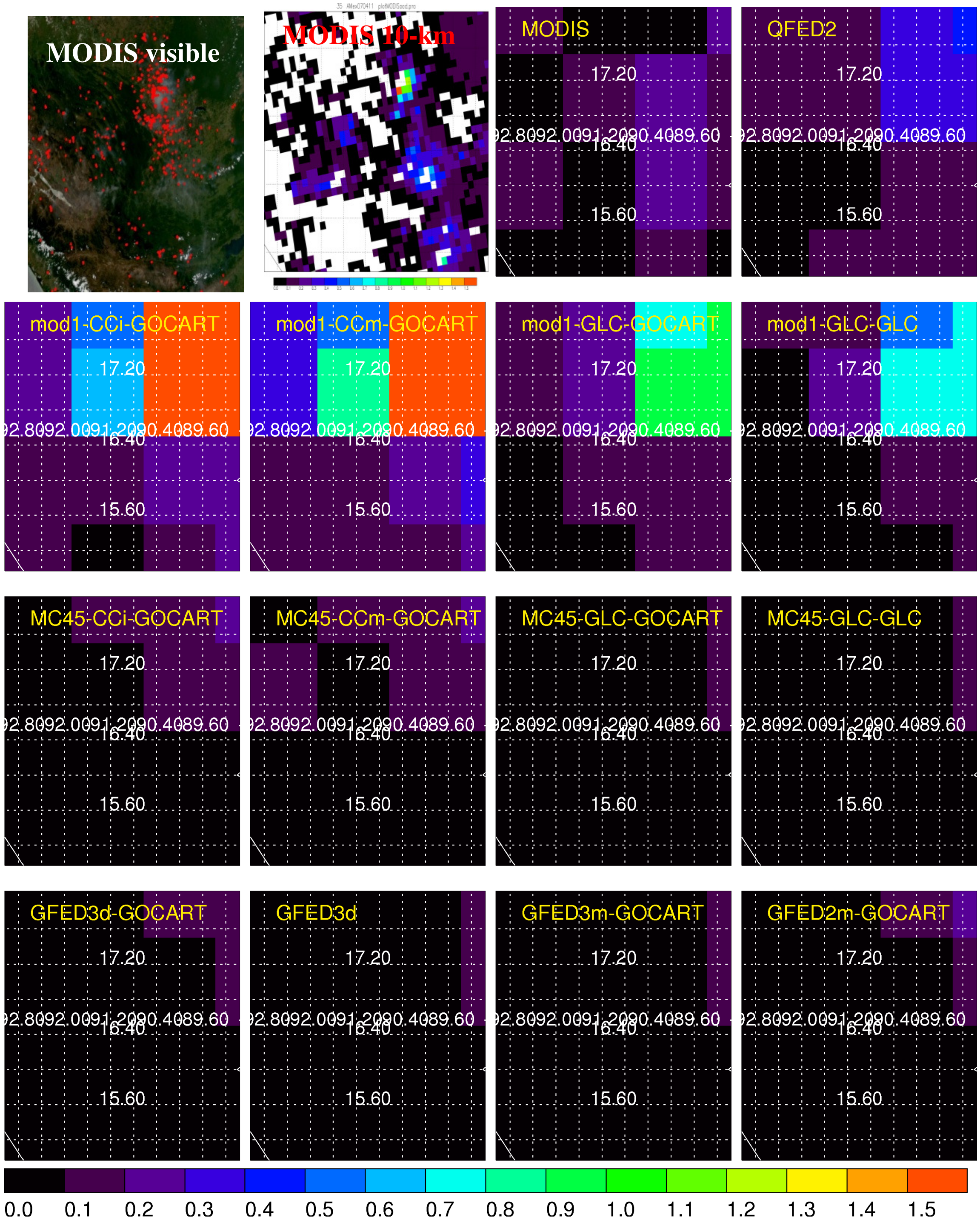

Figure A - 45 MODIS and GOCART AOD for case 35

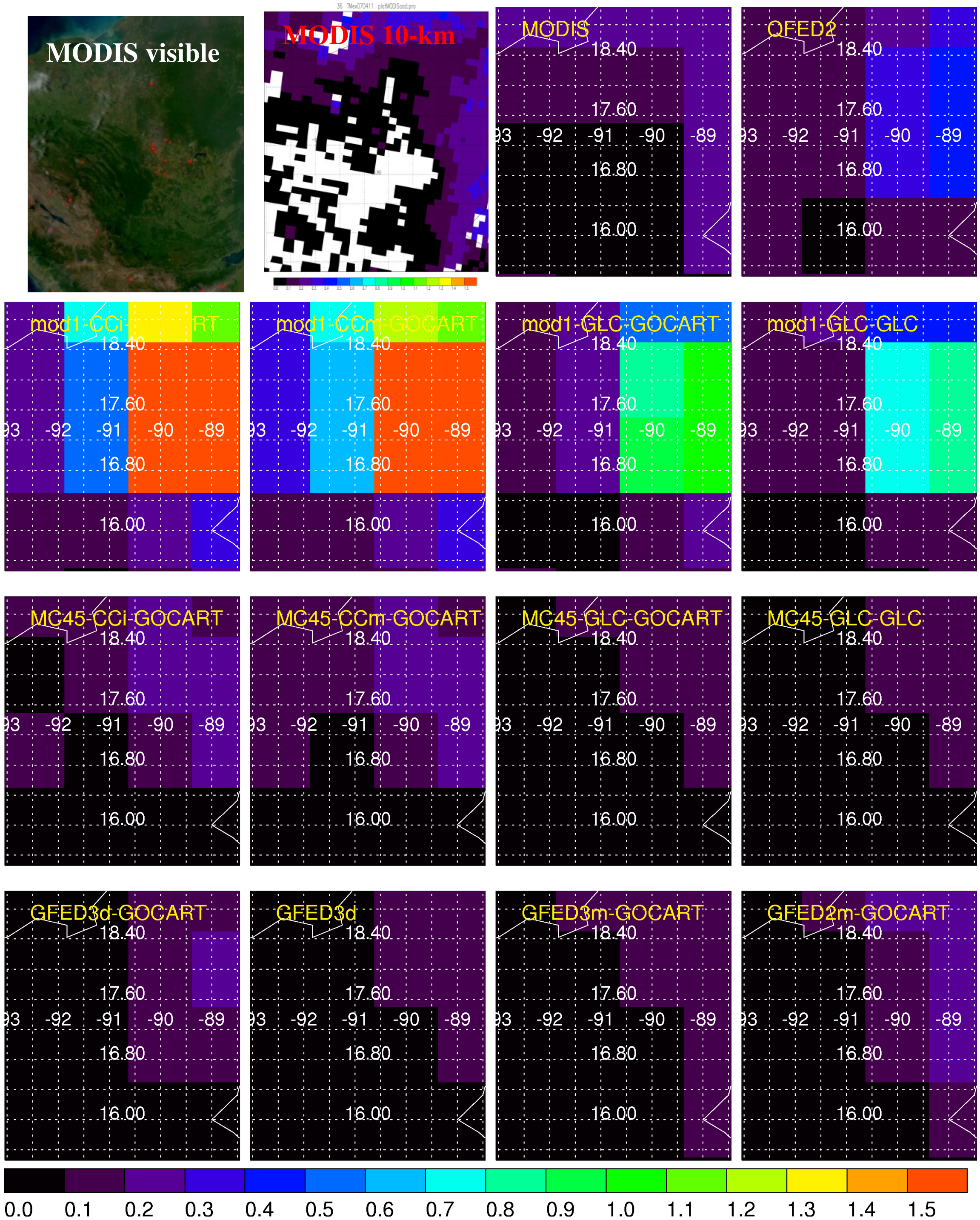

Figure A - 46 MODIS and GOCART AOD for case 36

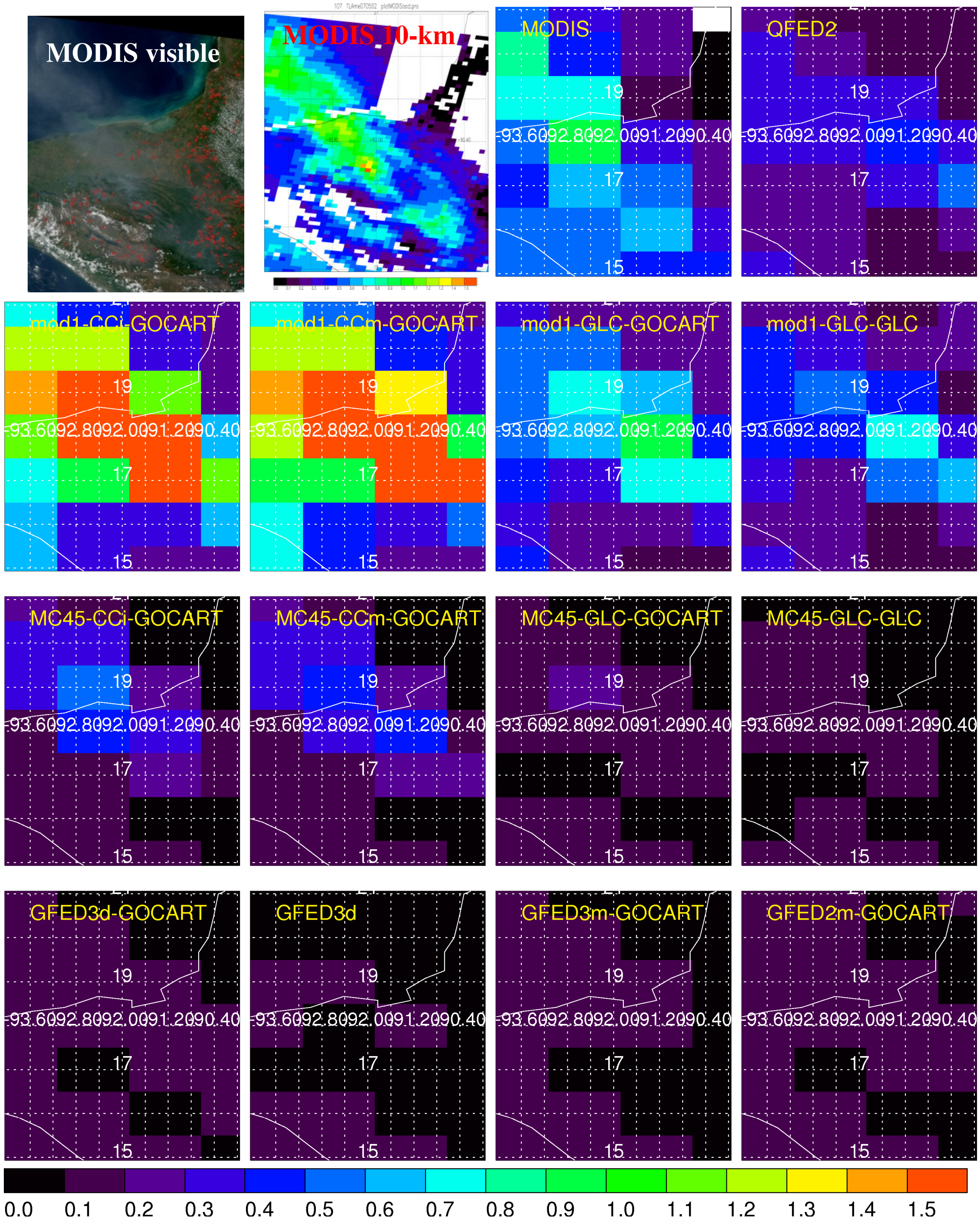

Figure A - 47 MODIS and GOCART AOD for case 107

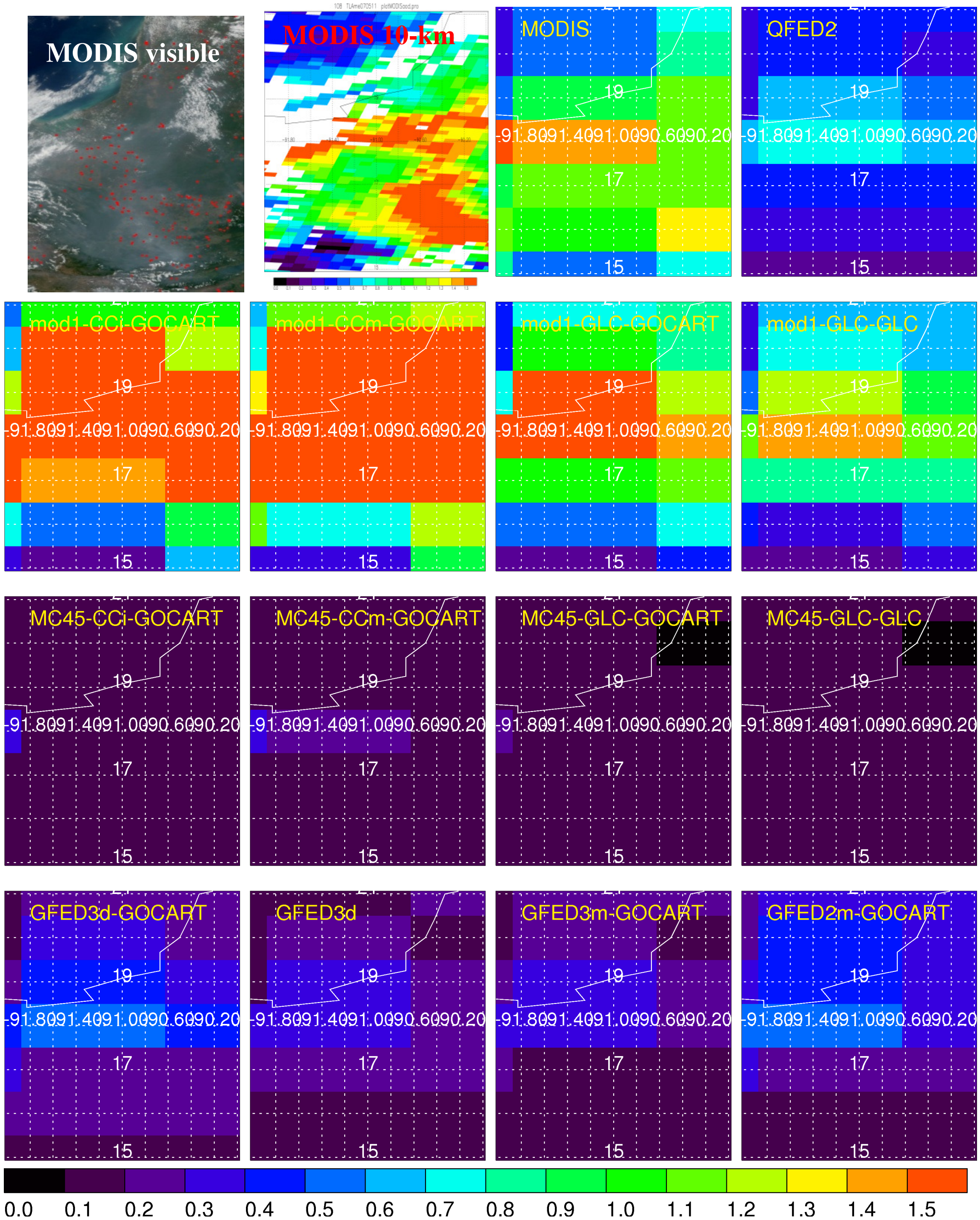

Figure A - 48 MODIS and GOCART AOD for case 108

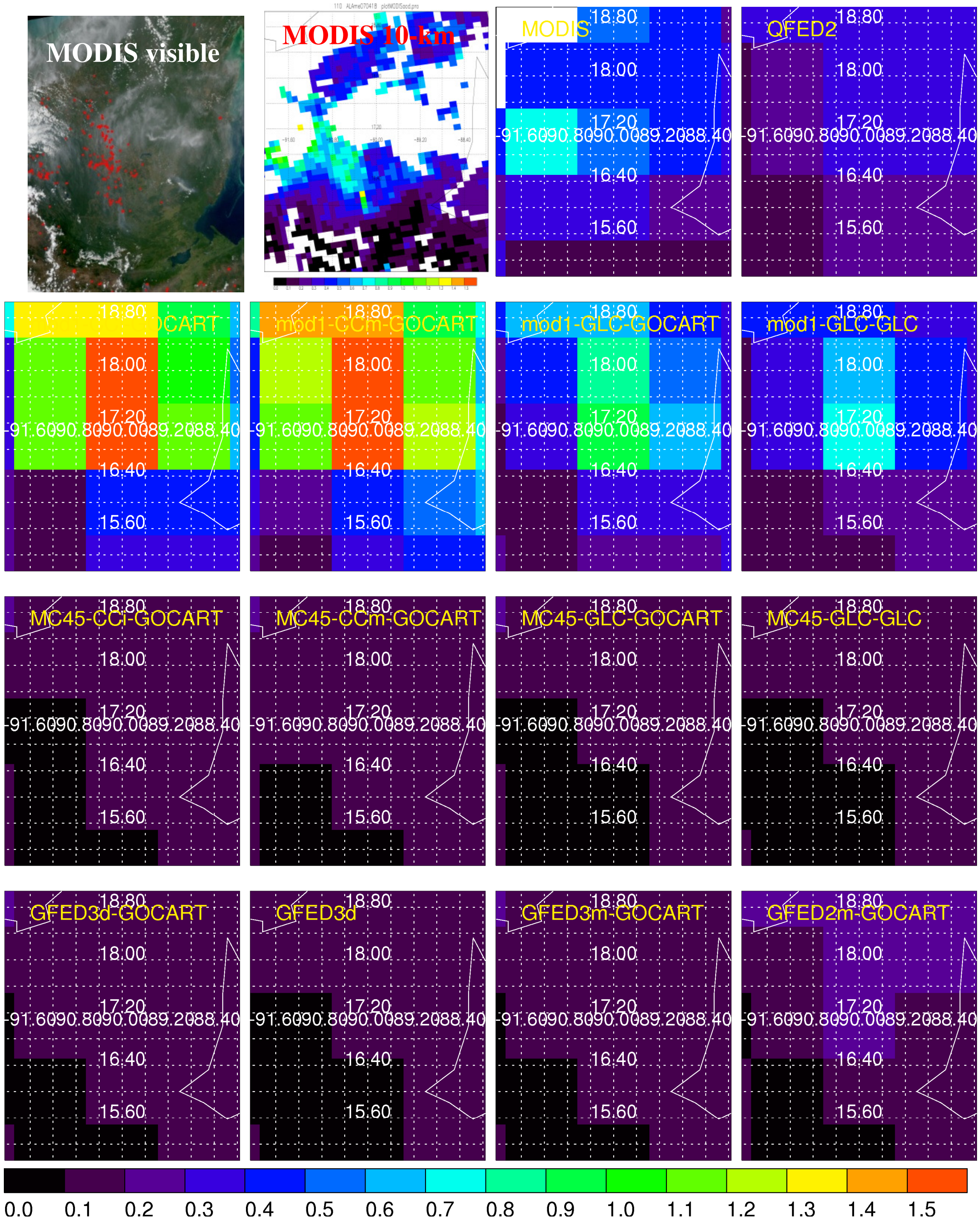

Figure A - 49 MODIS and GOCART AOD for case 110

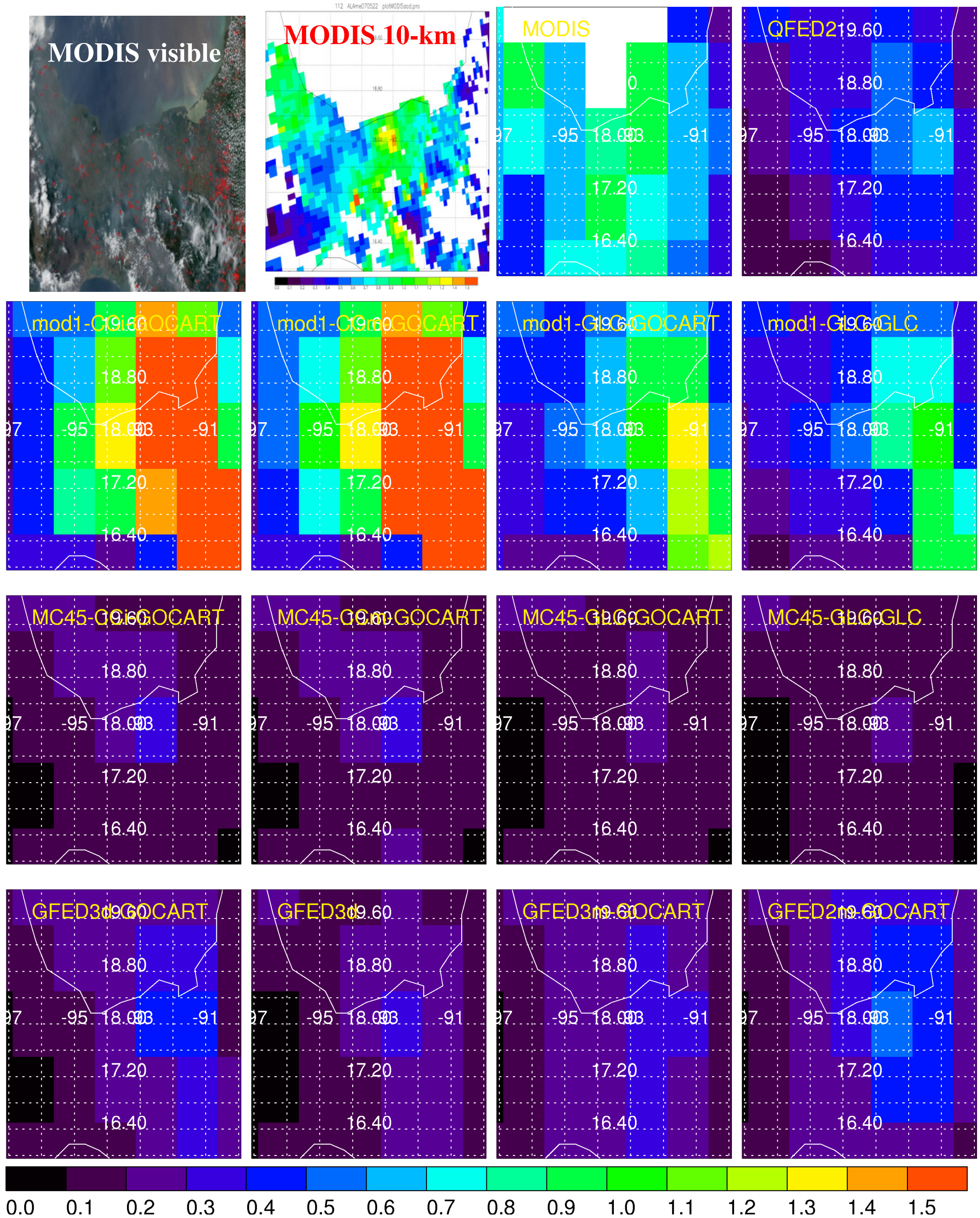

Figure A - 50 MODIS and GOCART AOD for case 112

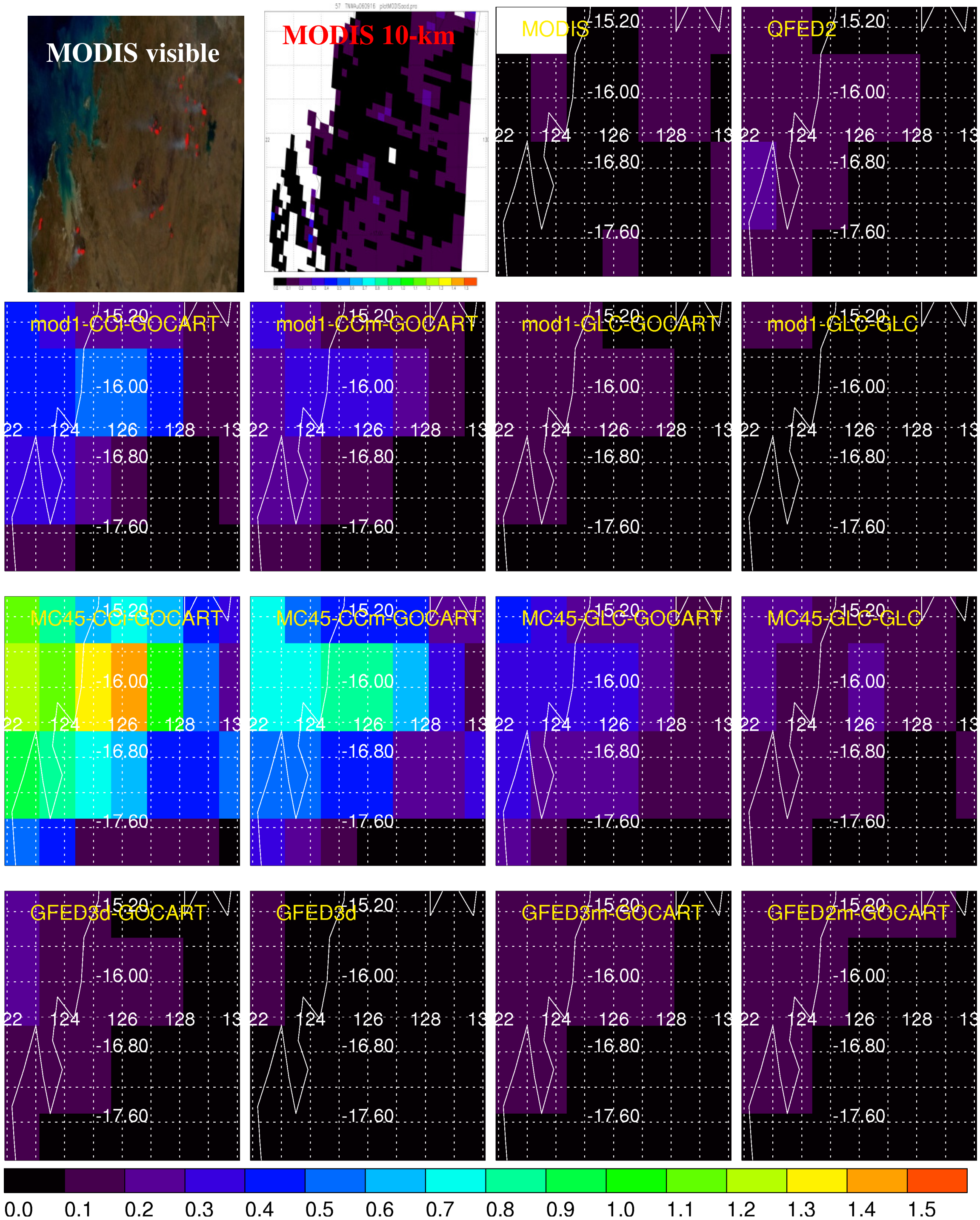

Figure A - 51 MODIS and GOCART AOD for case 57

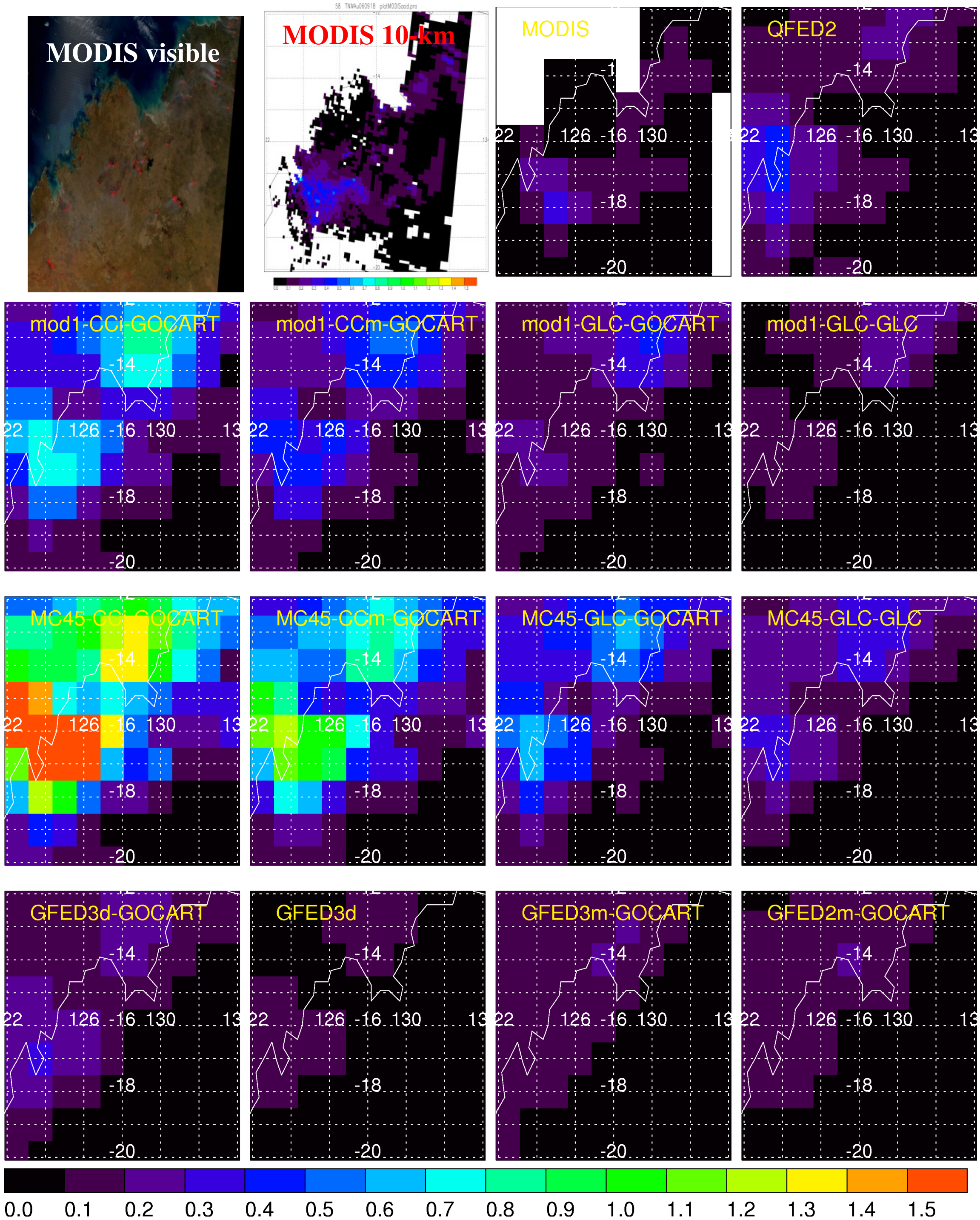

Figure A - 52 MODIS and GOCART AOD for case 58

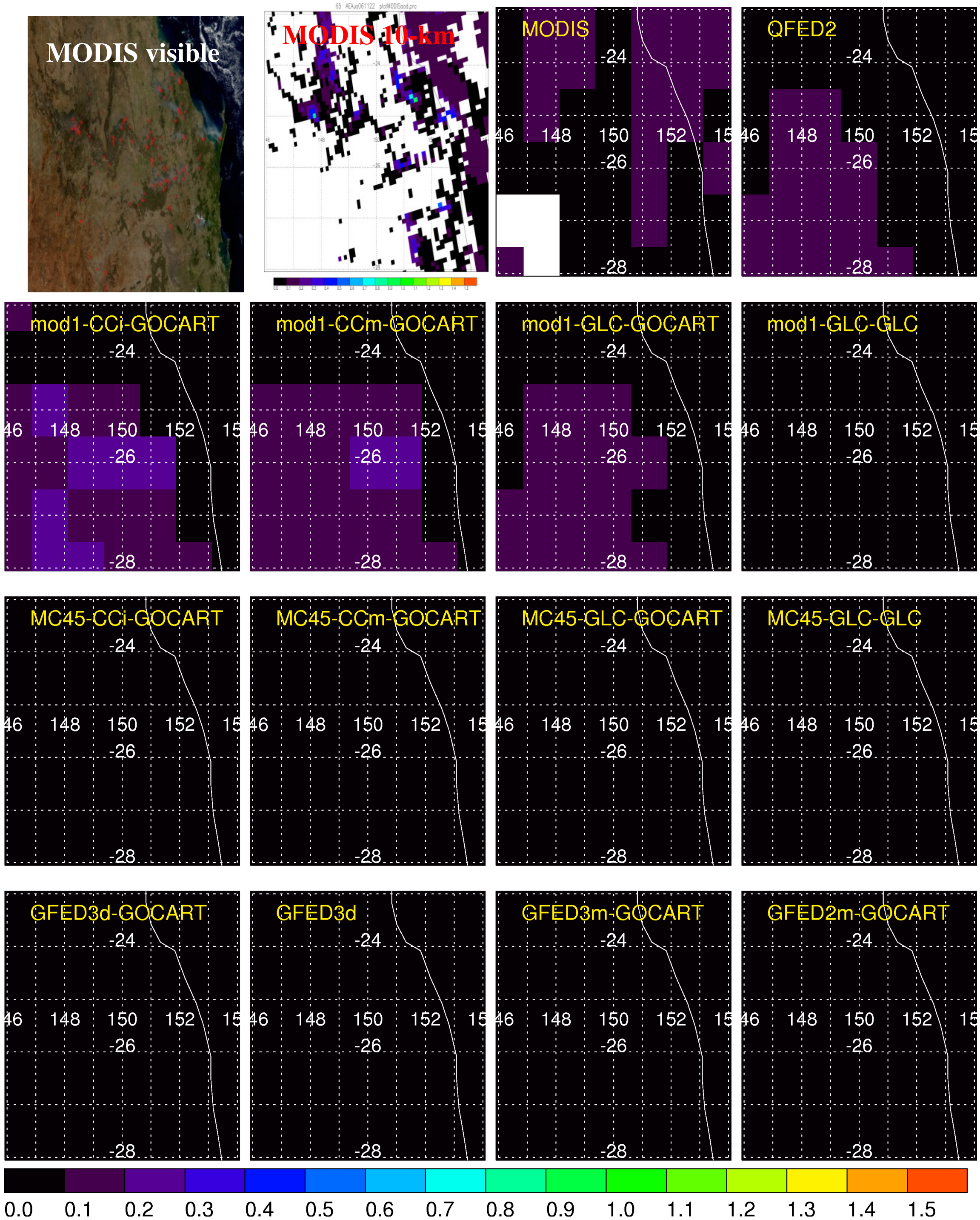

Figure A - 53 MODIS and GOCART AOD for case 65

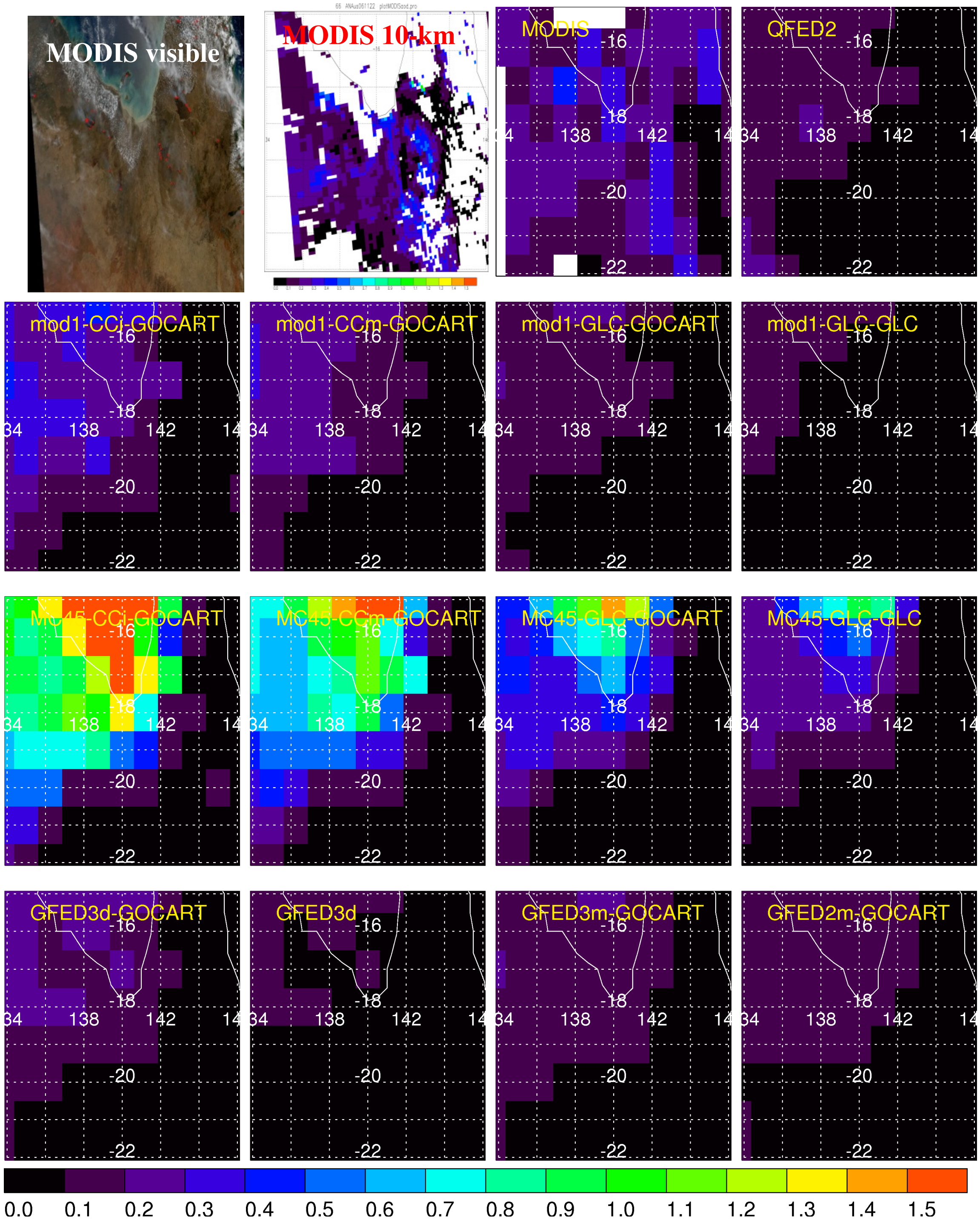

Figure A - 54 MODIS and GOCART AOD for case 66

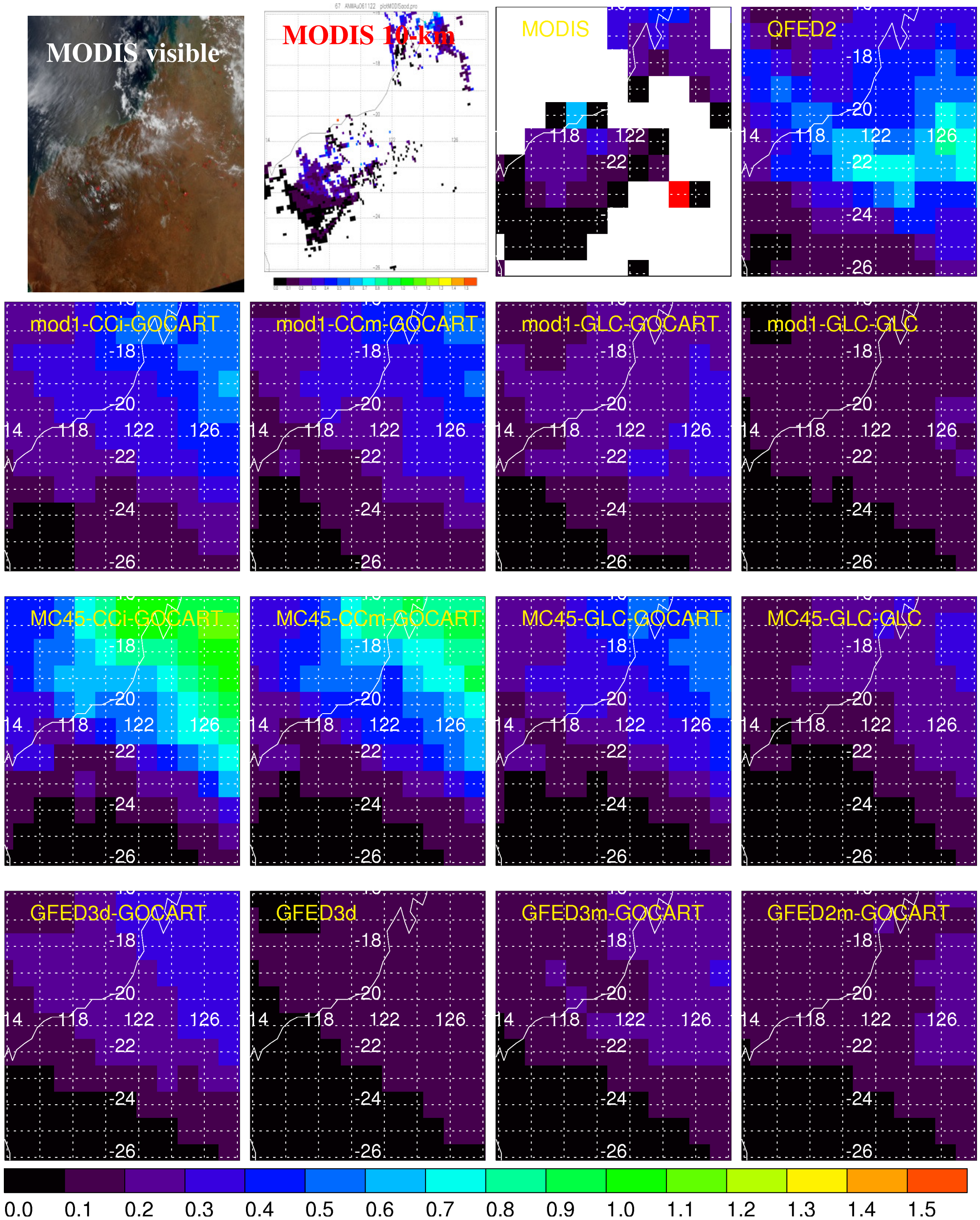

Figure A - 55 MODIS and GOCART AOD for case 67

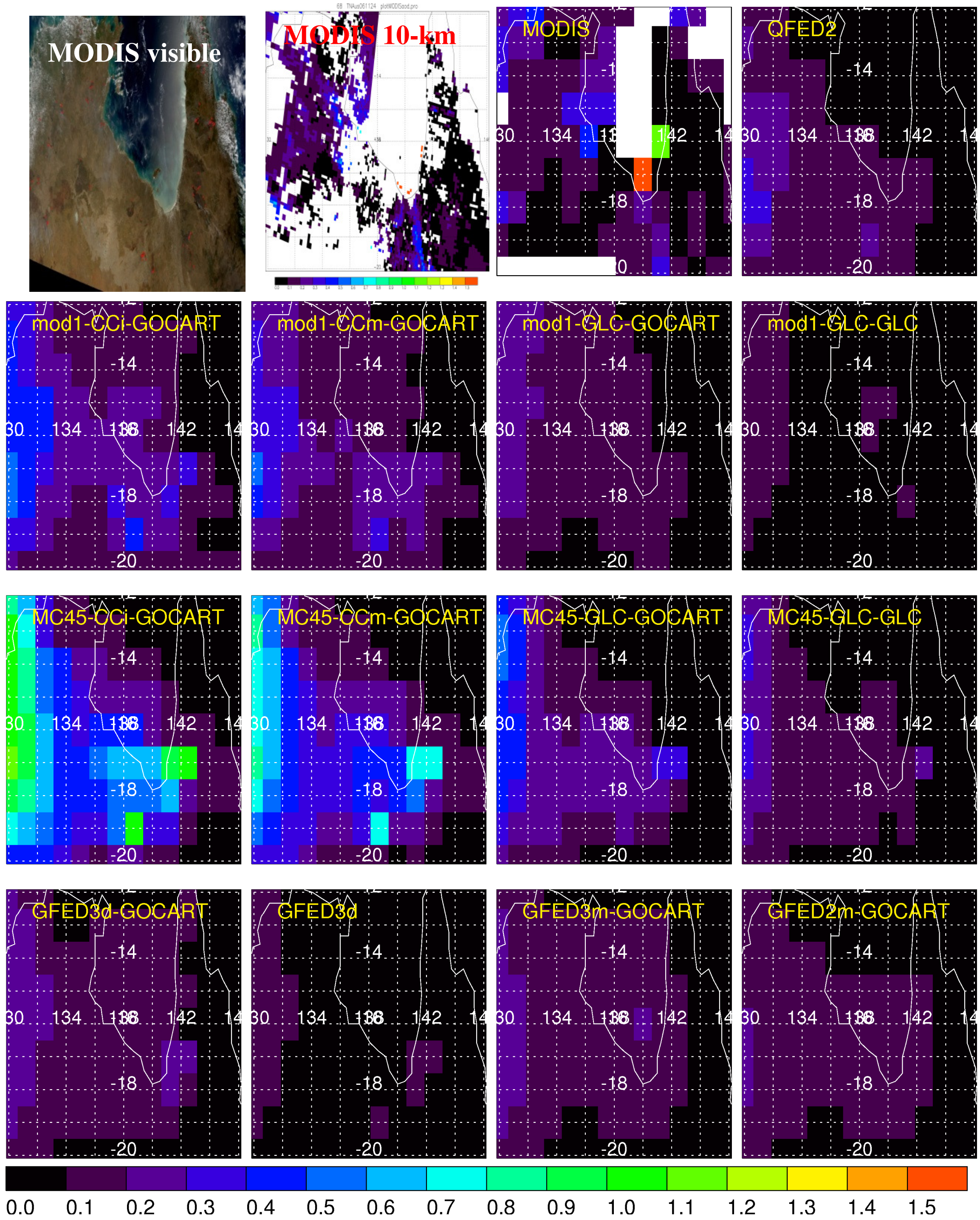

Figure A - 56 MODIS and GOCART AOD for case 68

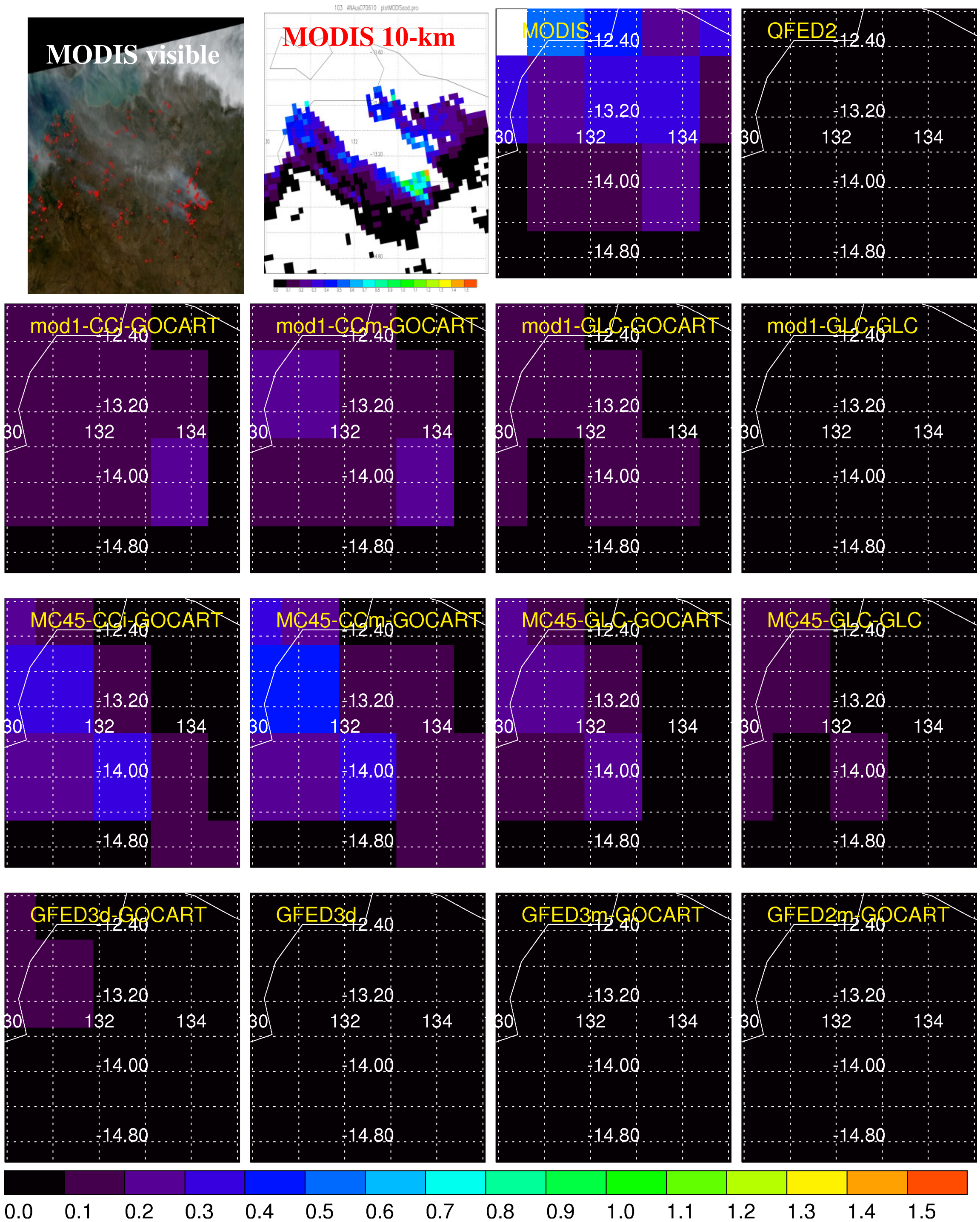

Figure A - 57 MODIS and GOCART AOD for case 103

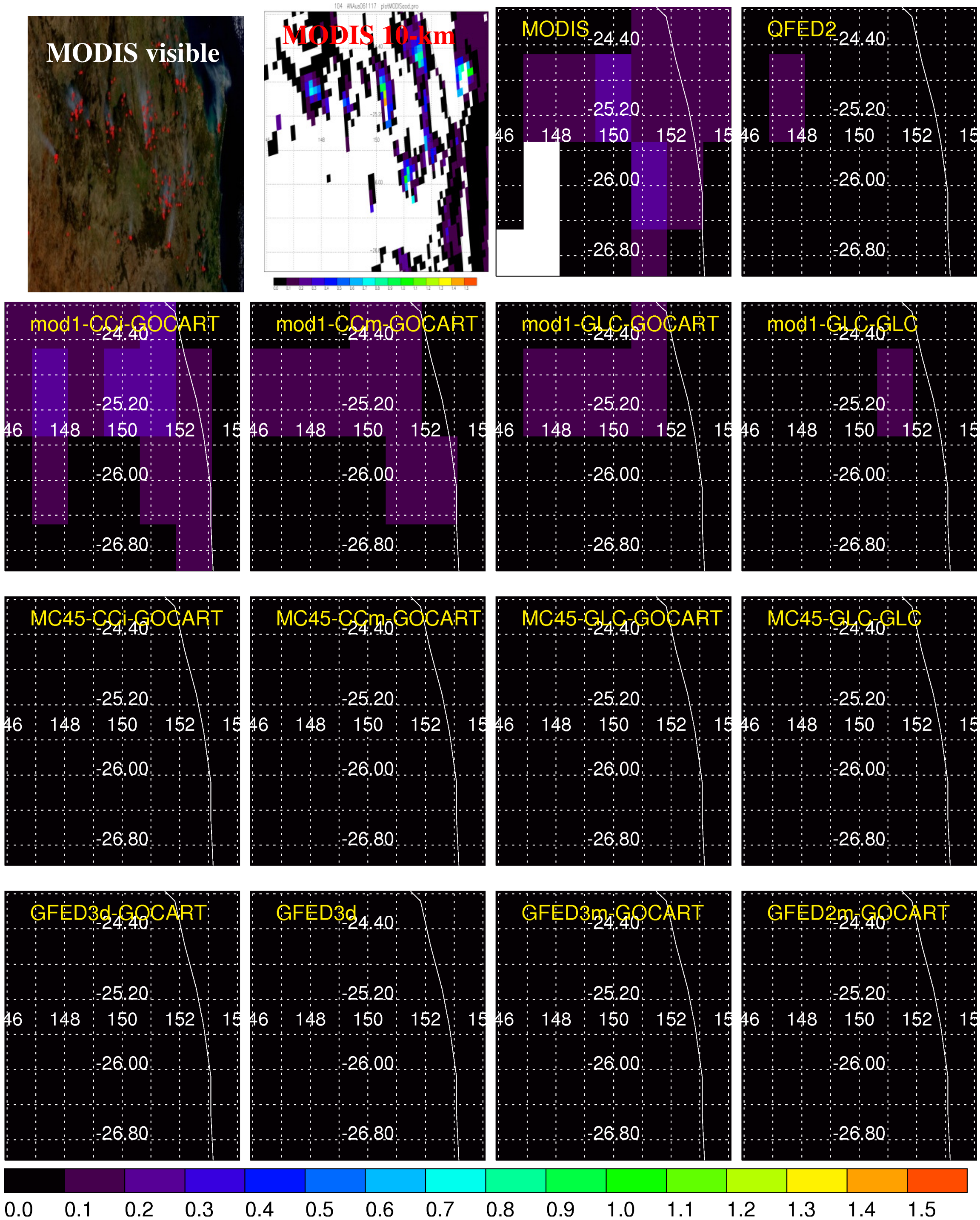

Figure A - 58 MODIS and GOCART AOD for case 104

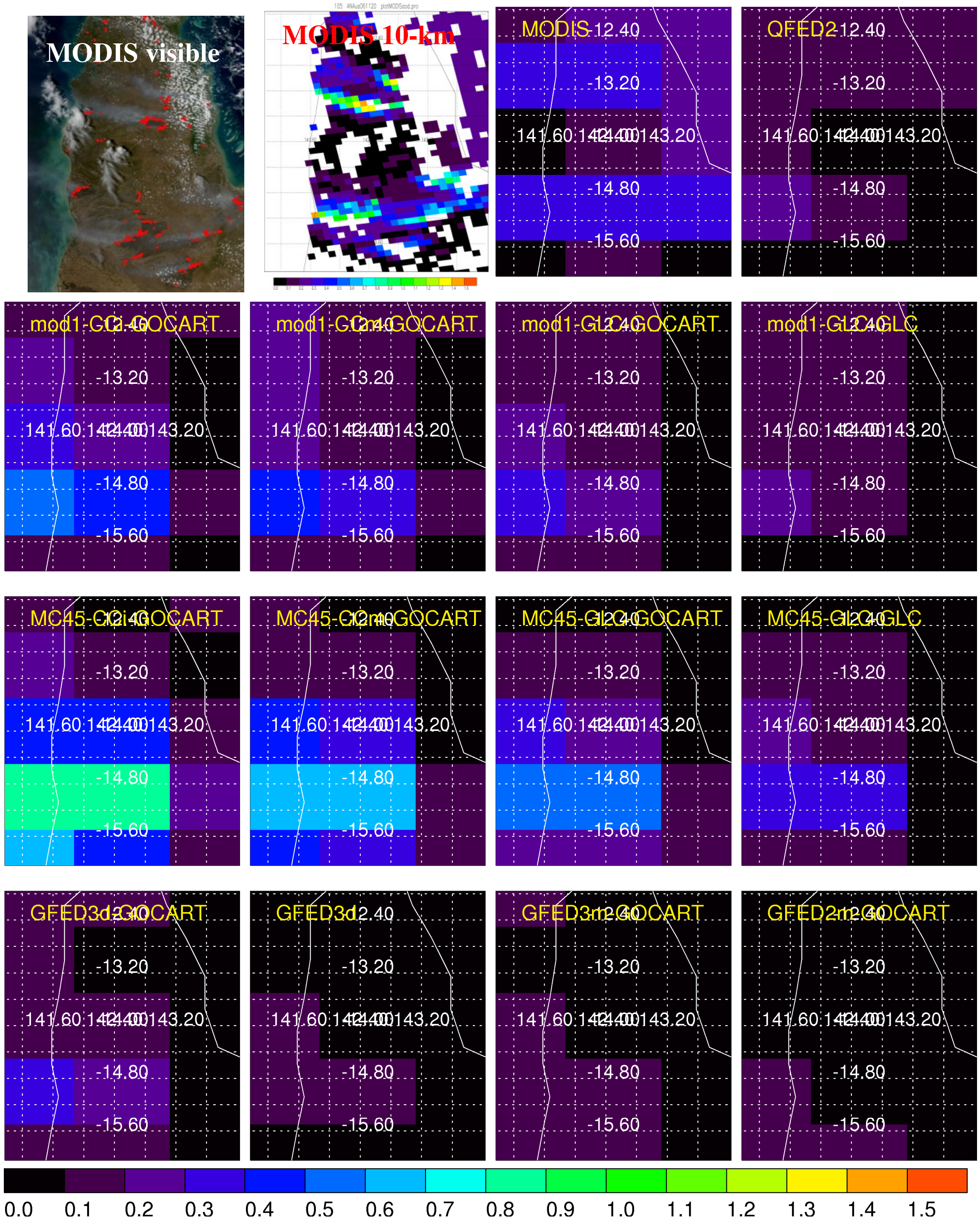

Figure A - 59 MODIS and GOCART AOD for case 105

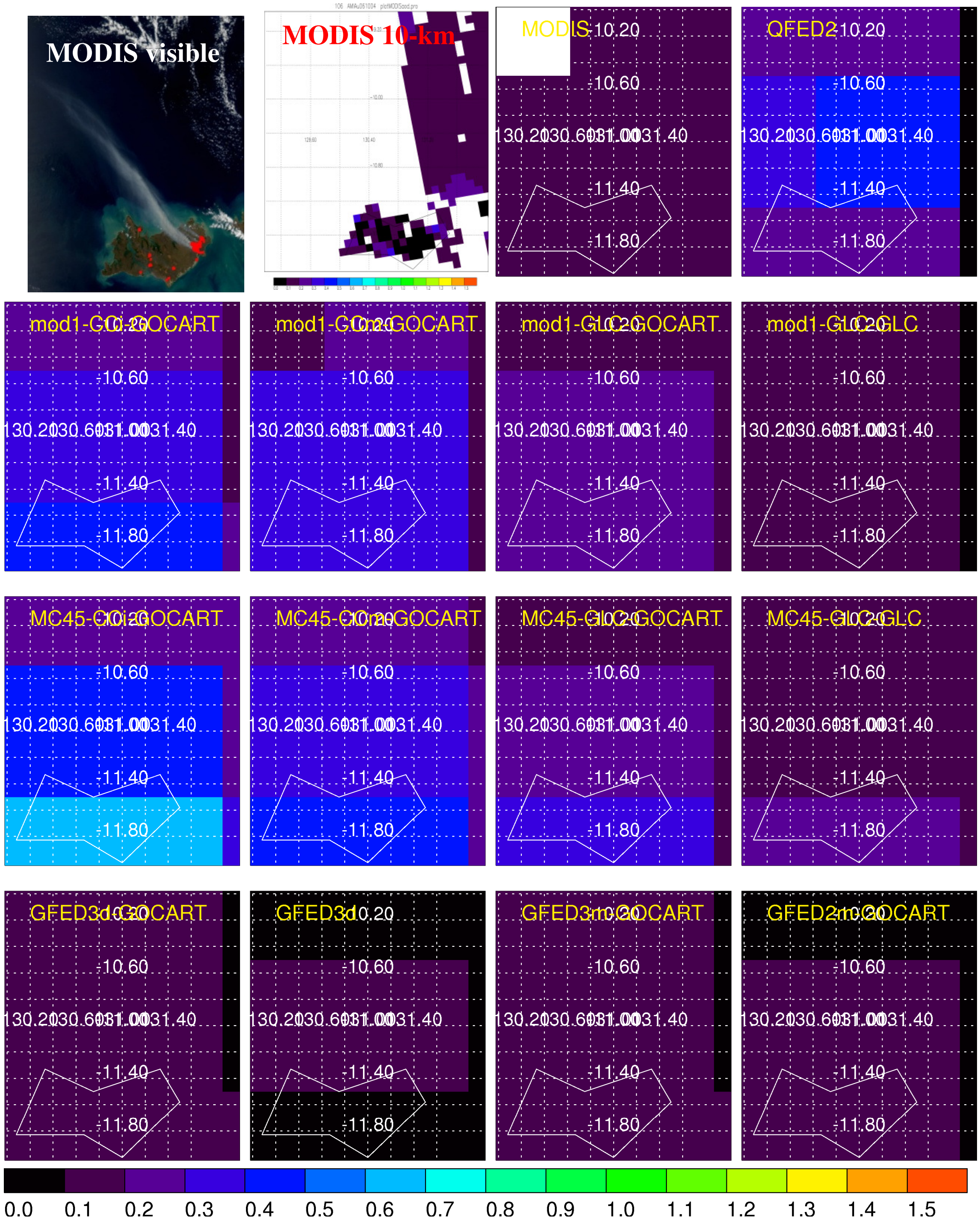

Figure A - 60 MODIS and GOCART AOD for case 106

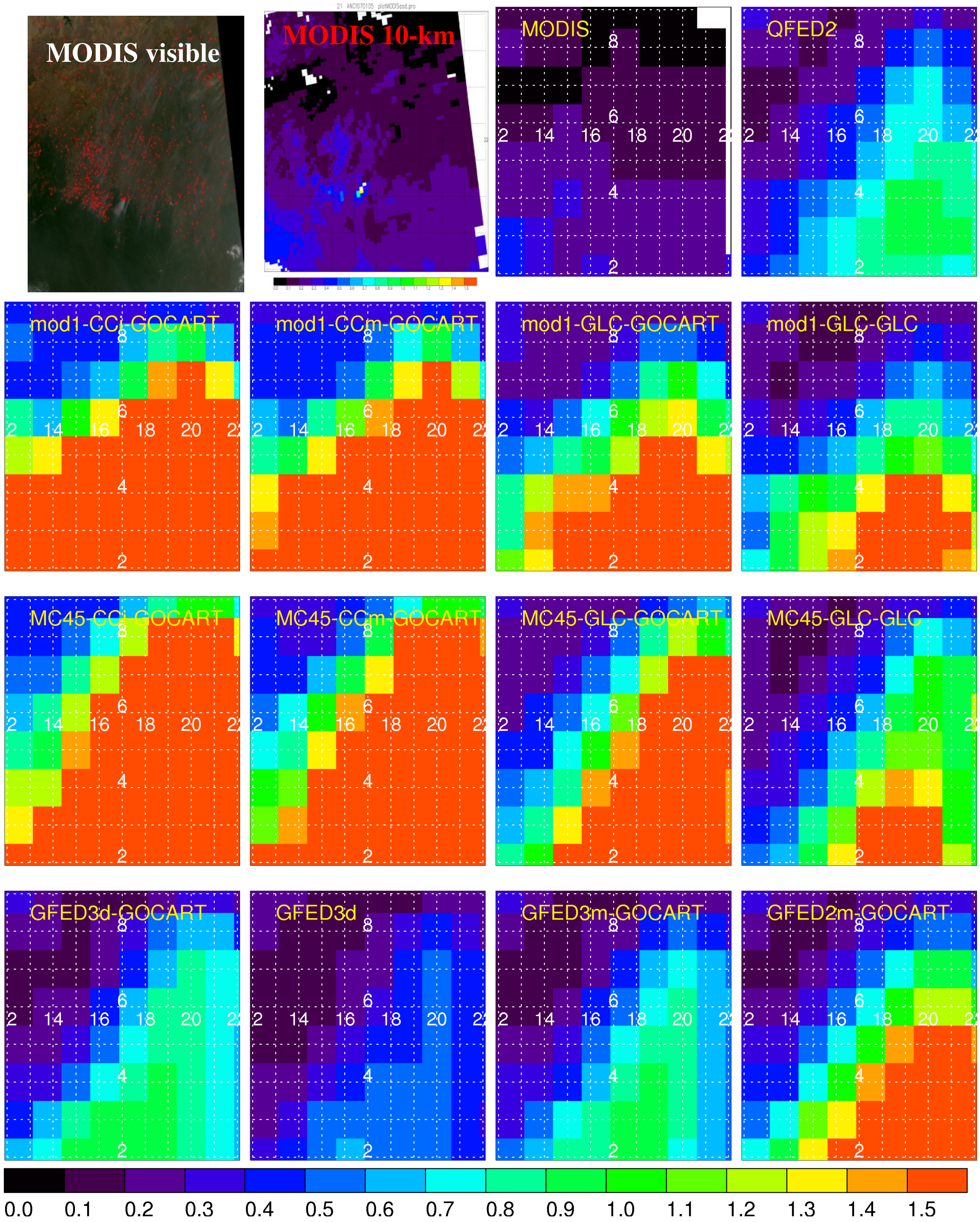

Figure A - 61 MODIS and GOCART AOD for case 21

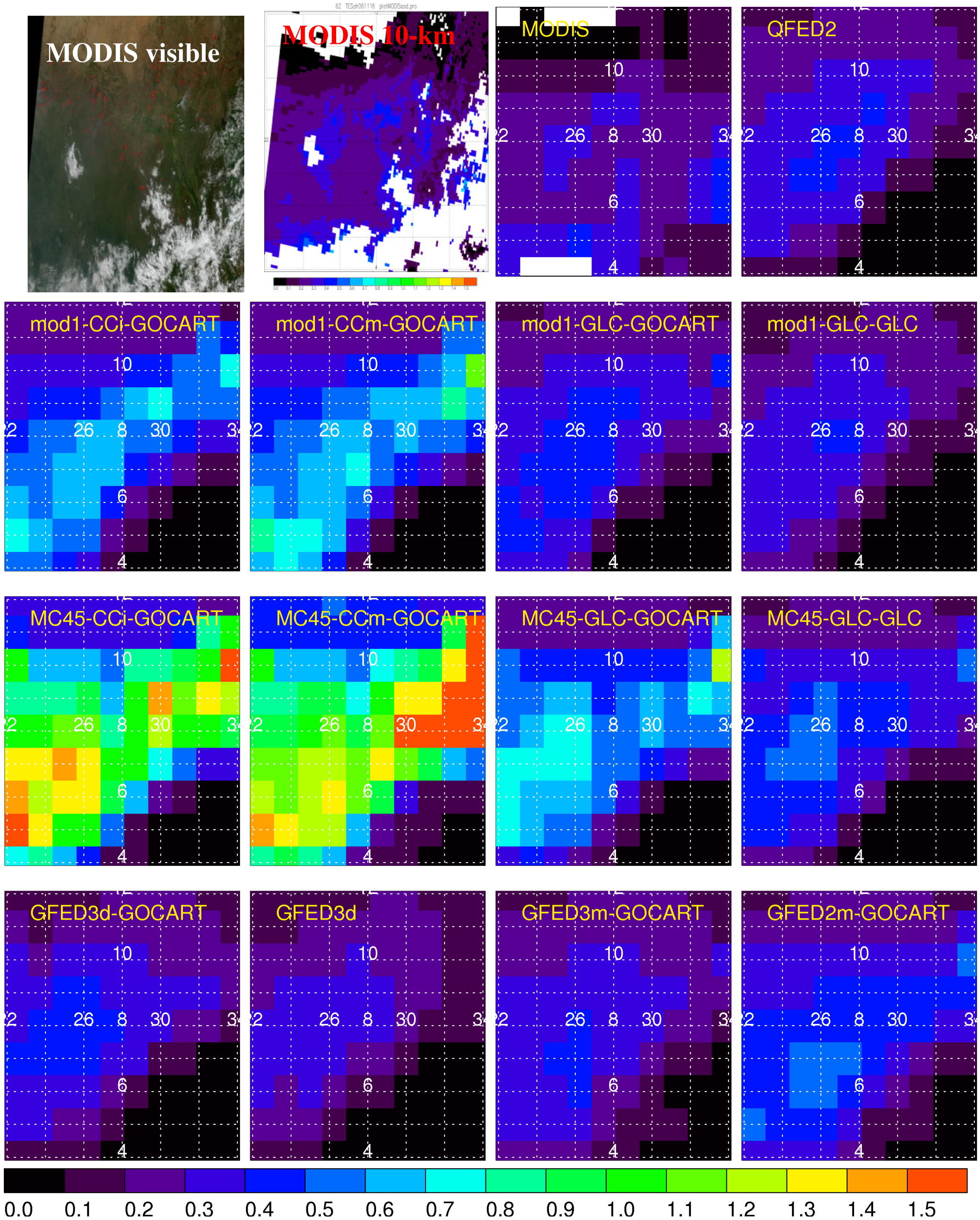

Figure A - 62 MODIS and GOCART AOD for case 62

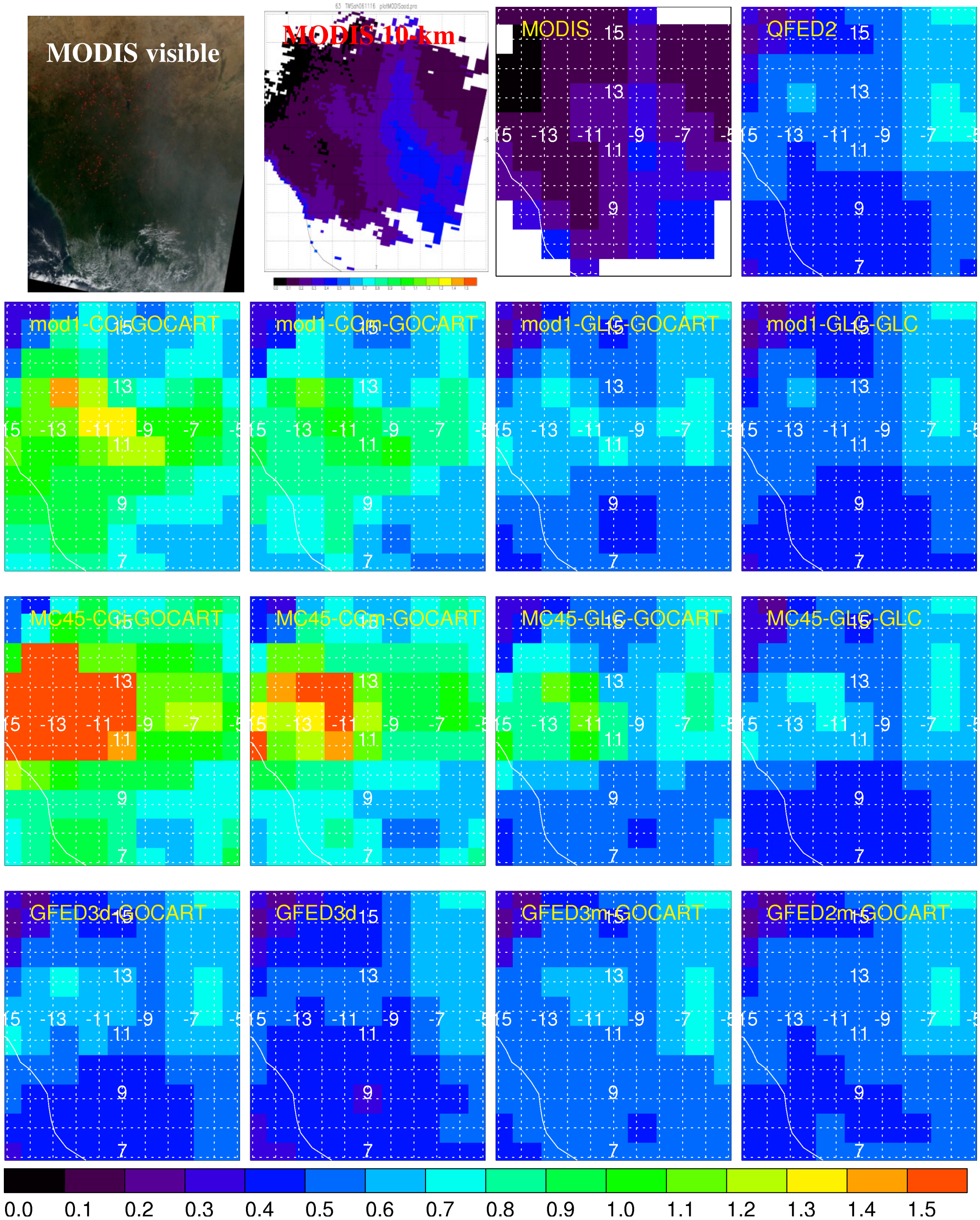

Figure A - 63 MODIS and GOCART AOD for case 63

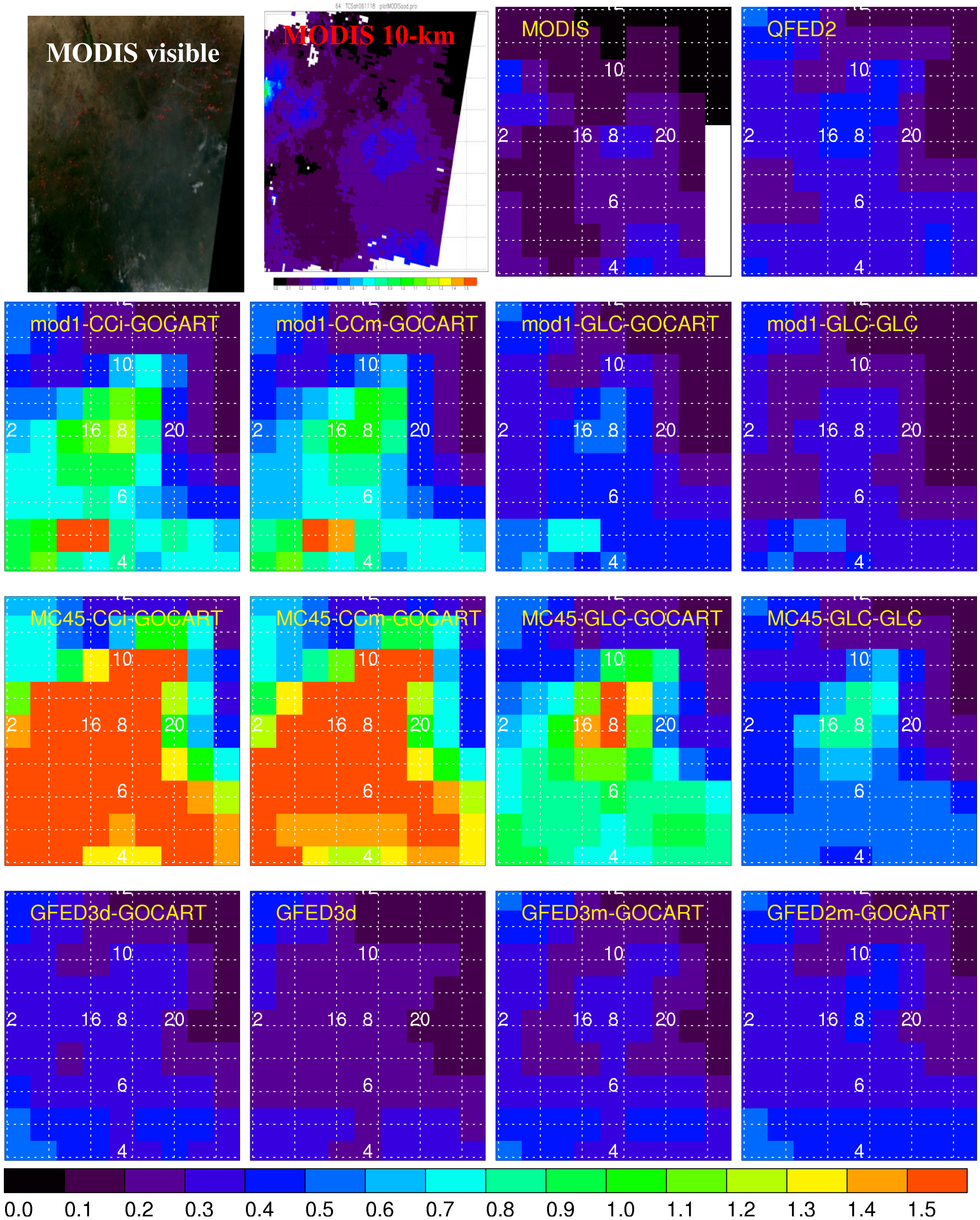

Figure A - 64 MODIS and GOCART AOD for case 64

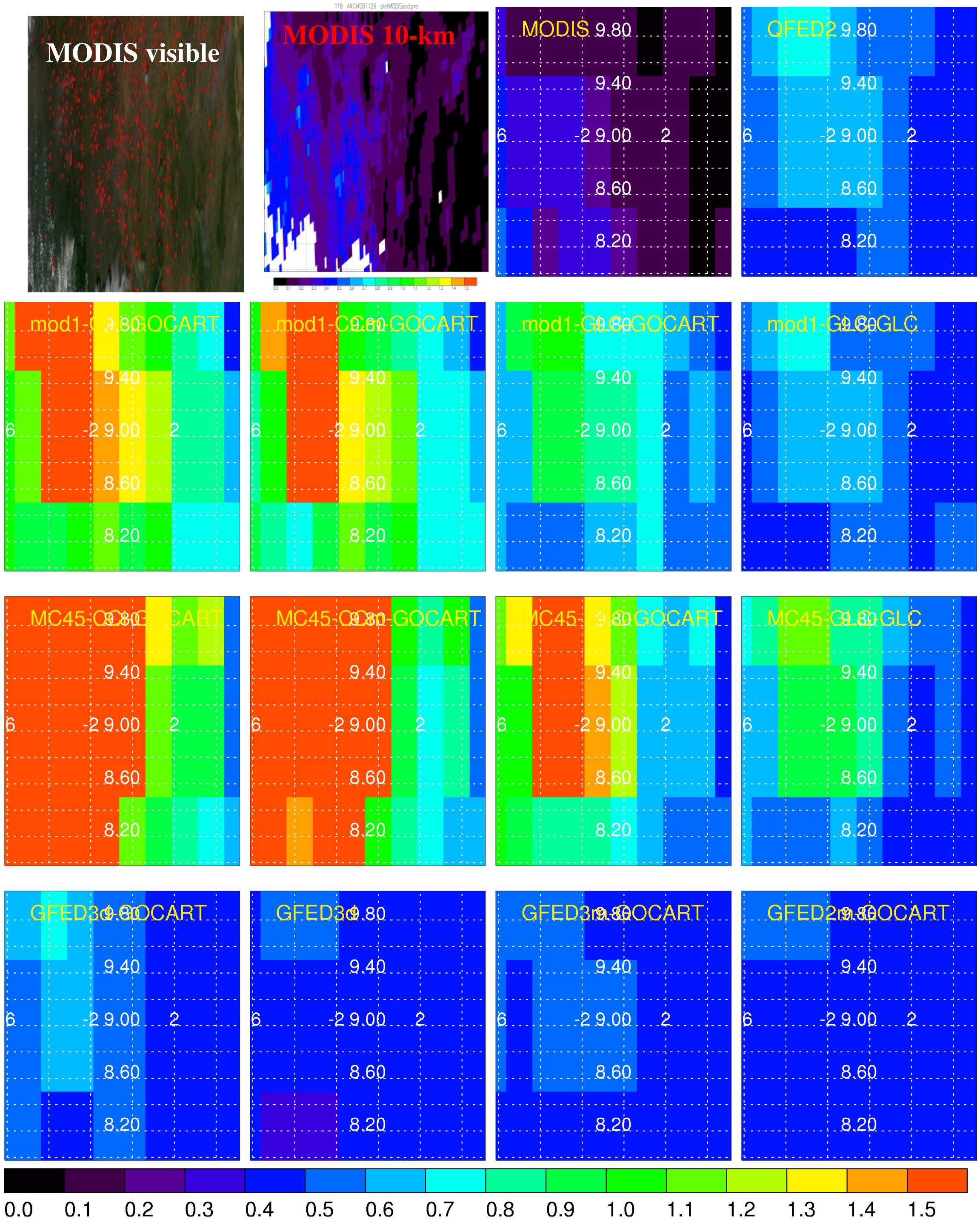

Figure A - 65 MODIS and GOCART AOD for case 118

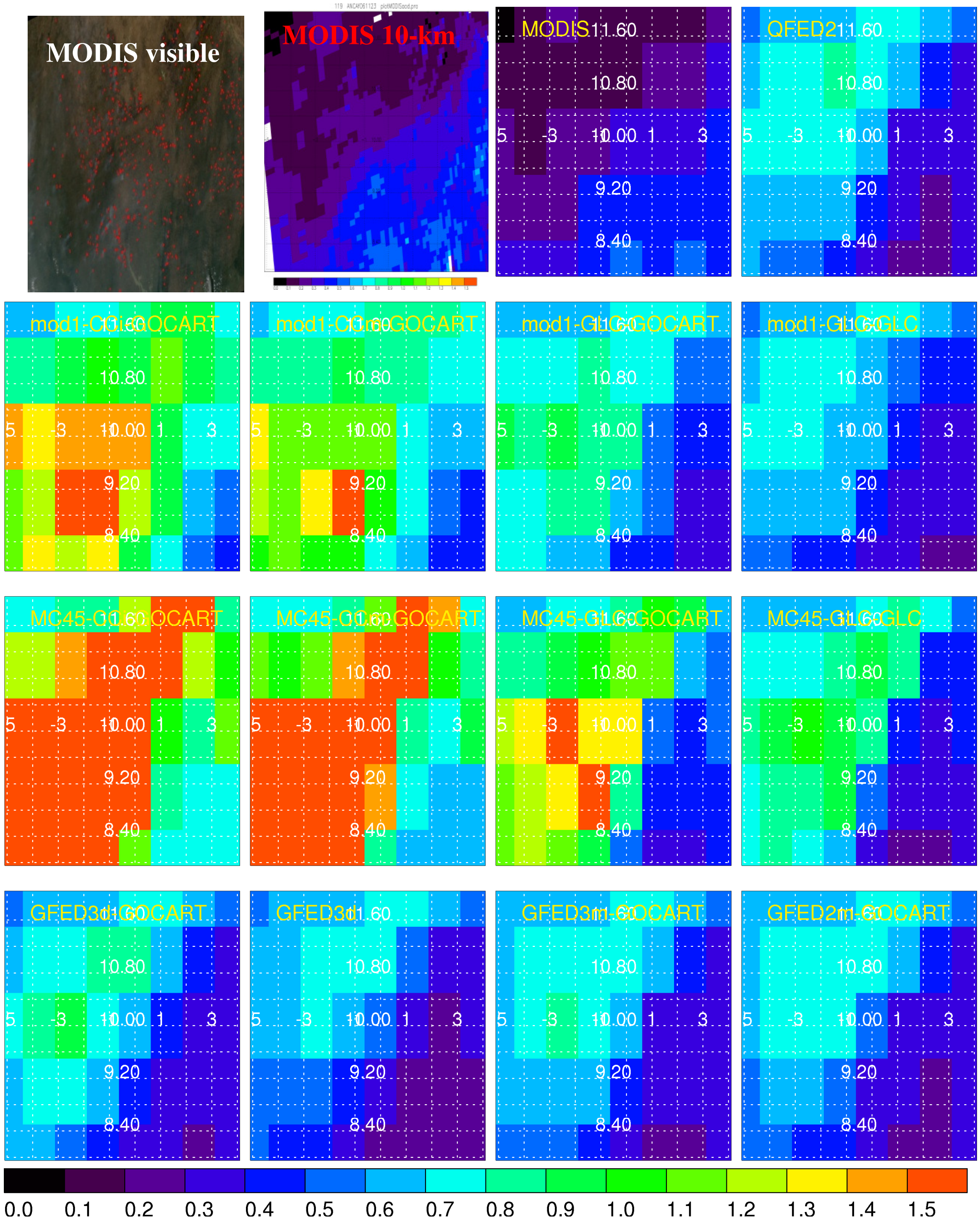

Figure A - 66 MODIS and GOCART AOD for case 119

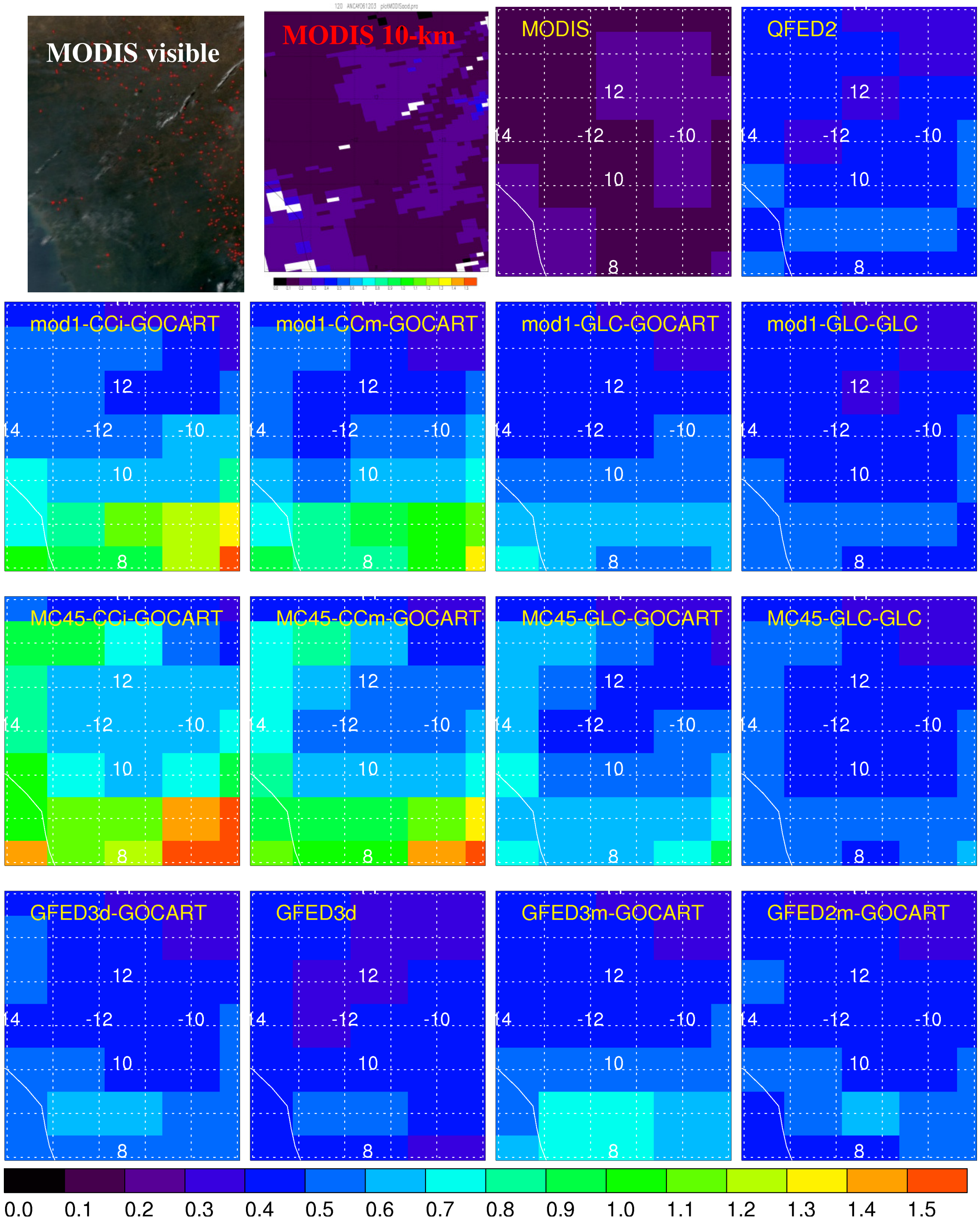

Figure A - 67 MODIS and GOCART AOD for case 120

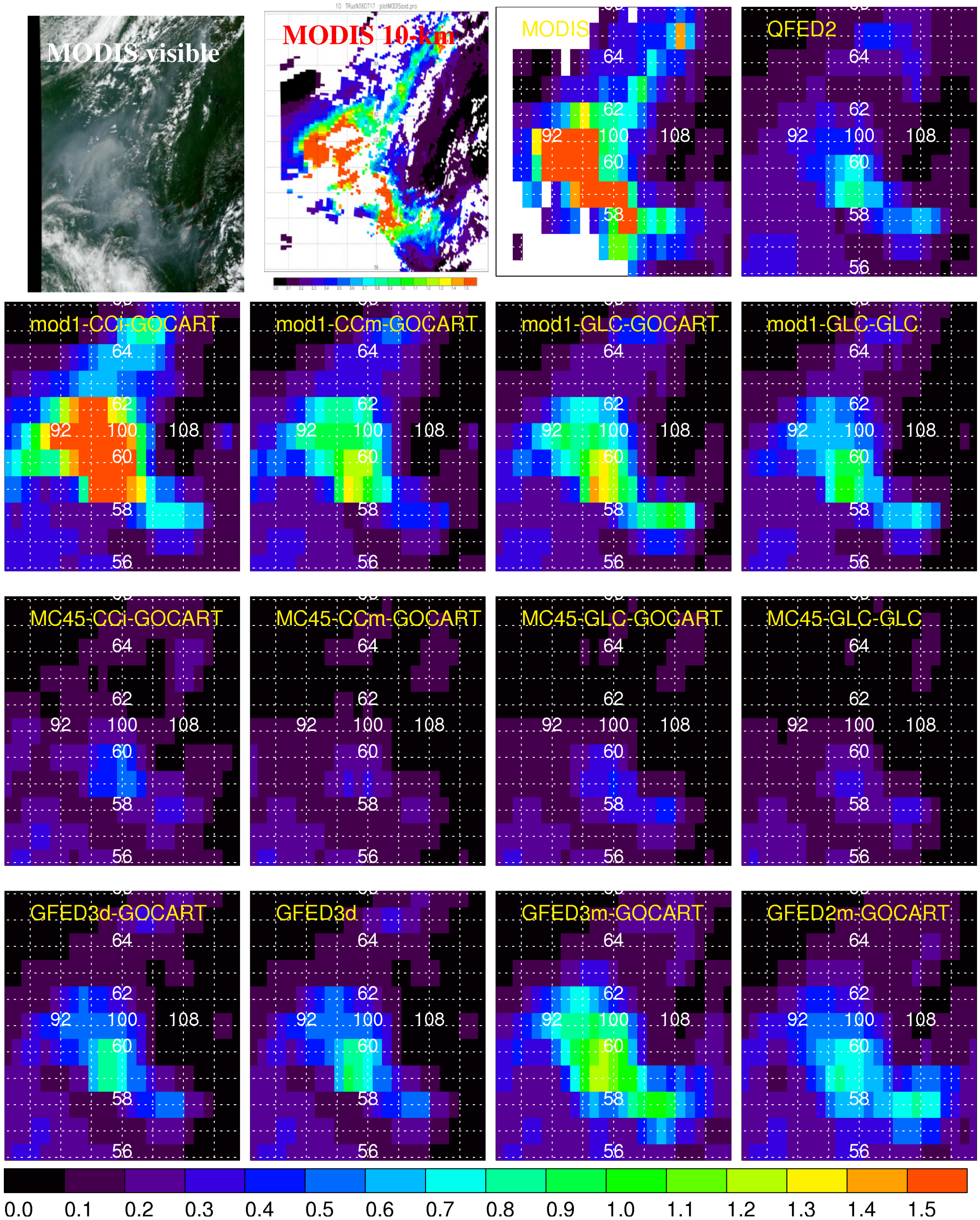

Figure A - 68 MODIS and GOCART AOD for case 10

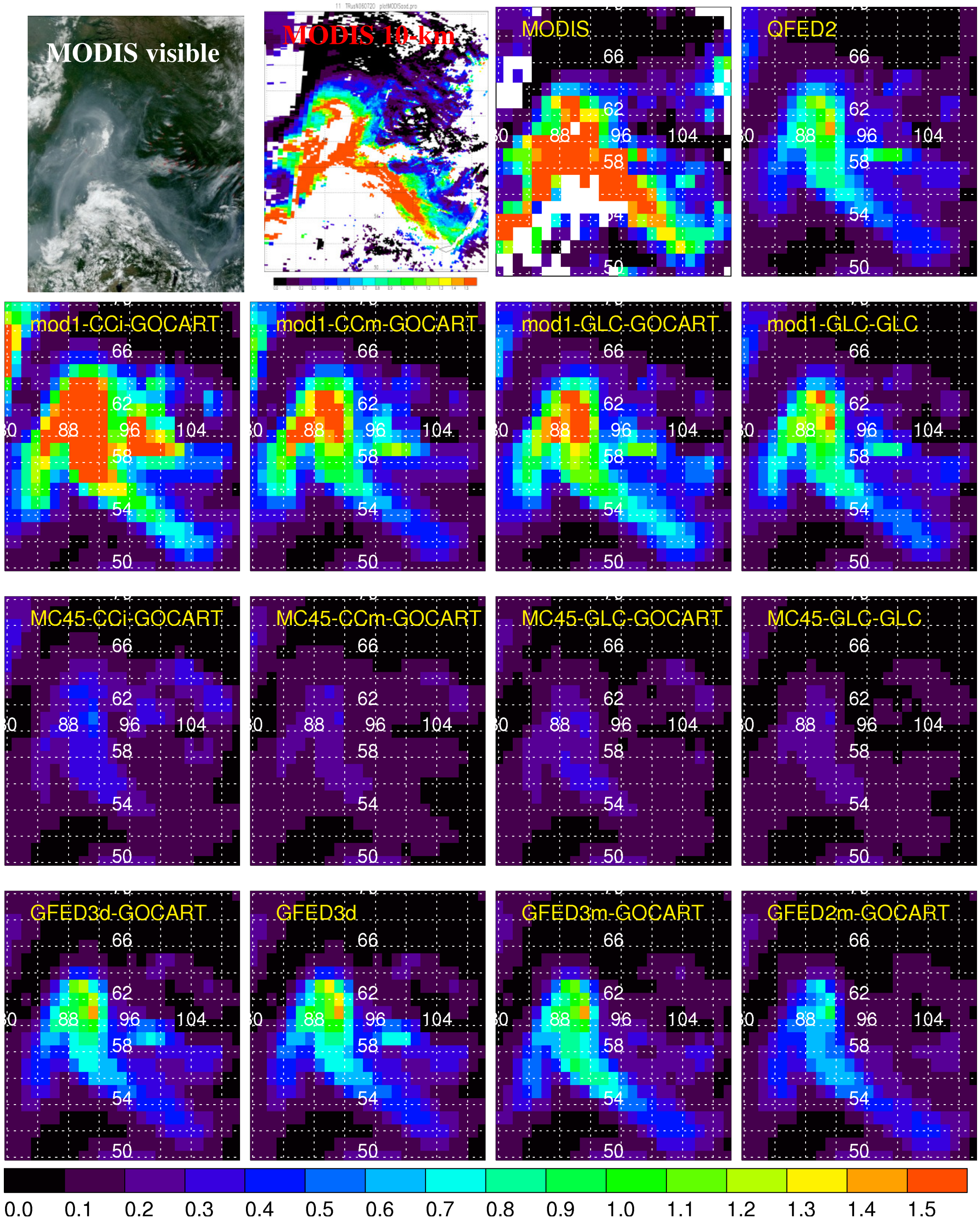

Figure A - 69 MODIS and GOCART AOD for case 11

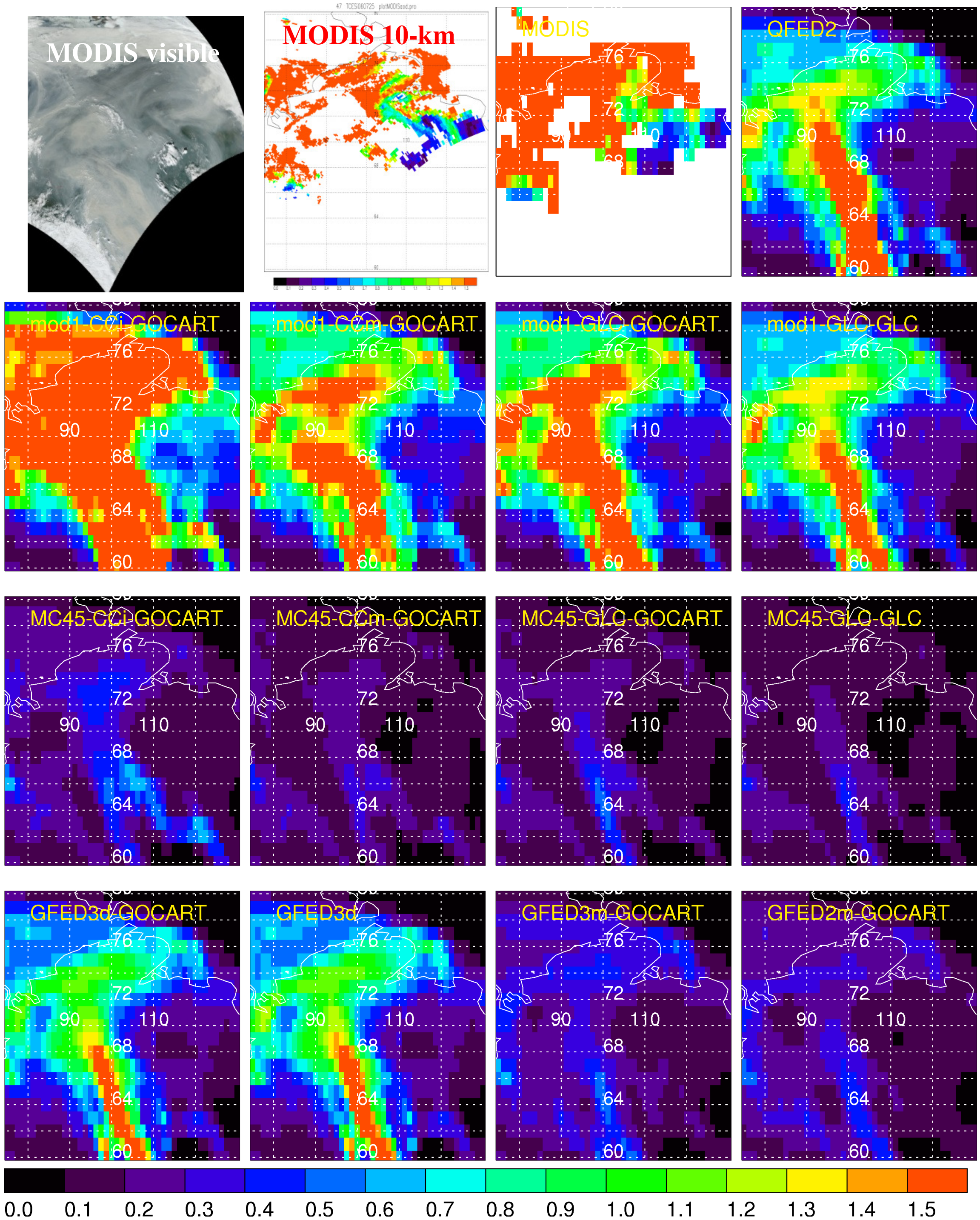

Figure A - 70 MODIS and GOCART AOD for case 47

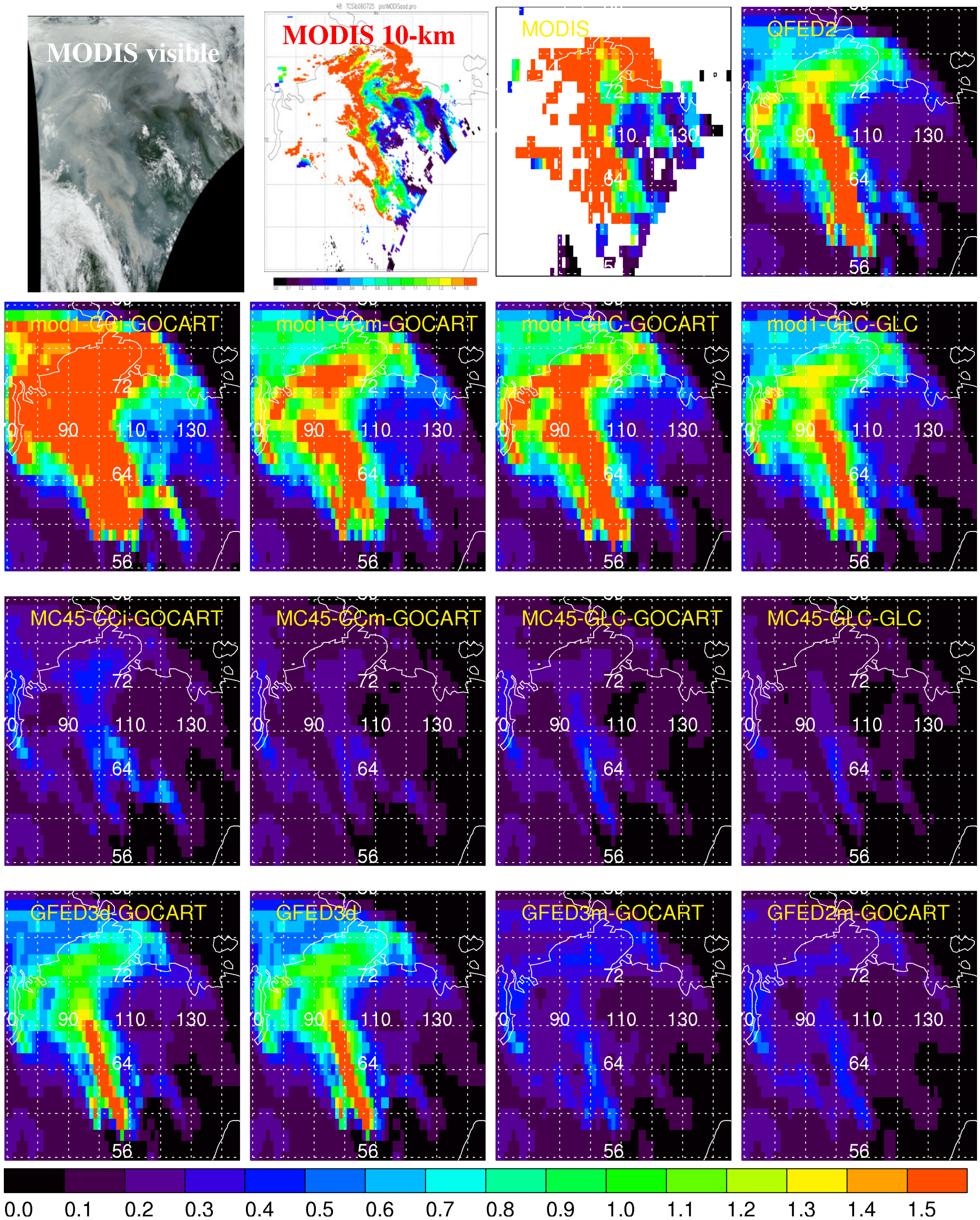

Figure A - 71 MODIS and GOCART AOD for case 48

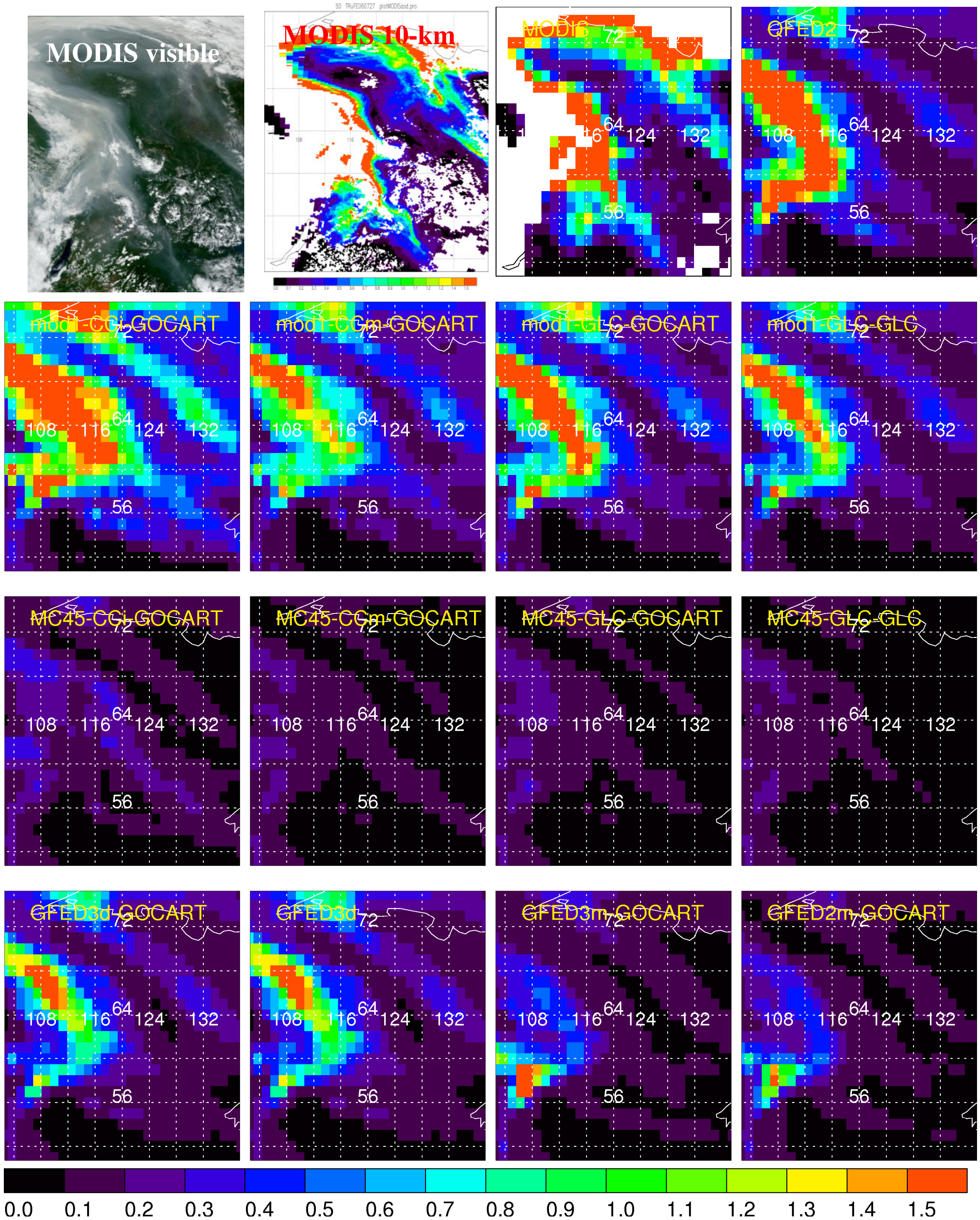

Figure A - 72 MODIS and GOCART AOD for case 50

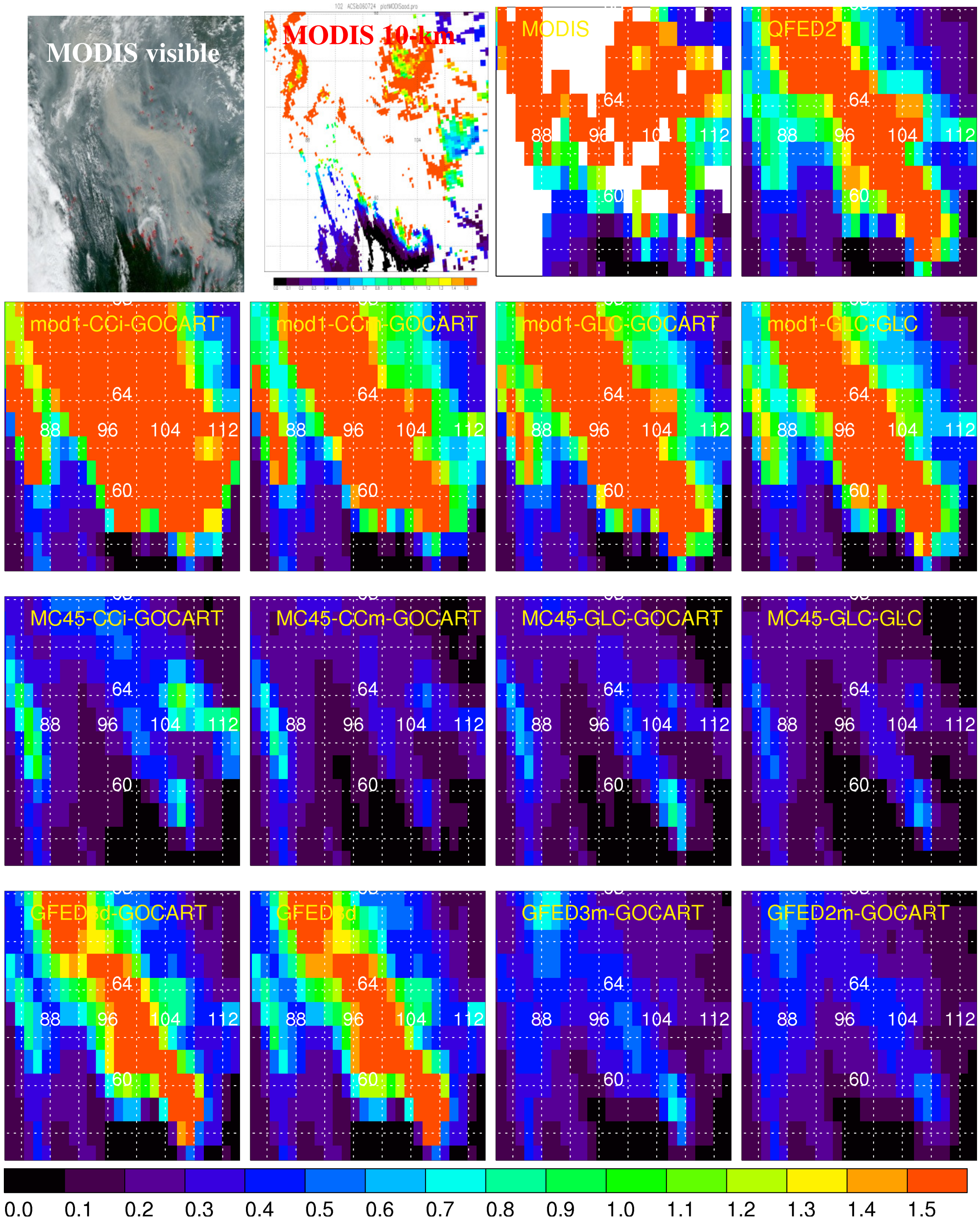

Figure A - 73 MODIS and GOCART AOD for case 102

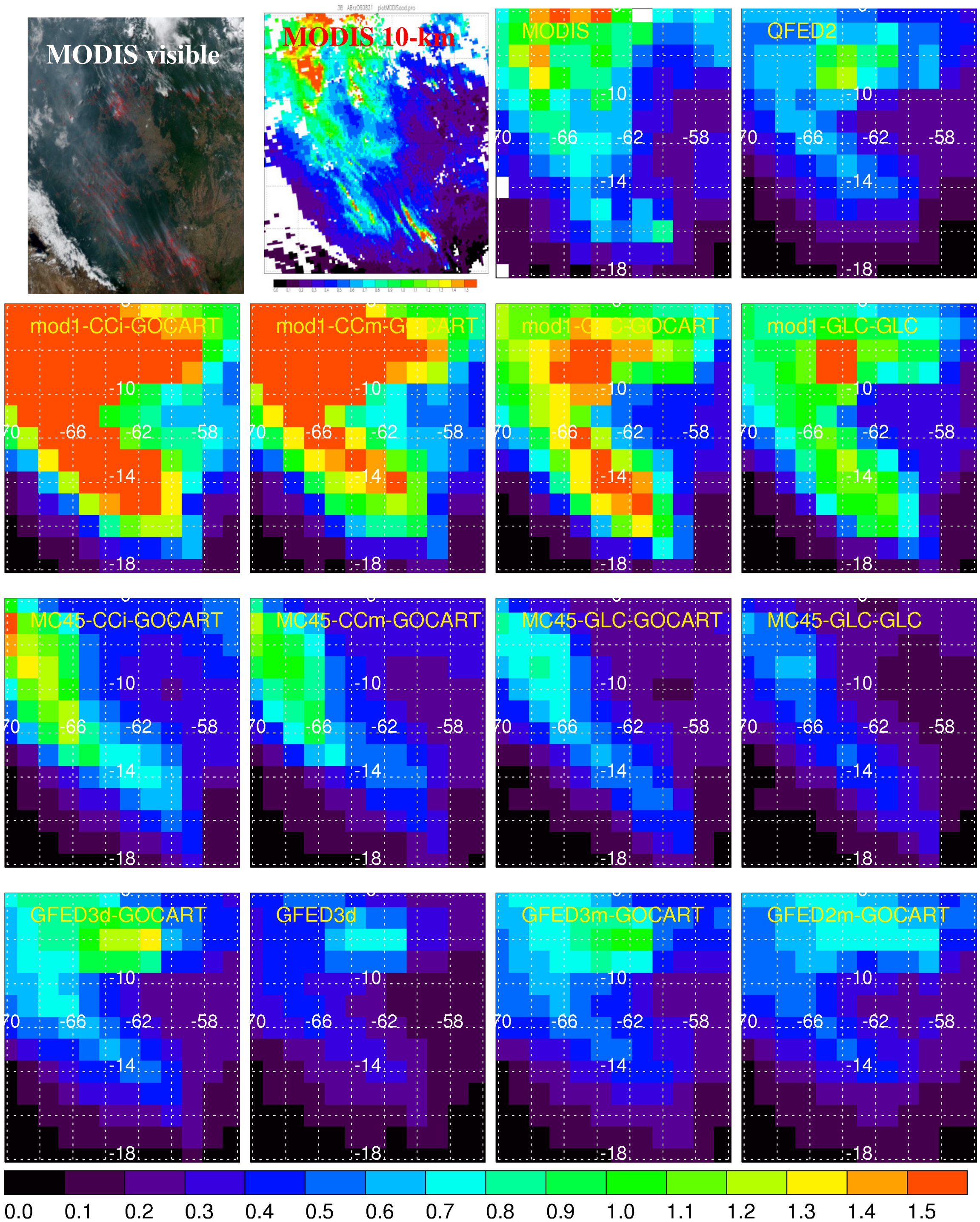

Figure A - 74 MODIS and GOCART AOD for case 38

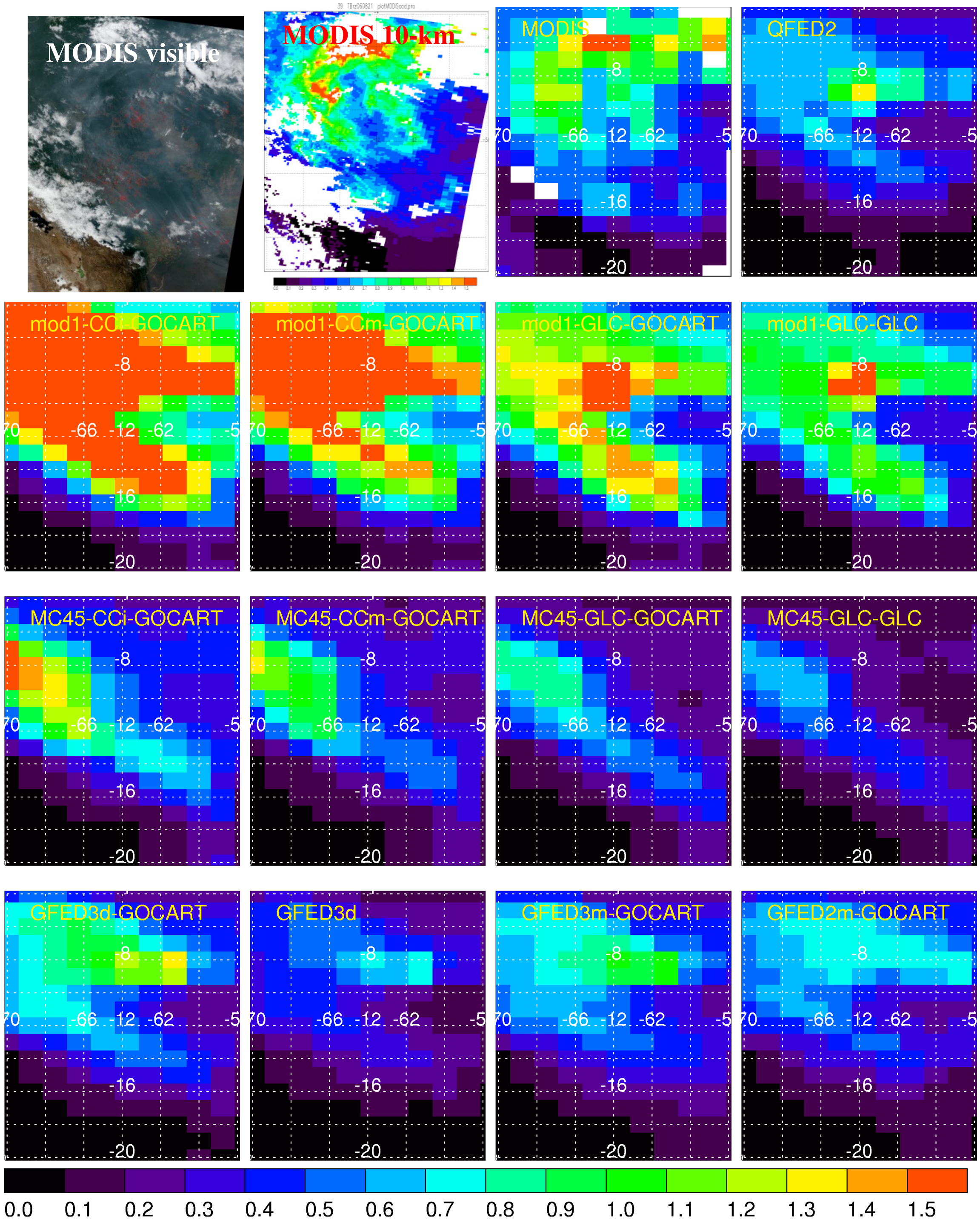

Figure A - 75 MODIS and GOCART AOD for case 39

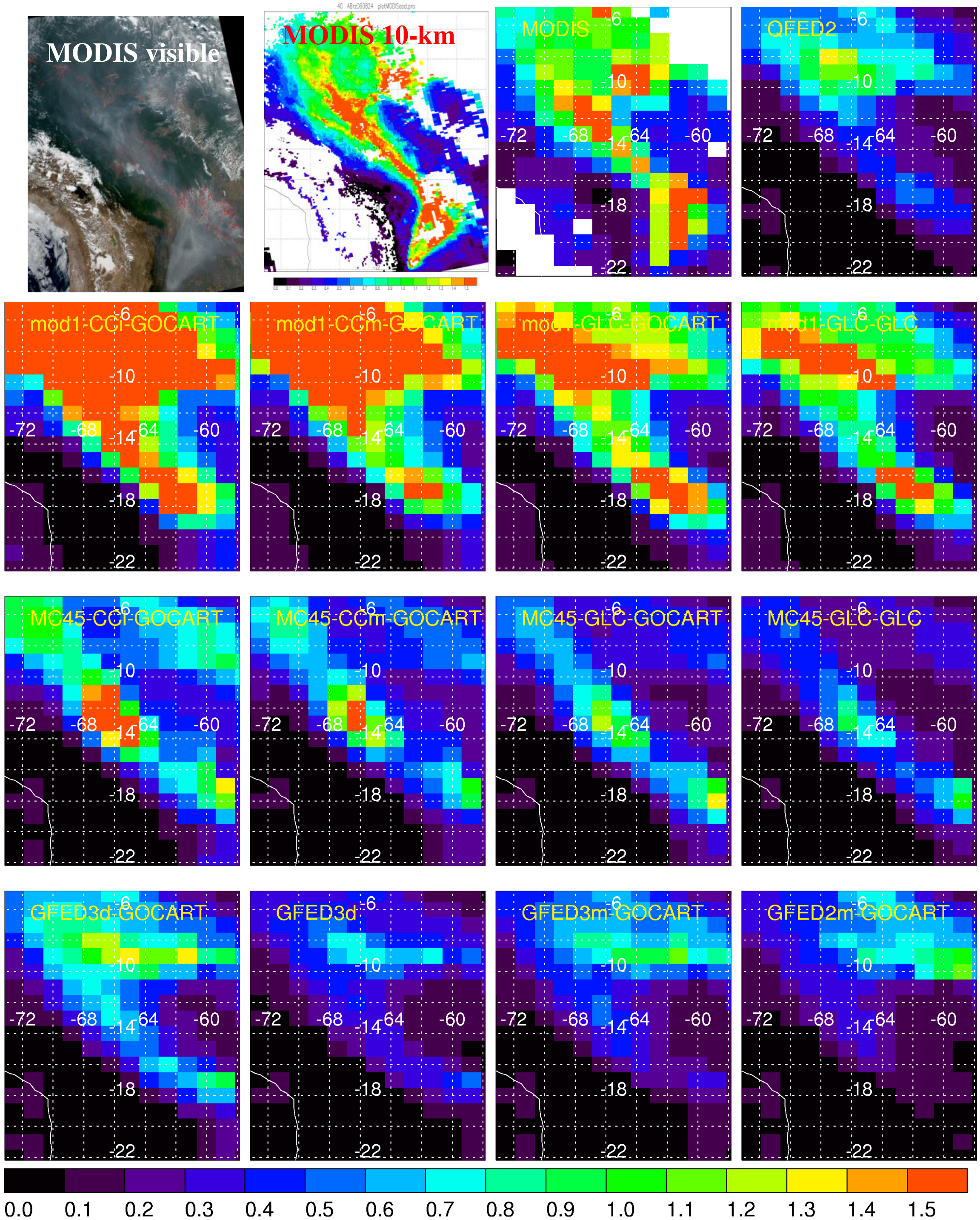

Figure A - 76 MODIS and GOCART AOD for case 40

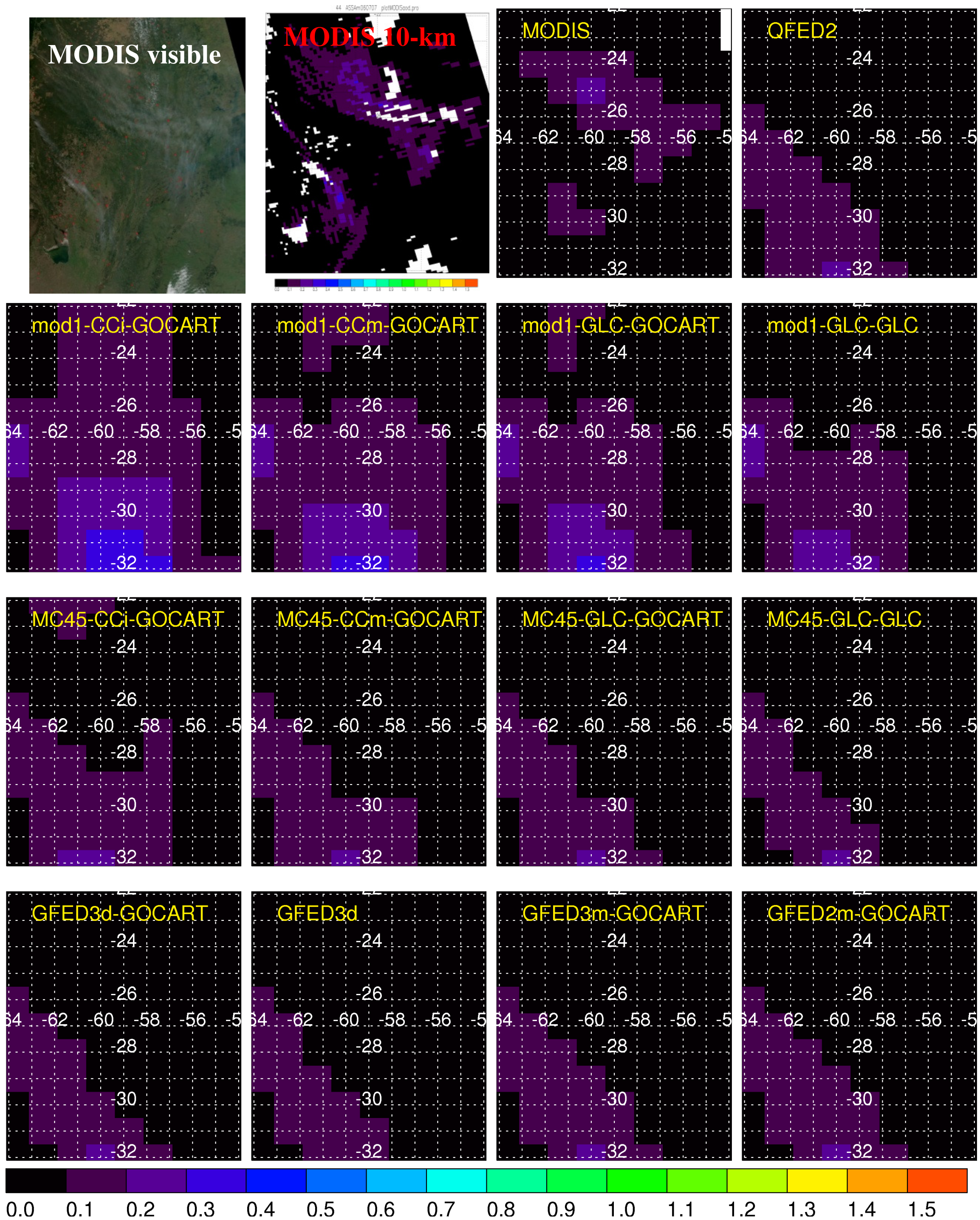

Figure A - 77 MODIS and GOCART AOD for case 44

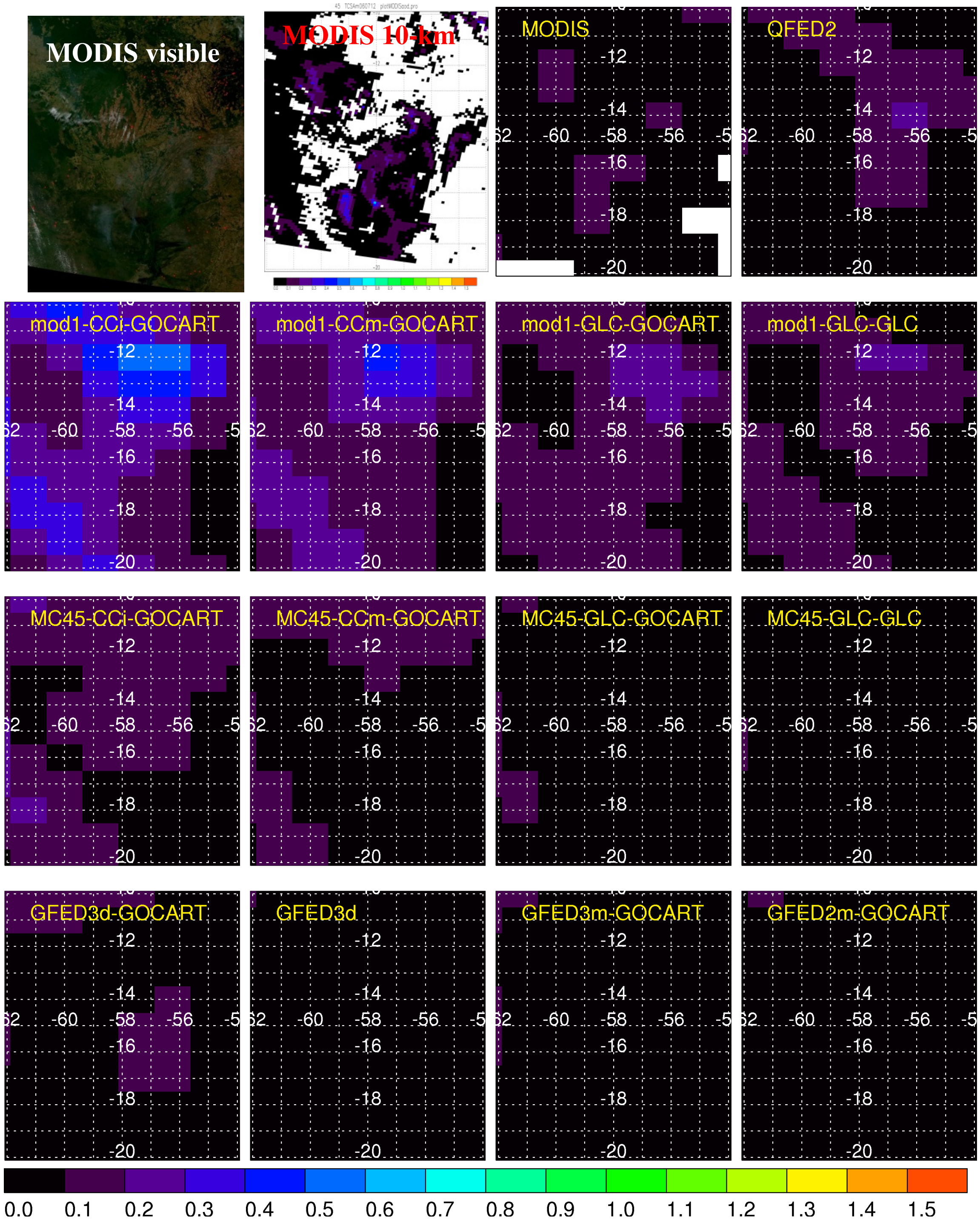

Figure A - 78 MODIS and GOCART AOD for case 45

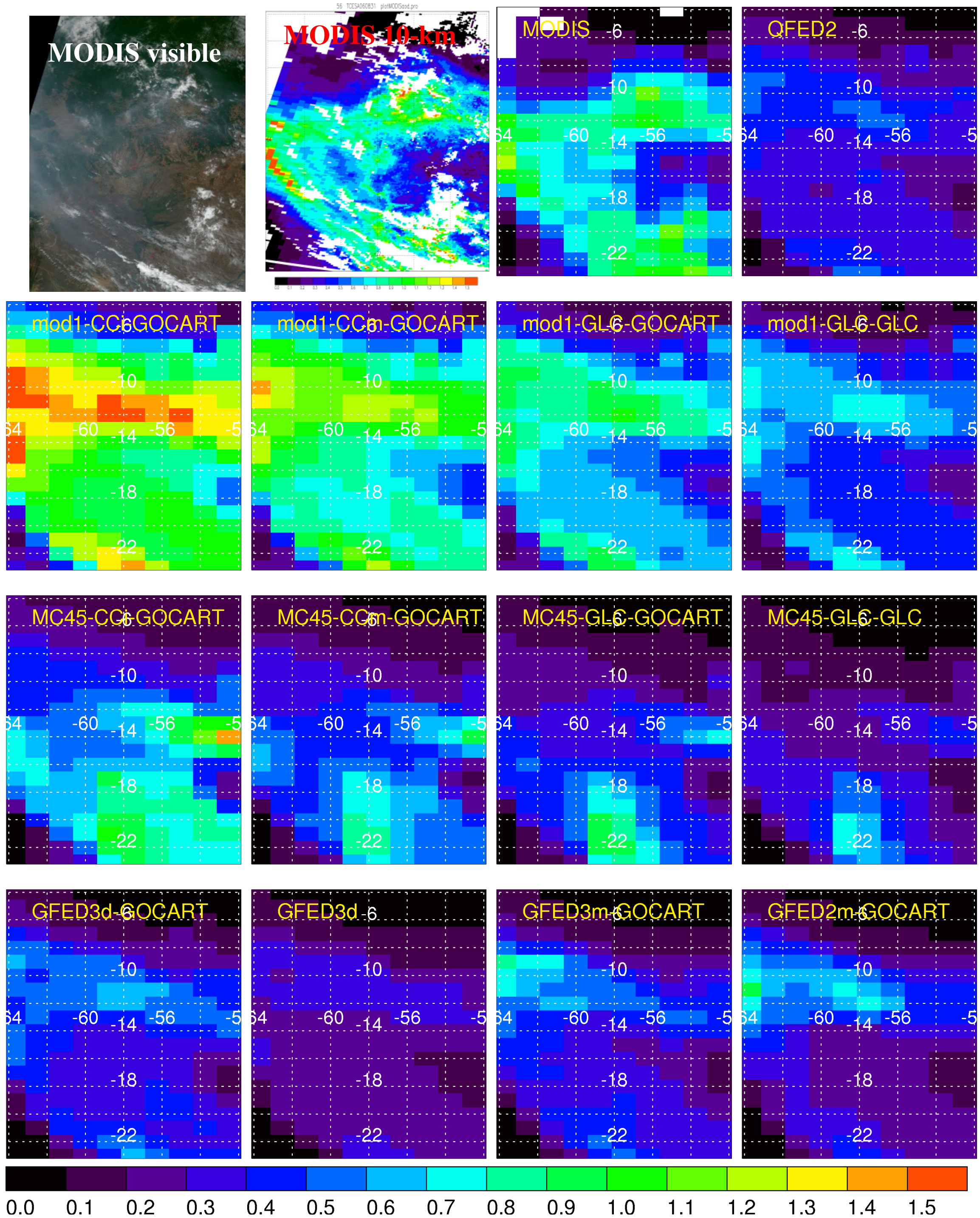

Figure A - 79 MODIS and GOCART AOD for case 56

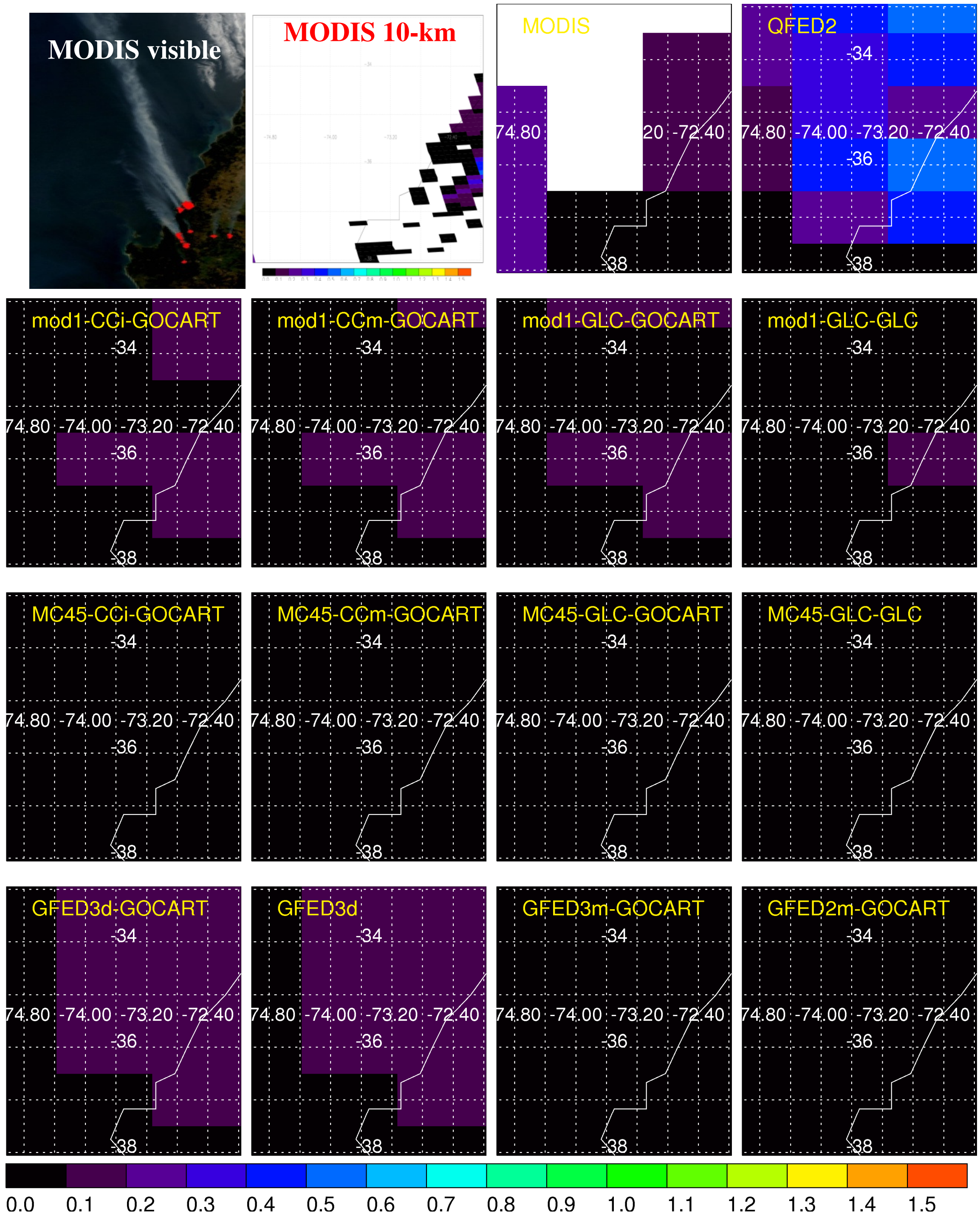

Figure A - 80 MODIS and GOCART AOD for case 89

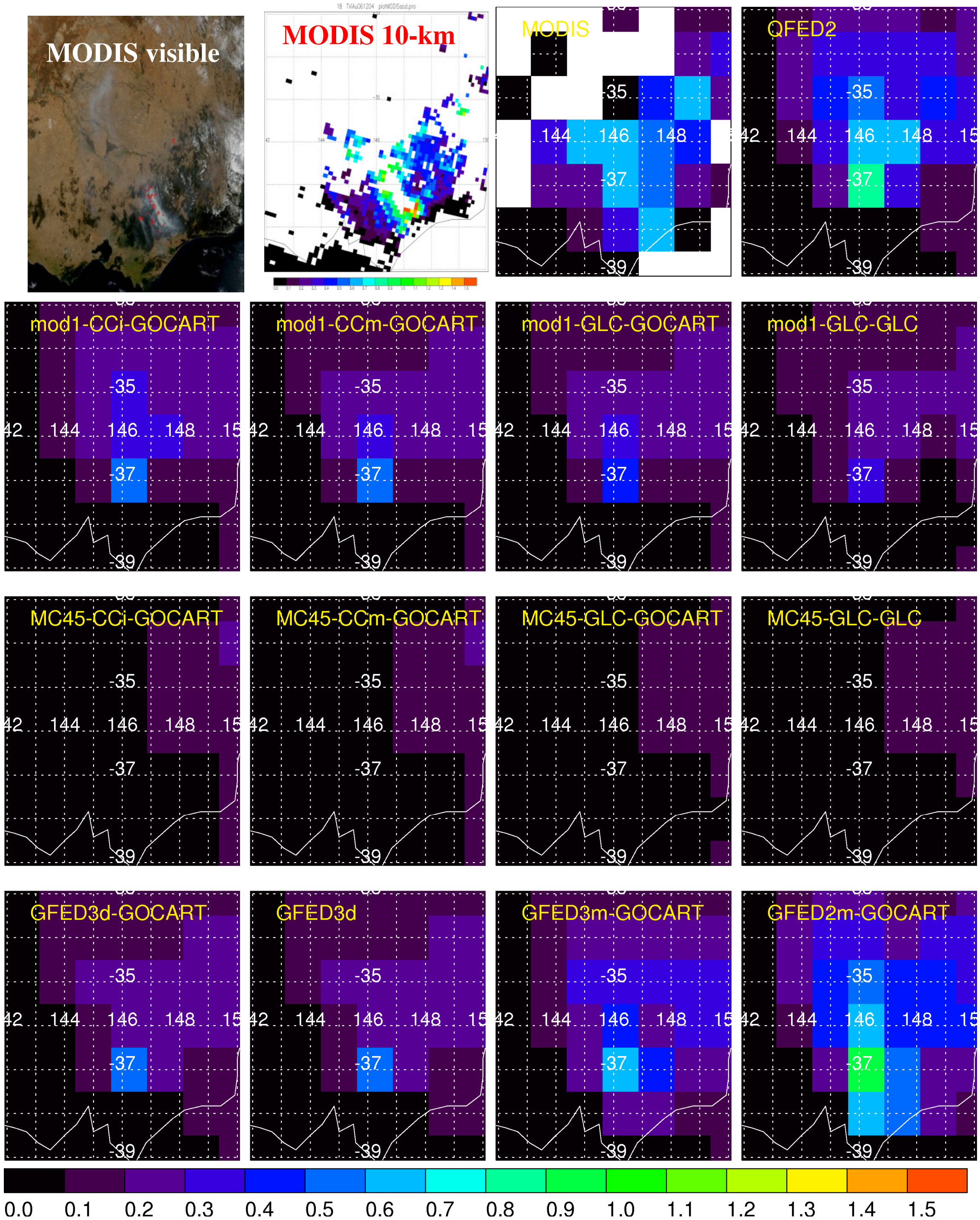

Figure A - 81 MODIS and GOCART AOD for case 18

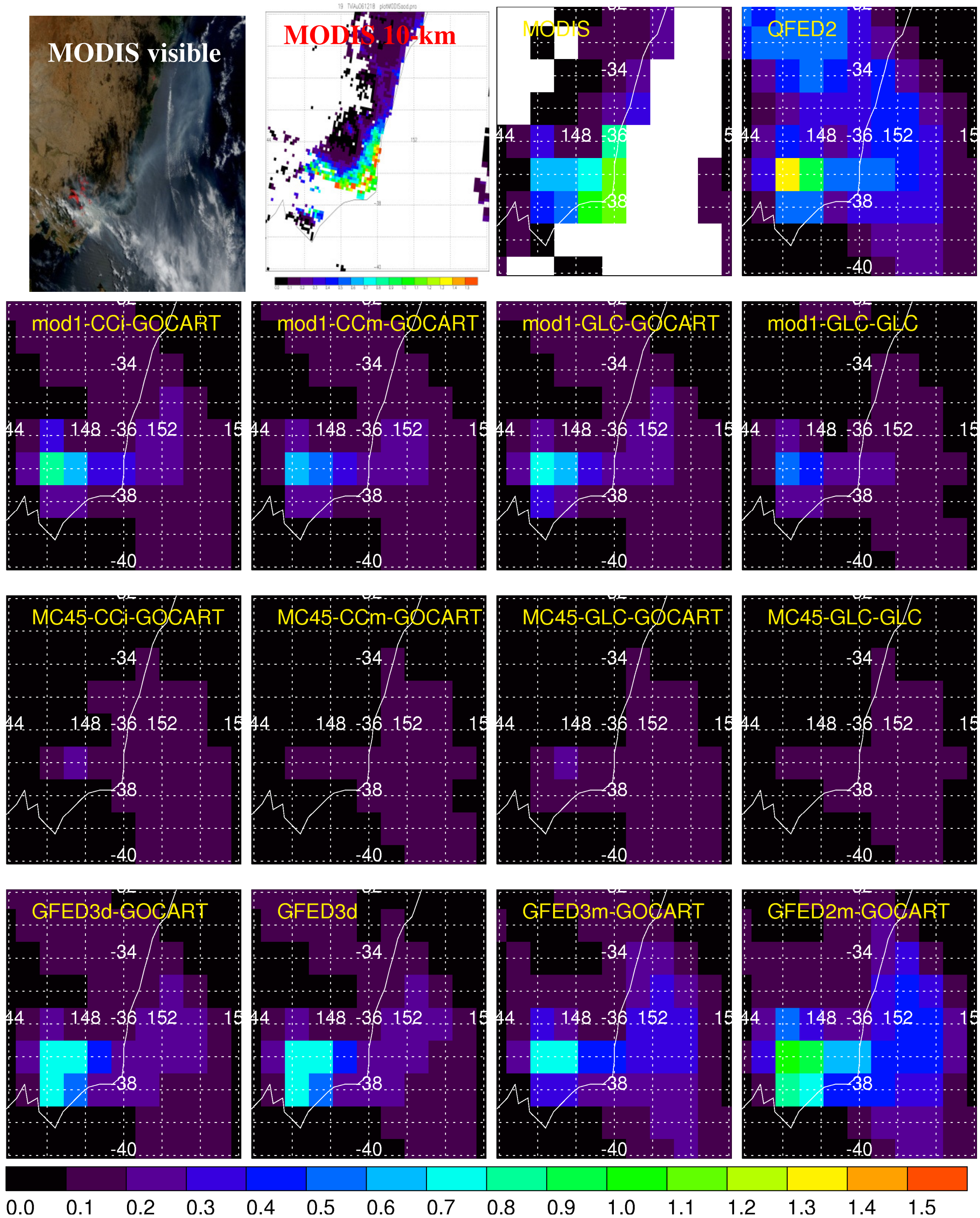

Figure A - 82 MODIS and GOCART AOD for case 19

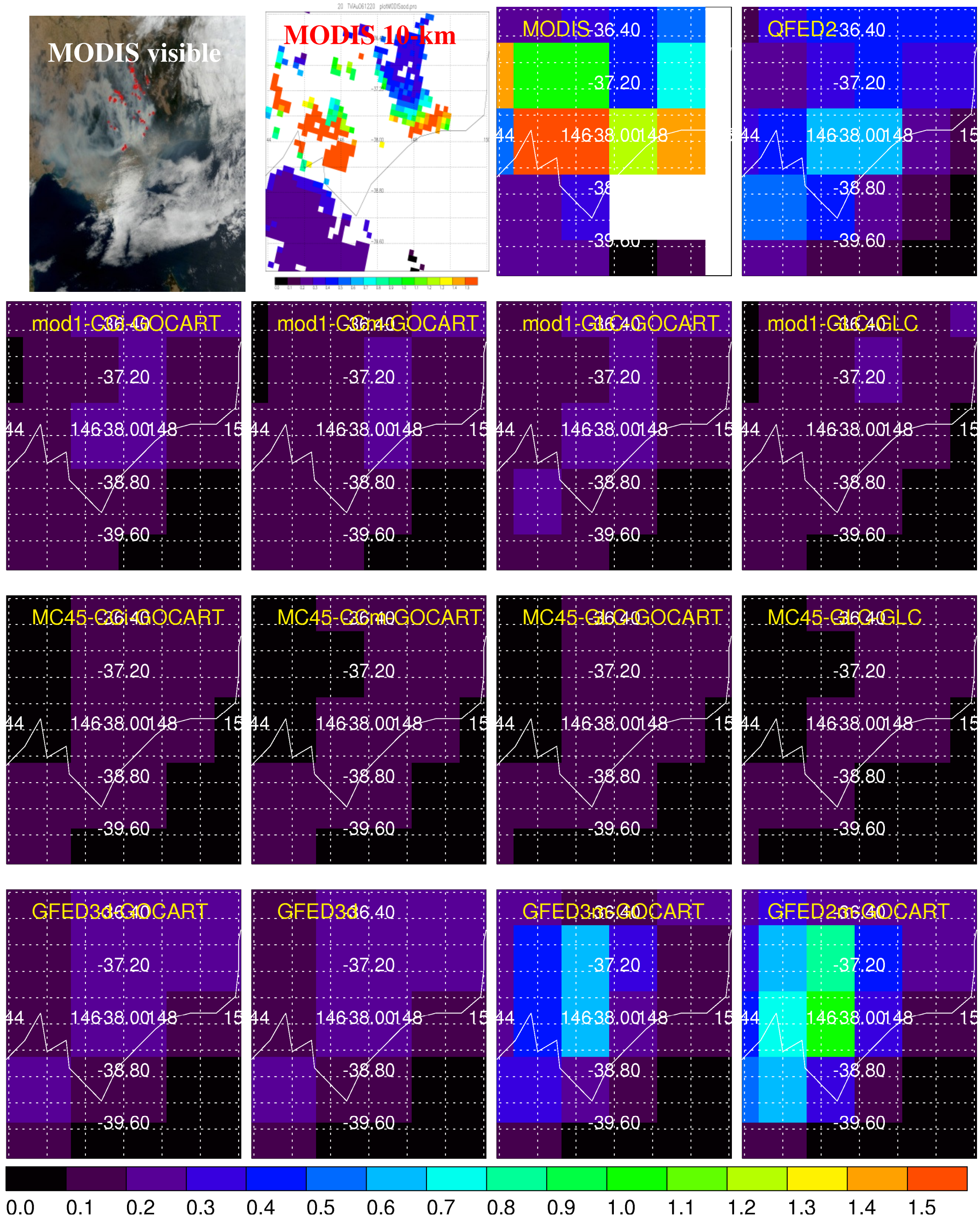

Figure A - 83 MODIS and GOCART AOD for case 20

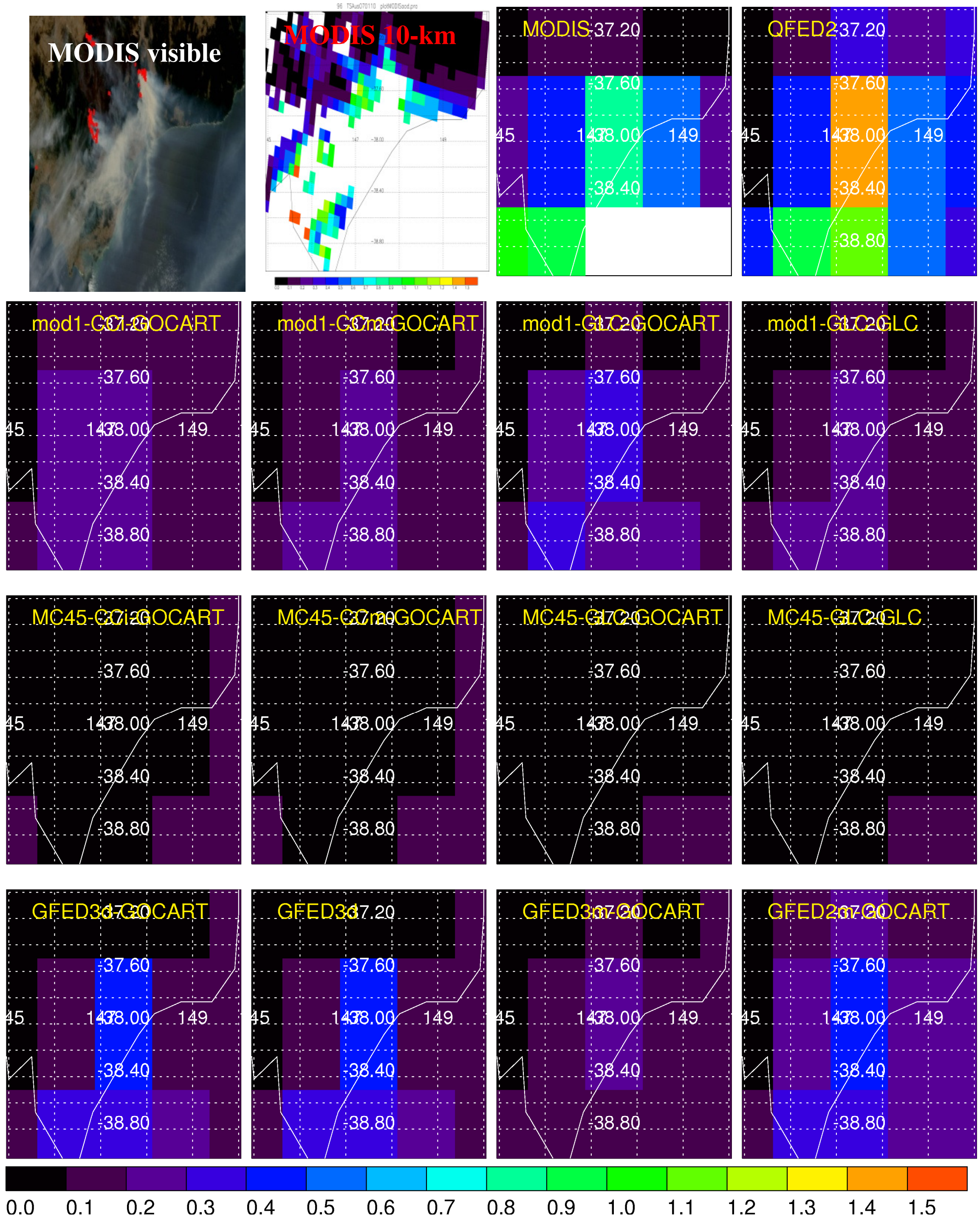

Figure A - 84 MODIS and GOCART AOD for case 96

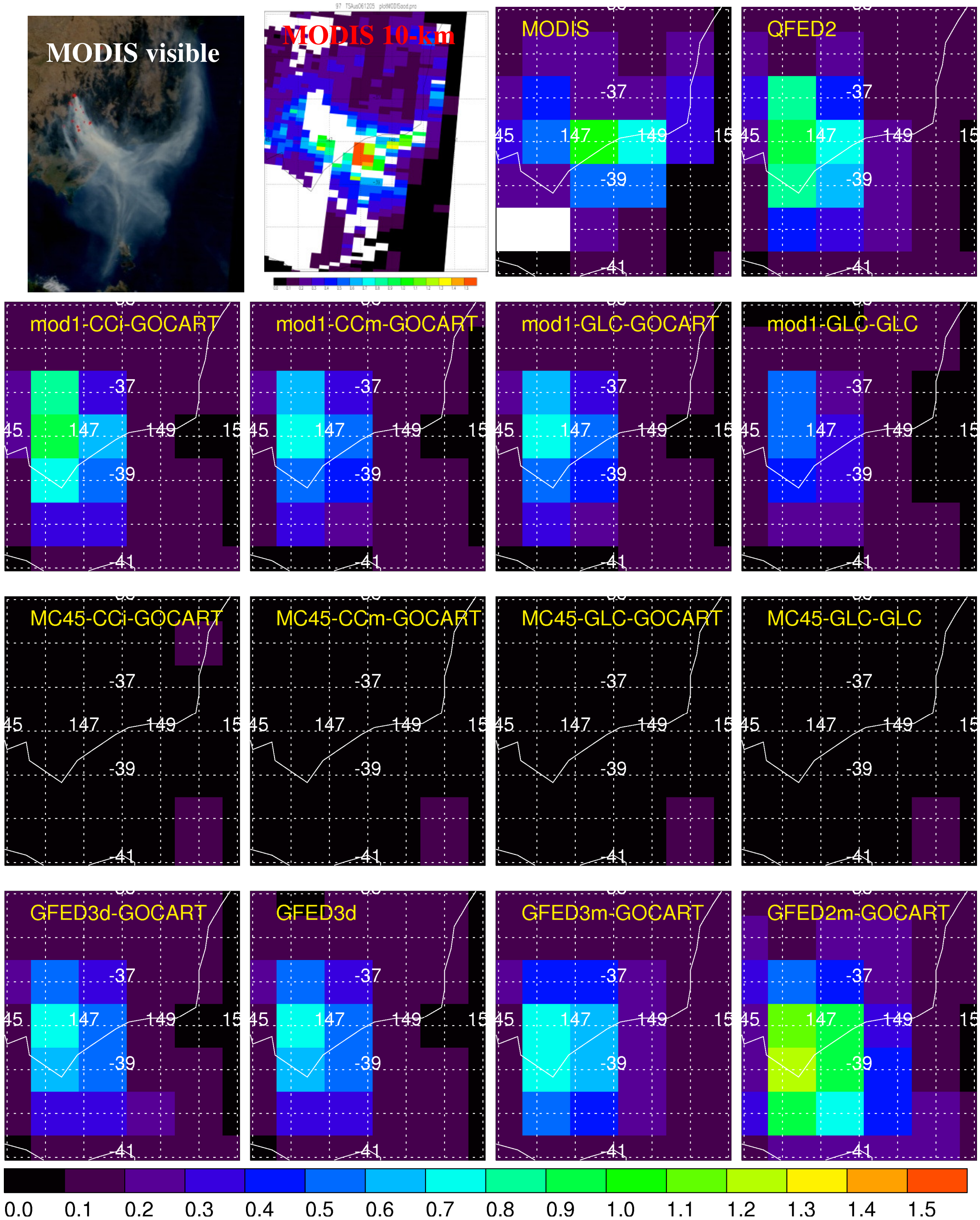

Figure A - 85 MODIS and GOCART AOD for case 97

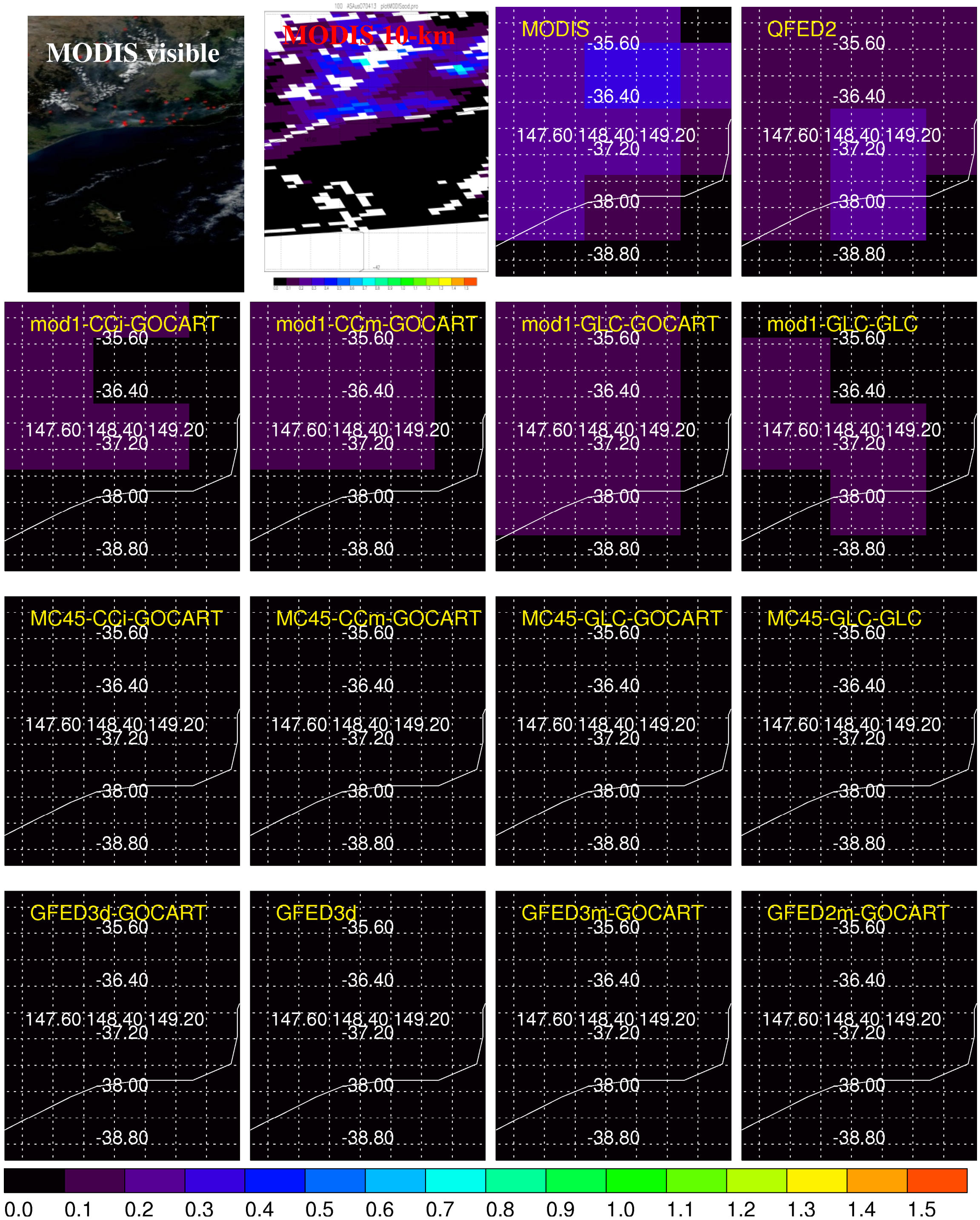

Figure A - 86 MODIS and GOCART AOD for case 100

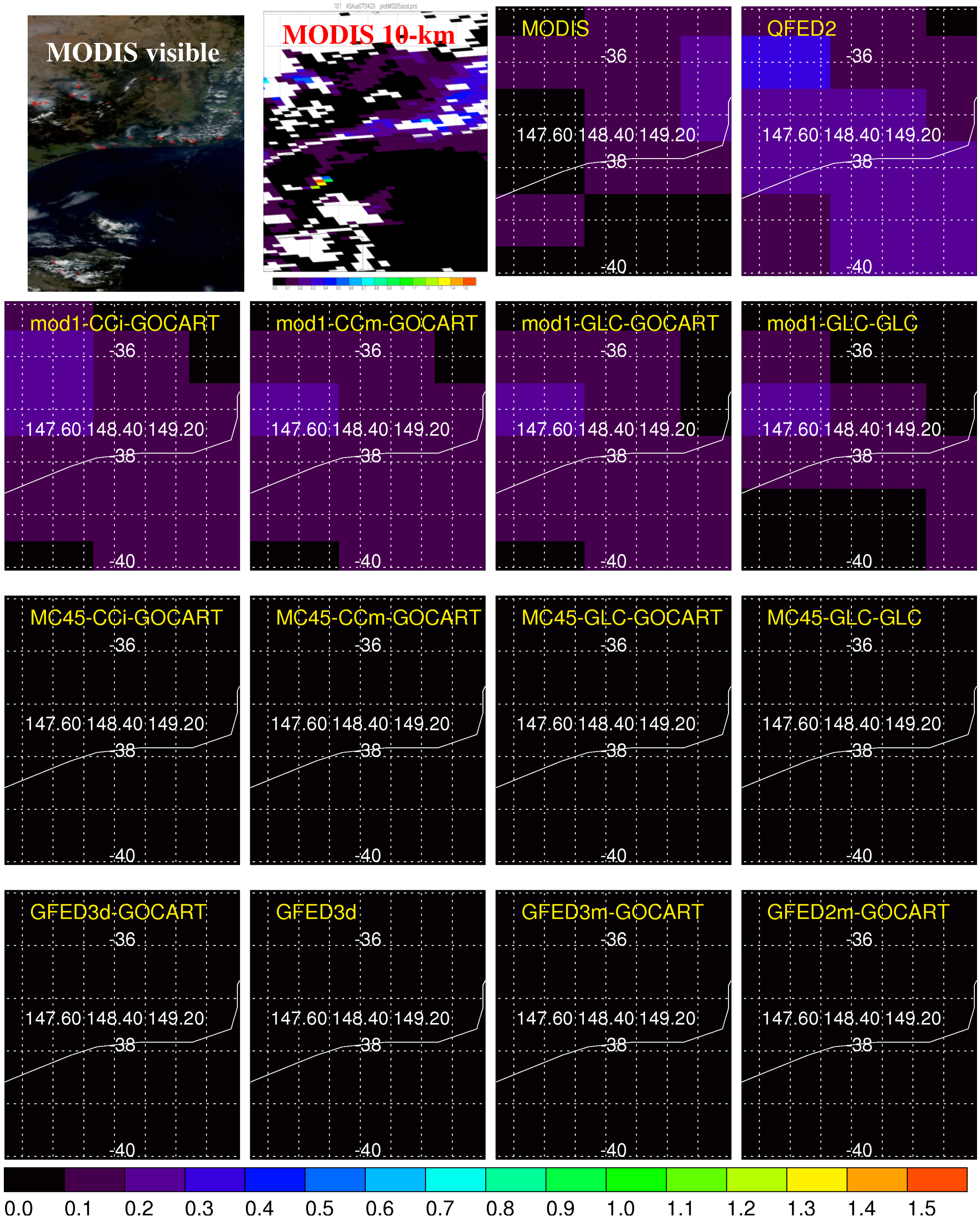

Figure A - 87 MODIS and GOCART AOD for case 101

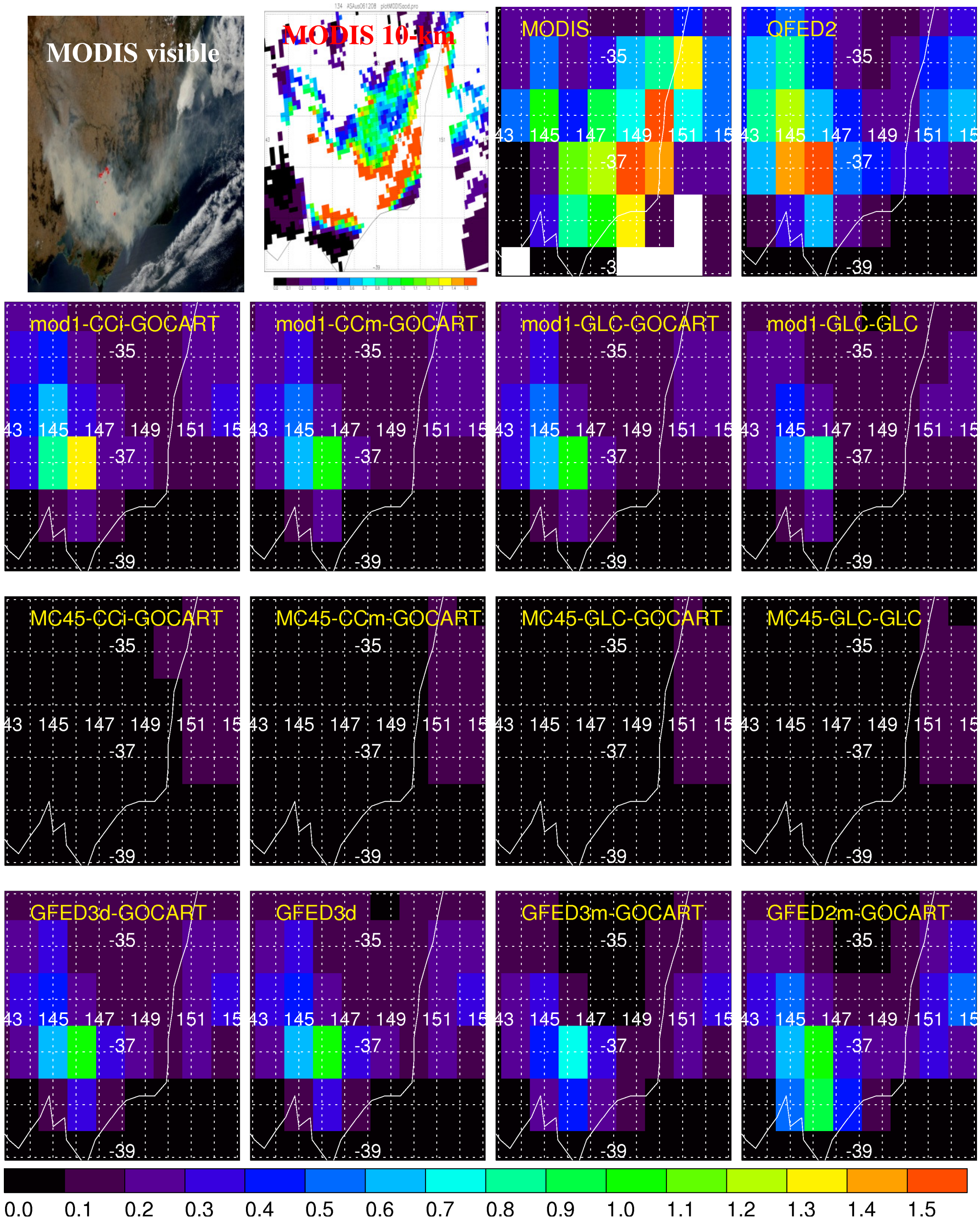

Figure A - 88 MODIS and GOCART AOD for case 134

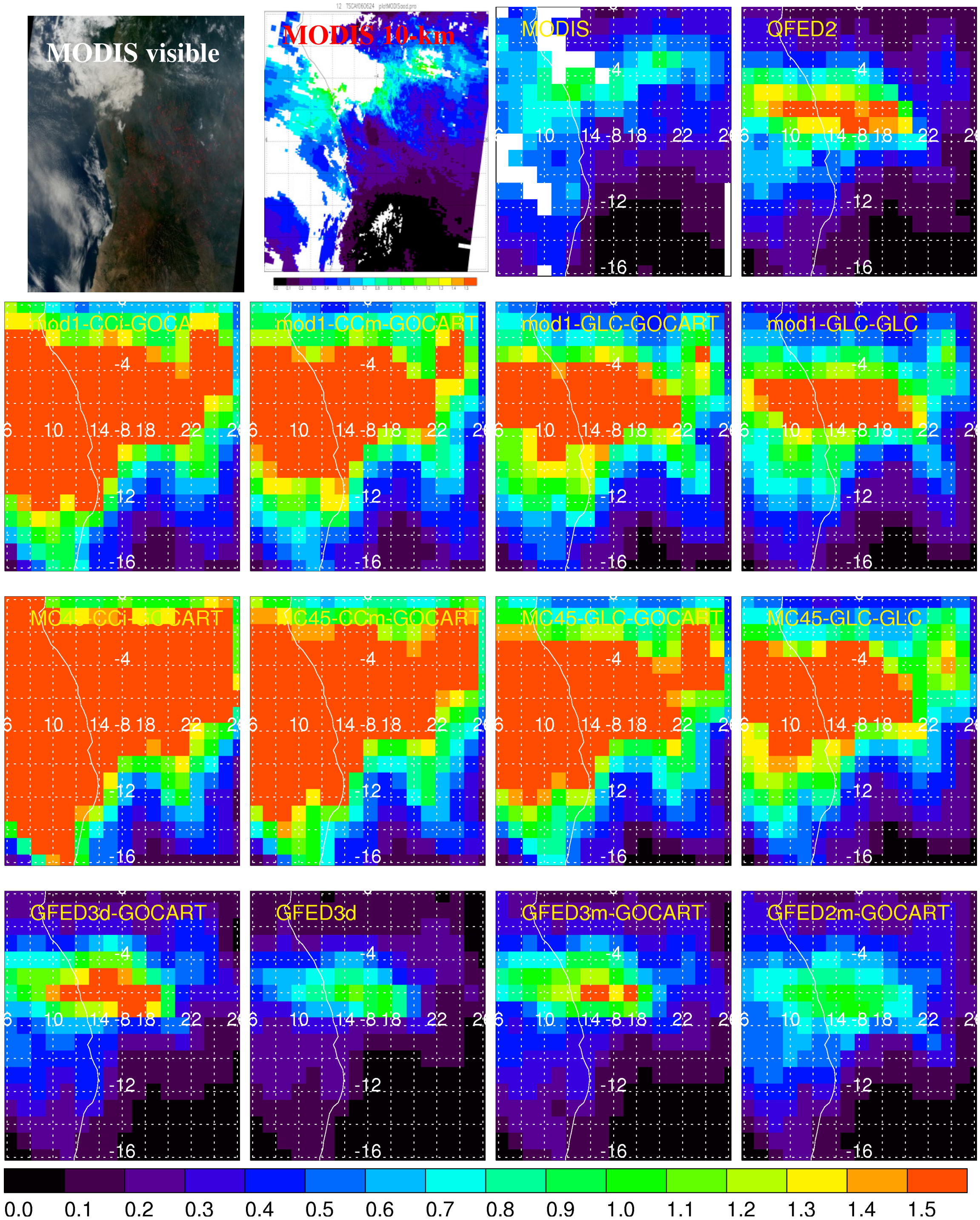

Figure A - 89 MODIS and GOCART AOD for case 12

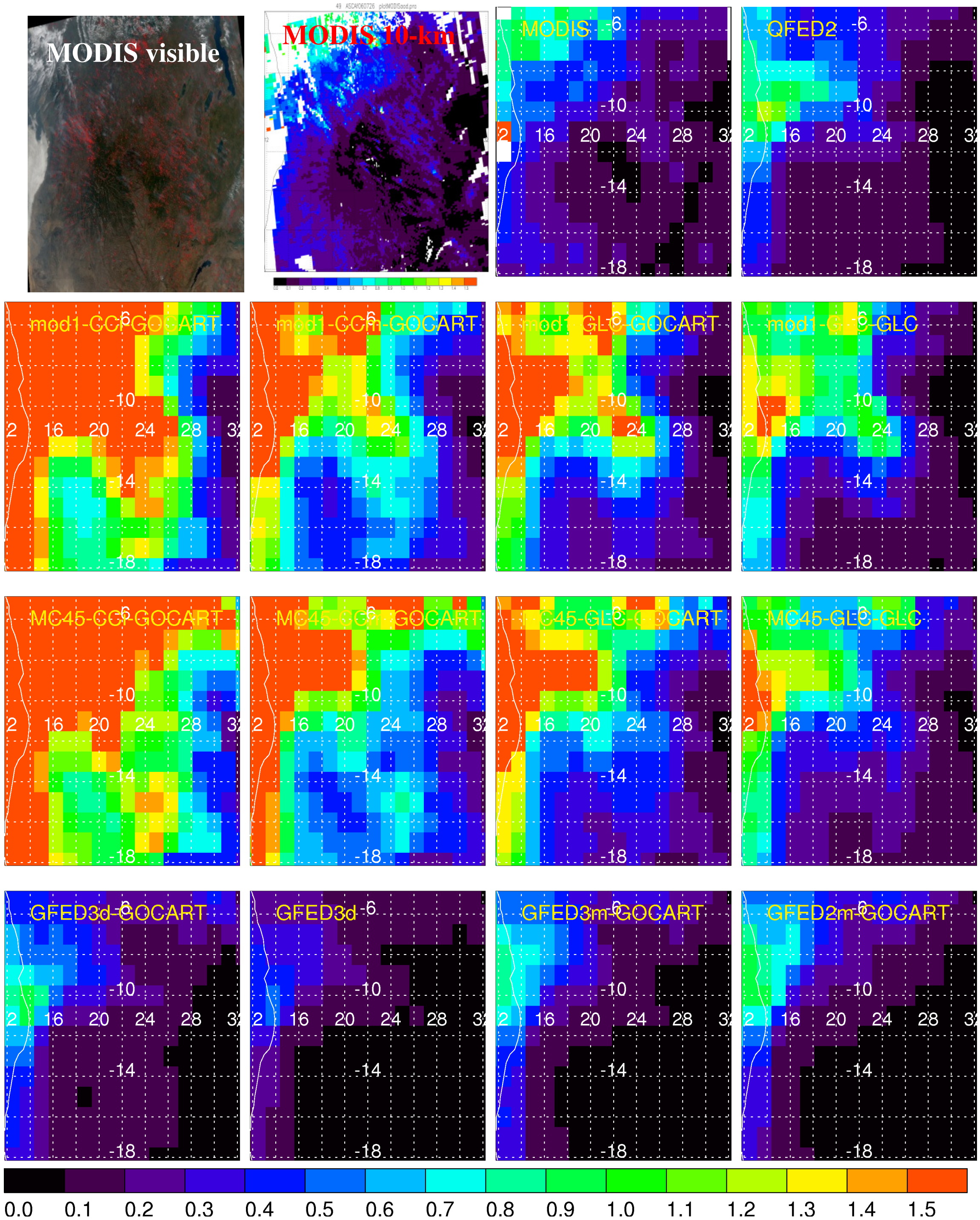

Figure A - 90 MODIS and GOCART AOD for case 49

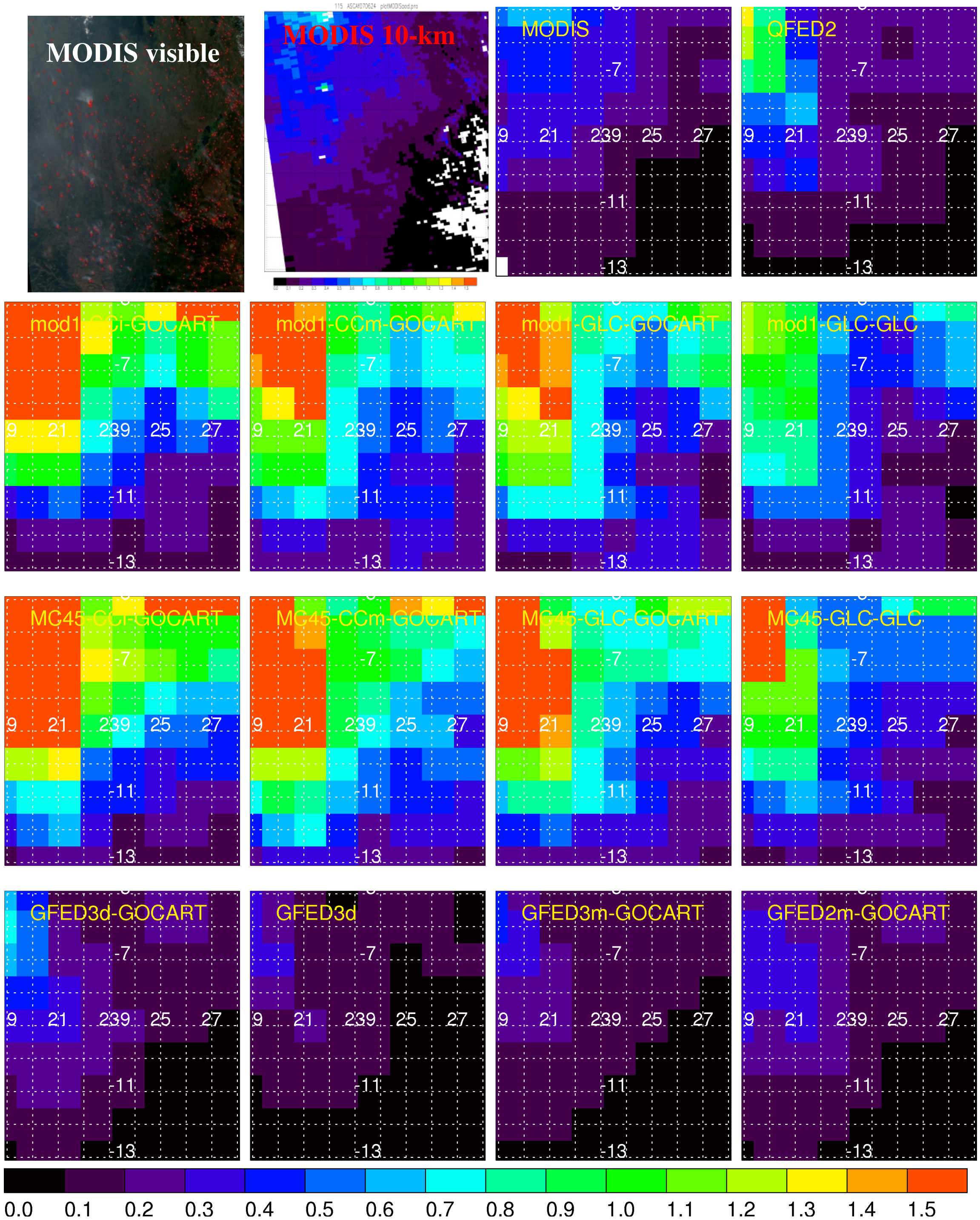

Figure A - 91 MODIS and GOCART AOD for case 115

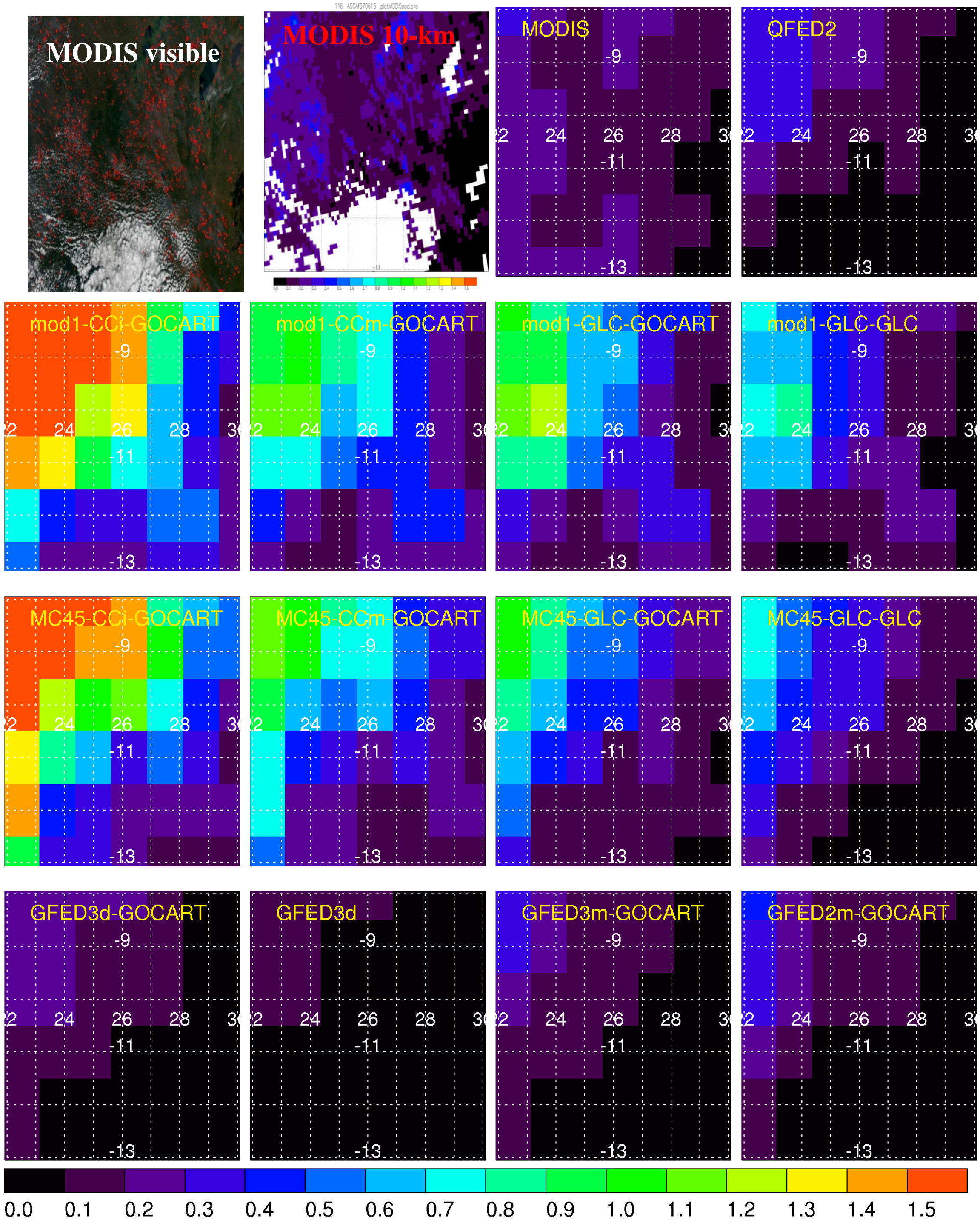

Figure A - 92 MODIS and GOCART AOD for case 116

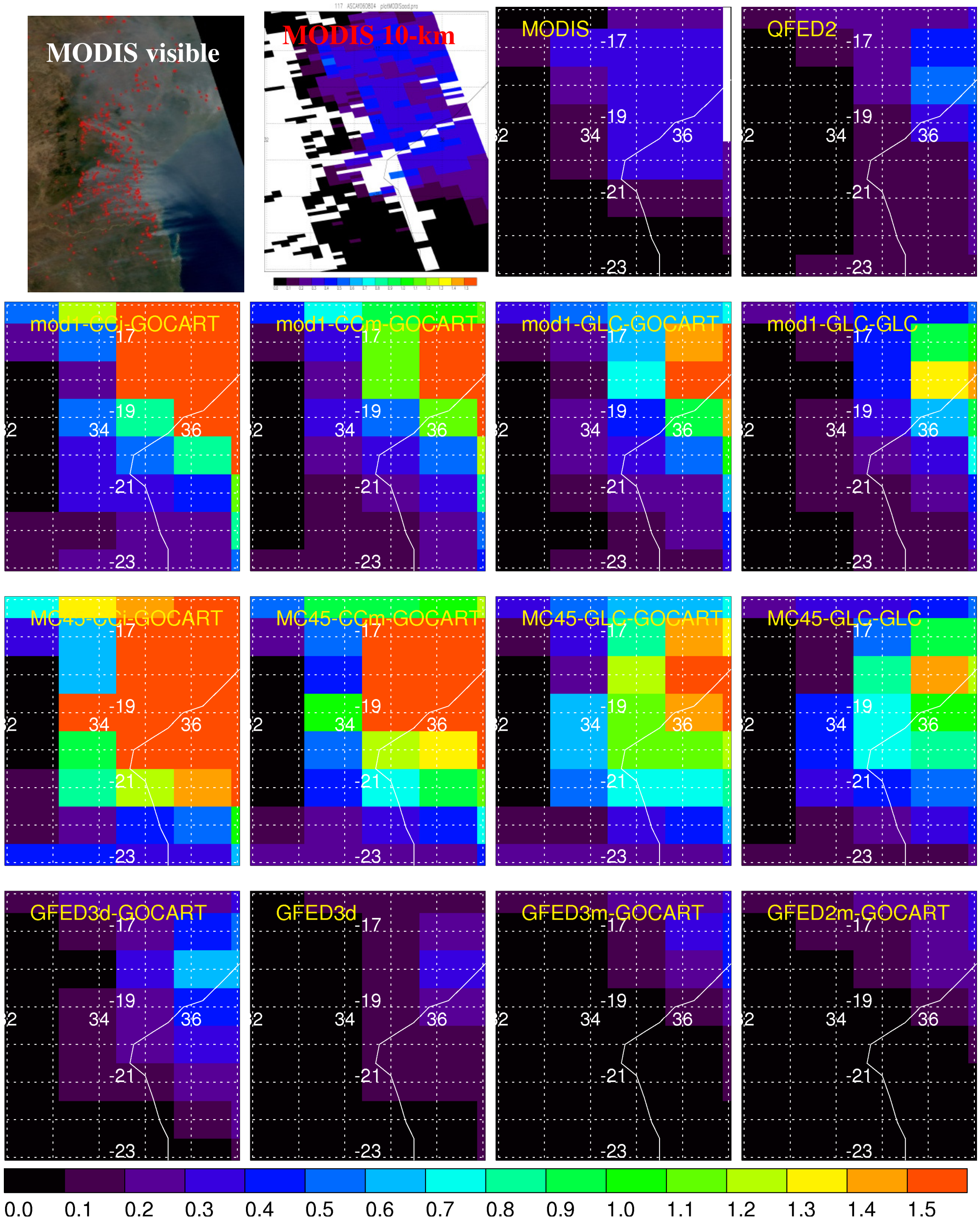

Figure A - 93 MODIS and GOCART AOD for case 117

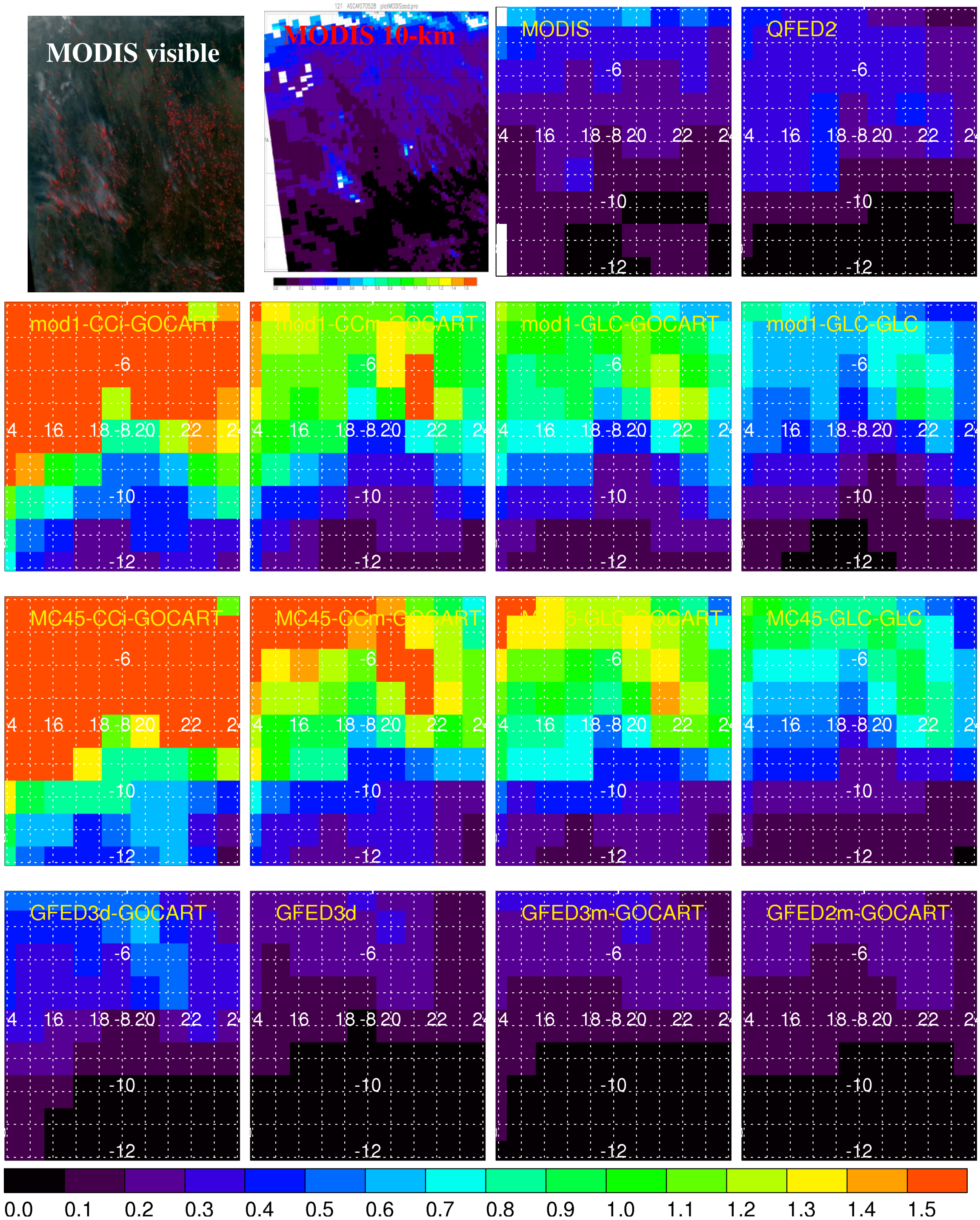

Figure A - 94 MODIS and GOCART AOD for case 121

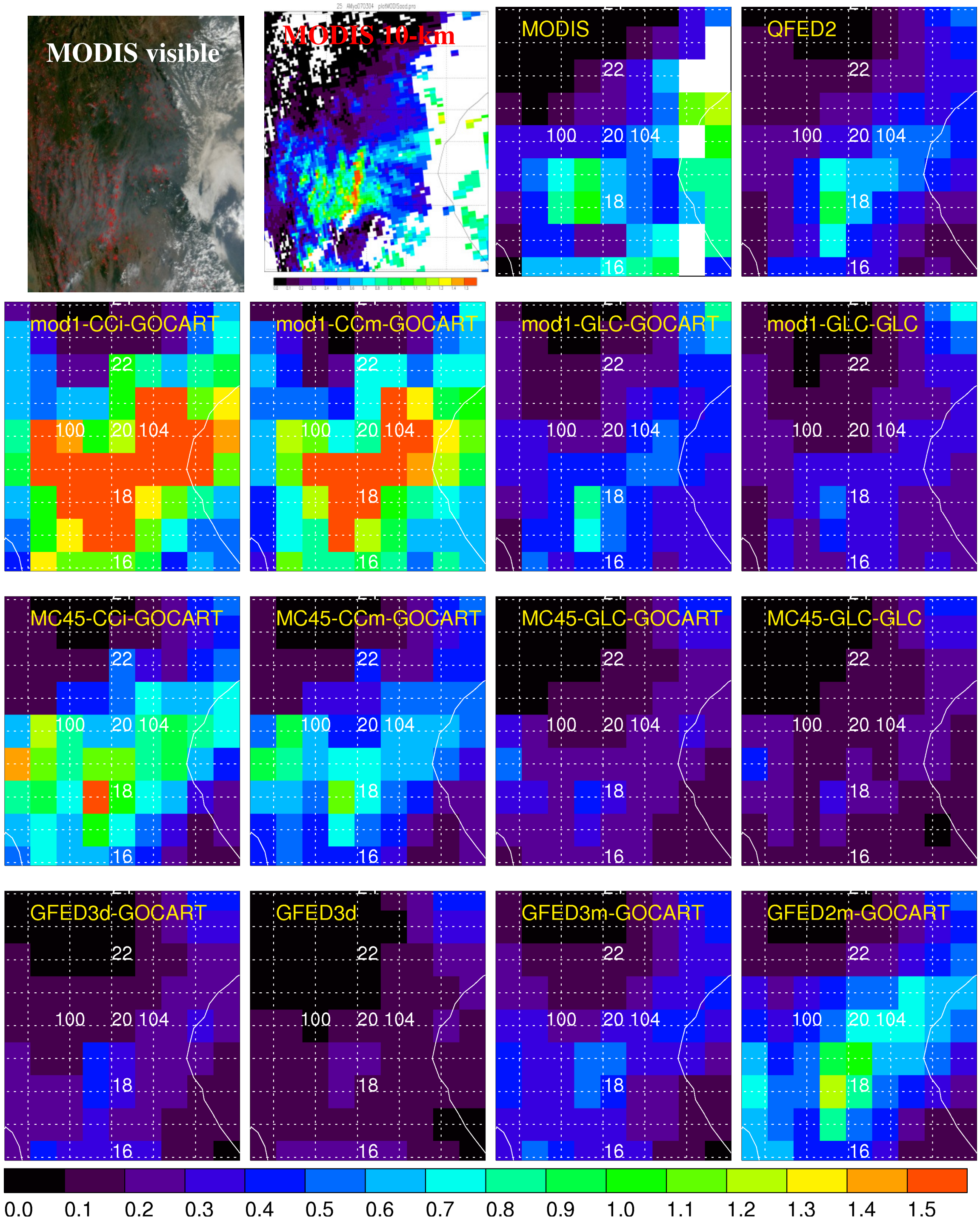

Figure A - 95 MODIS and GOCART AOD for case 25

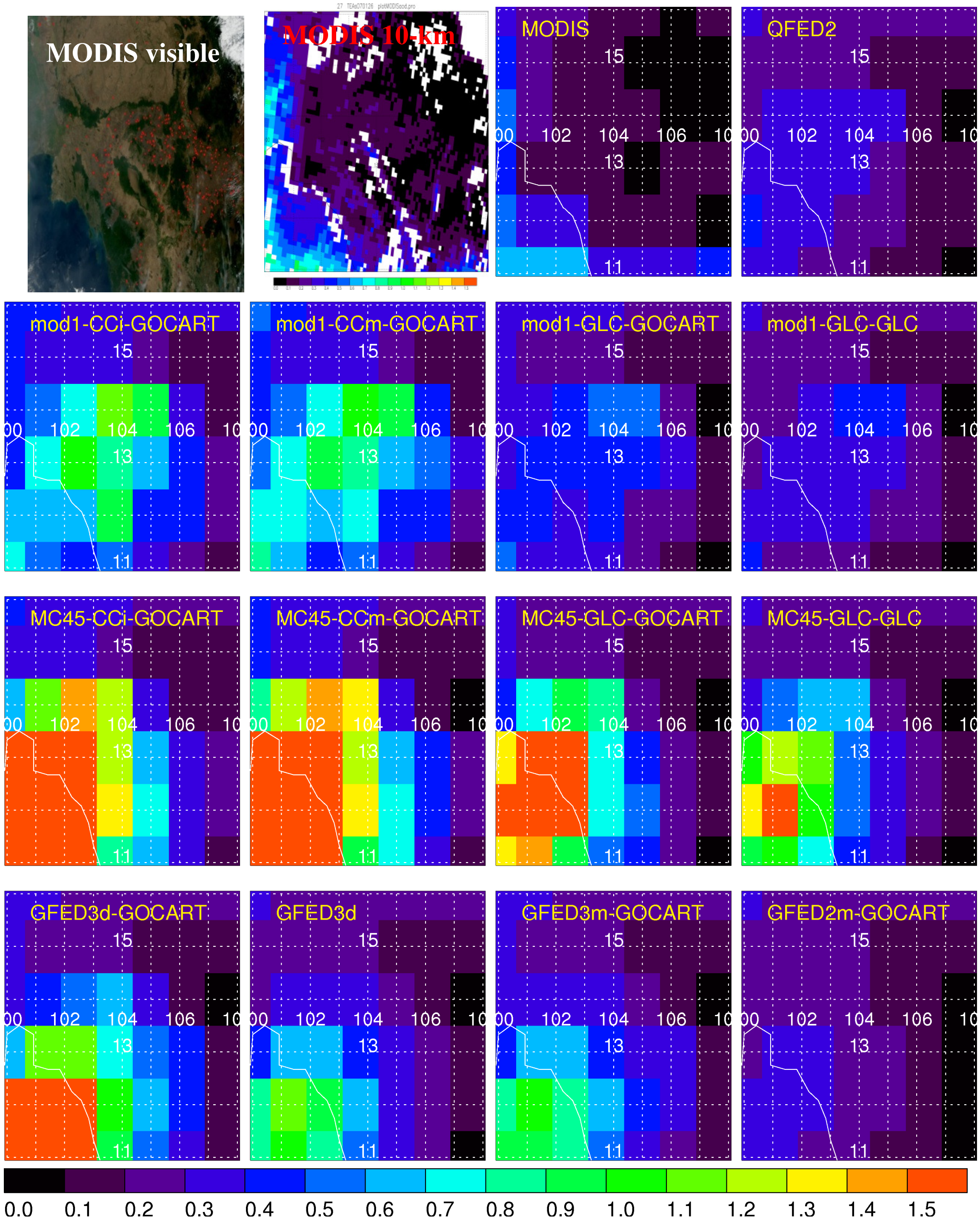

Figure A - 96 MODIS and GOCART AOD for case 27

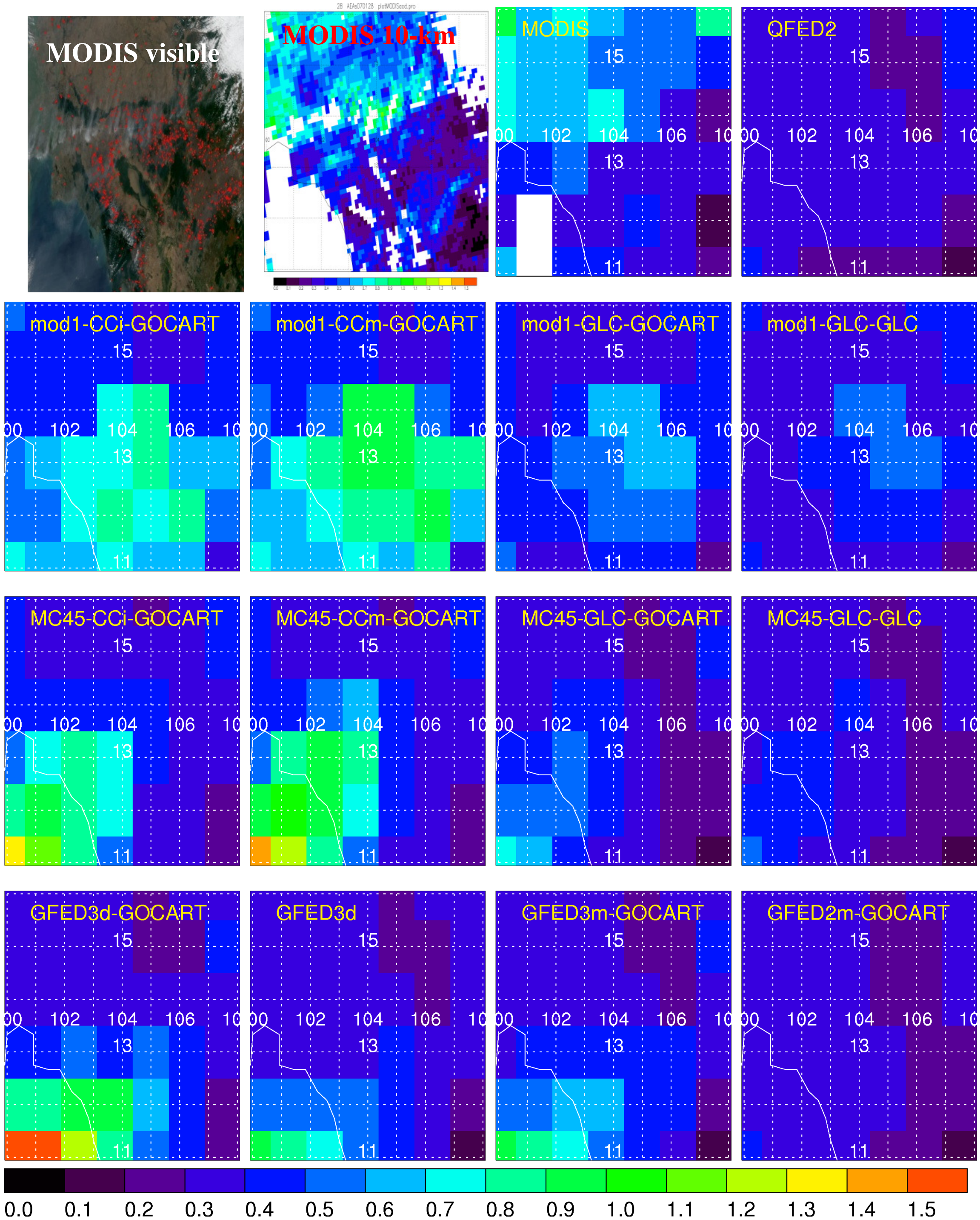

Figure A - 97 MODIS and GOCART AOD for case 28

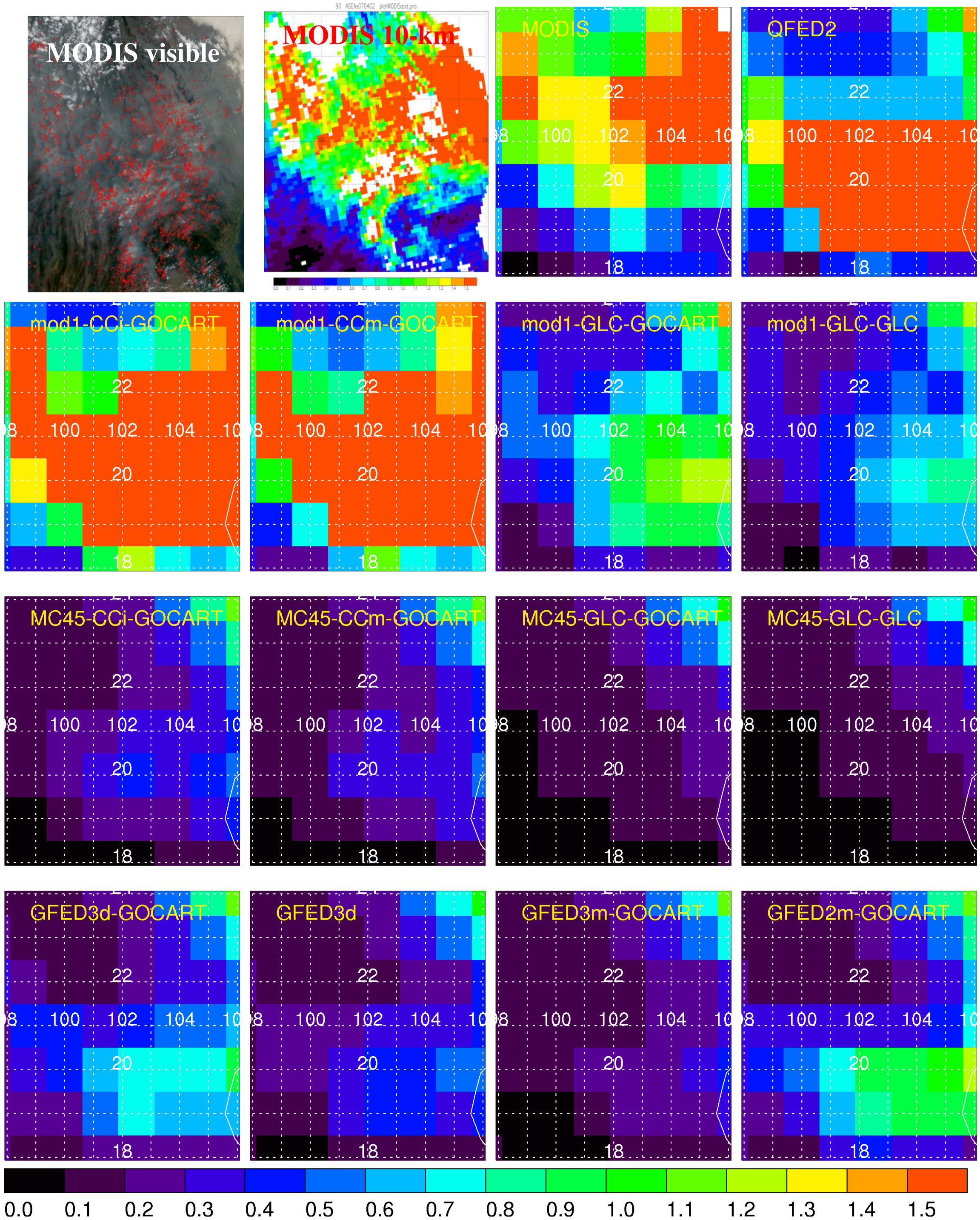

Figure A - 98 MODIS and GOCART AOD for case 90

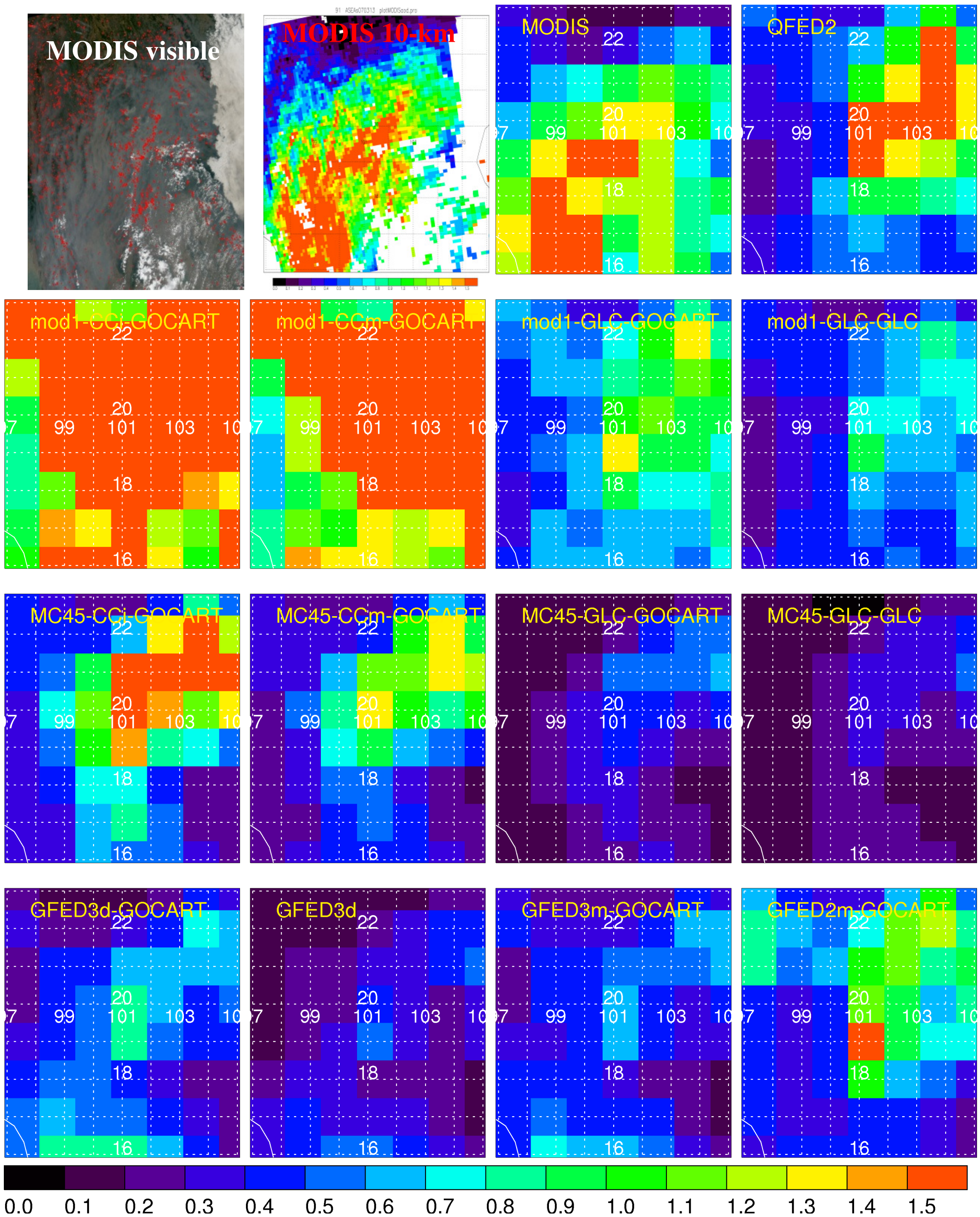

Figure A - 99 MODIS and GOCART AOD for case 91

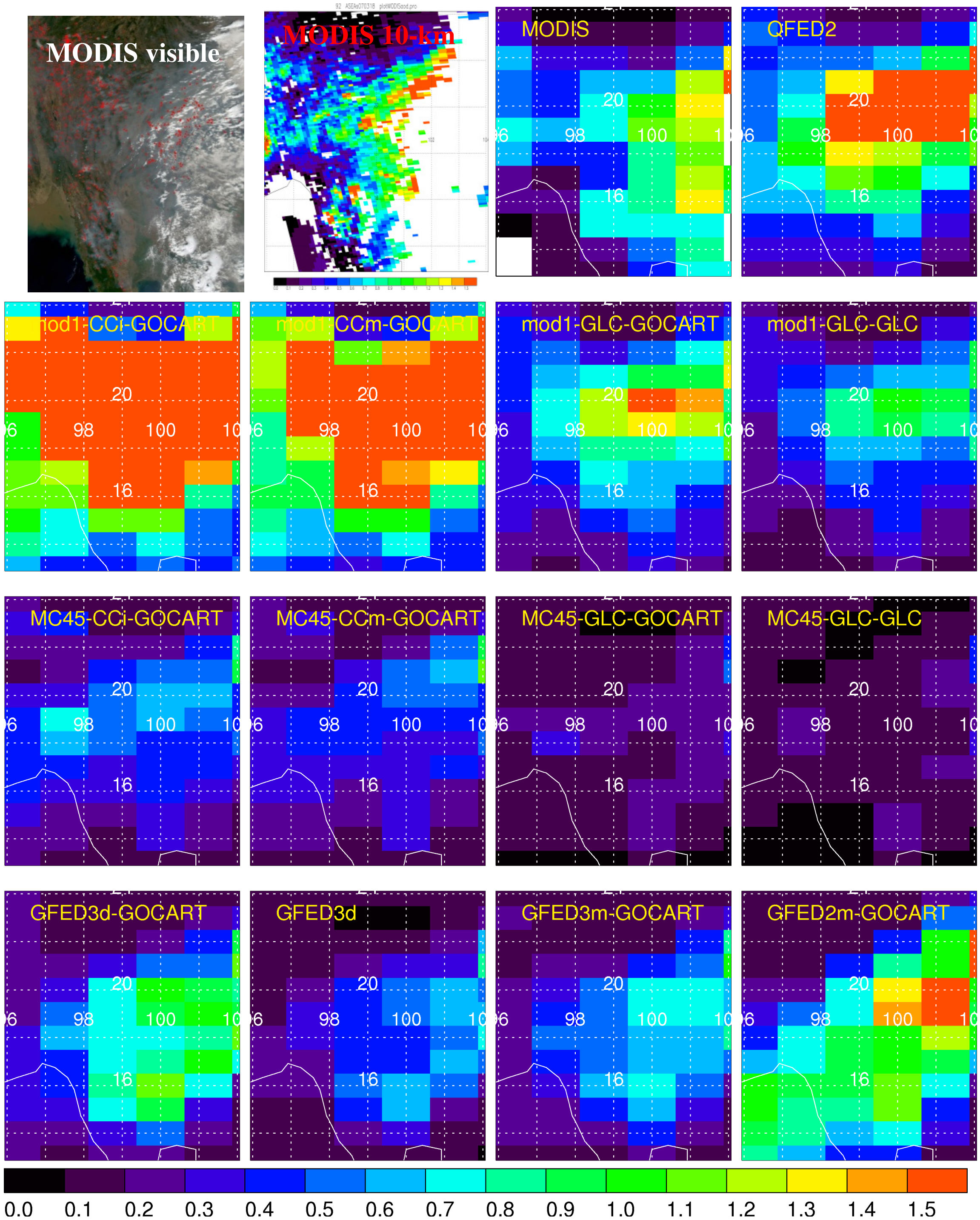

Figure A - 100 MODIS and GOCART AOD for case 92

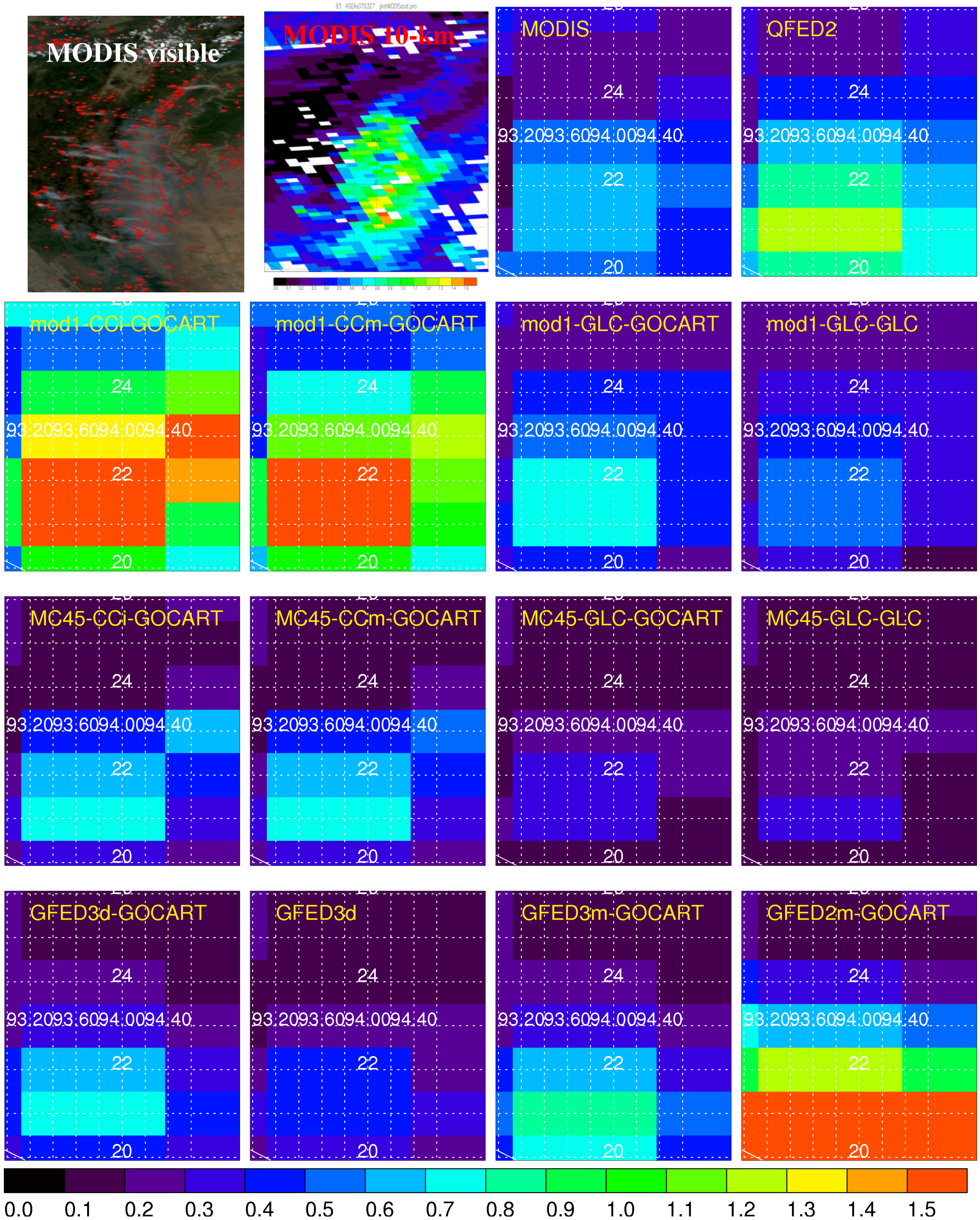

Figure A - 101 MODIS and GOCART AOD for case 93

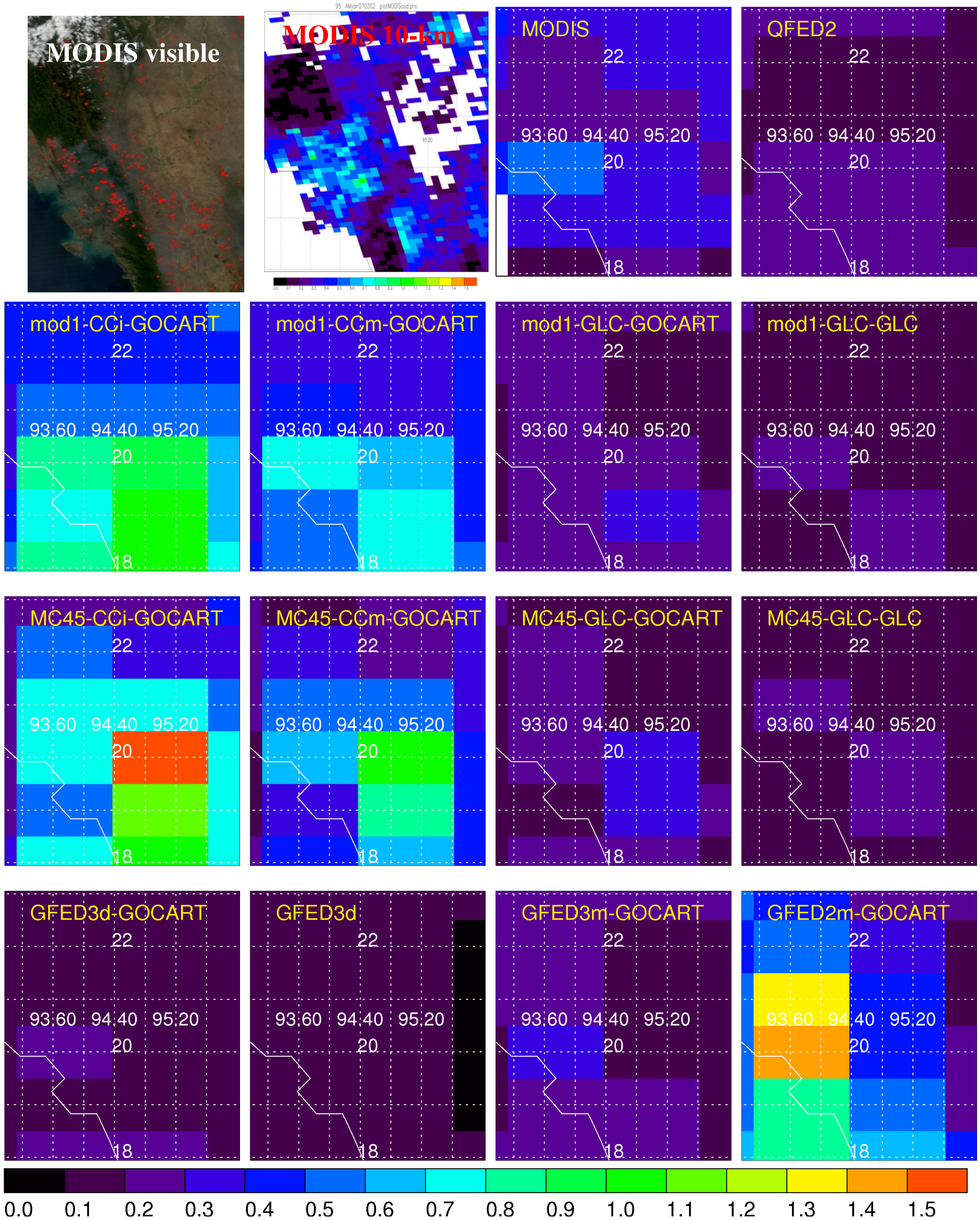

Figure A - 102 MODIS and GOCART AOD for case 95

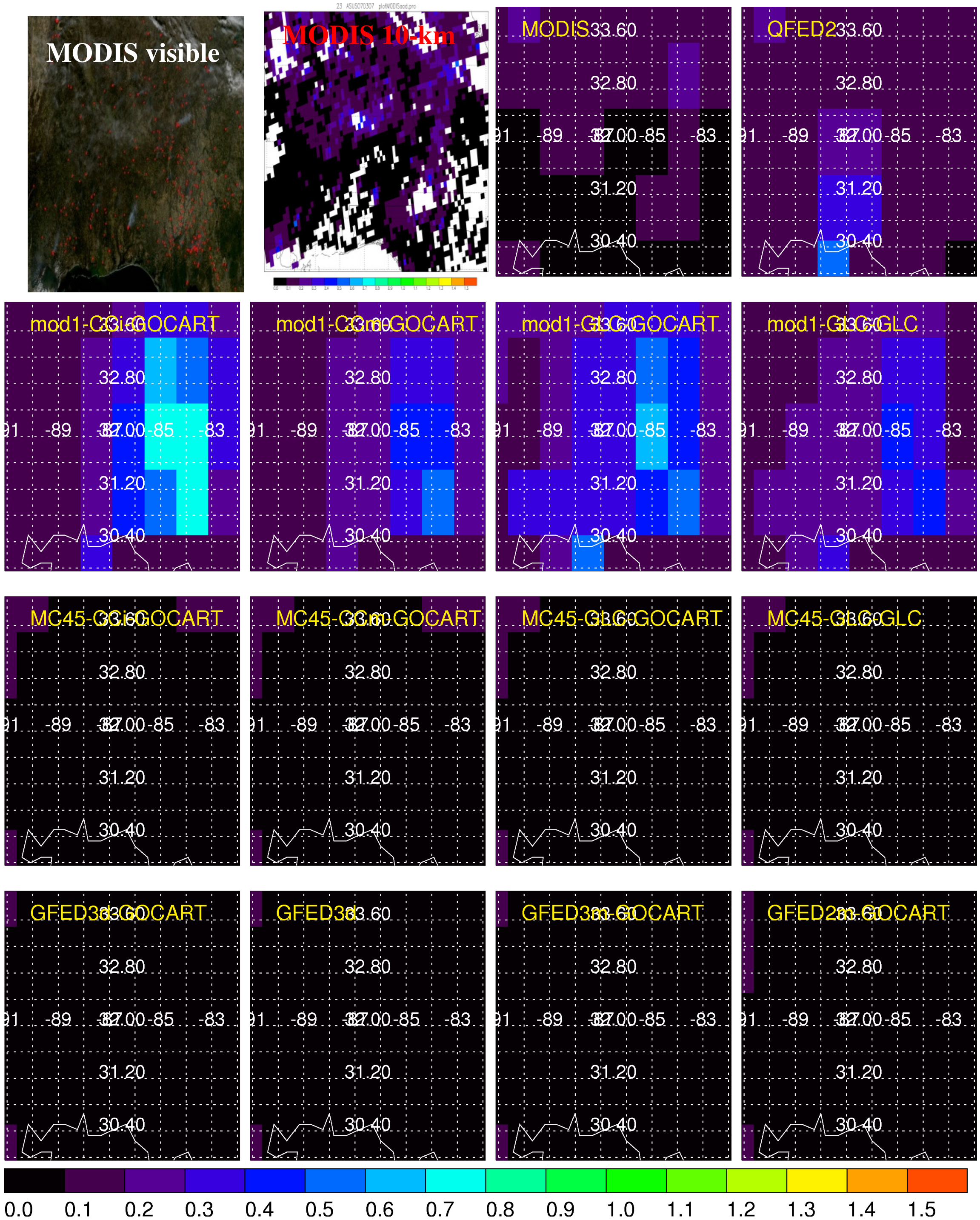

Figure A - 103 MODIS and GOCART AOD for case 23

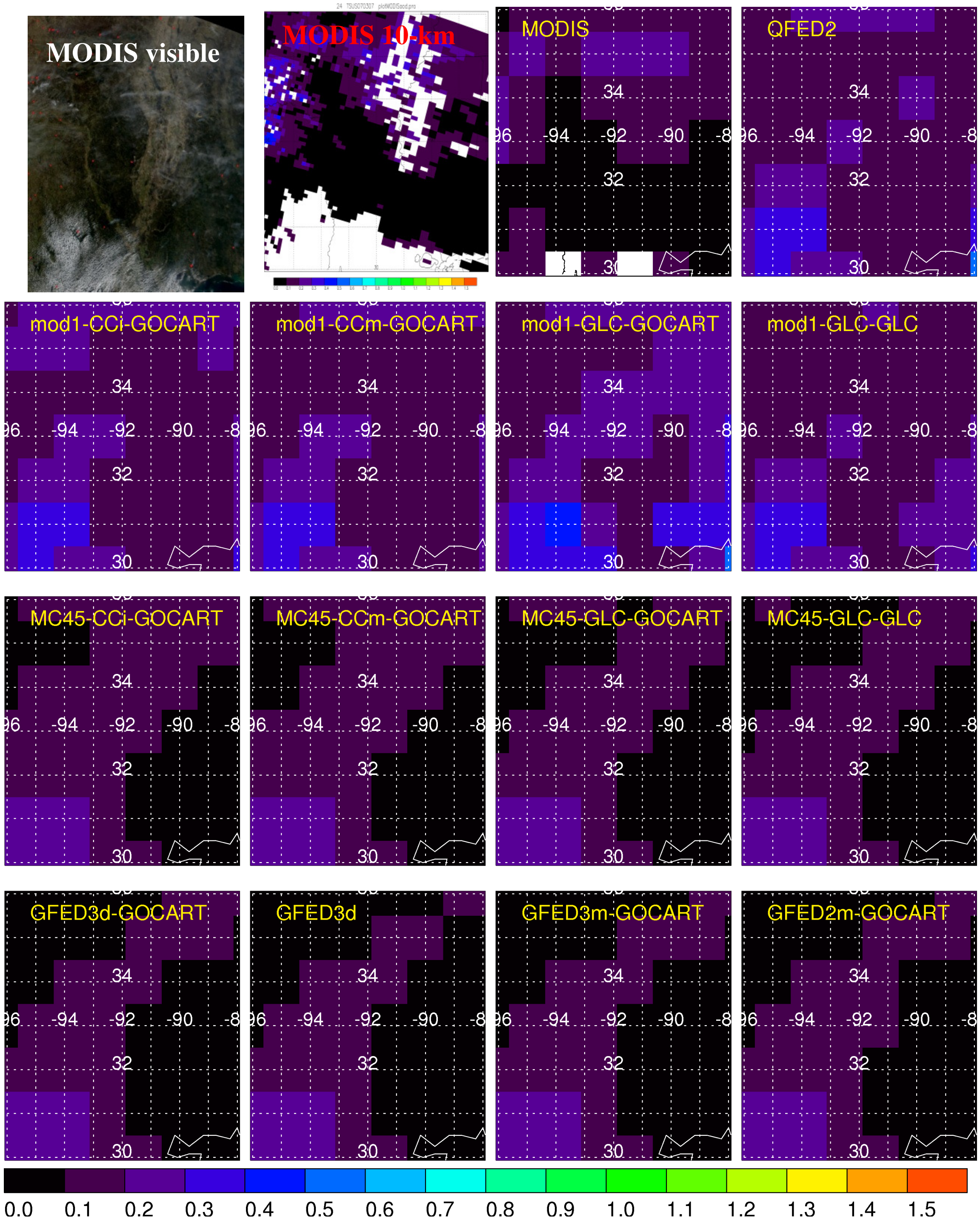

Figure A - 104 MODIS and GOCART AOD for case 24

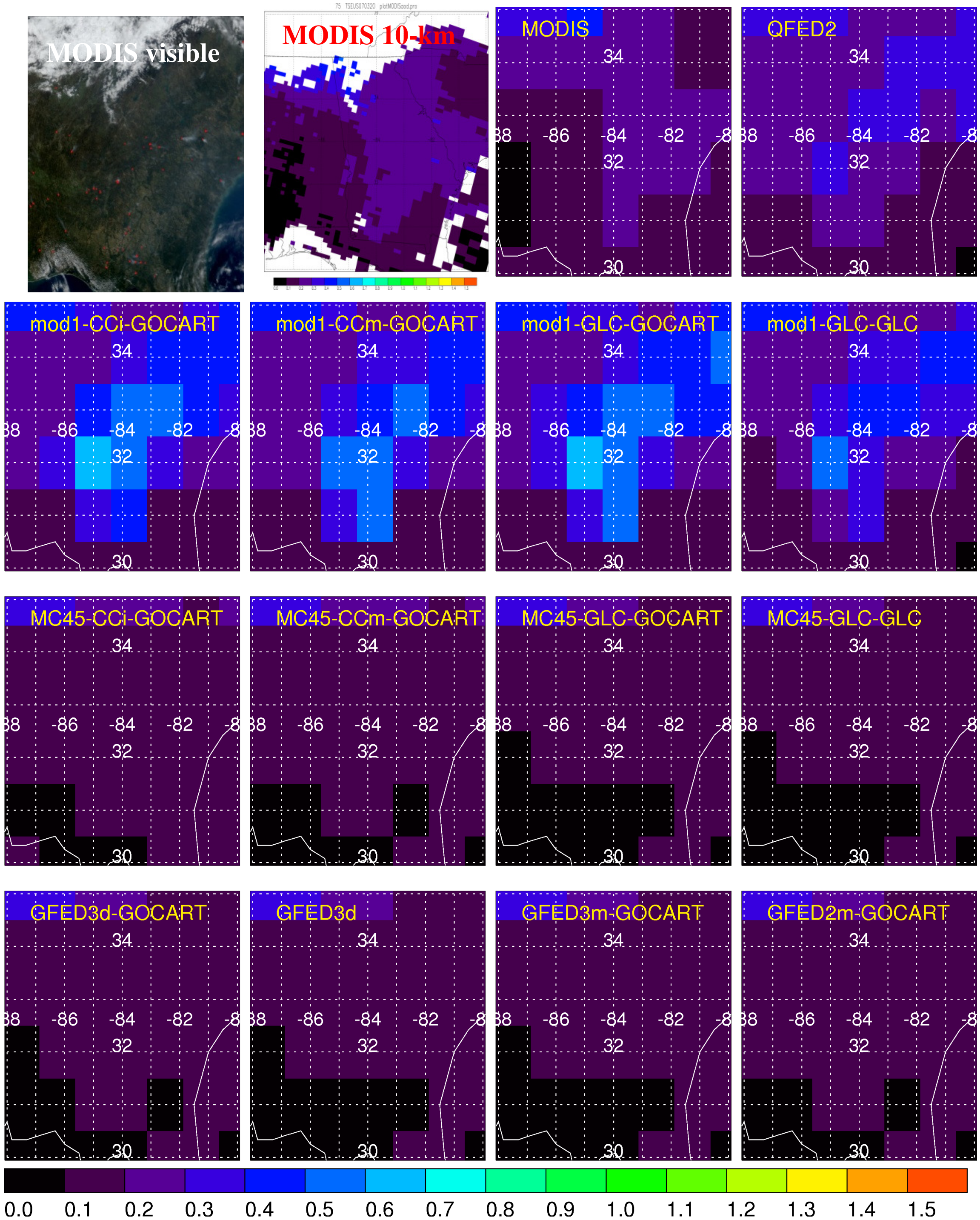

Figure A - 105 MODIS and GOCART AOD for case 75

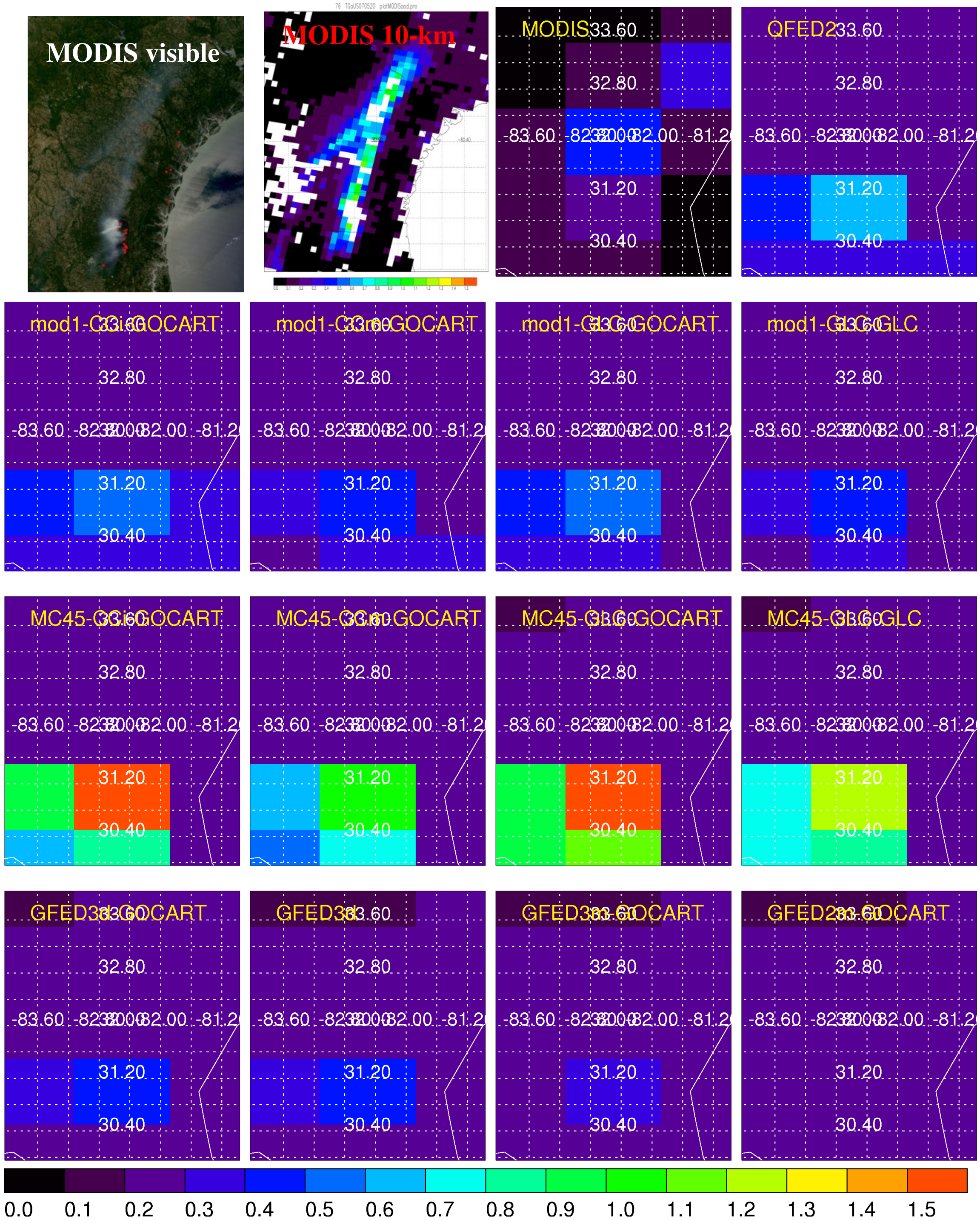

Figure A - 106 MODIS and GOCART AOD for case 76

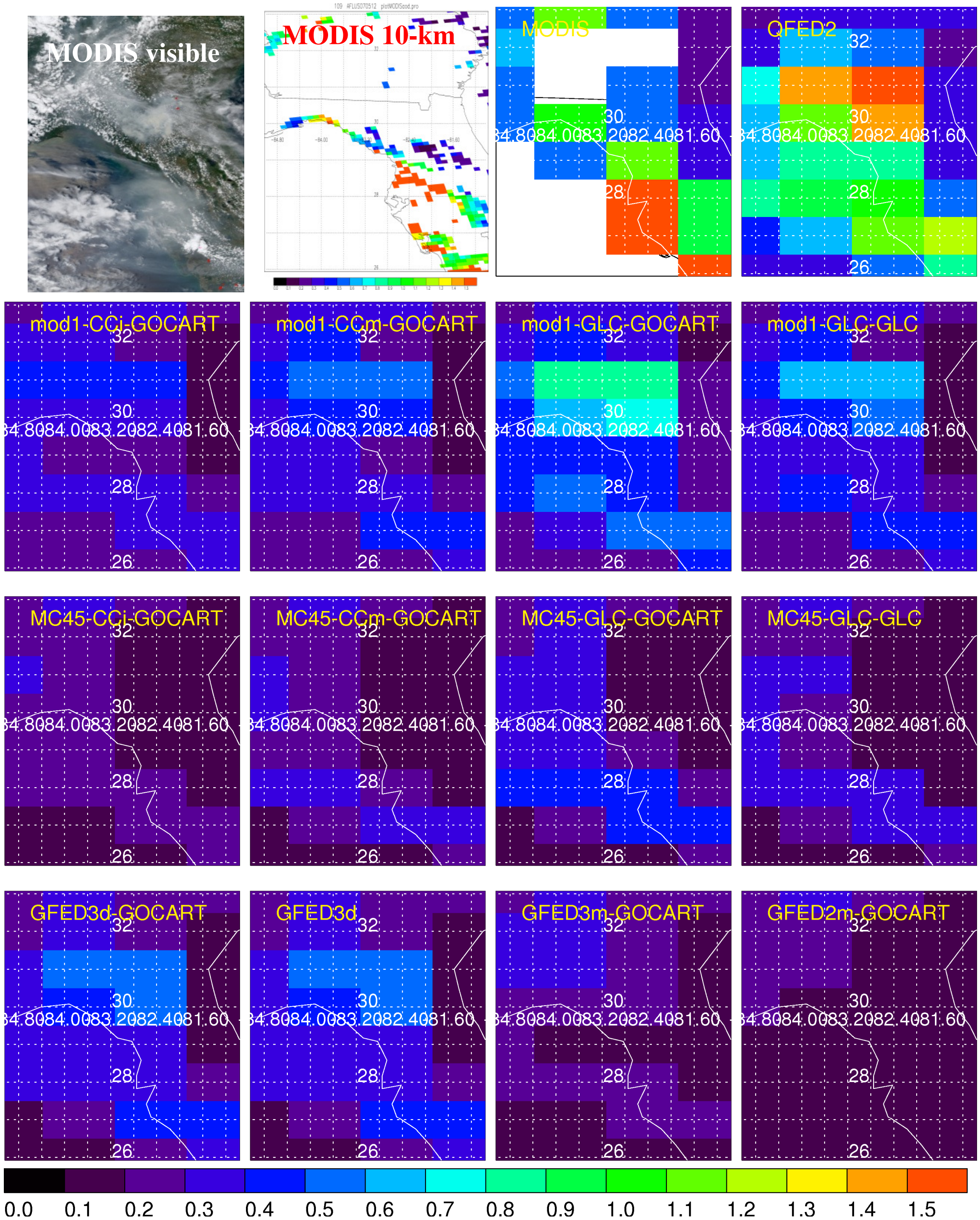

Figure A - 107 MODIS and GOCART AOD for case 109

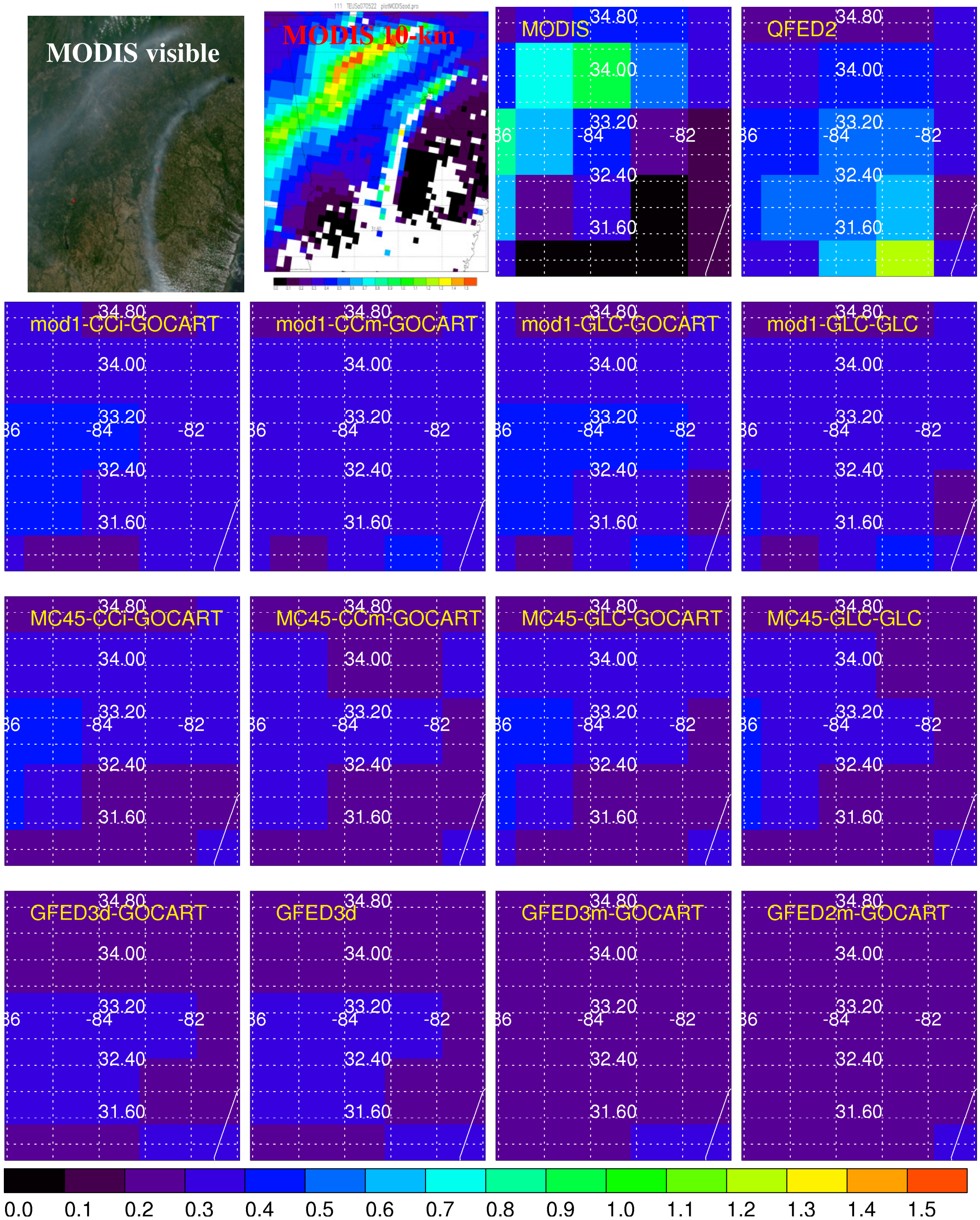

Figure A - 108 MODIS and GOCART AOD for case 111

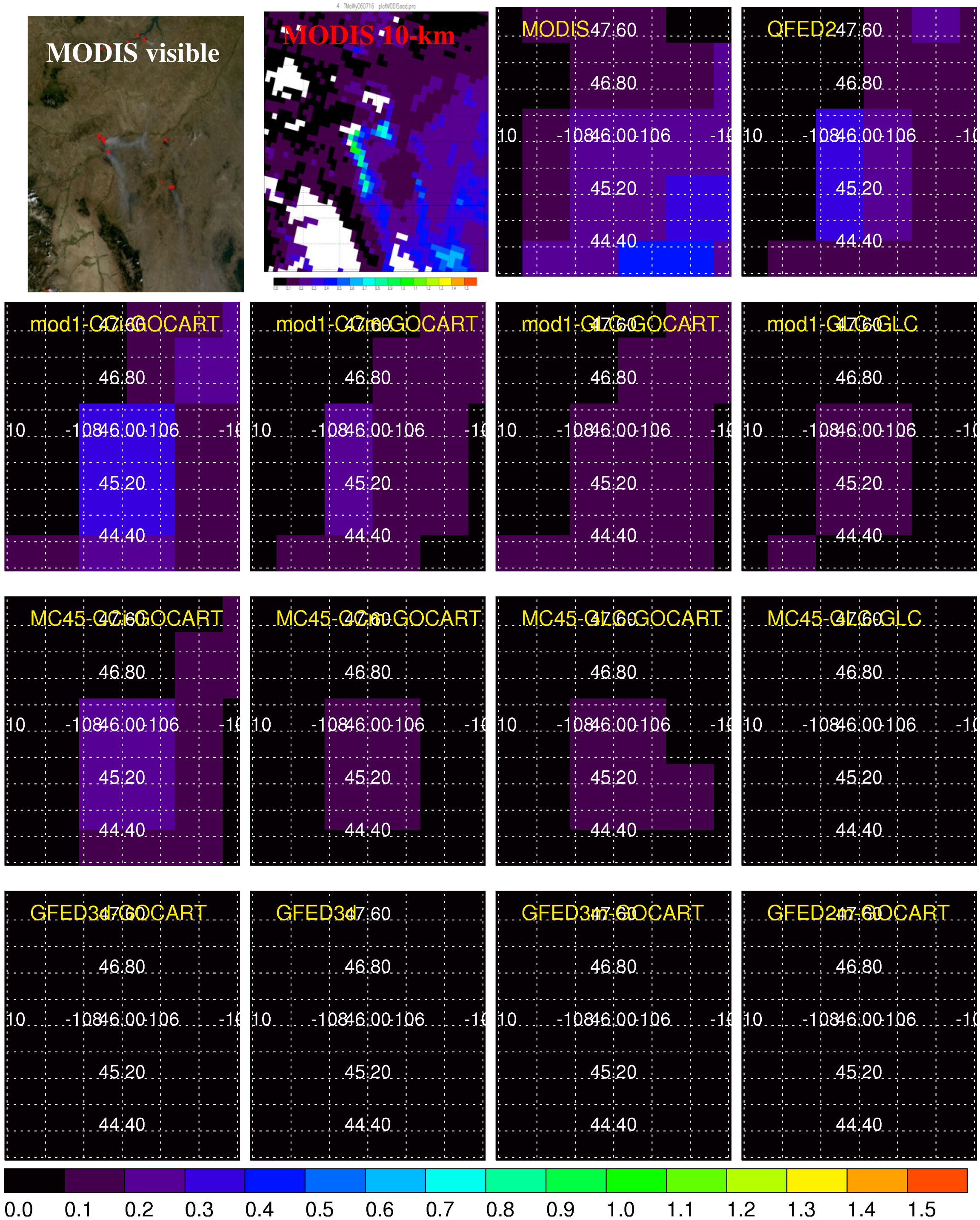

Figure A - 109 MODIS and GOCART AOD for case 4

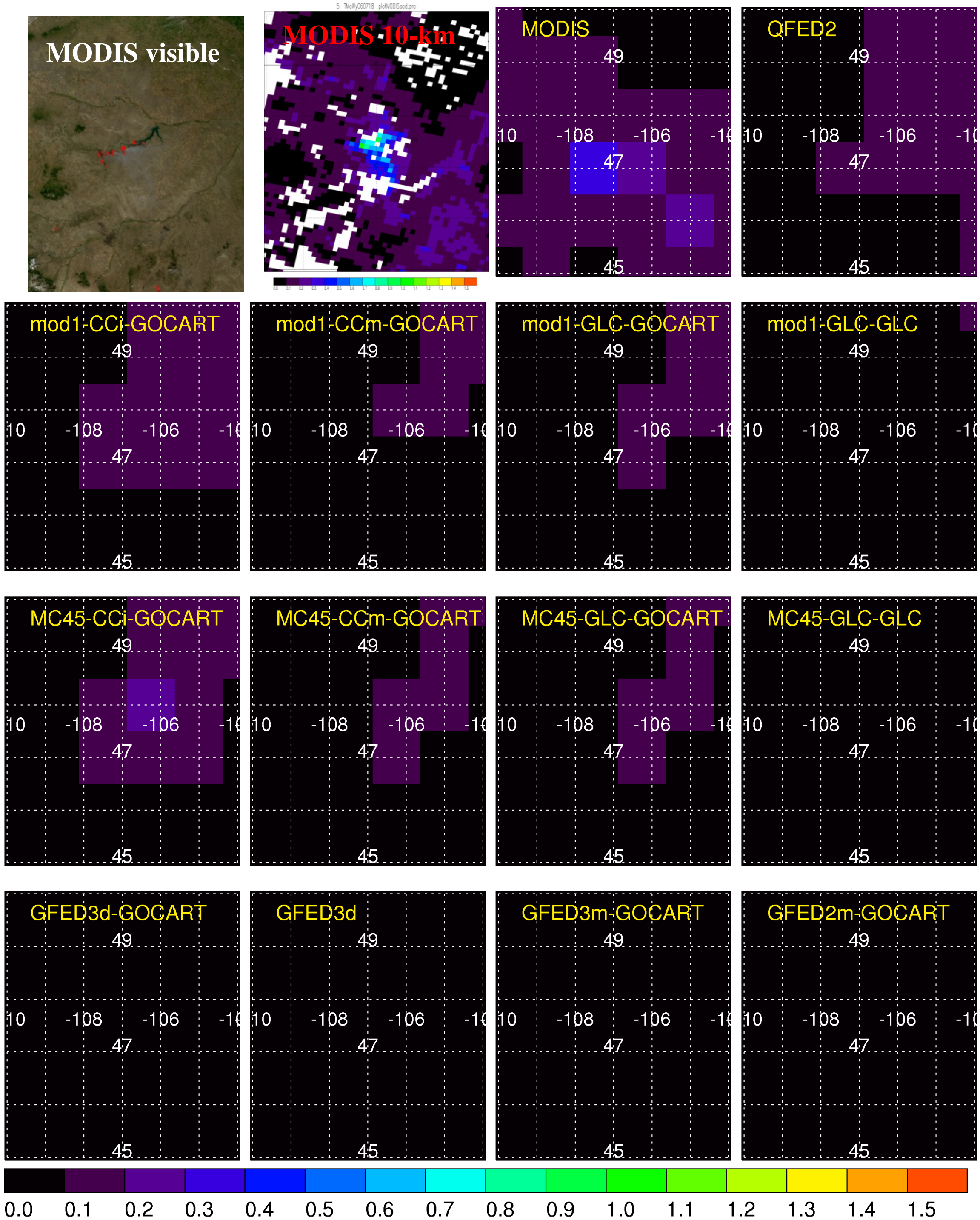

Figure A - 110 MODIS and GOCART AOD for case 5

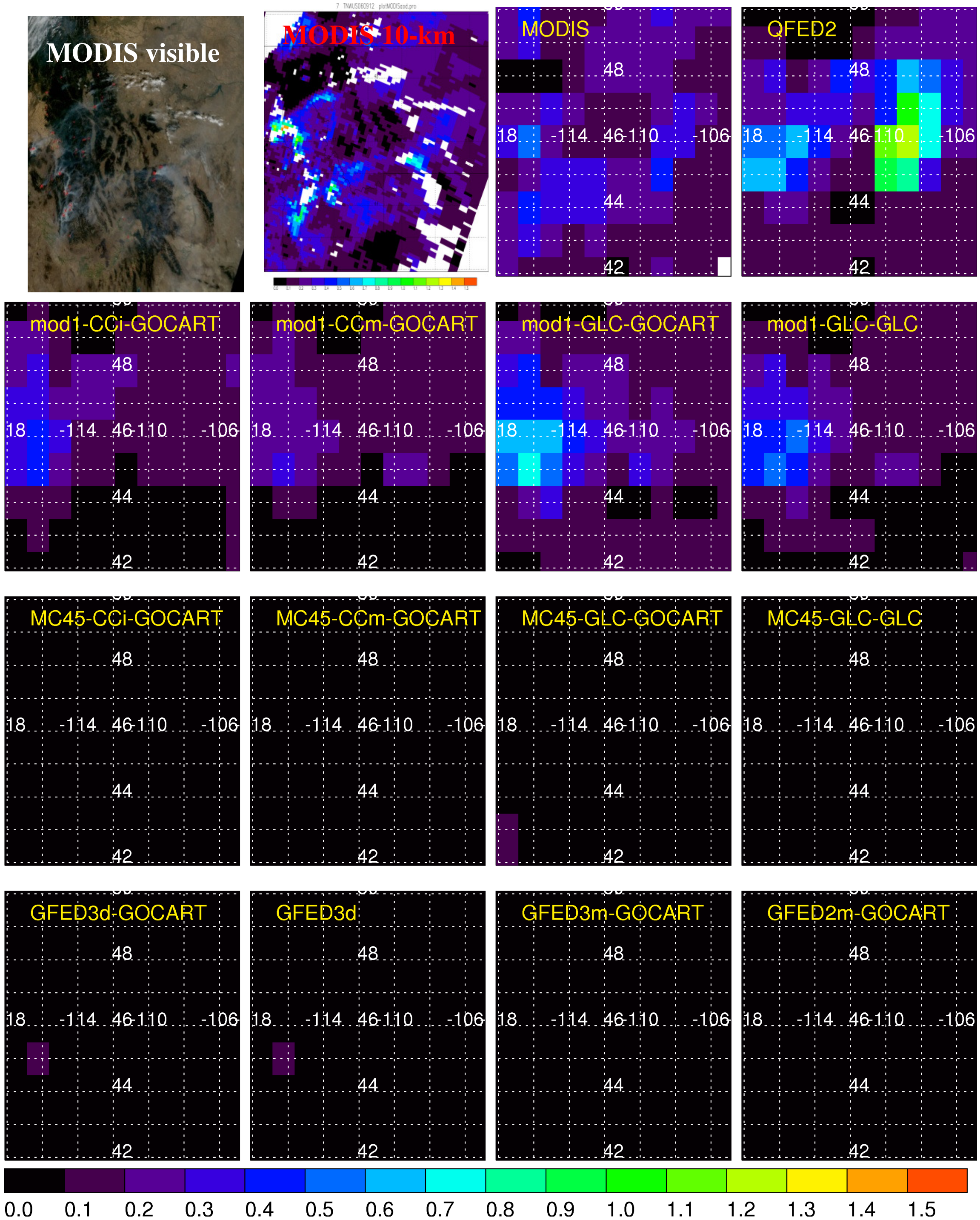

Figure A - 111 MODIS and GOCART AOD for case 7

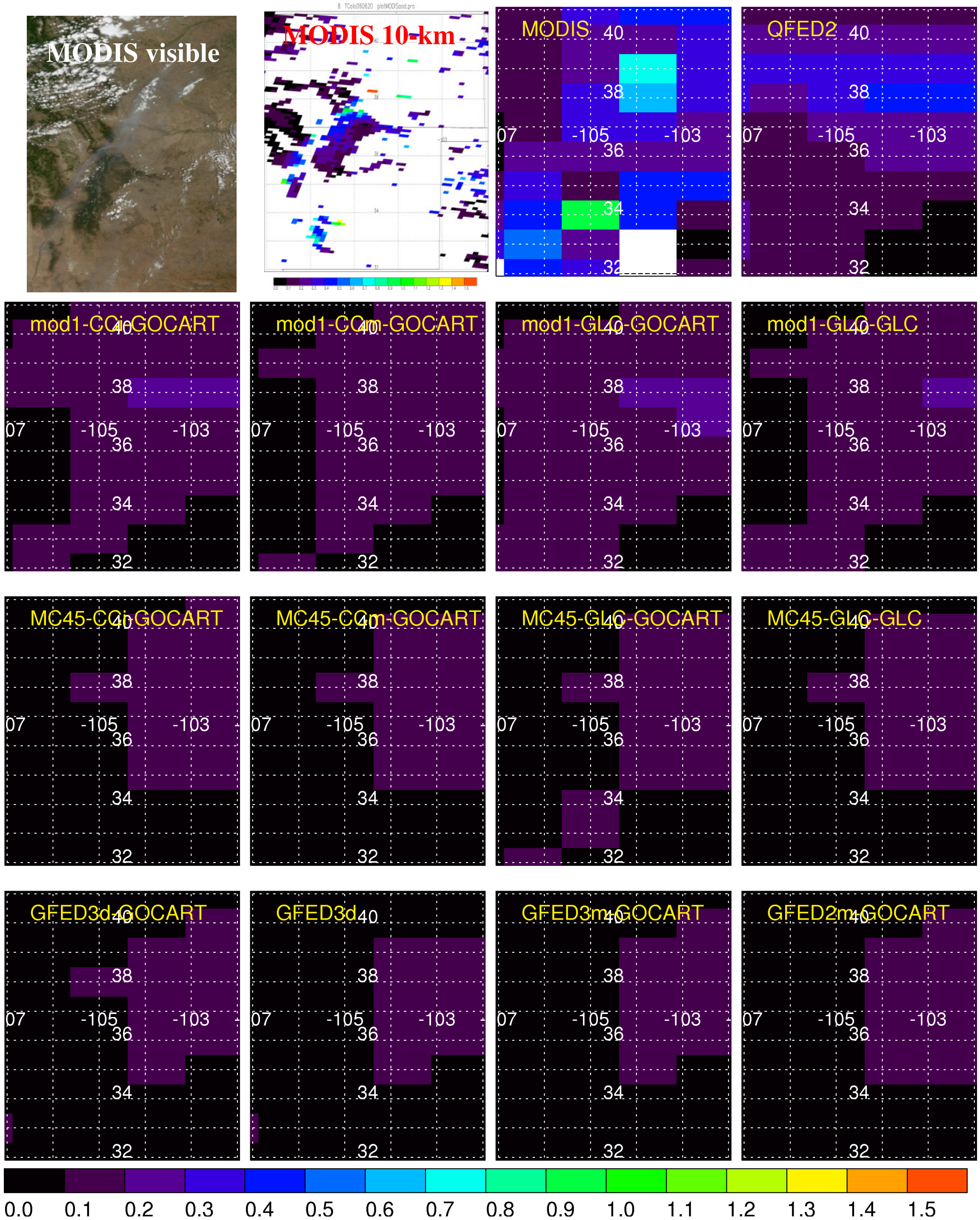

Figure A - 112 MODIS and GOCART AOD for case 8

Figure A - 113 MODIS and GOCART AOD for case 9

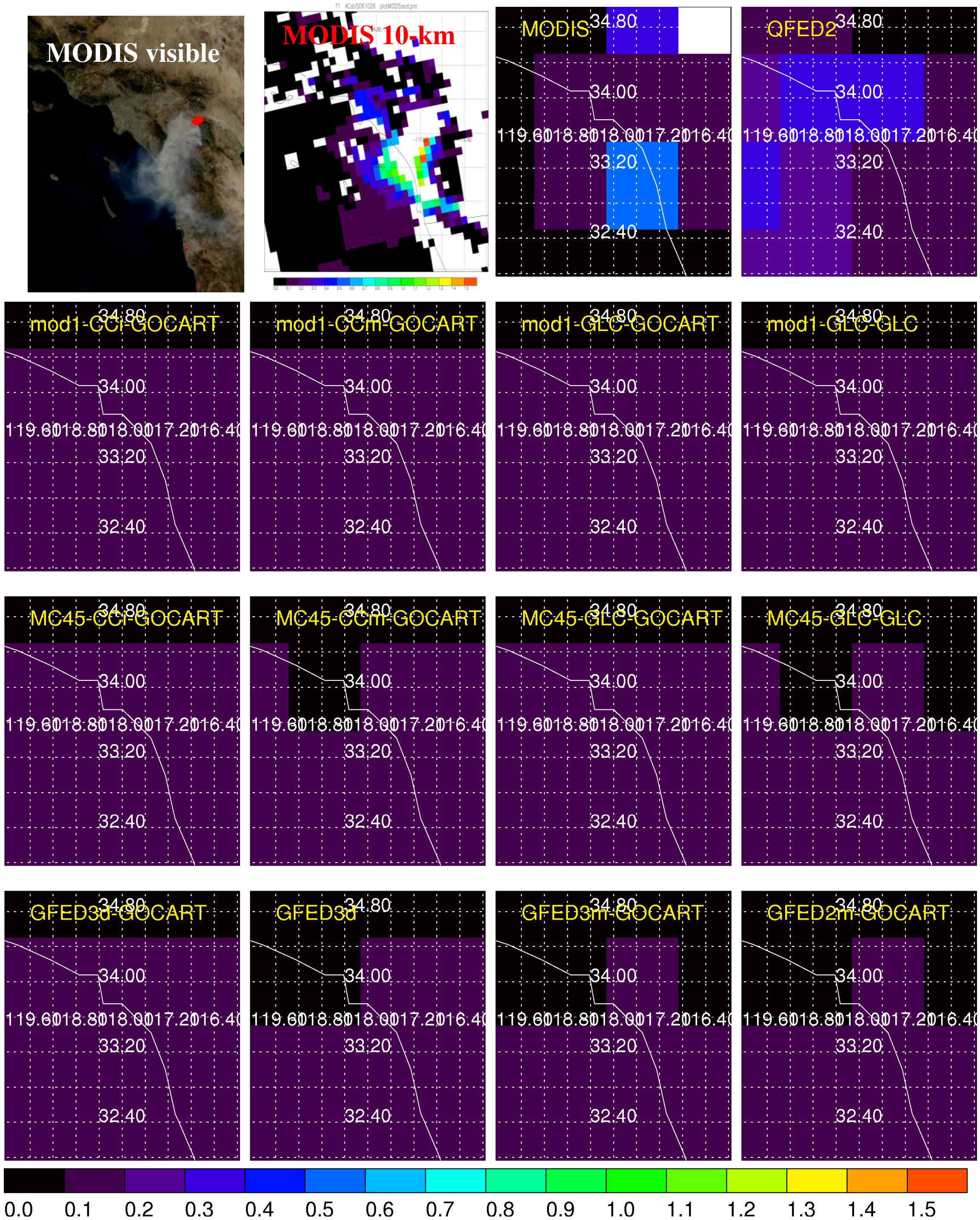

Figure A - 114 MODIS and GOCART AOD for case 71

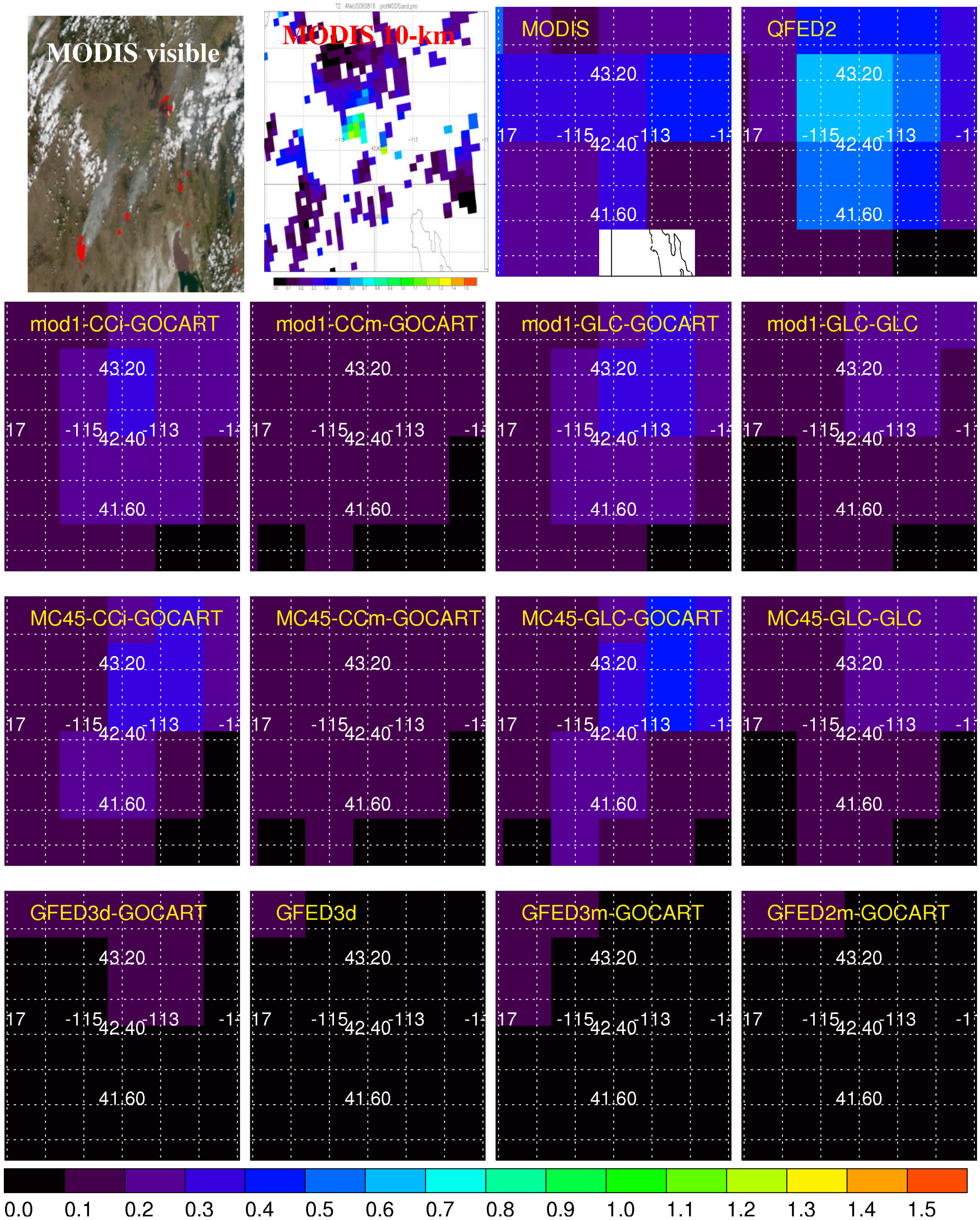

Figure A - 115 MODIS and GOCART AOD for case 72

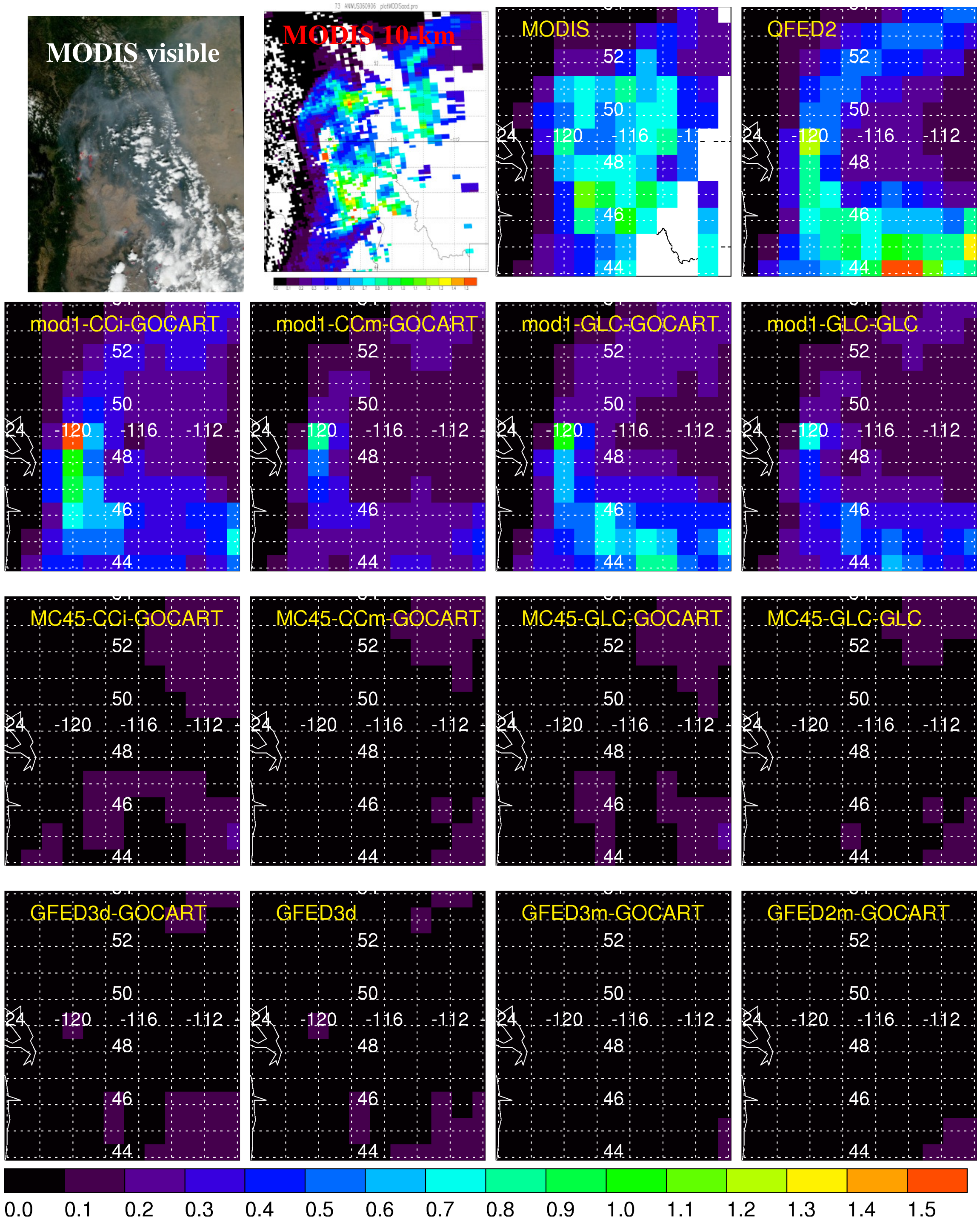

Figure A - 116 MODIS and GOCART AOD for case 73

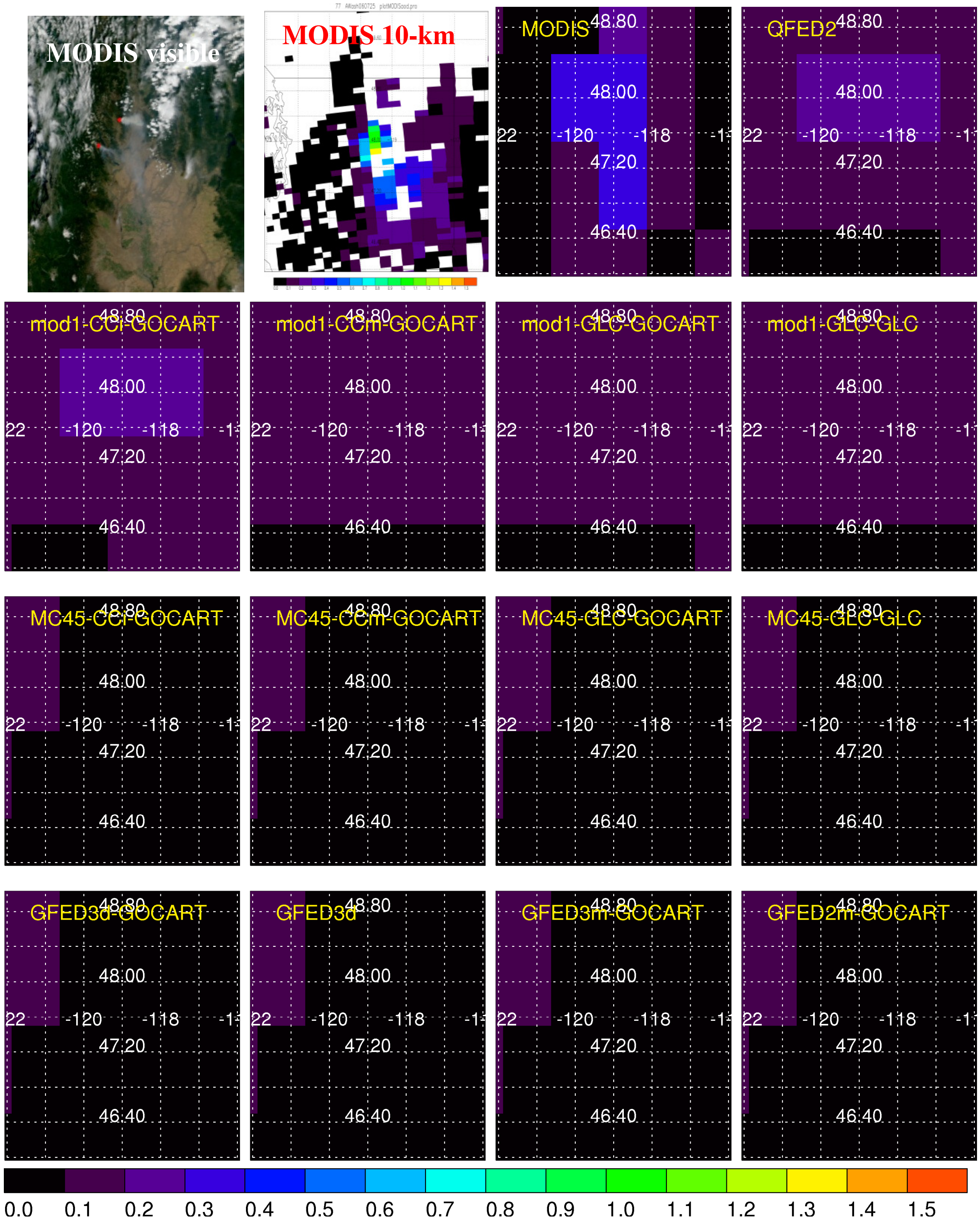

Figure A - 117 MODIS and GOCART AOD for case 77

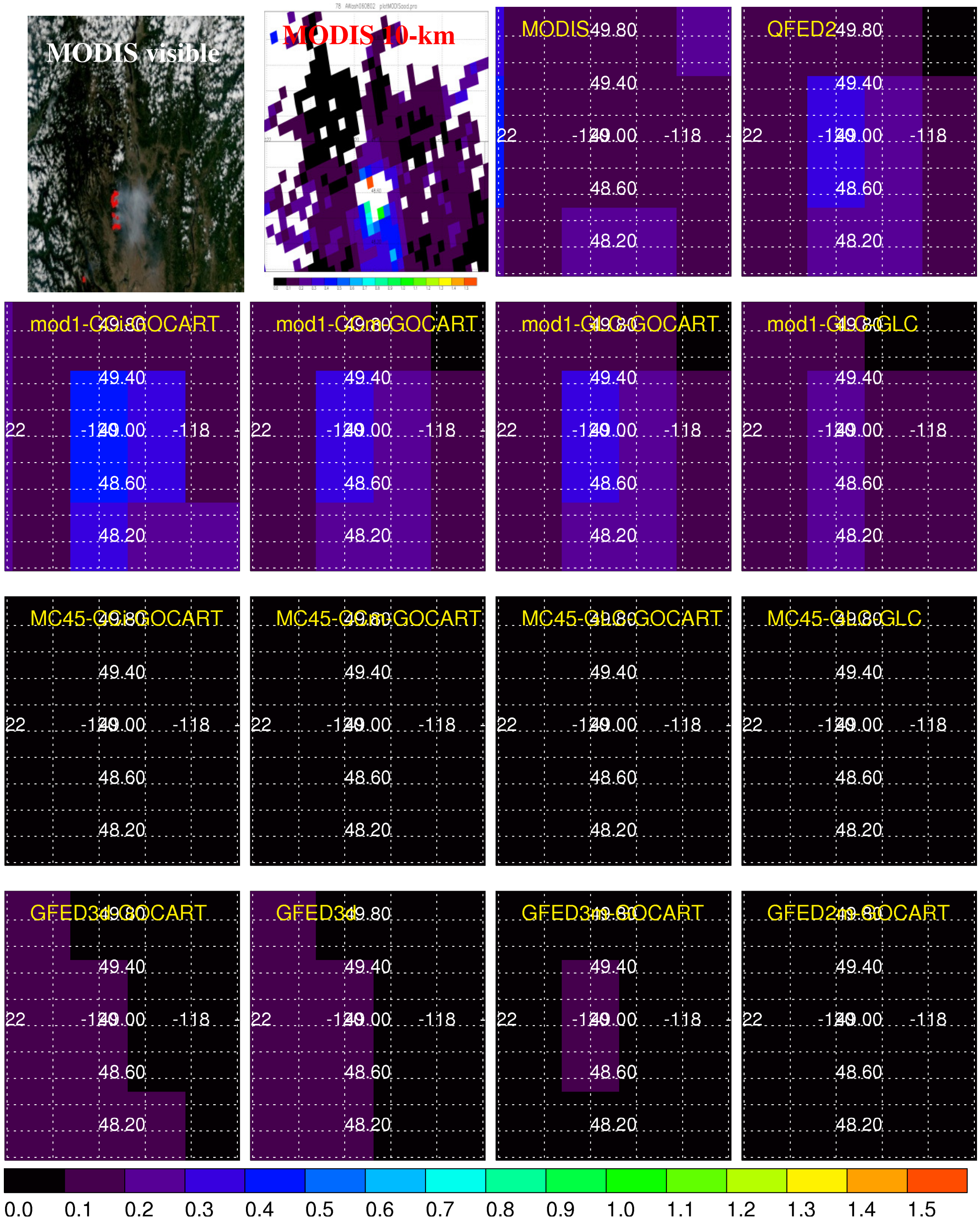

Figure A - 118 MODIS and GOCART AOD for case 78

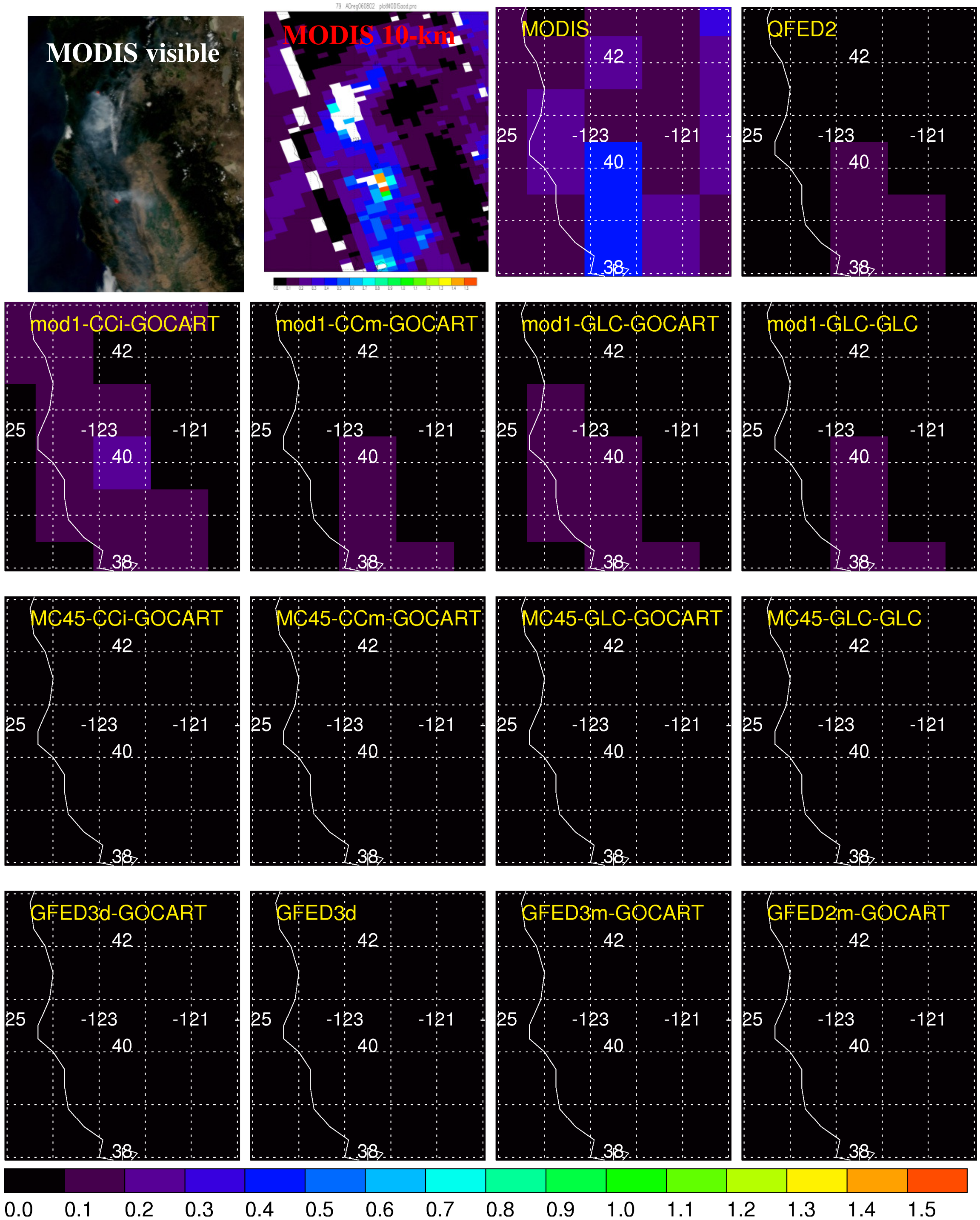

Figure A - 119 MODIS and GOCART AOD for case 79

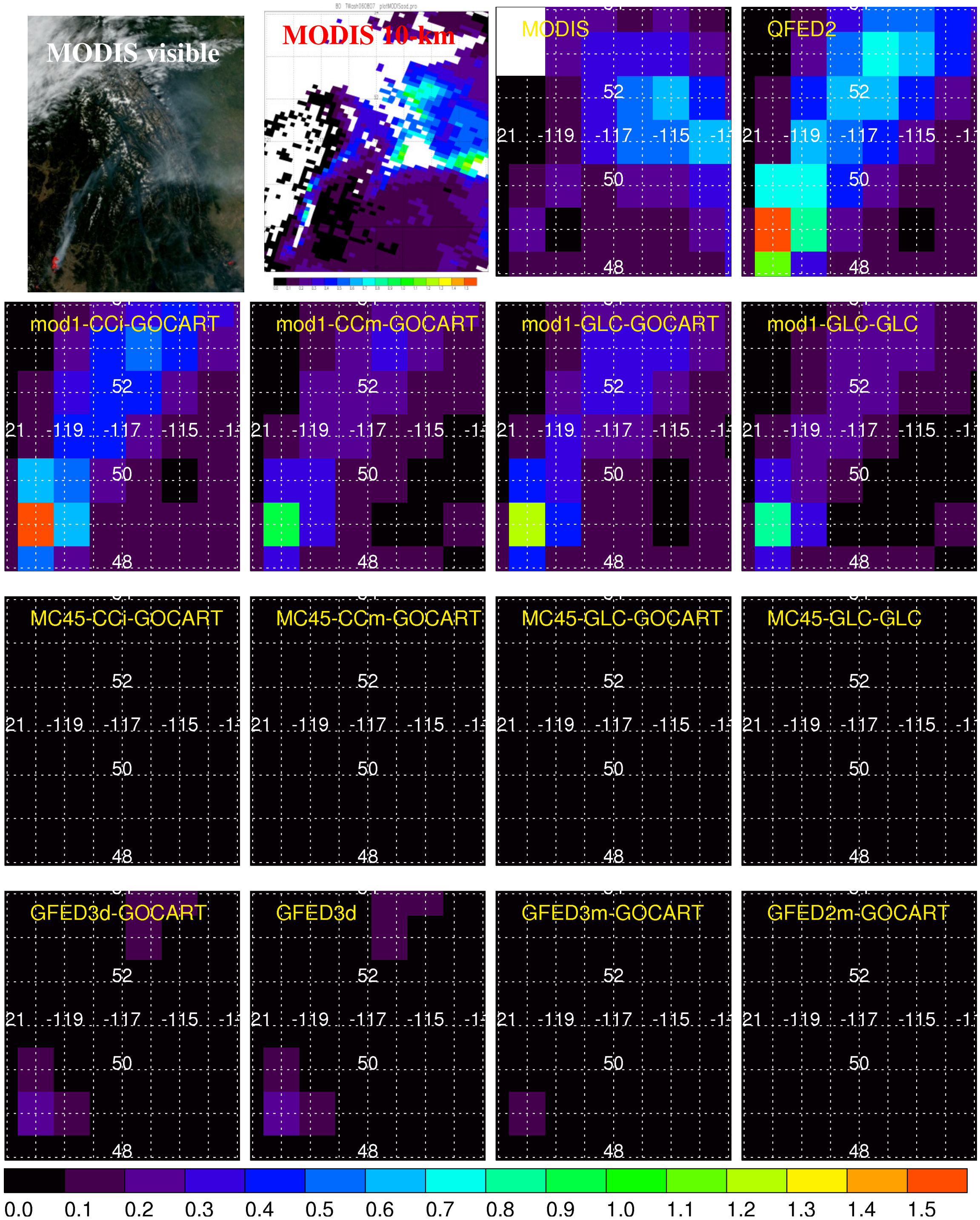

Figure A - 120 MODIS and GOCART AOD for case 80

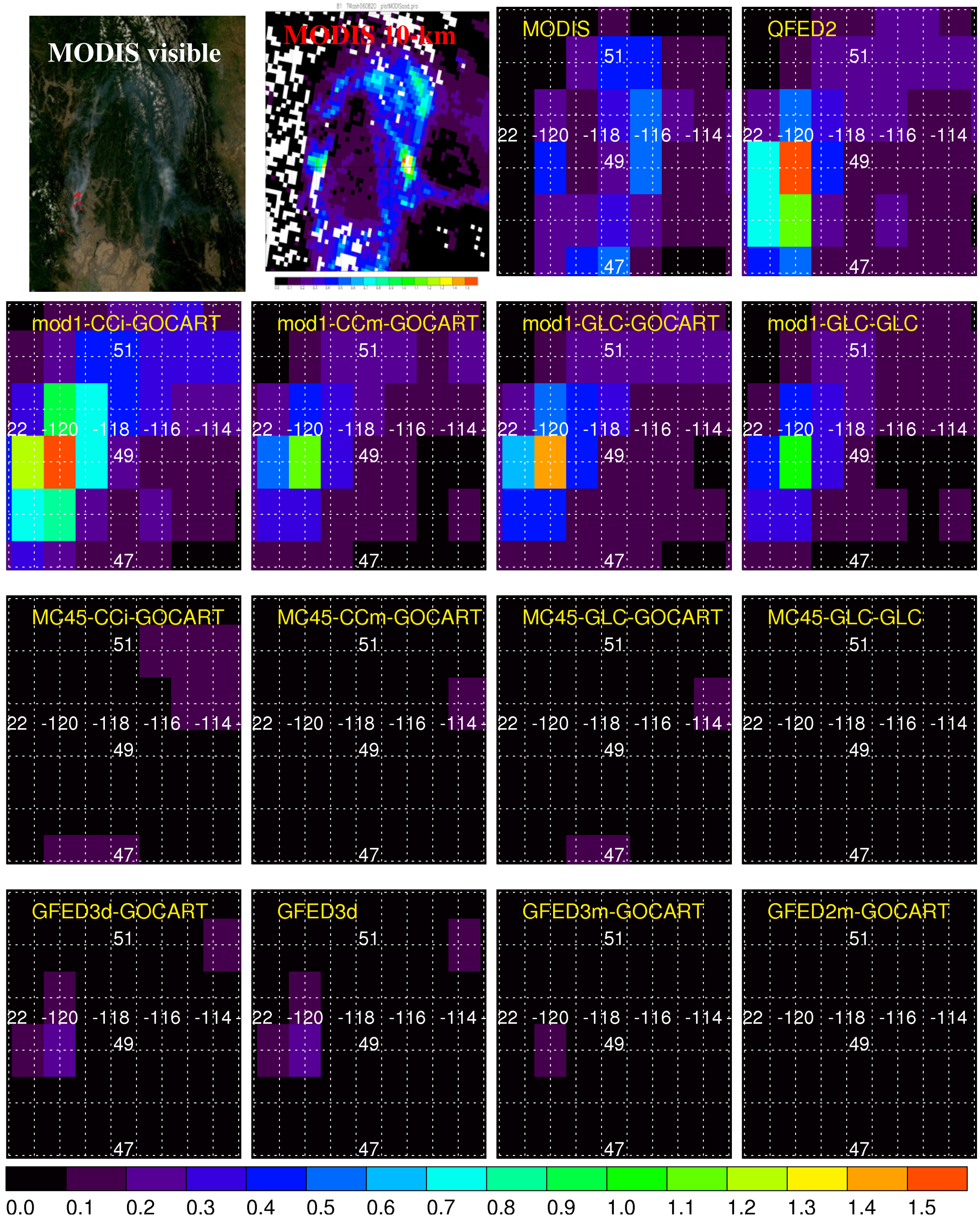

Figure A - 121 MODIS and GOCART AOD for case 81

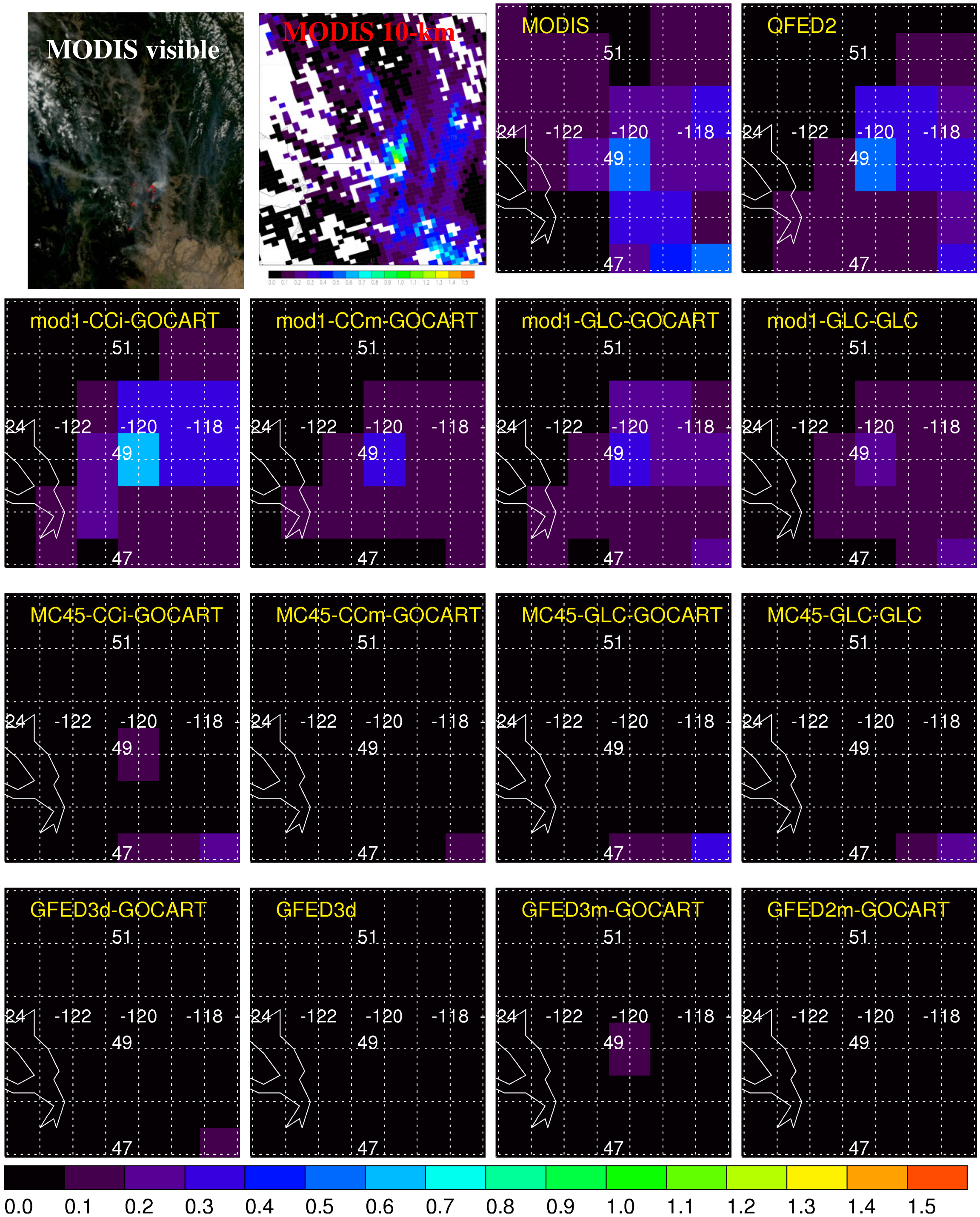

Figure A - 122 MODIS and GOCART AOD for case 82

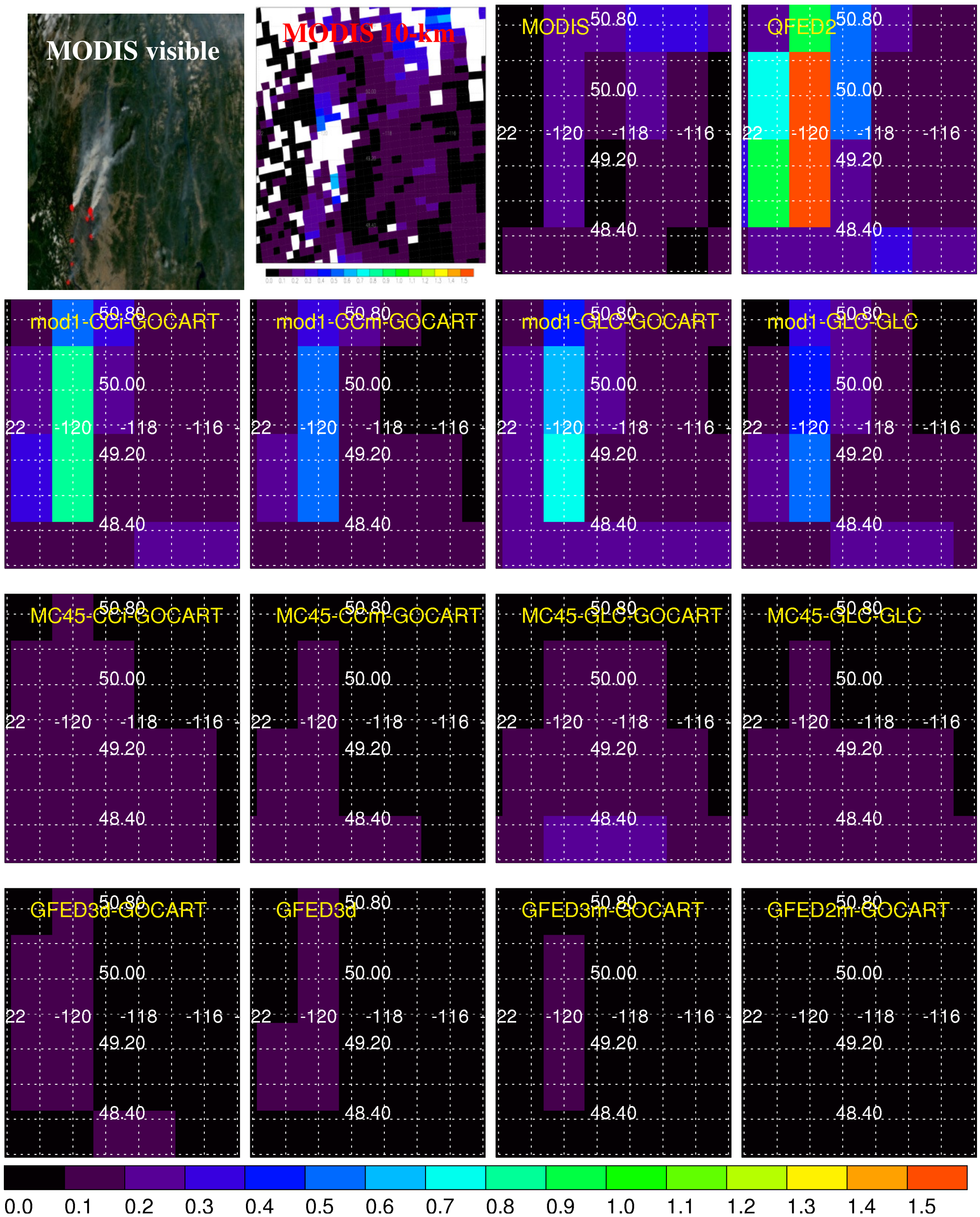

Figure A - 123 MODIS and GOCART AOD for case 83

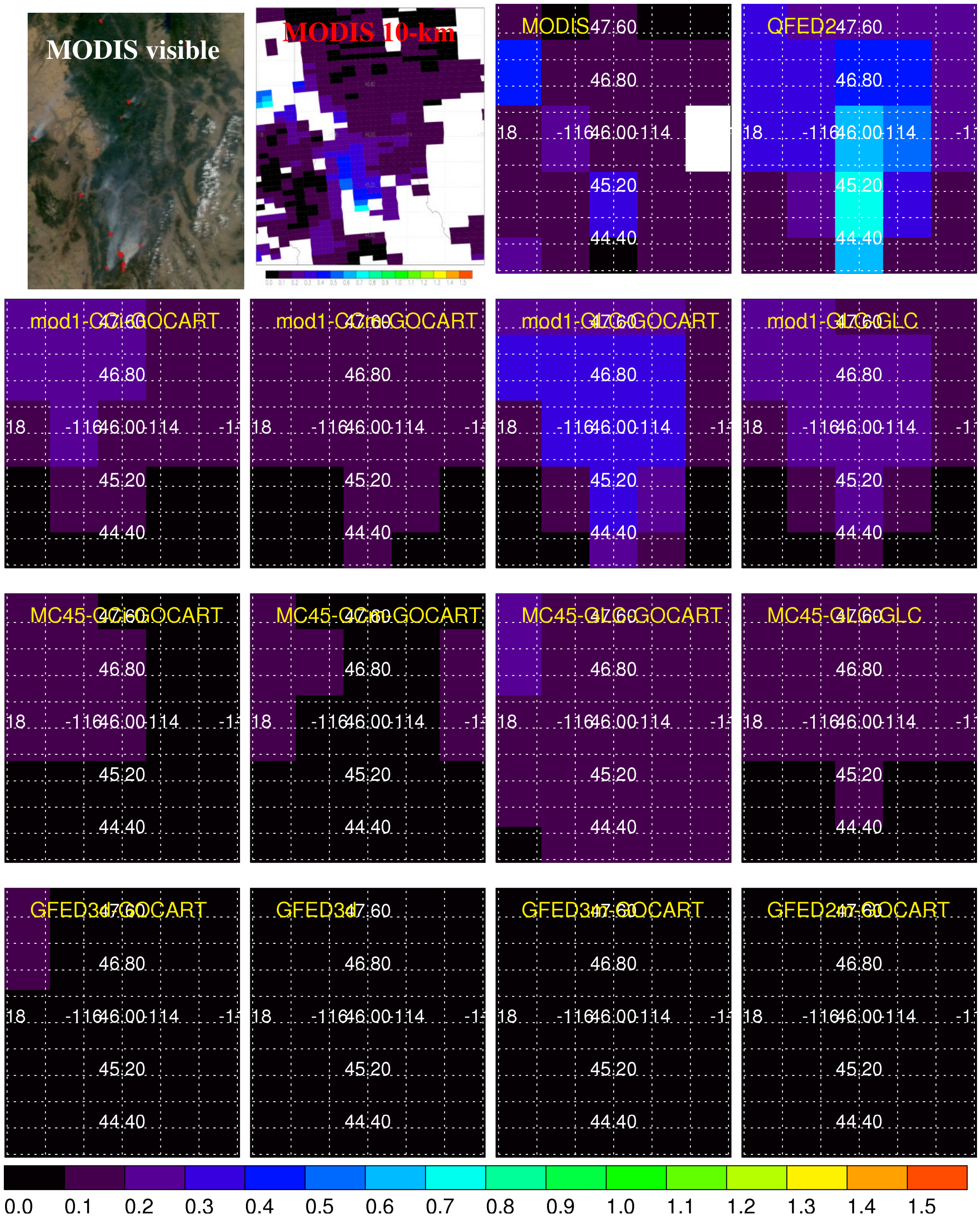

Figure A - 124 MODIS and GOCART AOD for case 84

VITA

VITA

Mariya Petrenko
Department of Earth and Atmospheric Sciences, Purdue University

Education

B.S., Environmental Science, 2003, National University of "Kiev-Mohyla Academy", Kyiv, Ukraine

M.S., Atmospheric Sciences, 2006, University of Wyoming, Laramie, Wyoming

Ph.D., Atmospheric Science, 2012, Purdue University, West Lafayette, Indiana

Research Interests

Modeling and Observations of Atmospheric Aerosols

Publications

Petrenko, M., R. Kahn, M. Chin, A. Soja, T. Kucsera, and Harshvardhan (2012), The use of satellite-measured aerosol optical depth to constrain biomass burning emissions source strength in a global model GOCART. Submitted to *Journal of Geophysical Research - Atmospheres*.

Montague D. C., **M. Petrenko**, Y. Cai, and T. Deshler (2012), Reconciling Measured Ambient Aerosol Mass and Size Distributions from an Aerodyne Aerosol Mass Spectrometer (AMS), a Scanning Mobility Particle Sizer, and from Filters: Implications for AMS Collection Efficiency, Filter Collection Artifacts, and Carbon Content of Aerosol Organics. To be submitted to *Aerosol Science and Technology*.

Maksymchuk, M. M., O. M. Kartavtsev, and **M. M. Shcherbyna** (2003), The Use of Corporate GIS in Public Health Services (in Ukrainian). *Hygiene of Inhabited Localities* (Journal of Ministry of Health of Ukraine), *41*, 463-467.

Conference Presentations

Petrenko, M., R. Kahn, M. Chin, T. Kucsera, A. Soja, and Harshvardhan, Using satellite aerosol observations to constrain biomass burning emissions in the GOCART model. *Fall Meeting of American Geophysical Union (AGU)*. San Francisco, California, USA. December 12-16, 2011

Petrenko, M., R. Kahn, M. Chin, T. Kucsera, A. Soja, and Harshvardhan, Using spaceborne aerosol observations to constrain biomass burning emissions in the GOCART model. *Fall Meeting of American Geophysical Union (AGU)*. San Francisco, California, USA. December 13-17, 2010

Petrenko, M., R. Kahn, M. Chin, T. Kucsera, A. Soja, and Harshvardhan, Using satellite-measured AOD to constrain biomass burning emissions in the GOCART model. *NASA A-train symposium*. New Orleans, LA, USA, October 25-28, 2010.

Petrenko, M.M. Spatial and temporal resolution of satellite-based biomass burning emission inventories for the global aerosol model (GOCART). *Talk at the Junior Faculty Forum.* Boulder, CO, USA, 13-16 July 2010.

Petrenko, M., M. Chin, and Q. Tan, Relation of Lower Atmospheric Stability (Haines) Index to properties of fires and smoke plumes observed from satellites. *Fall Meeting of American Geophysical Union (AGU)*. San Francisco, California, USA. December 14-18, 2009

Petrenko, M., Chin, M., Tan, Q. and Kahn, R. Study of biomass burning plume heights using combined satellite measurements (poster presentation). *Fall Meeting of American Geophysical Union (AGU)*. San Francisco, California, USA. December 14-19, 2008

Petrenko, M., Chin, M., Diehl, T., Kucsera, T. and Soja, A.J. Investigation of properties of biomass and wildfires to improve global estimates of biomass burning emissions (poster presentation). *Fall Meeting of American Geophysical Union (AGU)*. San Francisco, California, USA. December 10-14, 2007

Selected Awards and Honors

2011 Outstanding Student Paper Award for poster presentation at the 2010 Fall Meeting in San Francisco, CA.

2008 – 2011 NASA Earth and Space Science graduate fellowship

2007 Third place student poster presentation at the 87th AMS Annual Meeting in San Antonio, Texas, USA

2007 Purdue University Women in Science Program travel grant (2007 AGU Fall Meeting)

2007 F. P. Low Travel Grant from Purdue Department of Earth and Atmospheric Sci. (2007 AGU Fall Meeting)

2007 Frederick N. Andrews Environmental Travel Grant (travel to 2007 summer school in Germany)

2007 Atmospheric Chemistry Travel Grant from NASA & AMS (87th AMS Annual Meeting)

2006 American Meteorological Society (AMS) Global Change Scholarship (86th AMS Annual Meeting)